Assessment and Optimisation of Digital Radiography Systems for Clinical Use

Philip Doyle, BSc. MSc.

Submitted in fulfilment of the requirements for the degree of Doctor of Philosophy

Department of Clinical Physics
Faculty of Medicine
University of Glasgow

December 2008

Abstract

Digital imaging has long been available in radiology in the form of computed tomography (CT), magnetic resonance imaging (MRI) and ultrasound. Initially the transition to general radiography was slow and fragmented but in the last 10-15 years in particular, huge investment by the manufacturers, greater and cheaper computing power, inexpensive digital storage and high bandwidth data transfer networks have lead to an enormous increase in the number of digital radiography systems in the UK. There are a number of competing digital radiography (DR) technologies, the most common are computer radiography (CR) systems followed by indirect digital radiography (IDR) systems.

To ensure and maintain diagnostic quality and effectiveness in the radiology department appropriate methods are required to evaluate and optimise the performance of DR systems. Current semi-quantitative test object based methods routinely used to examine DR performance suffer known short comings, mainly due to the subjective nature of the test results and difficulty in maintaining a constant decision threshold among observers with time. Objective image quality based measurements of noise power spectra (NPS) and modulation transfer function (MTF) are the 'gold standard' for assessing image quality. Advantages these metrics afford are due to their objective nature, the comprehensive noise analysis they permit and in the fact that they have been reported to be relatively more sensitive to changes in detector performance. The advent of DR systems and access to digital image data has opened up new opportunities in applying such measurements to routine quality control and this project initially focuses on obtaining NPS and MTF results for 12 IDR systems in routine clinical use.

Appropriate automatic exposure control (AEC) device calibration and a reproducible measurement method are key to optimising X-ray equipment for digital radiography. The uses of various parameters to calibrate AEC devices specifically for DR were explored in the next part of the project and calibration methods recommended. Practical advice on dosemeter selection, measurement technique and phantoms were also given.

A model was developed as part of the project to simulate CNR to optimise beam quality for chest radiography with an IDR system. The values were simulated for a chest phantom and adjusted to describe the performance of the system by inputting data on phosphor sensitivity, the signal transfer function (STF), the scatter removal method and the automatic exposure control (AEC) responses. The simulated values showed good agreement with empirical data measured from images of the phantom and so provide validation of the calculation methodology. It was then possible to apply the calculation technique to imaging of tissues to investigate optimisation of exposure parameters. The behaviour of a range of imaging phosphors in terms of energy response and variation in CNR with tube potential and various filtration options were investigated. Optimum exposure factors were presented in terms of kV-mAs regulation curves and the large dose savings achieved using additional metal filters were emphasised. Optimum tube potentials for imaging a simulated lesion in patient equivalent thicknesses of water ranging from 5-40 cm thick for example were: 90-110kVp for CsI (IDR); 80-100kVp for Gd_2O_2S (screen /film); and 65-85kVp for BaFBrI. Plots of CNR values allowed useful conclusions regarding the expected clinical operation of the various DR phosphors. For example 80-90 kVp was appropriate for maintaining image quality over an entire chest radiograph in CR whereas higher tube potentials of 100-110 kVp were indicated for the CsI IDR system. Better image quality is achievable for pelvic radiographs at lower tube potentials for the

majority of detectors however, for gadolinium oxysulphide 70-80 kVp gives the best image quality.

The relative phosphor sensitivity and energy response with tube potential were also calculated for a range of DR phosphors. Caesium iodide image receptors were significantly more sensitive than the other systems. The percentage relative sensitivities of the image receptors averaged over the diagnostic kV range were used to provide a method of indicating what the likely clinically operational dose levels would be, for example results suggested 1.8 μGy for CsI (IDR); 2.8 μGy for Gd_2O_2S (Screen/film); and 3.8 μGy for BaFBrI (CR).

The efficiency of scatter reduction methods for DR using a range of grids and air gaps were also reviewed. The performance of various scatter reduction methods: 17/70; 15/80; 8/40 Pb grids and 15 cm and 20 cm air gaps were evaluated in terms of the improvement in CNR they afford, using two different models. The first, simpler model assumed quantum noise only and a photon counting detector. The second model incorporated quantum noise and system noise for a specific CsI detector and assumed the detector was energy integrating. Both models allowed the same general conclusions and suggest improved performance for air gaps over grids for medium to low scatter factors and both models suggest the best choice of grid for digital systems is the 15/80 grid, achieving comparable or better performance than air gaps for high scatter factors. The development, analysis and discussion of AEC calibration, CNR value, phosphor energy response, and scatter reduction methods are then brought together to form a practical step by step recipe that may be followed to optimise digital technology for clinical use.

Finally, CNR results suggest the addition of 0.2 mm of copper filtration will have a negligible effect on image quality in DR. A comprehensive study examining the effect of copper filtration on image quality was performed using receiver operator characteristic

(ROC) methodology to include observer performance in the analysis. A total of 3,600 observations from 80 radiographs and 3 observers were analysed to provide a confidence interval of 95% in detecting differences in image quality. There was no statistical difference found when 0.2 mm copper filtration was used and the benefit of the dose saving promote it as a valuable optimisation tool.

Publications

List of peer reviewed publications resulting from this thesis, to date:

Doyle P, Gentle D, Martin CJ. Optimising automatic exposure control in computed radiography and the impact on patient dose. Radiat Prot Dosimetry 2005;114(1-3):236-9.

Doyle P, Martin CJ, Gentle D. Dose-image quality optimisation in digital chest radiography. Radiat Prot Dosimetry 2005;114(1-3):269-72.

Doyle P, Martin CJ, Gentle D. Application of contrast-to-noise ratio in optimizing beam quality for digital chest radiography: comparison of experimental measurements and theoretical simulations. Phys Med Biol 2006 Jun 7;51(11):2953-70.

Doyle P, Finney L. Performance Evaluation and Testing of Digital Intra-Oral Radiographic Systems. Radiat Prot Dosimetry 2005; 117(1-3):313-317.

Doyle P, Martin CJ. Calibrating automatic exposure control devices for digital radiography. Phys Med Biol 2006 Nov 7;51(21):5475-85.

Doyle P, Martin CJ, Workman A. A Recipe for Optimising Exposure Factors for Digital Radiography Systems. Radiology. In press 2009.

Doyle P, Honey I, Mackenzie A, Marshall NW, Smail M. Measurement of the Performance Characteristics of Diagnostic X-ray Systems: Digital Imaging Systems. Fairmount House, York: Institute of Physics and Engineering in Medicine; 2009. Report No.: 32 part vii.

Doyle P, Workman A, Johnston G. Practical application of IEC 62220-1 in determining DQE for twelve indirect digital radiography systems in a clinical setting. Med Phys. In press 2009.

Doyle P. Optimisation and Quality Assurance in Digital Imaging. In: Oakley J, editor. Digital Imaging - A Primer for Radiographers, Radiologists and Health Care Professionals. second ed. Cambridge University Press; In press 2009.

Martin CJ, **Doyle P**, Gentle D. Proceedings of the seventh international symposium for radiological protection: Digital Radiography and Optimisation.: Cardiff, UK; 2005.

Martin CJ, **Doyle P**. The importance of radiation quality for optimisation in radiology. Biomedical Imaging and Intervention Journal 2007;3(2):1-14.

Table of Contents

List of Tables

List of Figures

List of Equations

$$\Delta SNR_{Rose} = \frac{A(\overline{n}_b - \overline{n}_0)}{\sqrt{A\overline{n}_b}} = C\sqrt{A\overline{n}_b} \quad \text{.....Equation 3:1}$$

$$DQE(f) = G^2.\frac{MTF^2(f)}{NPS(f)}.K_a.SNR_{in}^2 \quad \text{.....Equation 3:2}$$

$$DQE(f) = \left(\frac{S}{Q}\right)^2.\frac{MTF^2(f)}{NPS(f)}.K_a.SNR_{in}^2 = \frac{MTF^2(f)}{NNPS(f).Q} \quad \text{.....Equation 3:3}$$

$$NPS(u_n, v_k) = \frac{\Delta x.\Delta y}{M.256.256}\sum_{m=1}^{M}\left|\sum_{i=1}^{256}\sum_{j=1}^{256}\left(I(x_i, y_j) - S(x_i, y_j)\right).\exp(-2\pi i(u_n x_i + v_k y_j))\right|^2 \quad \text{.... 3:4}$$

$$SNR_{in}{}^2 = \frac{\left(\int_0^{kVp}\varphi(E).E.dE\right)^2}{\int_0^{kVp}\varphi(E).E^2.dE} \quad \text{.....Equation 3:5}$$

$$NEA = \left(2\pi\int_0^{f_N} MTF^2(f)fdf\right)^{-1} \quad \text{.....Equation 3:6}$$

$$N_{bin} = M.R.bin_{mean} \quad \text{.....Equation 3:7}$$

$$E = I + \beta(I - S) \quad \text{.....Equation 3:8}$$

$$A(E) = E\{1 - \exp[-\mu_{en}((E)/\rho).\rho.t]\} \quad \text{.....Equation 4:1}$$

$$A(kV, filt) = \frac{\int_0^{E_{kV}}\psi_E.E\{1 - \exp[-\mu_{en}((E)/\rho).\rho.t]\}.dE}{\int_0^{E_{kV}}\psi_E.dE} \quad \text{.....Equation 4:2}$$

$$\psi_r(E) = \psi_i(E)\sum_t^T e^{\frac{\mu_t(E)}{\rho_t}\cdot p_t d_t} \quad \text{.....Equation 5:1}$$

$$K_{airV} = \sum_0^{E=kVp}\psi_{rV}(E)\cdot E\cdot\frac{\mu_{en}}{\rho} \quad \text{.....Equation 5:2}$$

$$A(E) = \psi_r(E)(1 - e^{\frac{\mu_{en}(E)}{\rho_x}\rho_x d_x}) \quad \text{.....Equation 5:3}$$

$$C(E) = \frac{I_1(E) - I_2(E)}{I_1(E)} = \frac{\Delta I(E)}{I(E)} = 1 - e^{-[\mu_1(E) - \mu_2(E)]d} \approx \Delta\mu(E)d \quad \text{.....Equation 5:4}$$

$$CNR = \frac{\Delta\overline{N}}{\sqrt{\overline{N}}} = \Delta\mu d\sqrt{\overline{N}} \quad \text{.....Equation 5:5}$$

$$N = \sum_{0}^{E=kVp} \psi_r(E) \cdot A \quad \text{.....Equation 5:6}$$

$$K_{airVI} = \sum_{0}^{E=kVp} \psi_{iVI}(E) \cdot E \cdot \frac{\mu_{en}}{\rho} \quad \text{.....Equation 5:7}$$

$$ED_V = K_{airVI} \cdot BSF_V \cdot C_V \quad \text{.....Equation 5:8}$$

$$FOM_{VI} = CNR_{VI}^2 / ED_V \quad \text{.....Equation 5:9}$$

$$CNR_{Vs} = CNR_V \sqrt{(1 - S_{oV})} \quad \text{.....Equation 5:10}$$

$$CNR_{igV} = CNR \sqrt{[T_{pV}(1 - S_{gV})]} \quad \text{.....Equation 5:11}$$

$$\sigma_{pe} \propto \frac{Z^4}{E^3} \quad \text{.....Equation 6:1}$$

$$\sigma_{ce} = \frac{\mu_{ce}}{\rho} \cdot \frac{A}{N_A} \quad \text{.....Equation 6:2}$$

$$CNR_{if} = \frac{CNR_{sr}}{CNR_{p\&s}} \quad \text{.....Equation 6:3}$$

$$CNR_{if}^q = T_p \times \sqrt{B} \quad \text{.....Equation 6:4}$$

$$N_{amp} = NEQ_q + NEQ_s = NEQ_t \quad \text{.....Equation 6:5}$$

$$CNR_{if}^T = CNR_{if}^q \times \sqrt{\frac{1 + NEQ_s / NEQ_{q0}}{1 + B \cdot NEQ_s / NEQ_{q0}}} \quad \text{.....Equation 6:6}$$

$$DQE = \frac{(CNR_{out})^2}{(CNR_{in})^2} = \frac{NEQ_t}{(CNR_{in})^2} \quad \text{.....Equation 6:7}$$

$$SN = \frac{TP}{TP + FN}$$ ..... Equation 7:1

$$SP = \frac{TN}{FP + TN}$$ ..... Equation 7:2

$$a = \frac{\mu_D - \mu_H}{\sigma_H} \quad \text{and} \quad b = \frac{\sigma_H}{\sigma_D}$$ ..... Equation 7:3

$$Sensitivity = b.(1 - Specificity) + \varphi.a$$ ..... Equation 7:4

$$A(z) = \varphi\left(\frac{a}{\sqrt{1 + b^2}}\right)$$ ..... Equation 7:5

$$P_{\text{det}} = \frac{TP + TN}{TP + TN + FP + FN} = \frac{SN + SP}{2}$$ ..... Equation 7:6

List of Abbreviations

AEC	Automatic Exposure Control
Az	Area under a Receiver Operator Characteristic Curve
BKE	Background Known Exactly
CEC	Council of European Communities
CNR	Contrast-to-noise Ratio
CR	Computed Radiography
CsI	Caesium Iodide
CT	Computed Tomography
DAK	Detector Air Kerma
DAK_{ref}	Reference Detector Air Kerma
DAP	Dose Area Product
DDI	Detector Dose Indicator
DDR	Direct Digital Radiography
DQE	Detective Quantum Efficiency
DR	Digital Radiography
EAK	Entrance Air Kerma
EP	Exposure Point
FDD	Focus to Detector Distance
FOM	Figure of Merit
GE	General Electric
HVL	Half-Value Layer
IDR	Indirect Digital Radiography Systems
IEC	International Electro-technical Commission
IP	Imaging Plate
IQAP	Image Quality Assurance Programme
IT	Information Technology
kVp	Peak Kilovoltage
MRI	Magnetic Resonance Imaging
MTF	Modulation Transfer Function
NEA	Noise Equivalent Aperture
NHS	National Health Service
NNPS	Normalised Noise Power Spectra
NPS	Noise Power Spectrum
PA	Postero-anterior
PMT	Photomultiplier Tube
PSL	Photo-stimulated Luminescence
PVC	Polyvinylchloride
QA	Quality Assurance
QC	Quality Control
ROC	Receiver Operator Characteristics
ROI	Region of Interest
SAL	Scan Average Level
SID	Source-to-image Distance
SKE	Signal Known Exactly
SN	Sensitivity
SNR	Signal-to-Noise Ratio
SP	Specificity
STF	Signal Transfer Function
STP	Signal Transfer Properties

Acknowledgments

There are a few people who contributed to this thesis, for which I would like to acknowledge and express my thanks.

Firstly, I want to thank Colin Martin my supervisor both professionally, for his scientific guidance and support and personally for his seemingly unending enthusiasm and encouragement - particularly during the wilderness of the 'middle years' of the project. Special thanks also to David Gentle and John Robertson who were great people to bounce ideas off.

I am indebted to my parents for supporting me and always keeping my feet on the ground. I will never forget the words of wisdom from my mother in stating "I wouldn't worry about it Phil, these things always sort themselves out in the end". But most of all guys, thanks for just being there.

Finally, I am forever indebted to my wife Laura, for marrying me when this dark cloud loomed over me and for guiding me to the end of this project never loosing faith in my ability. Your cunning in imprisoning me in a cell of emotional boundaries and positive encouragement is exactly what I needed for that final memorable 4 month push. To her I dedicate this thesis.

Declaration

1 Introduction

1.1 Preamble

Digital imaging has long been available in radiology in the form of computed tomography (CT), magnetic resonance imaging (MRI) and ultrasound. Initially the transition to general planar radiography was slow and fragmented but in the last 10-15 years in particular, huge investment by the manufacturers, greater (and cheaper) computing power, inexpensive digital storage and high bandwidth data transfer networks have lead to an enormous increase in the number of digital radiography systems in the UK. The rate of transition to a fully digital hospital environment was also accelerated by government initiatives and investment in the National Health Service (NHS) information technology (IT) infrastructure (the National Programme for IT, *NPfIT*). There are a number of competing digital technologies; the most common in the UK are computed radiography (CR) systems followed by indirect digital radiography (IDR) systems.

1.2 Aims

The principle objective of this project was to investigate and determine ways to assess and optimise digital radiography systems for clinical use.

1.3 Structure of this Thesis

This thesis consists of eight chapters. Chapter 2 begins with a review of quality control in digital radiography. The technologies of popular digital radiography systems are explored

and tabulated lists of appropriate quality control tests and recommended tolerances are given. Chapter 3 describes a detailed study of the measurement of quantitative image quality metrics for twelve indirect digital radiography systems. Experiences of the application of what were traditionally the 'gold standard' laboratory type tests for measuring image quality are shared and practical knowledge of the experimental uncertainties and expected variations is sought. Chapter 4 focuses on automatic exposure control (AEC) devices and compares empirical assessments of the performance of the devices with different digital radiography systems with a theoretical model based on the energy absorbed in the image receptor. Appropriate AEC device calibration with a reproducible measurement technique is key to optimising X-ray equipment for digital radiography. Chapter 5 details the development of a model used to simulate the performance of an indirect digital radiography system to predict contrast-to-noise ratio (CNR) values and allow an assessment of gross image quality in chest radiography. The results of the model are compared with practical measurements from a chest phantom. It is hoped the model could then be used to simulate clinical details for examining what exposure factors and techniques are appropriate for different X-ray detector technologies. Chapter 6 explores the application of this model, using lesion equivalent materials *e.g.* muscle with different image receptors, to characterise detector performance based on CNR and energy absorbed in the phosphors. The chapter was also expanded to include other factors relevant to optimising digital radiography systems such as the effects of additional filtration, tube potential and choice of scatter reduction method. Chapter 6 also proposes a practical strategy or recipe for optimising digital equipment for clinical use. Chapter 7 is a specific study detailing the investigation of whether the addition of copper filtration has a measurable effect on image quality with an indirect digital radiography detector. The study uses receiver operator characteristic methodology to examine high and low contrast materials in a phantom to simulate bone and soft tissue features and the cost–benefit implications of using additional filtration are explored. Finally, Chapter 8 summarises and

concludes the salient points of the investigation and developments addressed in the thesis, indicating areas for potential future development.

2 Quality Control in Digital Radiography

2.1 Introduction

Quality assurance (QA) in digital radiography is a term which represents a comprehensive program developed to evaluate the performance of all aspects of the medical imaging chain. Such programs will typically include methods to test the performance of each piece of equipment or process forming a link in this chain, and for example may include tests on the X-ray tube, the image receptor, the image archive and the image display monitor. The individual tests required to assure that the level of quality is being maintained are termed quality control (QC) tests. QC typically refers to the performance of specific tests to determine equipment performance on a periodic basis.

Acceptance testing however, involves specific tests to determine whether initial performance of a system are accepted to met the tender purchase specifications. Acceptance tests often overlap with tests which are legally required [1] to commission digital equipment for clinical use, termed commissioning tests. An important function of commissioning tests is to allow baselines of performance to be established for comparison against future performance, to detect subtle long term degradation in image quality.

In digital radiography QC tests are performed at recommended intervals and the outcomes are compared to commissioning results to verify that the system is operating to preset levels of performance. Such testing however rarely assesses the fundamental determinants of image quality for example the modulation transfer function (MTF) or noise power spectrum (NPS). These tests are usually performed under controlled laboratory

conditions by the manufacturers and are rarely performed by users of the systems (most often being used to compare specification data or acceptance test results at the time of purchase). QC performed as part of acceptance and commission testing and routinely thereafter are generally simplified measures of specific parameters derived from the fundamental image quality metrics. For example threshold contrast detail detectability for an object detail of different sizes is a simplified measurement of the NPS and the limiting resolution measured with a bar pattern is a surrogate test of the MTF at the Nyquist frequency.

In this chapter all recommended QC tests for digital radiography are summarised. First, the fundamental principles of operation of digital radiography systems are explored, so that the specific QC tests appropriate for the technology may be presented in context.

2.2 Digital Radiography Technology

Digital imaging has long been available in radiology in the form of computed tomography (CT), magnetic resonance imaging (MRI) and ultrasound. Initially the transition to general planar radiography was slow and fragmented but in the last 10-15 years in particular, huge investment by the manufacturers, greater (and cheaper) computing power, inexpensive digital storage and high bandwidth data transfer networks have lead to an enormous increase in the number of digital radiography systems in the UK. The rate of transition to a fully digital hospital environment was also accelerated by government initiatives and investment in the National Health Service (NHS) information technology (IT) infrastructure (the NHS National Programme for IT, *NPfIT*). There are a number of competing digital technologies, the most common in the UK are computer radiography (CR) systems followed by indirect digital radiography (IDR) systems. Brief reviews of the

technology of both systems are given in the following sections, a more comprehensive examination of the technology and underlying physics are available in the literature [2-6].

2.2.1 Computed Radiography

CR X-ray detectors or imaging plates (IPs) are housed in a protective case, similar in size and appearance to screen/film cassettes. An image processor known as the CR 'reader' or 'digitiser' processes the latent image captured by the detector. After latent image readout the signal is digitised, stored as a two-dimensional array and transferred to a display device for review. The phosphor layer deposited on the IP to detect incident X-rays is typically manufactured from barium fluro-hailde crystals with europium dopant. Bromine is most commonly used as the halide element and some manufacturers also add small quantities of iodine or strontium. Phosphor layers are typically ~200 μm thick.

When X-rays interact with the phosphor electron hole pairs are created and immediately begin to recombine, emitting light through the process of fluorescence. Some of the electrons get trapped at positions in the crystal lattice where the dopant has created imperfections or F-centres (areas where the local energy levels are perturbed). Fortunately the number of electrons that get trapped is proportional to the X-rays absorbed in the phosphor, allowing for the formation of a latent image. The trapped electrons spontaneously and randomly return to a more stable energy state (called ground) with time in a process called latent image decay.

An electron may be deliberately released from its 'trap' to the ground state if stimulated with enough energy, *e.g.* red light from a diode laser (680 nm wavelength). The return of the electron to the ground state is accompanied by the emission of a light photon with a shorter wavelength than the one absorbed, closer to blue light (~ 415 nm). The

capture of the blue light, the photostimulated luminescence (PSL) completes the process whereby the latent image from an IP is used to produce an image signal in the CR reader.

Mechanically the IP is readout inside the reader in a raster fashion, figure 2.1. The laser light is guided to a position on the IP through a series of mirrors and lenses. Because at any one time only a single point (defined by the laser beam spot size) on the IP is irradiated, the capture of PSL within the light guide will generate a signal that corresponds to that point. The limiting resolution of the system will ultimately depend on the sampling frequency which is limited by the laser beam spot size and the decay lag of PSL. The decay lag is most limiting in the scan direction and is responsible for relatively poorer resolution of CR systems in that direction. The mechanical process of removing the IP from the cassette and passing it through the reader will eventually result in damage to the IP either as a result of malfunction or wear and tear and image artefact and uniformity tests are recommended as part of routine QC.

Typically only one third of the PSL photons are collected by the light guide and presented to the bi-alkali of the photomultiplier tube (PMT). The PMT then converts the PSL to electrons with only 25% efficiency. The noise inherent in the few electrons representing a single X-ray is the weakest link in the CR system and is the "secondary quantum sink". CR system gain [2] is approximately 1 electron per 10 keV and the success of the technology may be attributed to the very high signal gain and inherent low noise of the PMT. The output of the PMT is passed through a logarithmic or square root amplifier. An analogue to digital converter then quantises the signal to 4096 or 16384 grey levels (corresponding to 12 bits and 14 bits for more recent systems). The non-linear amplifier is used so that the dynamic range of the signal may be compressed and digitisation accuracy preserved over the limited number of discrete grey levels.

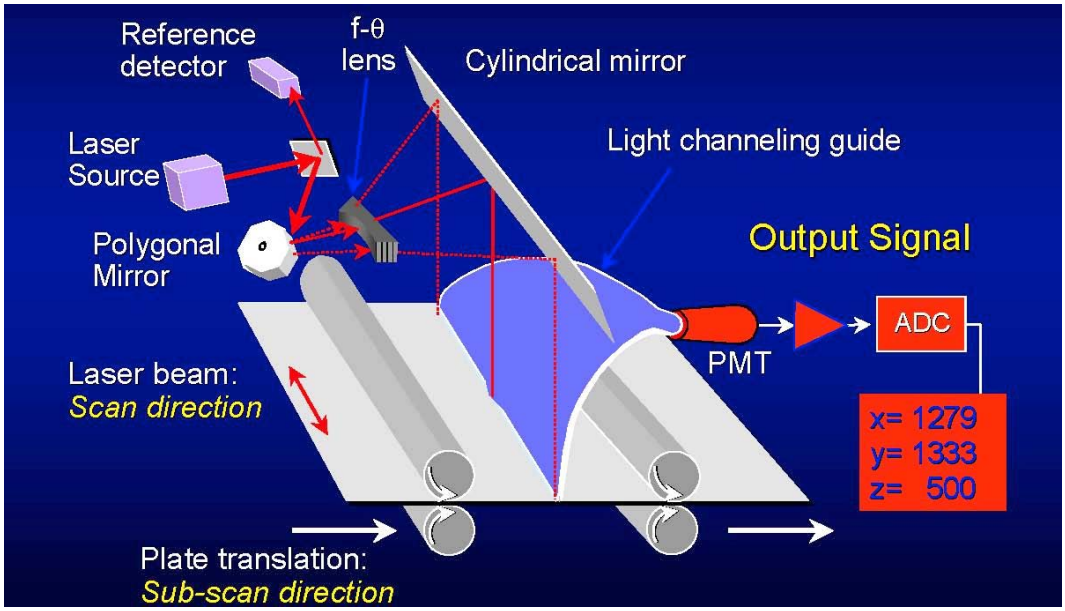

Figure 2:1 Internal components of a CR reader. The plate is moved in a continuous motion through the laser beam scan by mechanical rollers (image adapted from AAPM Monograph No.30 [6]).

The readout process described, fails to remove all traces of the latent image. Before the IP is returned to the cassette inside the reader, it is first flashed with high intensity white light to remove any residual signal.

2.2.2 Indirect digital radiography

CR as with conventional radiography is a two stage process. After X-ray exposure of the cassette, user intervention is required to transfer the cassette to the film processor or CR reader. This can take many minutes particularly in busy departments performing hundreds of examinations per week. Indirect radiography detectors (commonly refereed to as flat panel detectors) form integrated systems where the detector is integrated with the X-ray generator. IDR systems require no user interaction, other than the control of the X-ray exposure, and the image is acquired and sent for reporting at the click of a button. The improvement in work flow IDR systems afford is obvious. However, they require a

significant capital investment and thought must also be given to patient flow or the 'bottle neck' will simply move from the X-ray room to the patient waiting /changing facility or supporting services.

A flat panel detector consists of a large two-dimensional array of X-ray absorption material fabricated on a thin glass sheet and divided into individual square regions, corresponding to pixels. The X-ray absorption materials used may be classified into two main types: those that produce charge on interaction with X-rays *i.e.* photoconductors and those which produce light *i.e.* phosphors. The active components of the pixels are made from hydrogenated amorphous silicon (a-Si:H). The pixels are designed to measure charge if a photoconductor is being used or light and then charge if a phosphor is being used. It is thus, the output of the X-ray detection material rather than the X-rays themselves that is measured and flat panel systems are energy integrating rather than photon counting detectors. In the phosphor approach X-ray energy is first converted to light before eventually being converted to charge in the sensing element of the a-Si:H pixel. For this reason digital detectors employing phosphors are coined as 'indirect' digital radiography systems. Flat panel systems using photoconductors or 'direct' digital radiography systems were used in the past for general radiography but are now mostly confined to specialist areas such as mammography and electronic portal imaging devices in radiotherapy.

There are many prompt emitting phosphors which could be used in IDR systems. The most common are gadolinium oxysulphide (used extensively in screen/film systems) and thallium doped caesium iodide (used extensively in image intensifiers but doped with sodium instead). CsI IDR systems are the most common in the UK. CsI can be grown in crystal needle like structures which act as light guides to the emitted fluorescent light. As a result, relatively thick phosphor layers can be used (up to 600 μm thicknesses) which improves X-ray detection efficiency while maintaining acceptable spatial resolution. A

schematic showing the flat panel array with associated electronics is shown in figure 2:2. One striking aspect of this technology is the surface area of the flat panel which is taken up by the electronics. For IDR systems the fractional area of the sensing element which is photosensitive is known as the geometric fill factor. This is a major issue confronting the design of arrays for high resolution applications such as mammography because the smaller the pixel size the larger the relative area the electronic components take up. Pixel sizes of 150 μm used in general radiography IDR systems typically have fill factors of 0.6 [5].

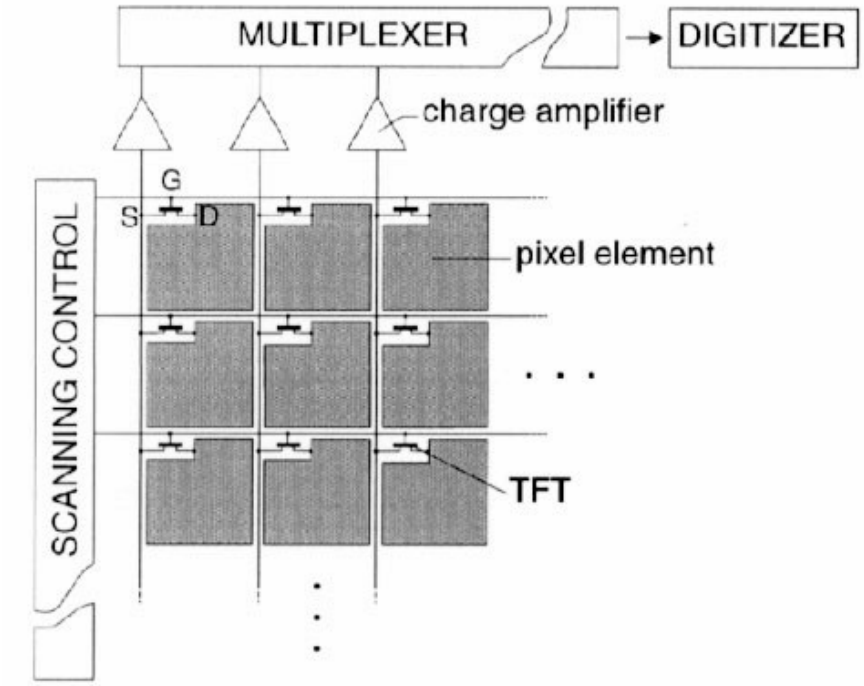

Figure 2:2 Schematic depicting a flat panel array. The pixel element or sensitive area may either be simply a storage capacitor if a photoconductor is used or is a photodiode if a phosphor is used. In either case a semiconductor will store the charge generated the magnitude of which will be accessed and read line by line during readout, controlled by the TFT switch.

To acquire a radiographic image with a general radiography IDR system the flat panel is put into an initialisation state ready for an incoming signal. The scanning control circuitry holds all thin film transistor (TFT) switches off while the X-ray exposure is made.

When the exposure has completed the switches of the first row of the array are switched on and the charge stored in each pixel element is amplified, recorded and addressed to its specific location of the array, figure 2:2. The first array is then switched off and the second array is switched on, the process continues until the image is reconstructed line-by-line. It is interesting to note that a fundamental difference between the applications of IDR systems in general radiography and fluoroscopy is in the readout mode. For fluoroscopic applications pixel elements are readout in a similar manner however, when a particular line of pixels is being readout the other pixels remain sensitive to radiation and are combined to provide imaging information [5].

To reduce costs flat panel detectors are usually manufactured in smaller substrates and tiled together to cover the imaging area. Two or four detector tiles are generally used. This results in a stitching artefact (best seen with a fine wire mesh) between the tiles as well as slight differences in sensitivity. The difference in sensitivity may be correct for by the system (known as a gain correction). The amount of dark current present in the semiconductor electronics in each pixel will also vary and this correction is known as an offset correction. The gain correction is made using multiple exposures, usually with a metal filter in place to approximate a specific beam quality (*e.g.* 21 mm Aluminium), to calculate the correction required for each pixel in the array to achieve equal sensitivity. The offset correction is made by acquiring an image with no exposure and then correcting for the variation across all pixels. Gain and offset corrections are performed during what the manufacturers' term detector calibration or flat field correction. Systems usually require recalibration after a fixed no of acquisitions or time period has reached and is usually performed by the user.

2.3 QC Tests for Digital Radiography

There are many tests which relate to system performance or image quality in an indirect way which are important in assuring the performance and effectiveness of a digital radiography system. Table 2.1 and Table 2.2 list the set of tests for CR and IDR recommended in IPEM Report 32 vii which is currently in press [7]. The report aims is to give guidance on acceptance testing and routine QC for CR and IDR systems, building on the various sources of existing guidance [6,8,9]. Further details and background on performing the specific tests are provided in IPEM Report 91 [8] and technical protocols may be downloaded from www.kcare.co.uk.

For testing image quality however, Fourier based objective image quality metrics such NPS and MTF have advantages over the simpler semi-quantitative test object based methods in that they no longer rely on the observer maintaining a constant decision threshold with time. The MTF and NPS have also been shown to be more sensitive to changes in detector performance than test object based tests[10]. The measurement methods are well established [11] and have been used in numerous studies to evaluate: direct and indirect digital radiography systems [12]; computed radiography systems [13,14] and digital mammography systems [15]. To date, such tests can only verify if digital detectors are functioning according to the manufacturers' specification. Much work is needed to gain an appreciation of how common detector faults manifest as changes in MTF and NPS with time and what the expected experimental uncertainties are. The study described Chapter 3 aims to examine the practicalities and experimental uncertainties in performing these measurements in a busy clinical X-ray department so that protocols may be developed to eventually include the measurements in routine QC.

Table 2:1 IPEM Report 32 vii draft 'QC tests for Computed Radiography'.

QC TEST	AIM	Remedial Level	Suspension Level
Detector dose indicator (DDI) calibration	Indicated exposure (IE) = the expected computed exposure (E)	IE/E < 0.8, IE/E > 1.2 IE/E for any image > 10%	IE/E < 0.5, IE/E > 1.5
Signal transfer properties	simple relationship	mean IE/E trend line R2 fit < 0.95	
DDI consistency – short-term	Coef. Of variation (CoV) of IE = 0%	CoV of IE > 10%	CoV of IE > 20%
Matching of CR plates	IE same for all plates	IE varies by > 20% between plates	
DDI consistency – long-term	IE = baseline	baseline ± 20%	baseline ± 50%
Differences between CR readers	IE same for all readers	IE varies by > 20% between readers	n/a
Dark noise	Agfa: SAL < 100		
	Fuji: pixel value < 280		
	Kodak: EI < 80 or < 380 (High Resolution)	baseline + 50%	
Condition of cassettes and image plates	clean and undamaged	dirt on image plate	damage to image plate
Visual check of uniformity	no obvious artefacts	dots and lines apparent	gross non-uniformity
Measured uniformity	CoV of STP- corrected ROI values = 0%	CoV of STP- corrected ROI values > 10%	STP (Signal Transfer Properties of detector)
Erasure cycle efficiency	no ghosting visible	visible ghost	STP-corrected pixel values in ghost & surrounding area > 1%
Threshold contrast detail detectability	fitted curve similar to baseline & reference	deviation of curve from baseline >15%	
Limiting high contrast spatial resolution	approach Nyquist limit	baseline - 25%	
Laser beam function	edge continuous across whole image uniform 'stair' characteristics across whole image	obvious jitter	
Moiré patterns	not visible		visible

Table 2:2 IPEM Report 32vii Draft QC tests for Indirect Digital Radiography**.**

QC TEST	AIM	Remedial Level	Suspension Level
DDI calibration		indicated exposure should agree with measured exposure within 20%	
DDI consistency	no gross artefacts	variation in calculated indicated exposures normalised to receptor dose should not differ by > 20% from baseline	variation in calculated indicated exposures normalised to receptor dose should not differ by > 50% from baseline
Linearity & System transfer properties	simple relationship	trend line fit should have R^2 fit > 0.95	
Dark noise		50% increase from baseline	
Uniformity	no obvious artefacts	CoV of 5 STP corrected ROI values < 5%	CoV of 5 STP corrected ROI values < 10%
Blurring / line defects / Stitching artefacts		Two broken lines together or separated by one line	
Measuring stitching artefacts			> 2´ pixel pitch
Dead pixel map/detector element failure		Refer to manufacturer tolerance	Clusters of broken pixels particularly near centre of detector are the biggest concern Two broken lines together or separated by one line
Uncorrected defective detector elements		All defective pixels should be corrected out by the system	
Image retention	No obvious ghost image	>0.5%	>1%
Threshold contrast detail detectability		One point on smoothed curve Baseline ± 30%	
Limiting spatial resolution	may be limited by display if scored from review workstation, particularly in no or limited zoom	should approach Nyquist limit; Baseline+/-20%	

2.4 References

[1] The Ionising Radiations Regulations. London: The Stationary Office Limited; 1999. Report No.: SI 1999 / 3232 Health and Safety.

[2] Rowlands JA. The physics of computed radiography. Phys Med Biol 2002 Dec 7;47(23):R123-R166.

[3] Yaffe MJ, Rowlands JA. X-ray detectors for digital radiography. Phys Med Biol 1997 Jan;42(1):1-39.

[4] Neitzel U. Status and prospects of digital detector technology for CR and DR. Radiat Prot Dosimetry 2005;114(1-3):32-8.

[5] Rowlands JA, Yorkston J. Flat Panel Detectors for Digital Radiography. In: Beutel J., Kundel H.L., Van Metter R.L., editors. Handbook of Medical I maging: Volume 1. Physics and Psychophysics.Bellingham, USA: SPIE; 2000. p. 223-328.

[6] L.W.Goldman, M.V.Yester. Specifications, performance evaluations, and quality assurance of radiographic and fluoroscopic systems in the digital era. Wisconsin, US: Medical Physics Publishing; 2004. Report No.: 30.

[7] Doyle P, Honey I, Mackenzie A, Marshall NW, Smail M. Measurement of the Performance Characteristics of Diagnostic X-ray Systems: Digital Imaging Systems. Fairmount House, York: Institute of Physics and Engineering in Medicine; 2009. Report No.: 32 part vii.

[8] Institute of physics and Engineering in Medicine (IPEM). Recommended standards for routine performance testing of diagnostic X-ray imaging systems. Fairmount House, York: IPEM; 2005. Report No.: 91, 2nd Edition.

[9] Samei E, Seibert JA, Willis CE, Flynn MJ, Mah E, Junck KL. Performance evaluation of computed radiography systems. Med Phys 2001 Mar;28(3):361-71.

[10] Marshall NW. Retrospective analysis of a detector fault for a full field digital mammography system. Phys Med Biol 2006 Nov 7;51(21):5655-73.

[11] Metz CE, Wagner RF, Doi K, Brown DG, Nishikawa RM, Myers KJ. Toward consensus on quantitative assessment of medical imaging systems. Med Phys 1995 Jul;22(7):1057-61.

[12] Samei E, Flynn MJ. An experimental comparison of detector performance for direct and indirect digital radiography systems. Med Phys 2003 Apr;30(4):608-22.

[13] Samei E, Flynn MJ. An experimental comparison of detector performance for computed radiography systems. Med Phys 2002 Apr;29(4):447-59.

[14] Workman A, Cowen AR. Signal, noise and SNR transfer properties of computed radiography. Phys Med Biol 1993;38:1789-808.

[15] Evans DS, Workman A, Payne M. A comparison of the imaging properties of CCD-based devices used for small field digital mammography. Phys Med Biol 2002 Jan 7;47(1):117-35.

3 Quantitative Image Quality Metrics

3.1 Introduction

3.1.1 Background theory

The limitation imposed by the statistical nature of image quanta on image quality was first recognised by Rose in 1948. The relationship between the number of image quanta and perception was described in terms of a change in signal-to-noise ratio (ΔSNR) for the detection of a uniform detail in a uniform background. The defining equation, known as the Rose Model is given by

$$\Delta SNR_{Rose} = \frac{A(\overline{n}_b - \overline{n}_0)}{\sqrt{A\overline{n}_b}} = C\sqrt{A\overline{n}_b} \qquad \textbf{Equation 3:1}$$

where n_0 is the mean quanta per unit area of an object detail of area A, resulting in contrast C (defined as $[n_b\text{-}n_0]/n_b$) and n_b is the mean quanta per unit area of an equal area of the background[1].

The limitations of this model have however quickly become apparent with modern digital systems (discussed in detail by Burgess 1999)[2]. The most salient shortcoming of the Rose method is the oversimplification of noise as evident in digital X-ray systems. Noise in the Rose model is treated as both uncorrelated and Poisson distributed where in practical situations neither may be the case[3]. The Rose model gives misleading results when the image quanta are statistically correlated, or when the sampling function – normally the point spread function of the system, does not correspond well with the size or shape of the object detail[4]. Only if the details diameter is large with respect to the

correlation distances does the noise variance become independent of the detail shape and the Rose method gives an accurate approximation of image noise[4]. Burgess (1999) describes using detection theory how the model corresponds to a very specific detection task called 'signal known exactly' (SKE) and background known exactly (BKE) detection task[2].

The Rose model forms the bases of much work carried out by medical physicists in assessing the performance of digital X-ray systems. There are many contrast-detail test objects available with a range of object details of various sizes and contrasts to suit particular imaging modalities. The detectability of low contrast details increases with detail diameter and contrast as expected from equation (1) in a SKE/BKE detection task. Rose showed that the ΔSNR must have a value of 5 or greater for reliable detection of the uniform object detail.

Unfortunately such experiments are far removed from providing a thorough analysis of the actual X-ray detector. The semi-quantitative test object approach relies heavily on the subjective evaluation of images by an observer. Furthermore, the noise associated with such systems is complex and may include components of primary quantum noise, secondary quantum noise, aliasing noise, additive noise such as electronic noise or dark current and multiplicative noise such as structure noise[3,5]. The use of transfer theory with Fourier based metrics facilitates the analysis needed to include these sources and allows a more through examination of image signal and noise[2].

3.1.2 Objective image analysis metrics

The frequency dependant detective quantum efficiency DQE is currently the most common method used when comparing digital radiographic systems, because it characterizes the

systems overall signal-to-noise transfer properties under ideal (low scatter) conditions. The method is well established[6] and has been used in numerous studies to evaluate: direct and indirect digital radiography systems[7]; computed radiography systems[8,9] and digital mammography systems[10].

The DQE(*f*) may be defined in terms of the pre-sampled modulation transfer function (MTF) and the noise power spectrum (NPS) as follows[11]

$$DQE(f) = G^2 . \frac{MTF^2(f)}{NPS(f)} . K_a . SNR_{in}^2 \qquad \textbf{Equation 3:2}$$

where G is the detector gain, K_a is the detector incident exposure in μGy, and SNR_{in}^2 is the number of incident quanta per unit area per μGy. When detector gain is defined as signal output, S for a given X-ray quanta per unit area Q at the input of the detector, equation (2) may be defined as

$$DQE(f) = \left(\frac{S}{Q}\right)^2 . \frac{MTF^2(f)}{NPS(f)} . K_a . SNR_{in}^2 = \frac{MTF^2(f)}{NNPS(f).Q} \qquad \textbf{Equation 3:3}$$

where NPS/S^2 is the normalised noise power spectra (NNPS) and $Q = K_a.SNR_{in}^2$.

The use of objective image analysis based on MTF and NPS has advantages over the semi-quantitative test object based method in that it no longer relies on the skill of the observer maintaining a constant decision threshold with time. The MTF and NPS have also been shown to be more sensitive to changes in detector performance than test object based tests[12].

3.2 Study aim

The aim of this study is to examine the Fourier based image quality metrics MTF, NPS and DQE in the evaluation of a number of indirect digital radiographic systems of the same type. The study will also examine the practicalities and experimental uncertainty in performing these measurements in a busy clinical X-ray department (as opposed to a dedicated laboratory) with the hope of eventually including the measurements in a routine QA program.

3.3 Materials and Methods

To address potential differences in measured DQE arising from variations in test methodology the International Electrotechnical Commission (IEC) developed guidelines published in IEC 62220-1[11]. The IEC 62220-1 standard specifies the conditions under which the MTF, NPS and linearization of data are to be measured and defines the method of calculating the DQE(*f*) using these quantities and the measured air kerma at the detector, as defined in equation 3:2. The standard details the acquisition and processing conditions and the nature of the test device for determining the MTF (precision machined Tungsten edge). A standardized radiation beam quality must also be used and is achieved using a specified thickness of 99.9% pure Aluminium filtration and a nominal tube voltage which is adjusted to give a specific half value layer. For the purposes of this study the IEC 62220-1 standard was adopted as faithfully as practicable.

3.3.1 Indirect digital radiography systems studied

Data are presented for 12 indirect digital radiography detectors marketed as part of the 'Digital Diagnost' range by Philips. The detector is a Trixell Pixium 4600, which has a caesium iodide (CsI) scintillator coupled to a photodiode thin film transistor array. The detector area is 43 x 43 cm^2 with 3120 x 3120 pixel matrix and a pixel pitch of 143 μm. The detectors are all clinically operational in six rooms of the main X-ray department in the Imaging Centre at Belfast Royal Victoria Hospital.

The data required to calculate the quantitative parameters was obtained during scheduled routine QA visits to each room over a two week period. The images were transferred from each individual system to the PACS archive and were downloaded from PACS to an office PC in uncompressed DICOM format via a remote access network.

3.3.2 X-ray factors and technique

A Philips diagnostic X-ray tube (SRO2550), a wall stand detector and a table detector were situated in each of six rooms. Exposures were made with radiation beam quality RQA 5, using 21 mm of Aluminium filtration inserted at the tube head and adjusting the tube potential around 70kVp to get a HVL of 7.1 mmAl[11]. In some cases particularly for table detectors a source-to-image distance (SID) of greater than 180 cm was the not possible and therefore an achievable SID of 140 cm was chosen. All measurements used a small focal spot and an irradiated field size of 25 x 25 cm^2. A calibrated solid state dosemeter (Barracuda R100, Molondal, Sweden) was placed on the detector cover in the centre of the beam. The dose area product (DAP) meter reading and the mAs were also recorded for each acquisition. The exposure to the detector was calculated using the inverse square law for the distance to the actual image receptor surface, an allowance of 3% was made to correct for the transmission of the detector cover. To acquire the images for quantitative

analysis, the tube output was calculated in terms of mAs/μGy to deliver the intended exposures and the DAP meter readings were used to monitor the output and correct for any minor deviations.

3.3.3 Image acquisition settings

It is not possible to get raw image data off the Philips system and all images used for quantitative analysis had some amount of pre-processing applied. A previous study of this detector type found two pre-processing steps applied to all raw image data[7]: (a) an unsharp-mask filter is applied where the enhancement factor increases from 0 to 1.5 linearly with exposure up to an exposure of 2.4 μGy, beyond which the factor is constant at 1.5. (b) De-striping filters are applied in the horizontal and vertical directions, presumably to reduce detector structure noise. Philips confirmed that these pre-processing steps are applied to all 'raw' image data acquired with 'Digital Diagnost' systems.

3.3.4 Image analysis software

The software routines used to measure the edge spread function and the NPS for this study were developed in IDL (RSI Inc, Boulder, USA) for use on CR systems by Workman[9]. As Fourier based metrics are increasingly utilised software routines to compute them have become more widely available to clinical medical physics departments outside of specialised laboratories. An analysis of six common routines used for the determination of the pre-sampled MTF with the edge technique, including the algorithm prescribed in the IEC 62220-1 standard, was performed by Samei *et al* (2005)[13]. The results were analysed in terms of variability as well as accuracy of the resulting MTF and the difference between the individual MTFs and the mean MTF was below 0.02. The agreement of the MTF

results was judged sufficient for the measurement of MTF necessary for the determination of DQE.

3.3.5 Signal Transfer Property

Multiple uniform images were acquired at seven exposure levels (covering the clinical range of use) for each detector. The averages of the pixel values in regions covering ~ 80% of each image area were determined and the results plotted as a function of exposure for each detector, figure 3:1. This function is known as the conversion function or signal transfer function and defines the signal transfer properties (STP) of each detector. The pixel values were proportional to the logarithm of exposure and all systems demonstrated good linearity with a correlation coefficient, $R^2 > 0.99$. The STP relationship was used to linearize the image data before quantitative analysis.

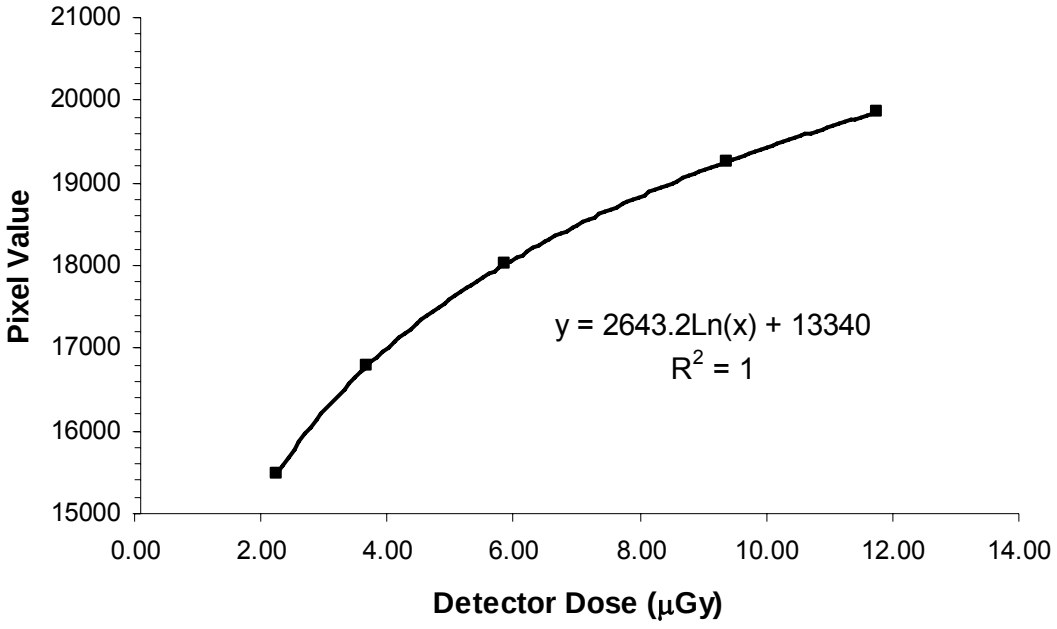

Figure 3:1 Signal transfer property of a Trixell Pixium 4600 detector**.**

3.3.6 The modulation transfer function

The pre-sampled MTF was measured using the edge technique[13-16]. The pre-sampling MTF characterises the frequency response of the detector up to the point of sampling by the discrete pixel matrix. This includes the response of the X-ray converter (CsI) and an aperture function depending on the system readout (the active area of each pixel in an integrating detector)[17]. *Note: a difficulty arises with digital detectors because the detector response to a signal may depend on not just the properties of the detector itself but also on the signal pattern and its location relative to the pixel matrix. Therefore the signal transfer is a two step process influenced by the 'analogue' stage of the signal described by the pre-sampled MTF and the sampling*[18]. The pre-sampled MTF is a property of the detector and independent of the signal pattern.

The test object consisted of a tungsten sheet with dimensions 100 mm x 100 mm x 1 mm with a precision machined and polished edge. The edge was positioned on the table top to assess table detectors and on the detector housing for the wall stand measurements. The detector surface at the three unpolished sides of the test object was covered by lead aprons to minimise the effect of secondary radiation from the test object. X-ray beam alignment was verified using a cylindrical alignment tool with two steel bearings (Gammex-RMI, Nottingham, UK). The test object was imaged at a slight angle (typically 3 degrees) between the machined edge and the pixel matrix at an exposure level of 4 μGy to the detector.

The images were then imported into IDL and the algorithm used to compute the MTF consisted of the following main steps: (a) A linearized region of interest (ROI) of approximately 50 mm x 50 mm was defined with the edge at the centre. (b) The edge angle was determined using a simple method. The image was displayed magnified on the screen and the user was required to select two points, either end of the edge, by clicking

the mouse on the edge at each location. (c) The two dimensional (2D) image data were re-projected around the edge and oversampled to form an edge spread function (ESF) with a bin spacing of 0.1 pixels. The data were then filtered with a median filter to reduce noise. (d) The ESF is differentiated to form the line spread function (LSF). The LSF tails were smoothed to zero, this ensures it remains a periodic function, required by Fourier analysis. (e) The MTF is calculated in the direction perpendicular to the edge by taking the modulus of a fast Fourier transform (FFT) of the LSF and normalising its value to unity at zero spatial frequency.

The Trixel Pixium 4600 detector consists of four subpanels tiled together. MTF measurements were made at the centre of each subpanel for two detectors, measurements on the remaining 10 detectors were made at the centre of a subpanel chosen at random. Differences in the MTF measured in each subpanel were expected to be minimal, as noted in a previous study[7] where the correlation coefficients of the MTFs were greater than 0.997.

3.3.7 The normalised noise power spectrum

The noise power spectra of the systems were measured using four uniform images acquired at 4 μGy exposure level and RQA 5 for each detector (the number of images are such that at least 4 million pixels are used for analysis[11]). The NPS is essentially the pixel variance (noise) as a function of spatial frequency. The contributions to the total NPS are the result of many processes including: X-ray quantum noise; Poisson excess noise (resulting from variations in secondary quanta detected, e.g. light photons, electrical charge); electronic noise from preamplifiers in the readout stage; and fixed pattern or structure noise from sources such as the CsI or pixel array structure[5,10].

The acquired images were imported to IDL and the NPS analysis algorithm was applied. The algorithm consists of the following main steps: (a) A region of approximately 125 mm x 125 mm was delineated at the centre of each image (defined as ROI_{main}). (b) Data in ROI_{main} were linearized using the STP, effectively converting the image segment into variations in air kerma as opposed to variations in pixel values. (c) Trend removal was performed by subtracting a 2D second order polynomial from ROI_{main}. This removes the influence of low frequency non-uniformities or artefacts on the NPS. (d) The analysis region was broken up into half overlapping 256 pixels x 256 pixels regions of interest, ROI_{sub}. The squared modulus of the 2D Fourier transform was calculated for each ROI_{sub}. (e) The 2D transforms from each ROI_{sub} were averaged to give the 2D NPS ensemble. (f) Finally the normalised noise power spectra (NNPS) is obtained by dividing the ensemble by the square of the mean value of ROI_{main} (i.e. by air kerma^2)

The IEC standard recommends the display of one dimensional NPS in each orthogonal direction. For each direction, this was done by taking seven spatial frequency bins on either side of the axis, excluding the axis itself.

The working equation for the NPS according to the standard is[11]

$$NPS(u_n, v_k) = \frac{\Delta x.\Delta y}{M.256.256} \sum_{m=1}^{M} \left| \sum_{i=1}^{256} \sum_{j=1}^{256} \left(I(x_i, y_j) - S(x_i, y_j) \right) . \exp(-2\pi i (u_n x_i + v_k y_j)) \right|^2 \quad \textbf{3:4}$$

where,

$\Delta x \Delta y$ is the pixel spacing in the horizontal and vertical directions

M is the number of ROIs (i.e. the number of ROI_{sub}'s)

$I(x_i,y_i)$ is the linearized data (after correction by the STP)

$S(x_i,y_i)$ is the trend removal polynomial (optionally fitted).

Uniform images were also acquired at approximately 0.5, 1.2, 2.4 and 6.2 μGy to examine NPS at multiple exposure levels and at 50, 60, 81, 91 and 117 kVp to examine the effect of beam quality.

3.3.8 Detective quantum efficiency

Detective quantum efficiency was calculated for the 12 detectors in this study by substituting the MTF and NNPS values into equation 3:3. The number of photons per unit μGy mm^2 (SNR_{in}^2) for RQA 5 was taken from the IEC report[11] and the standard exposure level used for the NNPS and MTF measurements was 4 μGy.

The effect of beam quality on DQE was investigated for a clinically representative range of beam qualities, provided by peak tube potentials ranging from 50 to 117 kVp, table 1. To calculate the DQE for each beam quality an accurate estimate of SNR_{in}^2 must be made, equation 3:3. Depending on whether the X-ray detector is being considered as an ideal photon counting detector or an ideal energy integrating detector, the value of SNR_{in}^2 is weighted either by the no. of exposure quanta per unit area or the energy of all exposure quanta per unit area, respectively[11,19]. For the 'counting' detector the no. of photons per mm was obtained simply by integrating the X-ray spectrum. However for the 'energy integrating' detector SNR_{in}^2 was calculated as[19]

$$SNR_{in}^{\ 2} = \frac{\left(\int_0^{kVp} \varphi(E).E.dE\right)^2}{\int_0^{kVp} \varphi(E).E^2.dE} \qquad \textbf{Equation 3:5}$$

where $\varphi(E)$ is the X-ray spectrum with energy E.

Photon fluences were calculated from data on X-ray photon spectra generated at different tube potentials for a constant potential unit with a tungsten rhenium anode having

a of 16º target angle and filtered by 2.5 mm of aluminium[20]. The fluence was adjusted for attenuation with 21 mm Al using tabulated data on mass attenuation coefficients in a spreadsheet program. The spectra were also normalised to an exposure of 1 μGy using mass energy absorption coefficient data obtained from the same source[20] to calculate air kerma for each spectra.

Table 3:1 Spectra data used in examining the effect of beam quality on DQE.

Tube potential (kVp)	50	60	70	81	96	117
HVL (mmAl)	4.75	5.98	7.05	8.13	9.25	10.44
Mean energy (keV)	42.2	47.9	53.2	58.5	64.4	71.5
SNR_{in}^2 (counting)	23999	27860	30292	31787	32184	31311
SNR_{in}^2 (energy integrating)	23779	27448	29652	30924	31003	29606

3.4 Results and Discussion

3.4.1 Modulation transfer function

Figure 3:2 shows the pre-sampled MTF calculated along the vertical and horizontal directions for 12 detectors. The mean of the spatial frequencies at the 0.5 MTF point was 1.3 mm^{-1} and the standard deviation from 24 measurements was 0.13, giving a coefficient of variation (*cov*) of 10%. A value of 1.3 at the 0.5 MTF point was reported previously[7] for a CsI detector using a 200μm pixel pitch. It is interesting to note that the larger pixel pitch also resulted in a noticeable increase in aliasing due to under-sampling the MTF, at the Nyquist frequency the relative MTF values were 0.25 and 0.1 in the previous and present studies, respectively. Similar values were also reported in an alternative study[21] using a Pixium 4600 detector (0.5MTF = 1.4).

In an ideal system the line spread function would be a delta function with a width equal to the pixel pitch. The MTF of this ideal function is the sinc function. As can be

seen from figure 3:2 the measured pre-sampling MTF is significantly below the limit set by the pixel sampling aperture (0.143 μm). This has been reported in previous studies[7,12,21] and is possibly due to re-absorption of k-shell fluorescence at a position remote from the initial interaction [22] or charge trapping within the pixel electrodes[23,24].

Figure 3:3 shows the same data expressed as the area under each MTF curve from zero to the Nyquist frequency (3.5 mm^{-1}) calculated using 'Sigmaplot' software (version 10, Systat Inc., Germany). The average area under the MTF curve was 1.67, which can be seen to vary by approximately ±10%.

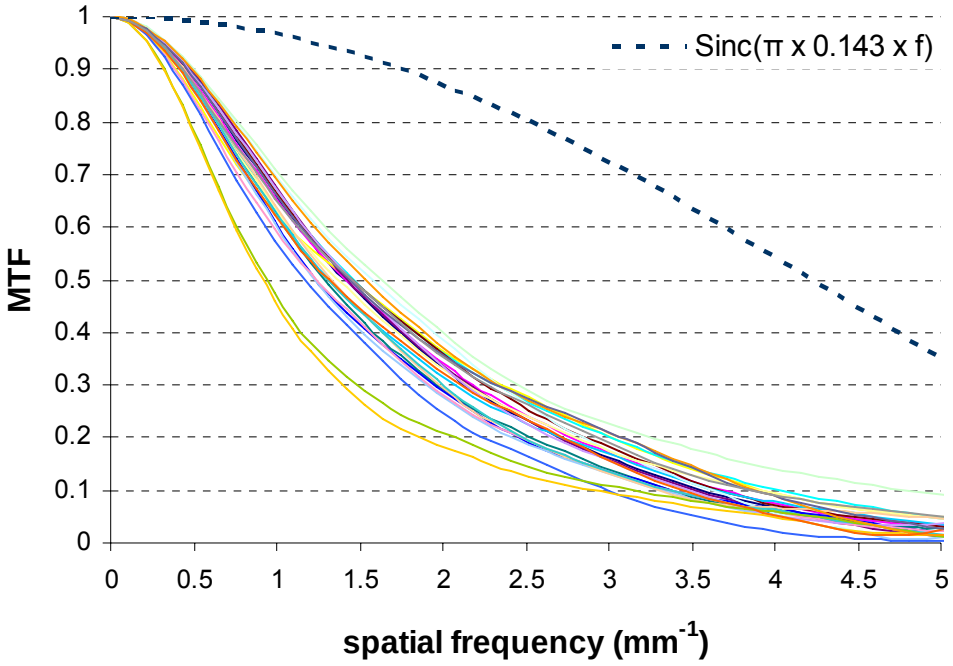

Figure 3:2 Measured MTF data for 12 Trixell Pixium 4600 detectors, measured in the horizontal and vertical directions.

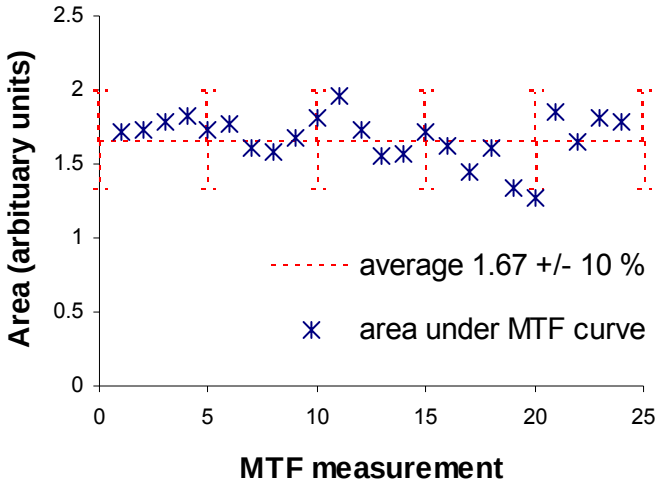

Figure 3:3 Computed area under each MTF curve, calculated from horizontal and vertical MTF measurements on 12 detectors.

Results for the means of the MTF measured in the vertical and horizontal directions were similar 1.8% ±0.5% (mean variation ± standard error); indicating that pre-sampling MTF is isotropic and does not exhibit directional dependence, figure 3:4.

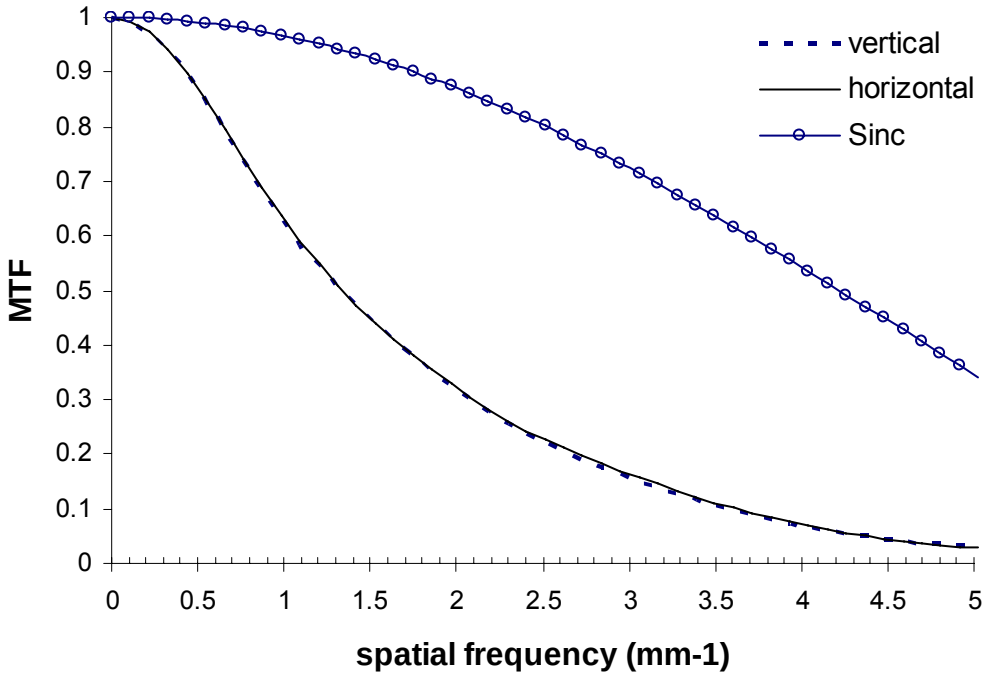

Figure 3:4 Average MTF measured in the horizontal and vertical direction.

The noise equivalent aperture (NEA) is a single figure measure that has been found to correlate well with the visual impression of image sharpness[9]. It is derived from the measured MTF from zero to the Nyquist frequency, f_N as follows:

$$NEA = \left(2\pi \int_0^{f_N} MTF^2(f) f df \right)^{-1} \qquad \textbf{Equation 3:6}$$

The NEA was calculated using the composite MTF for each detector (i.e. the MTF averaged in the horizontal and vertical directions). The mean NEA for 12 detectors in this study was 0.22 mm^2 ±0.02 mm^2 (mean ± standard error), comparable to an NEA of 0.21 reported previously[21].

Figure 3:5 examines the effect of the different geometries used to measure the MTF on the table top and wall stand. A slight difference was noticeable in the average values for the table and wall stand detectors. With the tungsten edge placed on the wall stand cover a slightly greater MTF is observed from 0.3 to 2.3 cycles/mm; above 2.7 cycles/mm however, the MTF is greater for the edge placed on the table top. A mean variation ± standard error of 3.3% ±0.5% up to the Nyquist frequency was observed.

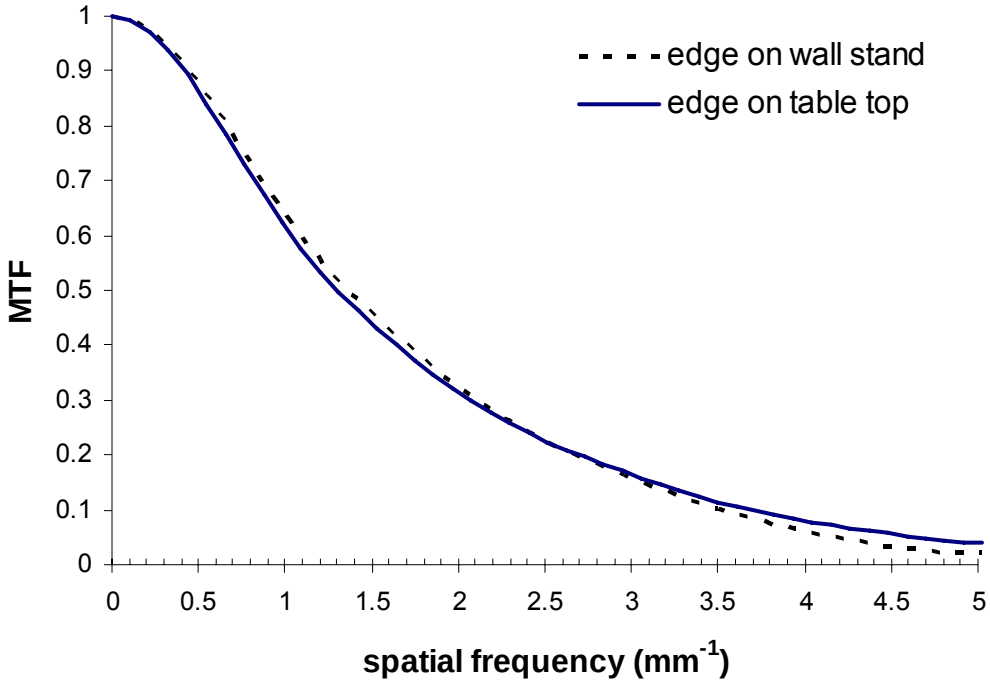

Figure 3:5 Average MTF measured with the table and wall stand detectors, using slightly different geometries.

The results for the MTF measurements made at the centre of each of 4 subpanels, for two different detectors were significant. A mean variation ± standard error of 3.5% ±0.7% from zero to the cut-off frequency was recorded.

The results presented in this study can be seen as field test measurements and the MTF was generally assessed with the edge test object placed on the outer cover of the wall stand or on the table top where appropriate. However, it was possible to obtain a set of repeated measurements with one detector whereby the test object was placed on the outer cover of the wall stand and directly onto the surface of the image receptor (*i.e.* with the outer cover and the AEC chamber layer removed). The results are shown in figure 3:6. There was surprisingly little variation between the measurement set-ups, with a mean variation of 1.7% ±0.2% up to the cut-off frequency.

The effect of an edge polished to submicron level smoothness at 90 degrees when compared with a standard cut unpolished edge on the assessment of MTF was also investigated and results are shown in figure 3:6. The MTF of the standard edge was lower by a mean variation of 2% ±0.4%.

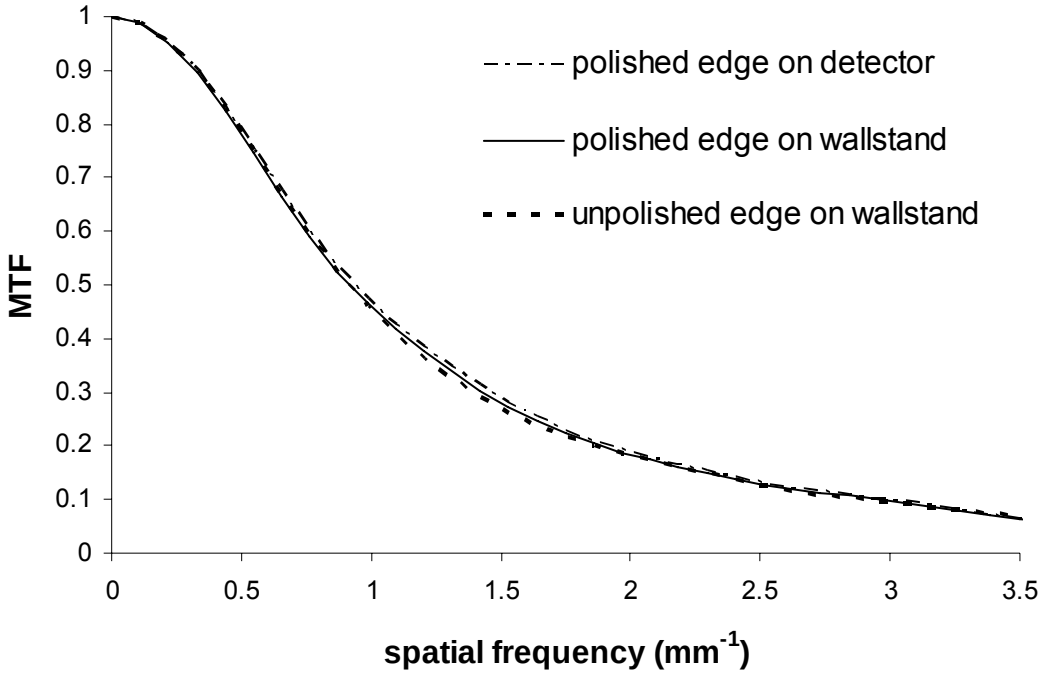

Figure 3:6 Effect of geometry and edge 'smoothness' on MTF.

In order to obtain an estimate of the reproducibility of the MTF algorithm, the analysis was repeated twelve times on the same image. The results showed a mean variation of 2.3% ±0.4%. The accuracy involved in sampling the image data to produce the edge spread function (using the method used in this study) was estimated previously[18]. The systematic error in the MTF estimate was reported to be approximately equal to 1/4N, where N is defined as the reciprocal of the tangent of the edge angle. In the present study we aimed to use a nominal edge angle of 3 degrees (achieved within a tolerance of ±2 degrees) giving a maximum error of 2.2% at the Nyquist frequency. Summing the two errors gives us a total expected uncertainty of 3.5% in the determination of MTF.

3.4.2 Normalised Noise Power Spectra

Figure 3:7 presents the NNPS results in the horizontal and vertical directions for the 12 detectors studied. The mean NNPS and percentage *cov* at: 1 mm^{-1}; 2 mm^{-1}; and 3 mm^{-1} are: $8.9x10^{-06}$ (10%); $6.8x10^{-06}$ (7%); and $4.7x10^{-06}$ (13%), respectively.

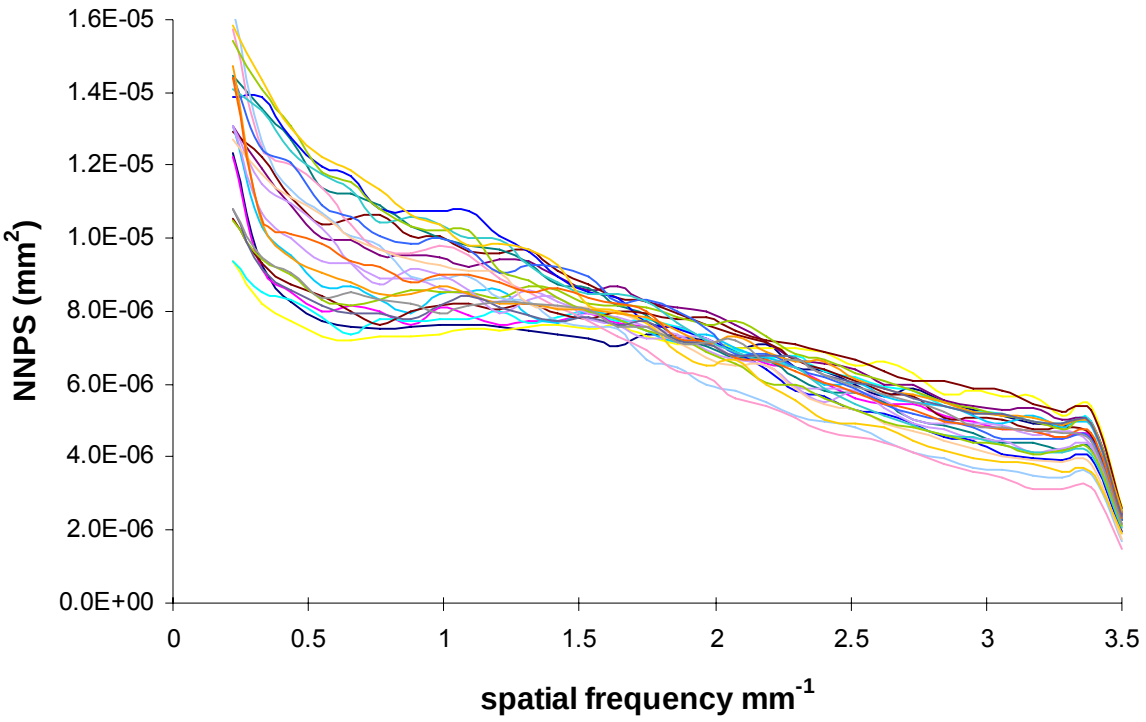

Figure 3:7 NNPS results in the horizontal and vertical directions for the 12 detectors studied.

Figure 3:8 illustrates the mean NNPS for the six table and six wall stand detectors, in each orthogonal direction. There was a significant difference between the vertical and horizontal NNPS values. The NNPS in the vertical direction was on average 2.4% higher from 0.2 to 2.0 cycles/mm; above that however, the NNPS was higher in the horizontal direction by an average of 6.2%. The difference observed in NNPS in the orthogonal directions may be attributed to the spatial structures of the TFT elements[7]. Figure 3:8 also illustrates a slight difference in the NNPS observed for the table and wall stand detectors, although this is within the uncertainty on the NPS estimates.

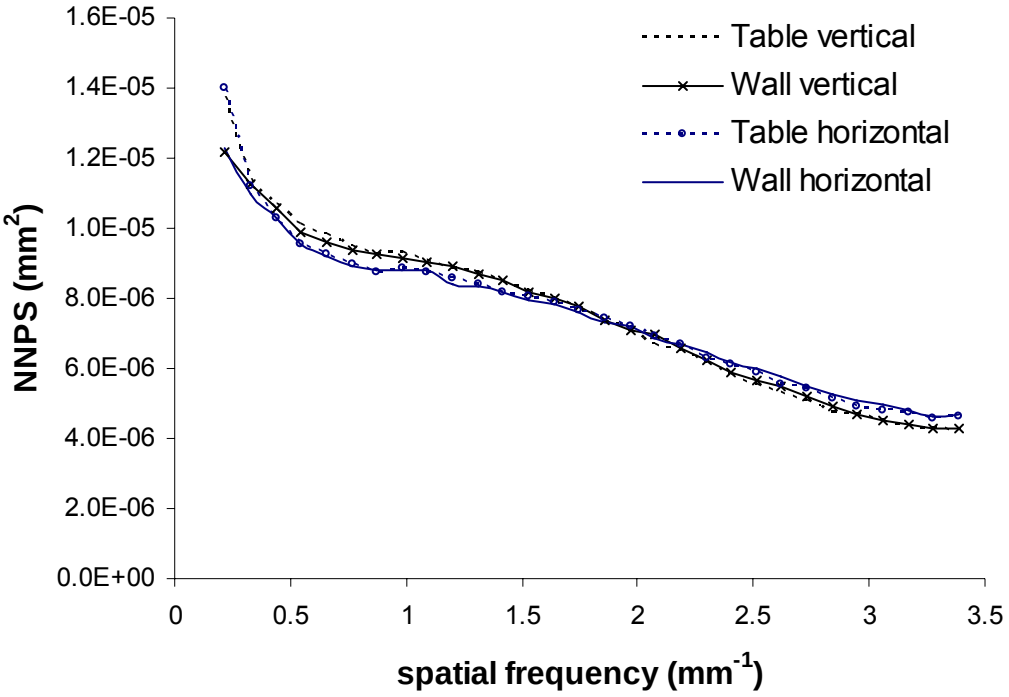

Figure 3:8 Average NNPS results in the horizontal and vertical directions for the table and wall stand detectors.

The relative uncertainty in the NPS estimate can be calculated as $1/\sqrt{N_{bin}}$, where N_{bin} is the number of independent frequency bins used[17,25]. N_{bin} is calculated as:

$$N_{bin} = M.R.bin_{mean} \qquad \textbf{Equation 3:7}$$

where M is the number of ROI_{sub} regions, R is the number of rows used to section ROI_{main} and bin_{mean} is the mean number of NPS points in a bin per row. The sampling frequency resolution of the NPS estimate was $(256 \times 0.143)^{-1} = 0.027$ mm^{-1} the data were then re-binned into 0.1 mm^{-1} bins for the 2D plots, giving $bin_{mean} = 4$. N_{bin} is therefore 64 x 8 x 4 = 2048 giving an uncertainty of 2.2% assuming non-overlapping regions of interest (ROIs). Dobbins *et al* (2006) have shown that when half-overlapping ROIs are used estimation of uncertainty is inversely proportional to the relative areas used, and in this case is reduced by $1/\sqrt{2}$ to 1.6%. The normalised NPS is also dependent on an accurate assessment of the air kerma at the image receptor. The overall uncertainty with the NNPS measurement is

thus given by the summation of the 1.6% NPS error with that of an estimated exposure uncertainty of 3%, giving a total of 3.4%.

Figure 3:9 represents a greyscale image of a 2D NPS for one of the detectors. The NPS shows a marked depression on the horizontal and vertical axis due to low frequency artefact and pre-processing applied to the images, as discussed previously. In particular the de-striping filters impact the NPS results and horizontal and vertical lines can be seen clearly. Ideally the quantitative image analysis would be performed on unprocessed image data. However, in situations where this is not possible careful image quality assessments can still be valid as long as they take note of exactly what pre-processing operations were preformed[7,26].

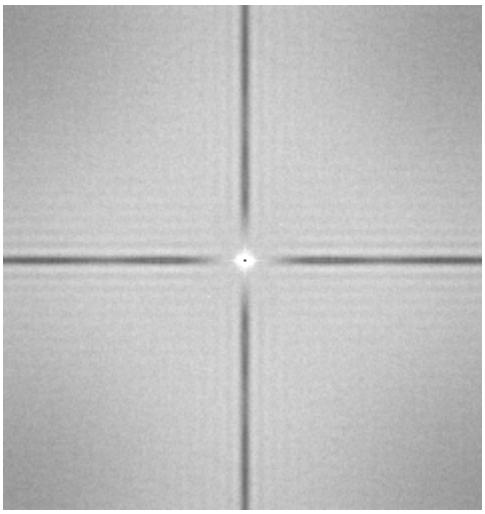

Figure 3:9 An example of the measured 2D NPS at 4μGy.

The one dimensional NPS data presented in this study (figures 3:7 & 3:8) are an average of 7 spatial frequency bins taken either side of each axis, excluding the axis data itself, as recommended by IEC 62220-1[11]. Averaging 14 bins and excluding the axes minimises the impact of the de-striping filter pre-processing on the NPS estimates presented. However an unsharp-mask filter was also applied and the effect of this filter on the image data was investigated.

The unsharp-mask algorithm may be defined as

$$E = I + \beta(I - S) \qquad \textbf{Equation 3:8}$$

where E is the enhanced image, I is the original image, S is the unsharp or smoothed version of I and β is a factor which controls the amount of enhancement. The frequency range enhanced depends on the size of the smoothing kernel; larger kernels enhance lower spatial frequencies; and smaller kernels enhance higher spatial frequencies. To understand the processing changes applied to the image data we need to consider how much enhancement is present, how it is scaled and how it affects the NPS, figure 3:10.

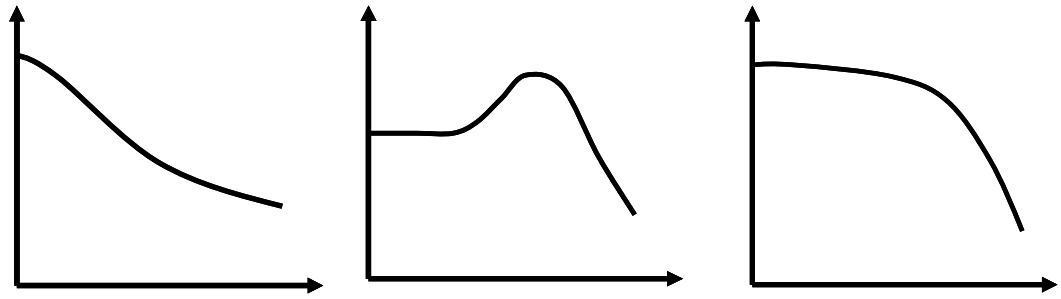

(a) (b) (c)

Figure 3:10 Schematic showing the effect of unsharp-mask processing. (a) Typical NPS spatial frequency distribution (b) An unsharp-mask filter (c) The resulting spatial frequency distribution.

The variation in NNPS with exposure is illustrated in figure 11. The relative noise power is seen to decrease with increasing exposure. At low doses the NNPS is quantum limited and the relative noise varies with the reciprocal of exposure. At higher doses however the NNPS approaches a lower limit as the relative contribution to the NNPS comes more from the fixed pattern or structure noise component.

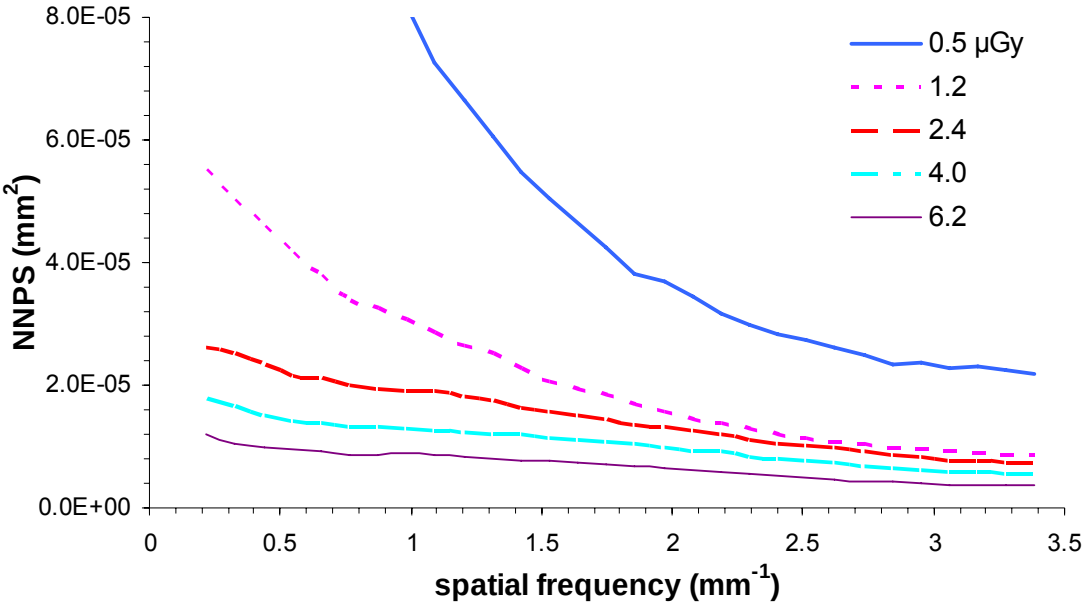

Figure 3:11 Measured variation in NNPS with spatial frequency for a range of exposure levels.

The data presented in figure 3:11 are re-plotted in figure 3:12, where the NNPS is shown as a function of detector air kerma for selected spatial frequencies. It is clear from figure 3:12 that primary quantum noise is the dominant noise component as the NNPS falls with a slope of minus one. For spatial frequencies above 0.2 mm^{-1} the NNPS can be seen to follow a different trend between approximately 1 and 2.5 µGy; above ~2.5 µGy however, it resumes a slope of approximately minus one. The change in the trend of the NNPS with exposure for different spatial frequencies is a characteristic of the unsharp-mask filtering applied in pre-processing the image data.

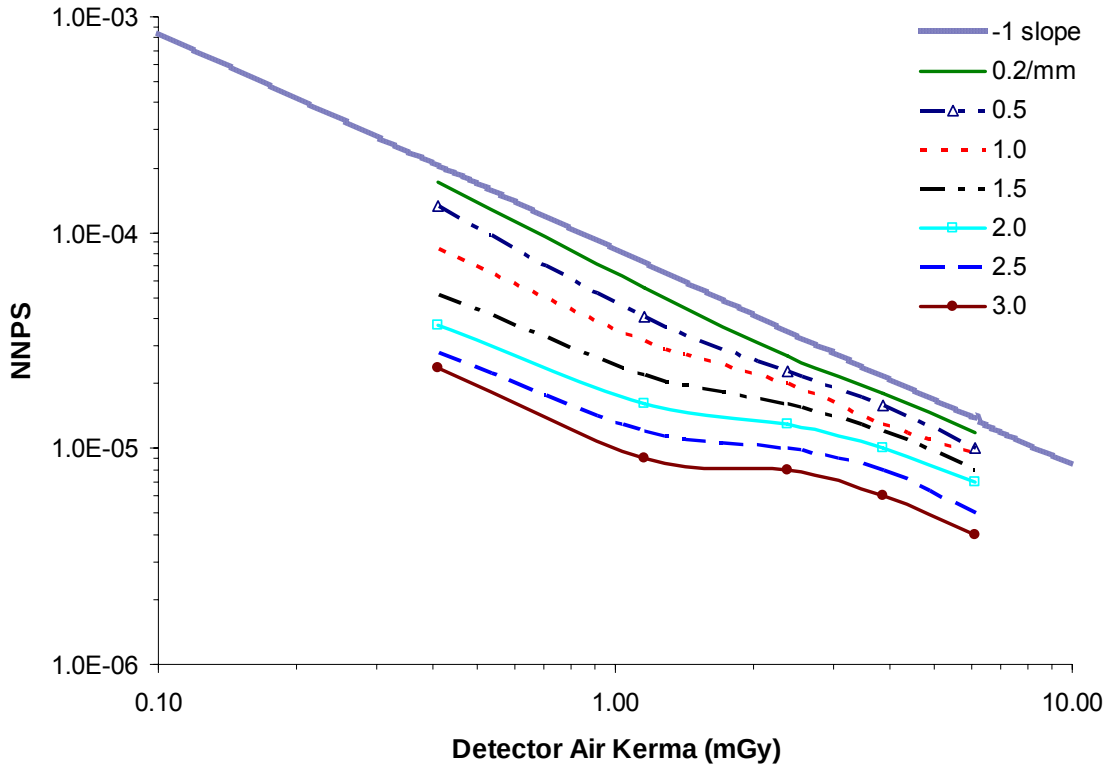

Figure 3:12 Variation in measured NNPS with detector air kerma for selected spatial frequencies.

Dividing the NNPS values measured at 1.2, 2.4, 4 and 6.2 μGy by the values measured at 0.5 μGy and normalising this ratio to unity at 0.2 mm^{-1} allows us to see the effect of the enhancement factor on the spatial frequency of the image data, figure 3:13. For exposures ≥ 1.2 μGy the relative NNPS increases with spatial frequency up to ~ 1.8 mm^{-1}, beyond 1.8 mm^{-1} the ratio remains constant at approximately 1.6.

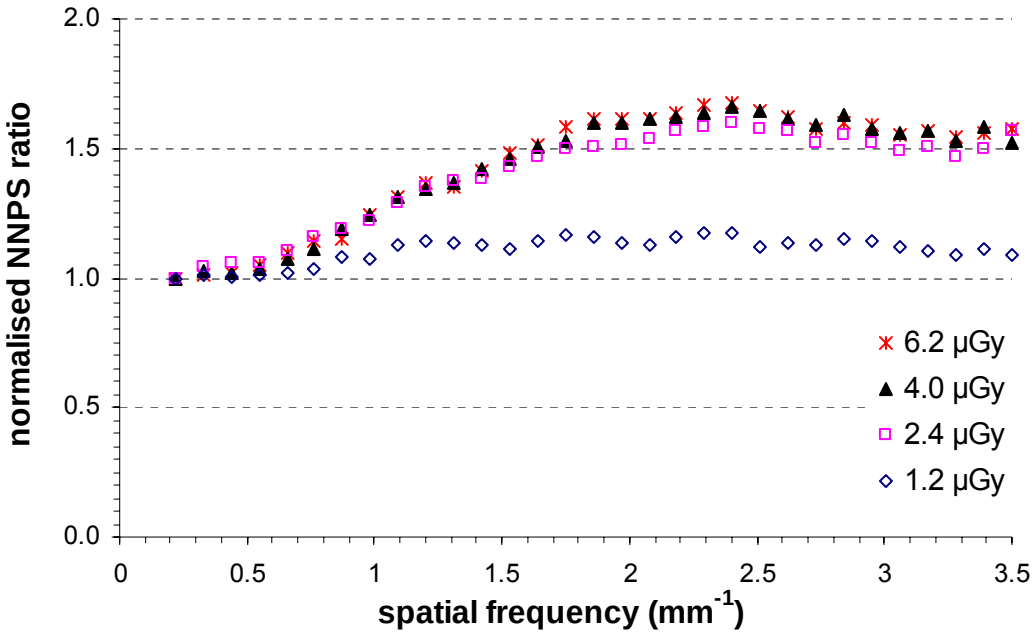

Figure 3:13 Measured NNPS for selected exposures, relative to those values at 0.5 µGy. This NNPS filter may be used to understand changes made to image data as a result of unsharp-mask pre-processing.

The results presented in this study can be seen as field test measurements and similar to the case with the MTF measurements, NNPS was generally assessed from uniform images acquired with detector covers, AEC chambers and a table in place, where appropriate. However, it was possible to obtain a set of repeated NNPS measurements with one detector whereby the outer cover of the wall stand and the AEC chamber layer were removed to expose the detector. The results are shown in figure 3:14. There was a statistically insignificant variation between the measurement set-ups, with a mean variation of 2.0% ±0.2% up to the cut-off frequency, well within the estimated NNPS measurement uncertainty of 3.4%.

The final set of NNPS measurements were acquired to assess the effect of using very high purity Al (type 11999 alloy) as specified in IEC 62220-1[11]. Standard Al of the type frequently used in medical physics departments to assess beam quality is 99.0% pure.

Apart from being relatively expensive, very high purity Al is also uncommon and has been shown in a previous study[27] to cause low frequency mottle in the 2D NPS. The effect of using very high purity Al and standard Al for NNPS measurements can be seen in Figure 3:15. The NNPS using standard Al is 1.5% ±0.3% less than that measured using very high purity between 0.3 mm^{-1} and 2.3 mm^{-1}. This difference is less than the uncertainty in the NNPS measurement. The measured NNPS at ≤ 2 mm^{-1} is however statistically significant where a 58% difference was observed. The gross overestimate in NNPS at low frequency is attributed to the manufacturing method and relatively larger grain size with very high purity Al compared to standard Al[27].

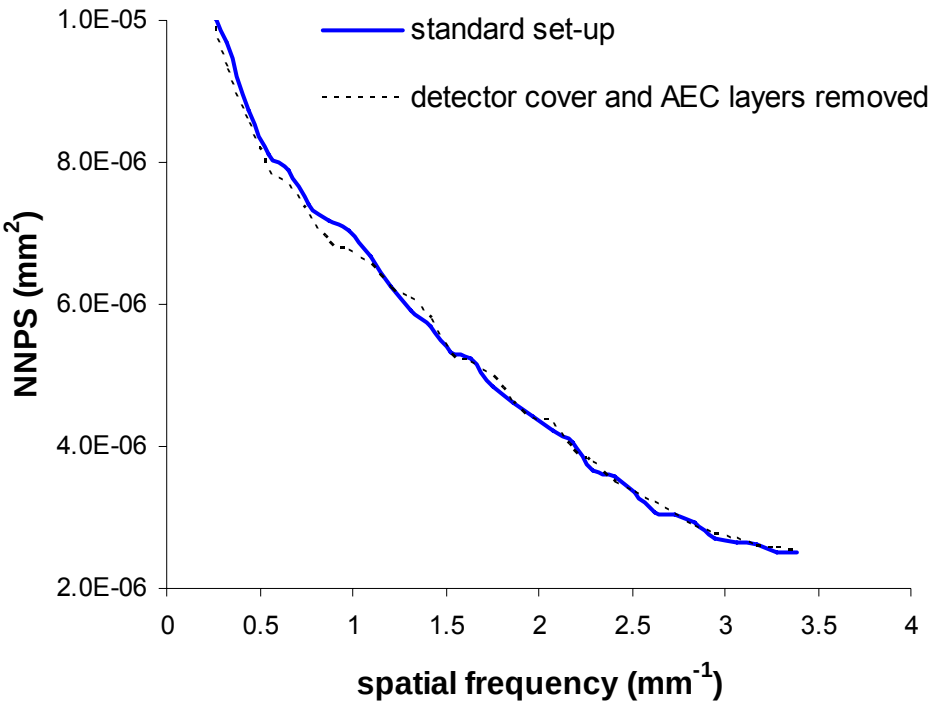

Figure 3:14 Measured NNPS at 4μGy with and without detector cover and AEC layers in place.

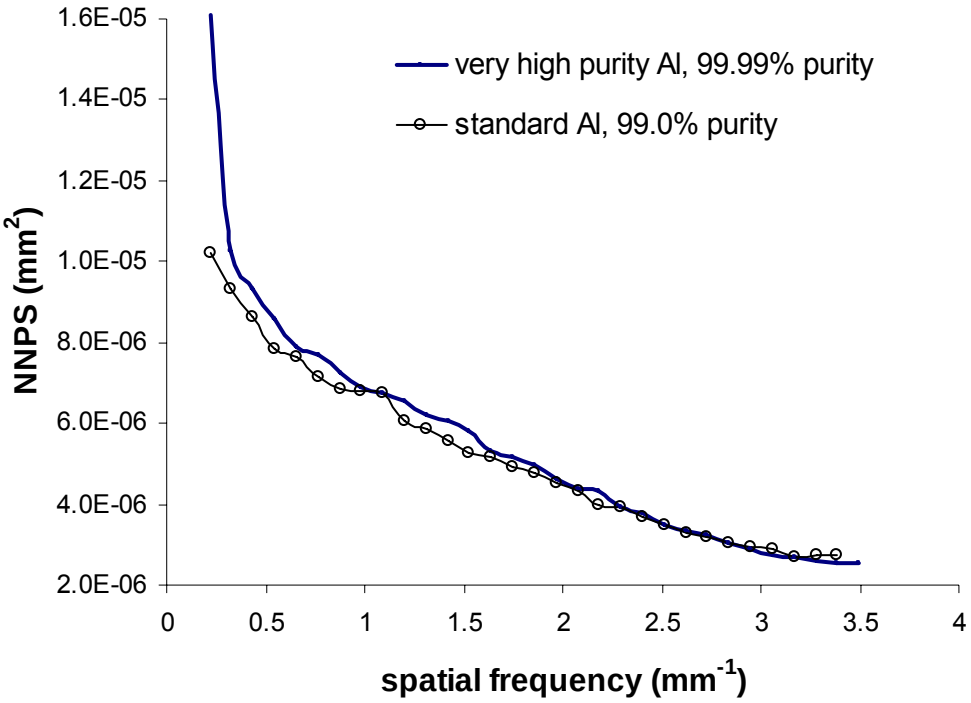

Figure 3:15 Measured NNPS at 4μGy comparing high purity Al (type 11999 alloy, 99.99% purity) and standard Al (type 1100 alloy, 99.0% purity) filters.

3.4.3 Detective Quantum Efficiency

Figure 3:16 reports the DQE calculated from the measured data in the horizontal and vertical directions for the 12 detectors studied. The DQE trend for each detector is seen to peak between approximately 0.3 and 0.4 mm^{-1}, below ~ 0.3 mm^{-1} the detector exhibits a linear decrease with frequency, resulting from artefact as NPS tends to infinity when the spatial frequency approaches zero. At frequencies above 0.4 mm^{-1} the slope decreases and the DQE asymptotically approaches zero. The average peak DQE was 0.68 with a mean variation of 11% ±0.6%. The uncertainty in the DQE measurements is a combination of the uncertainties in the measurements of MTF (3.5%) and NNPS (3.4%) *i.e.* the terms in equation (3), giving an overall uncertainty of 6%.

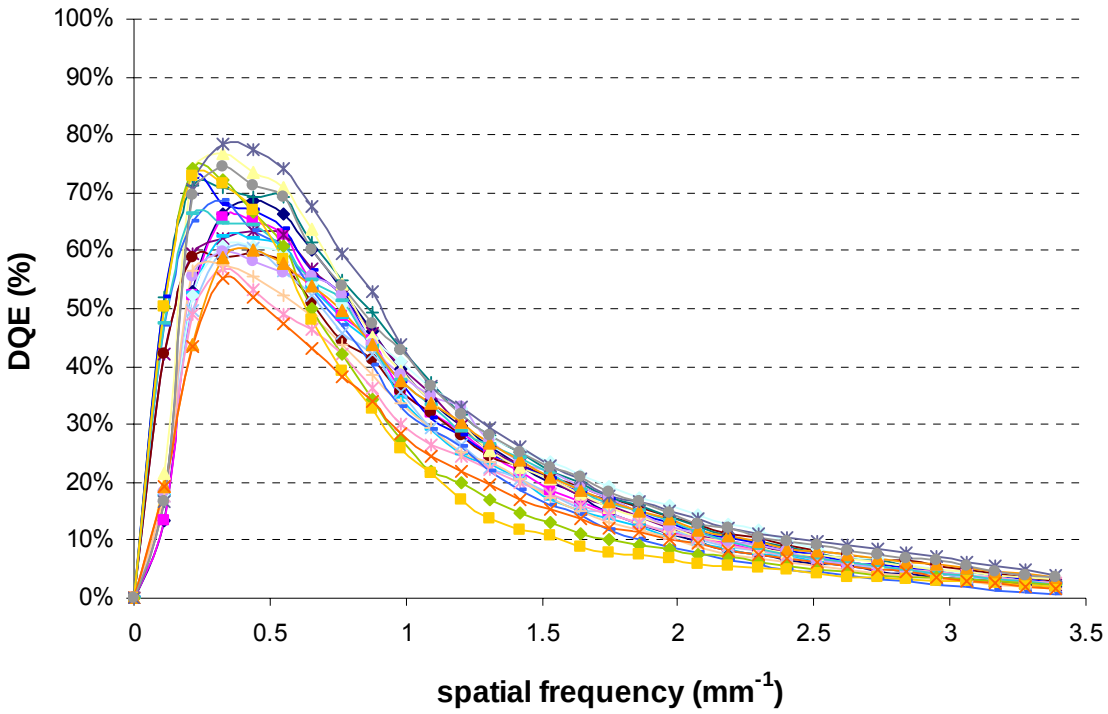

Figure 3:16 Measured DQE at 4µGy in orthogonal directions for 12 detectors studied.

The average DQE in the horizontal and vertical directions differ by only 4%, thus DQE values may be averaged and stated to be valid for both axes. The format of conformance statements to include DQE is outlined in the IEC standard[11]. Table 3:2 presents the average results for the 12 detectors in this format.

Table 3:2 Average DQE results for 12 detectors in IEC62220-1[11] format.

Irradiation RQA / µGy	**Spatial Frequency cycles/mm**	**DQE axes average**
5 / 4.0	0.5	0.62
	1.0	0.40
	1.5	0.20
	2.0	0.11
	2.5	0.07
	3.0	0.04

DQE was also investigated as a function of DAK. Figure 3:17 illustrates DQE in the graphical reporting format recommended in the IEC standard. Measurements are presented for four exposure levels; 1.2, 2.4, 4.0 and 6.2 μGy, plotted for discrete spatial frequencies from 0.5 mm^{-1} up to the cut-off frequency. The DQE reduces as the DAK is increased, due to the growing influence of structured noise on the DQE. Structured noise is a multiplicative noise source (multiplied by the X-ray signal), which becomes progressively more important as the exposure increases[25]. The magnitude of the drop in DQE is also accentuated by the changes in NNPS due to the unsharp mask enhancement factor.

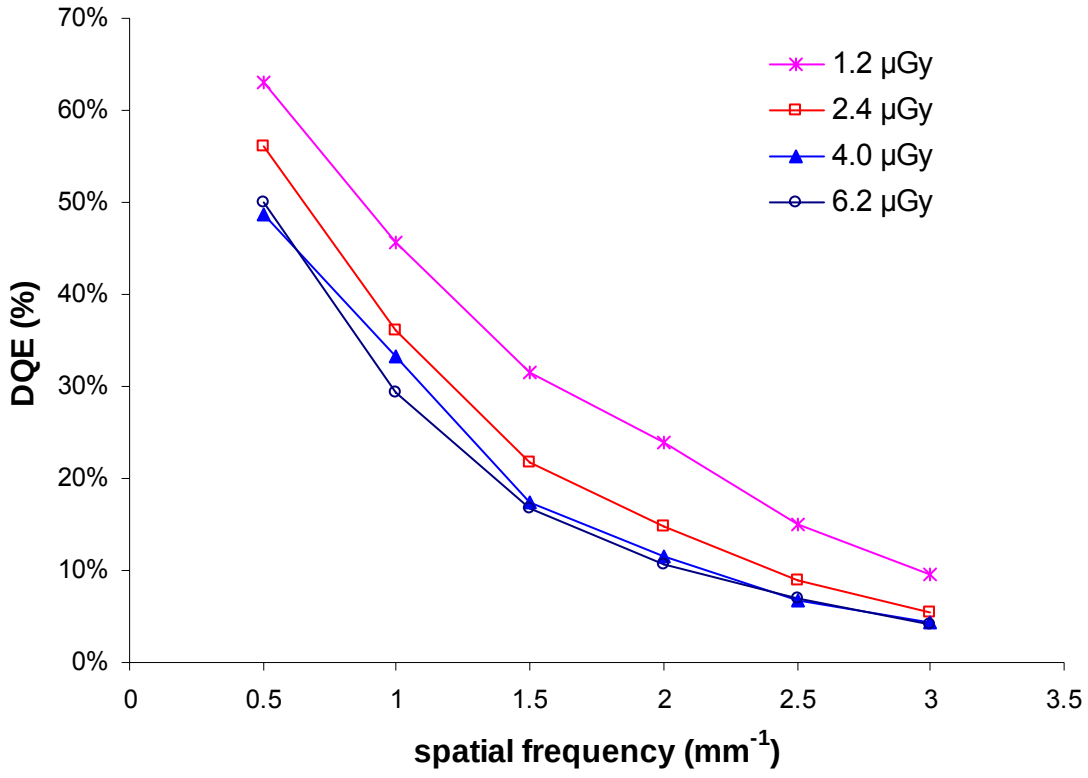

Figure 3:17 Measured DQE at selected exposure levels for one of the detectors studied.

Figure 3:18 shows the DQE as a function of DAK averaged from at 0.5 to 3.0 mm^{-1} spatial frequencies. There is a reduction in the average DQE from 0.34 to 0.2 or 41% as

the air kerma at the detector is increased from 0.4 to 6.2 μGy. Considering the images used in this study for quantitative analysis were corrected for offset and gain variations, a 40% reduction in DQE at this exposure level is surprising and may indicate the particular detector needs flat fielding recalibration. A similar drop in DQE with exposure was noted in previous studies on digital mammography[25] and indirect digital radiography[28] systems.

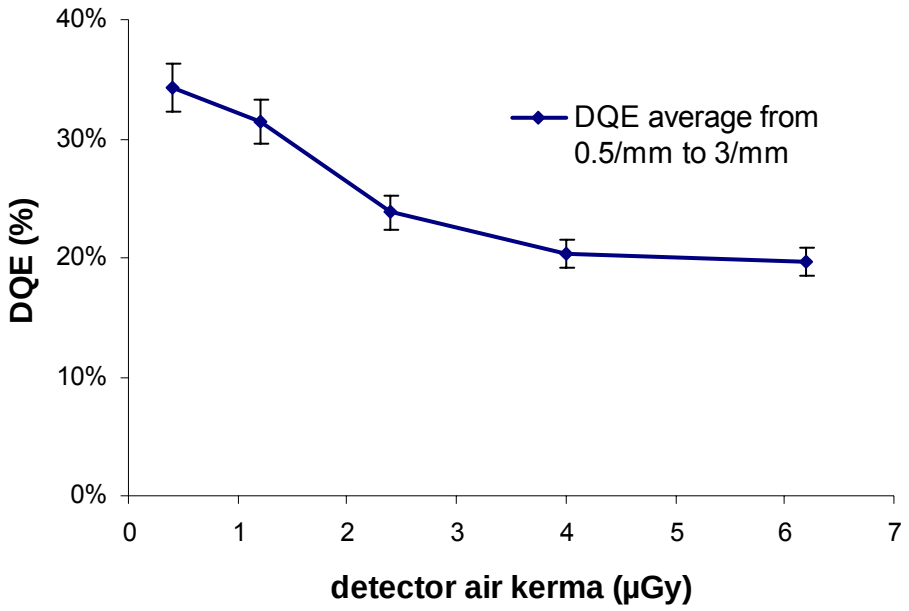

Figure 3:18 DQE as a function of DAK averaged from 0.5 to 3 cycles/mm. Error bars indicate a 6% uncertainty in DQE measurements.

The effect of beam quality on the DQE estimate is reported in figure 3:19, data on the X-ray spectra used are given in table 3:1.

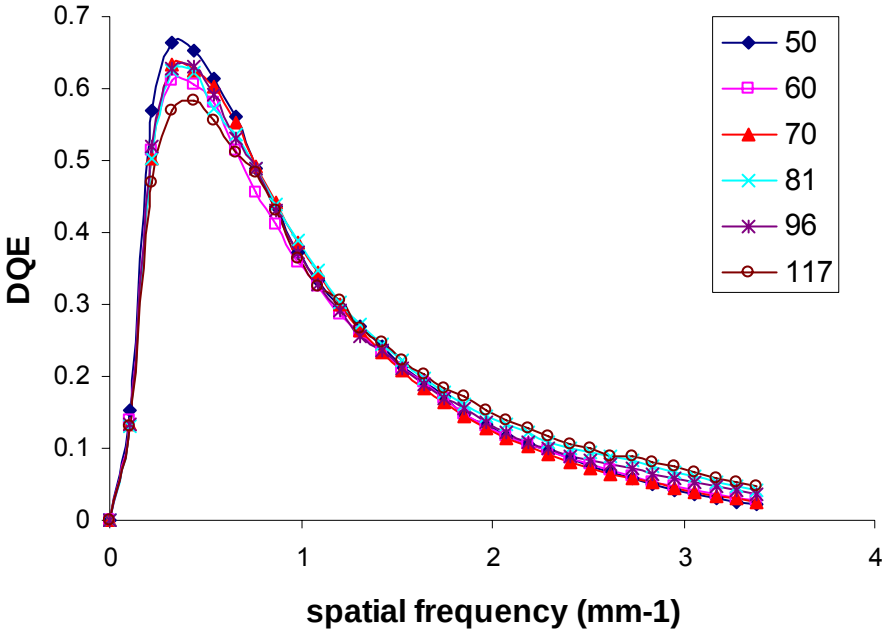

Figure 3:19 Measured DQE for a range of peak tube potentials.

The peak DQE varied by ± 9% from the mean at 50 and 117 kVp. For spatial frequencies greater than ~0.5 mm^{-1} the DQE falls initially with a similar slope but eventually the slope lessens for larger tube potentials approaching the cut-off frequency. This spatial frequency dependence should in theory allow the DQE to give a better estimate of detector performance with tube potential than estimates from the quantum efficiency of CsI calculated solely on the basis of the energy absorbed from incident photon fluence.

Peak DQE or DQE(0) as a function of tube potential is shown in Figure 3:20. DQE was calculated using equation 3:3 for the case of the ideal photon counting detector and the

ideal energy integrating detector. The calculated values of SNR_{in}^2 used for each case are listed in table 3:1. Error bars indicate a 6% uncertainty in the DQE estimate. As expected the DQE is a strong function of kVp. Decreasing the X-ray energy (*i.e.* tube potential) improves the DQE as the X-ray photons are more efficiently absorbed in the detector.

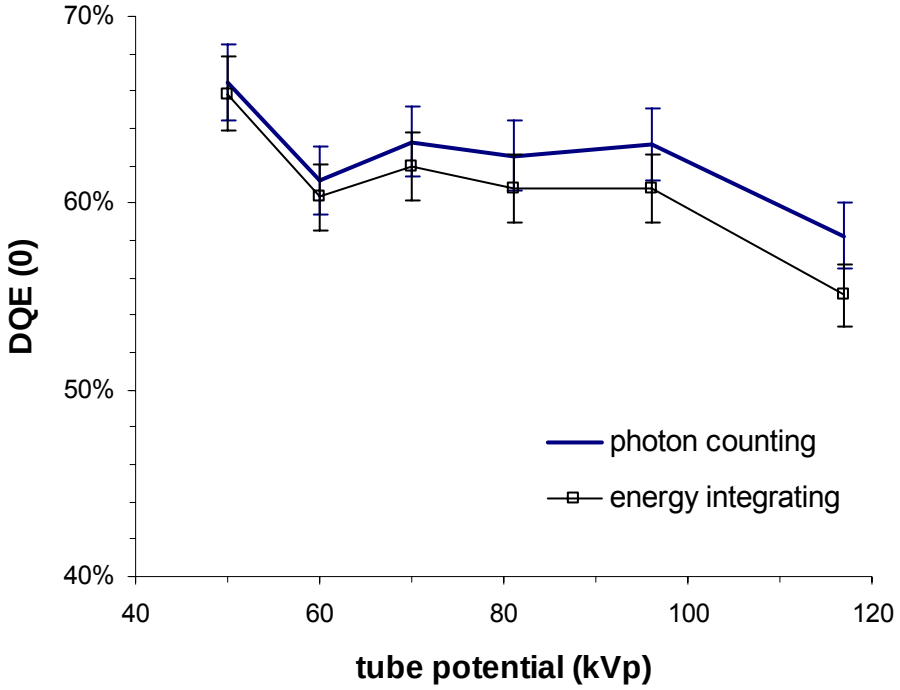

Figure 3:20 DQE(0) as a function of tube potential. Error bars indicate a 6% uncertainty in the DQE estimate.

3.5 Conclusions and Recommendations

This study has described the use of objective image performance parameters in characterising 12 indirect digital X-ray detectors of the same type. The IEC DQE measurement methodology was successfully applied to detectors in a clinical X-ray room. The following are comments and recommendations for the determination of DQE from measurements made on detectors in-situ:

- The uncertainty in the measurements of MTF was 3.5% and NPS was 3.4%. This gave a total uncertainty in the measurement of DQE of 6%, equal to the maximum uncertainty allowable following the IEC protocol[11].

- The mean DQE(0) value was 0.68 at 4μGy with a mean variation of 11% ±0.6%. This agrees will with published data[21] on the Trixel Pixium 4600 detector (0.65 @ 4.1 μGy)

- Very high purity aluminium (99.9%) has been shown to cause an overestimation in the low frequency NPS. Standard quality aluminium (99.0%) of the type commonly found in medical physics departments gives comparable results and is therefore recommended.

- There is no significant difference between the MTF measured with the polished and unpolished tungsten edges. An unsmoothed precision cut 90º edge is sufficient.

- There was also no significant difference between the MTF and NPS measurements made on the outer cover and directly on the detector face. This is an important point which helps motivate the use of the IEC standard in the clinical X-ray room and promotes comparison with published results from manufacturers' 'laboratory' type tests. In fact the actual definition of a 'Digital X-ray imaging device' quoted from the IEC standard is *"device consisting of a digital X-ray detector <u>including the protective layers installed for use in practice</u>, the amplifying and digitizing electronics, and a computer providing the original data of the image"*. 'In practice' could reasonably be assumed to be in clinical practice thus including the outer cover. It seems sensible that manufacturers are asked to provide 'system' figures for the detector as installed clinically *i.e.* including covers, AECs etc.

- All data in this study were acquired using the internal collimators to limit the beam area. This does not strictly adhere to the IEC protocol where the use of two external beam limiting devices is stipulated. Use of the internal collimators instead of the IEC specified external collimators has been shown to yield better estimates of the MTF and DQE while diminishing the complexity of image acquisition[27].

- Quantitative image quality measurements are possible with pre-processed image data but will only remain valid in light of a priori knowledge of the magnitude and type of processing applied.

- The DQE dependence on spatial frequency was shown to vary with tube potential (*i.e.* beam energy). Frequency dependant DQE should in theory give a better estimate of the detector performance with tube potential than estimates from the quantum efficiency of CsI calculated solely on the basis of the energy absorbed from incident photon fluence. Tube potentials between 60 and 100kVp are optimum for the Pixium 4600.

- The ideal signal-to-noise at the input of the detector is different for analysis which assumes the detector is an energy integrating detector, than that assuming it is a photon counting detector. Care is required when calculating SNR_{in}^2 for different beam qualities. As the indirect digital X-ray systems used in this study are energy integrating detectors, SNR_{in}^2 (energy integrating) values were used to assess beam quality dependence of DQE. (Note: The values of SNR_{in}^2 in the IEC protocol are photon counting values.)

- DQE results show significant changes with exposure due to the influence of structure noise but also the applied pre-processing filters. In general the relative noise increased with exposure leading to a reduction in DQE. However, as long as

the noise equivalent quanta is high enough for clinical diagnosis additional noise (at relatively higher exposures) may be inconsequential.

This study has shown that practically it is possible to include objective image quality parameters in an X-ray equipment quality assurance program, using IEC 62220-1[11] as a guide. However the determination of DQE and its constituent parameters is currently restricted to 'acceptance' tests to verify digital detectors are functioning as stated in the manufacturers' specification. Data will need to be collected over a period of time and lessons learned on how common detector faults manifest as changes in MTF or NPS. It is only then we can consider setting tolerances for the remedy or suspension of digital detectors from clinical service based on these parameters. A first step along this road is an appreciation of the measurement uncertainties involved and the variation of MTF and NPS values for multiple systems operating clinically and known to be in good adjustment, data which this study has provided.

3.6 References

[1] Rose A. The sensitivity performance of the human eye on an absolute scale. J Opt Soc Am 1948;38:196-208.

[2] Burgess AE. The Rose model, revisited. J Opt Soc Am A Opt Image Sci Vis 1999 Mar;16(3):633-46.

[3] Cunningham IA. Applied Linear Systems Theory. In: Beutel J., Kundel H.L., Van Metter R.L., editors. Handbook of Medical Imaging: Volume 1. Physics and Psychophysics.Bellingham, USA: SPIE; 2000. p. 79-159.

[4] Cunningham IA, Shaw R. Signal-to-noise optimization of medical imaging systems. J Opt Soc Am A 1999;(16):621-32.

[5] Mackenzie A, Honey ID. Characterization of noise sources for two generations of computed radiography systems using powder and crystalline photostimulable phosphors. Med Phys 2007 Aug;34(8):3345-57.

[6] Metz CE, Wagner RF, Doi K, Brown DG, Nishikawa RM, Myers KJ. Toward consensus on quantitative assessment of medical imaging systems. Med Phys 1995 Jul;22(7):1057-61.

[7] Samei E, Flynn MJ. An experimental comparison of detector performance for direct and indirect digital radiography systems. Med Phys 2003 Apr;30(4):608-22.

[8] Samei E, Flynn MJ. An experimental comparison of detector performance for computed radiography systems. Med Phys 2002 Apr;29(4):447-59.

[9] Workman A, Cowen AR. Signal, noise and SNR transfer properties of computed radiography. Phys Med Biol 1993;38:1789-808.

[10] Evans DS, Workman A, Payne M. A comparison of the imaging properties of CCD-based devices used for small field digital mammography. Phys Med Biol 2002 Jan 7;47(1):117-35.

[11] International Electrotechnical Commission. Medical electrical equipment: characteristics of digital X-ray imaging devices - part 1: determination of the detective quantum efficiency. Geneva, Switzerland: IEC; 2003. Report No.: 62220-1.

[12] Marshall NW. Retrospective analysis of a detector fault for a full field digital mammography system. Phys Med Biol 2006 Nov 7;51(21):5655-73.

[13] Samei E, Buhr E, Granfors P, Vandenbroucke D, Wang X. Comparison of edge analysis techniques for the determination of the MTF of digital radiographic systems. Phys Med Biol 2005 Aug 7;50(15):3613-25.

[14] Carton AK, Vandenbroucke D, Struye L, Maidment AD, Kao YH, Albert M, et al. Validation of MTF measurement for digital mammography quality control. Med Phys 2005 Jun;32(6):1684-95.

[15] Samei E, Flynn MJ, Reimann DA. A method for measuring the presampled MTF of digital radiographic systems using an edge test device. Med Phys 1998 Jan;25(1):102-13.

[16] Cunningham IA, Reid BK. Signal and noise in modulation transfer function determinations using the slit, wire, and edge techniques. Med Phys 1992 Jul;19(4):1037-44.

[17] Dobbins JT, III. Image Quality Metrics for Digital Systems. In: Beutel J., Kundel H.L., Van Metter R.L., editors. Handbook of Medical Imaging: Volume 1. Physics and Psychophysics.Bellingham, USA: SPIE; 2000. p. 161-219.

[18] Buhr E, Gunther-Kohfahl S, Neitzel U. Accuracy of a simple method for deriving the presampled modulation transfer function of a digital radiographic system from an edge image. Med Phys 2003 Sep;30(9):2323-31.

[19] Fetterly KA, Hangiandreou NJ. Effects of x-ray spectra on the DQE of a computed radiography system. Med Phys 2001 Feb;28(2):241-9.

[20] Aitchinger H, Dierker J, Joite-Barfus S, Sable M. Radiation Exposure and Image Quality in X-ray Diagnostic Radiology. Berlin: Springer; 2004.

[21] Centre for Evidence Based Purchasing. Digital Imaging Systems for General Radiography. A comparative technical report. London, UK: CEP; 2005. Report No.: 05078.

[22] Boone JM, Seibert JA, Sabol JM, Tecotzky M. A Monte Carlo study of x-ray fluorescence in x-ray detectors. Med Phys 1999 Jun;26(6):905-16.

[23] Zhao W, Ji WG, Debrie A, Rowlands JA. Imaging performance of amorphous selenium based flat-panel detectors for digital mammography: characterization of a small area prototype detector. Med Phys 2003 Feb;30(2):254-63.

[24] Siewerdsen JH, Antonuk LE, El-Mohri Y, Yorkston J, Huang W, Boudry JM, et al. Empirical and theoretical investigation of the noise performance of indirect detection, active matrix flat-panel imagers (AMFPIs) for diagnostic radiology. Med Phys 1997 Jan;24(1):71-89.

[25] Marshall NW. Early experience in the use of quantitative image quality measurements for the quality assurance of full field digital mammography x-ray systems. Phys Med Biol 2007 Sep 21;52(18):5545-68.

[26] Launders JH, Kengyelics SM, Cowen AR. A comprehensive physical image quality evaluation of a selenium based digital x-ray imaging system for thorax radiography. Med Phys 1998 Jun;25(6):986-97.

[27] Ranger NT, Samei E, Dobbins JT, III, Ravin CE. Measurement of the detective quantum efficiency in digital detectors consistent with the IEC 62220-1 standard: practical considerations regarding the choice of filter material. Med Phys 2005 Jul;32(7):2305-11.

[28] Illers H, Buhr E, Hoeschen C. Measurement of the detective quantum efficiency (DQE) of digital X-ray detectors according to the novel standard IEC 62220-1. Radiat Prot Dosimetry 2005;114(1-3):39-44.

4 Automatic Exposure Control Devices

4.1 Introduction

Automatic exposure control (AEC) devices are designed to improve the consistency of image acquisition in radiography. Such devices enable images to be recorded for patients of varying thickness, for different regions of the body, and with different tube potentials using exposures close to the optimum. This is achieved through automatic termination of exposures at preset air kerma levels at the image receptor. Conventional X-ray systems using film radiography are set to give similar optical densities, but the variation in sensitivity of digital detectors with photon energy is significantly different from that of screen-film phosphors. Calibrating AECs for the kV dependence of digital systems therefore requires the use of alternative parameters, ideally linked to the quality of the image. Digital radiography systems have broader dynamic ranges than film and since the grey levels in the displayed image can be adjusted, the image quality is not contrast limited. As a result, it is the amount of noise in the image which limits the perception of detail and so the image quality, for most digital radiography systems. Thus the signal-to-noise ratio (SNR) provides a useful quantity for judging image acceptability and so evaluating image quality. The level of SNR will be determined by the image receptor sensitivity and the exposure level.

Exposure tables are no longer needed to set radiographic parameters as the AEC systems of modern X-ray generators have the capability to take the energy response of image receptors into account. These systems typically have several calibration curves

stored in memory. Depending on the X-ray tube voltage selected, the cut-off dose of the AEC is changed according to these curves.

At installation, when the X-ray system is accepted into clinical use, the appropriate kV compensation curve is selected and adjusted if required. The chosen correction curve will need to simultaneously take into account the energy response of the image receptor and the energy response of the dosimeter forming part of the AEC device, usually an ionisation chamber. The curve may also be influenced by 'local' factors such as inherent beam filtration, choice of attenuating phantom used for testing, table top attenuation and Bucky design.

AEC calibration curves stored in the memory of X-ray generators are typically produced to suit the energy dependence of screen-film phosphors. These curves may not be optimised for DR systems and may need to be adjusted for use with a particular digital image receptor at installation. The ability to adjust the shape and position of the curve varies with X-ray generator manufacturer and model.

Some generators operate using an exposure point (EP) scale which logarithmically grades tube potential and tube current time products, producing exposure increments of $10^{[0.1]}$. Therefore, a change in exposure of 3 EPs for example, results in a doubling of the DAK $(10^{[0.1]})^3$. The ability of AEC systems based on the EP scale to achieve a specified target DAK at a reference kV (usually ~ 80 kV) can be achieved within a tolerance of ± 1/2 EP or a change of ± 12% in DAK. Once the target DAK of the curve is established at the kV reference point, the shape of the curve at other tube potentials (usually 60 and 125kV) may be manipulated within a tolerance of ± 1/8 EP or 3% in DAK.

There are many models of X-ray generator available in the UK and some are particularly suited for AEC calibration with DR systems. These systems enable the

reference voltage values which determine the AEC cut-off point to be entered into the system directly at each kV decade. Thus, allowing fully configurable and relatively precise AEC calibration curves to be established. Older X-ray generators which use analogue circuitry to adjust AEC sensitivity are often as configurable as modern software driven microprocessor generators which may only offer a selection of predefined curves.

Tests to evaluate the performance of AEC devices may be categorised into those necessary to commission DR equipment and those required to test AEC function routinely. Commissioning tests are more comprehensive and require the establishment of a kV compensation curve trend and the absolute detector air kerma level.

In this chapter, the variation in photon energy absorbed in the detector, which is a measure of the sensitivity of the image receptor, has been calculated for different X-ray beam qualities. This has been compared with responses of digital radiography detectors, assessed in terms of the detector dose indicator (DDI) registered by the different systems and the image SNR, for application in calibrating AECs for digital radiography. X-ray company engineers often use phantoms of aluminium or copper instead of more tissue equivalent materials, such as water or PMMA, when setting up AECs, because these are more convenient to handle. The use of phantoms made from different materials has been investigated and the influence of scatter on measurements made under a variety of conditions has been studied. The range of AEC calibration options available has been reviewed and the more practical methods are recommended for routine use.

4.2 Theory

The response of a phosphor when exposed to mono-energetic photons of energy *E* can be evaluated in terms of the absorbed energy *A (E)*.

$$A(E) = E\{1 - \exp[(-\mu_{en}(E)/\rho).\rho.t]\} \qquad \textbf{Equation 4:1}$$

where μ_{en} *(E)* is energy absorption co-efficient, ρ density and *t* the thickness of the phosphor layer. The energy absorbed in the phosphor for different detectors is a measure of the receptor sensitivity and is directly linked to the pixel value in the resulting image [1]. In order to assess the response of a phosphor or its sensitivity to X-ray beams, which have photons with a range of energies, the absorption must be averaged over all the photons impinging on the image receptor.

$$A(kV, filt) = \frac{\int_0^{E_{kV}} \psi_E.E\{1 - \exp[(-\mu_{en}(E)/\rho).\rho.t]\}.dE}{\int_0^{E_{kV}} \psi_E.dE} \qquad \textbf{Equation 4:2}$$

where *A (kV, filt)* is the absorbed energy for an X-ray beam of given tube potential (kV) and filtration, E_{kV} is the maximum photon energy in the spectrum and ψ_E is the photon fluence in energy interval E to E+dE [2]. The sensitivity has been calculated using equation (2) for X-ray beams with different radiation qualities in order to establish the expected variations with tube potential for several types of image receptor. The X-ray beam used in the calculations was for a 16^o target angle, filtered by 2.5 mm of aluminium, with a 0.2 mm copper filter added for some calculations [2]. The X-ray beams were corrected for transmission through a 200 mm thick water phantom to simulate the attenuation properties of a patient. No correction was made for scatter, but the differences between the spectra of the primary X-ray beam and scattered radiation transmitted in the forward direction are small [3]. These results have then been used to predict relative values for determining the AEC cut-off dose at different tube potentials for each type of image receptor.

4.3 Method

The manufacturers of digital imaging systems use a variety of detector dose indices (DDIs) related to the amount of light generated from the phosphor, either by photo-stimulable luminescence in the case of computed radiography (CR) or X-ray stimulated fluorescence for caesium iodide indirect digital radiography (IDR). The DDI values are calculated from analysis of the histogram of image pixel values over an appropriate region of interest and provide a quantity that is related to the detector sensitivity. Images with a similar value for the DDI should reflect a consistent level of absorbed dose to the detector at different tube potentials. Studies have been carried out using CR systems manufactured by Kodak, Fuji and Agfa, and Siemens IDR equipment. Exposures relating to the use of different parameters for setting up AECs were made using a 200 mm thick water phantom, comprising pairs of tanks with outer dimensions 300 mm x 300 mm x 100 mm with 5 mm thick Perspex walls. Air kerma was measured with an Unfors Xi solid state dosimeter (Unfors Instruments AB, Billdal, Sweden) for exposures with a range of mAs settings for each kV value. For CR the solid state dosimeter was set into a modified cassette to measure detector air kerma (DAK). Similar exposures were then repeated with a CR image plate and the DDI recorded. The same CR cassette, field size and region of interest at the centre of the image plate were used for each exposure and the time between exposures and readout kept at 120 s ± 20 s in order to minimise variations. The cassettes were readout using the processing options specified by the manufacturers to give a fixed dynamic range and linear greyscale. For the IDR system, the DAK was recorded by placing the solid state dosimeter on the surface of the detector array cover, behind the grid, in the centre of the X-ray field and similar exposures repeated with the dosimeter removed to determine the DDI values. The SNR was defined as the mean pixel value divided by the standard deviation and taken from regions of interest of approximately 10 cm^2 drawn at the centre of each image.

For some indirect digital radiography systems it is not possible to position a dosimeter behind the grid immediately in front of the image receptor. In such cases the DAK must be derived from a measurement of the incident air kerma at the surface of the image detector housing, which will include scattered radiation that will be removed by the grid. This must be taken into account in calibration of the AEC.

Practical measurements to assess the influence of the type of phantom and its position were made on a CR system, for which the AEC had previously been set up to terminate exposures at a similar air kerma level across the whole range of tube potentials. The 200 mm thick water phantom was first positioned at the tube adjacent to the light beam diaphragm and the measurements repeated with the phantom placed in front of the detector housing. Similar measurements were made with a 20 mm thick aluminium attenuator at the X-ray tube. The DAK was measured with the Unfors Xi dosimeter placed in the Bucky tray as already described, but measurements were also made of the air kerma at the detector housing in front of the grid with the dosimeter positioned in the centre of the beam, taking care to avoid overlap with the central AEC chamber. In all cases sets of measurements were made both with and without the grid in position. Some measurements were also made with a Keithley triad dosimeter with a 15 cm^3 ionisation chamber (Keithley Instruments Inc., USA), in order to assess the contribution made by backscatter to the value recorded.

4.4 Results

4.4.1 Theoretical Assessment

The relative responses of a gadolinium oxysulphide screen system (phosphor thickness 0.20 mm): a CR imaging plate made from $BaFBr_{85\%},I_{15\%}$ (phosphor thickness 0.22 mm); and a caesium iodide IDR image receptor (phosphor thickness 0.5 mm) were calculated

using equation 2 and are compared in Figure 4:1. Results for X-ray beams with an additional 0.2 mm of copper are compared with other data. Whereas the sensitivity of rare-earth screen-film systems increases between 60 kV and 100 kV, that for the CR system declines continuously with tube potential from 50 kV upwards, and that for the caesium iodide IDR system declines above 80 kV.

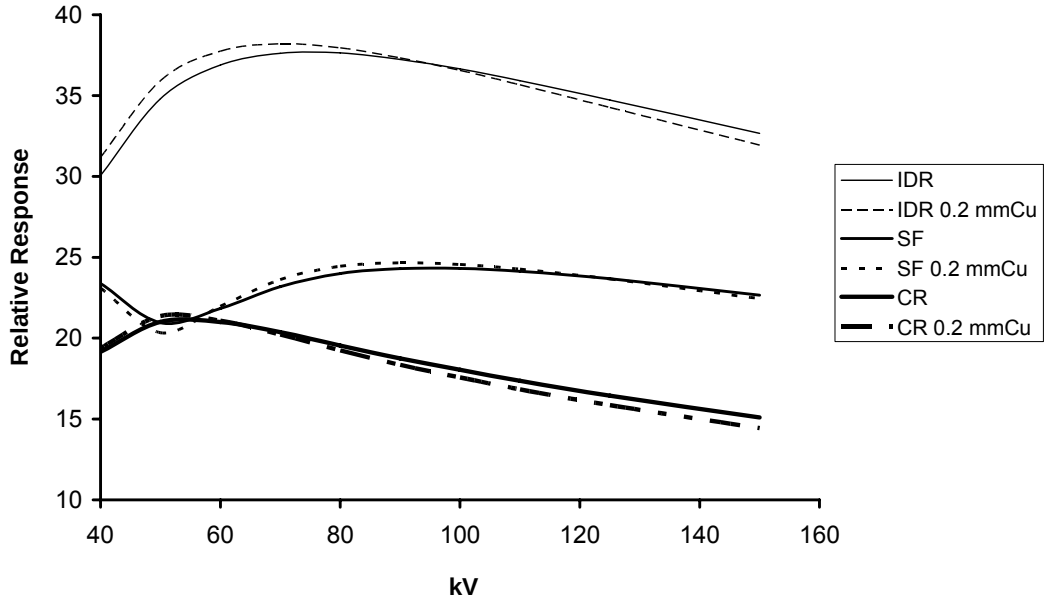

Figure 4:1 Variation of phosphor sensitivity with tube potential for a gadolinium oxysulphide (Gd_2O_2S) film-screen phosphor (0.20 mm thick), BaF(Br85%, I15%) CR phosphor (0.22 mm), and a CsI IDR phosphor (0.50 mm). Data is shown for X-ray beams filtered by 2.5 mm of aluminium, and by 2.5 mm of aluminium plus 0.2 mm of copper.

The expected relative AEC setting required to compensate for the differences in phosphor sensitivity in the diagnostic X-ray range have been computed for the three types of image receptor and are shown in Figure 4:2. The DAK should be increased by 8-10% between 80 kV and 100 kV for CR, and by 3-4% for IDR, whereas no change is required in screen-film air kerma. The DAK required by CR is 7-9% lower at 60 kV than 80 kV, whereas there is little change in the requirement for IDR and the dose required for the rare-earth screen-film system is 10-12% higher. If the X-ray beam is filtered by an additional

0.2 mm of copper, the ideal AEC setting at 100 kV relative to that at 80 kV is only changed by 1%, which is negligible compared with the accuracy with which most AECs can be adjusted.

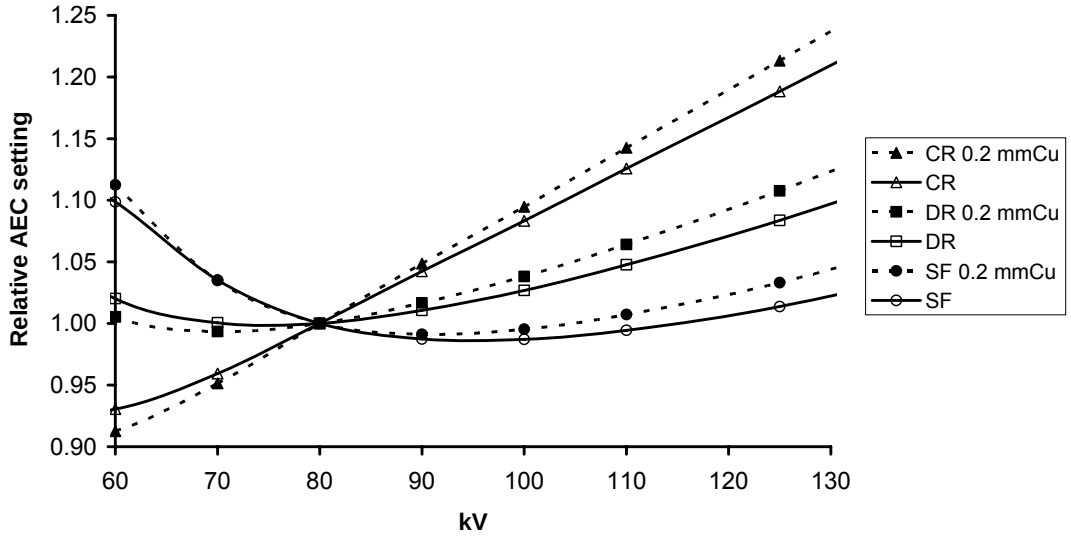

Figure 4:2 Theoretical evaluation of the variations in AEC setting for image receptor doses with a film-screen system, a CR system and an IDR system for X-ray beams with and without an additional 0.2 mm copper, normalised to the response at 80 kV.

4.4.2 Empirical Assessment

The relative sensitivity of an Agfa CR system at different tube potentials was evaluated empirically from measurements using different image performance indicators: pixel value, DDI, and SNR (Figure 4:3). It was possible to adjust the AEC cut-off values within a tolerance of 3%. All indicators show a similar trend within ±2% and should therefore have equal validity in determining the correct kV compensation curve required to calibrate the AECs for the loss in detector sensitivity with tube potential.

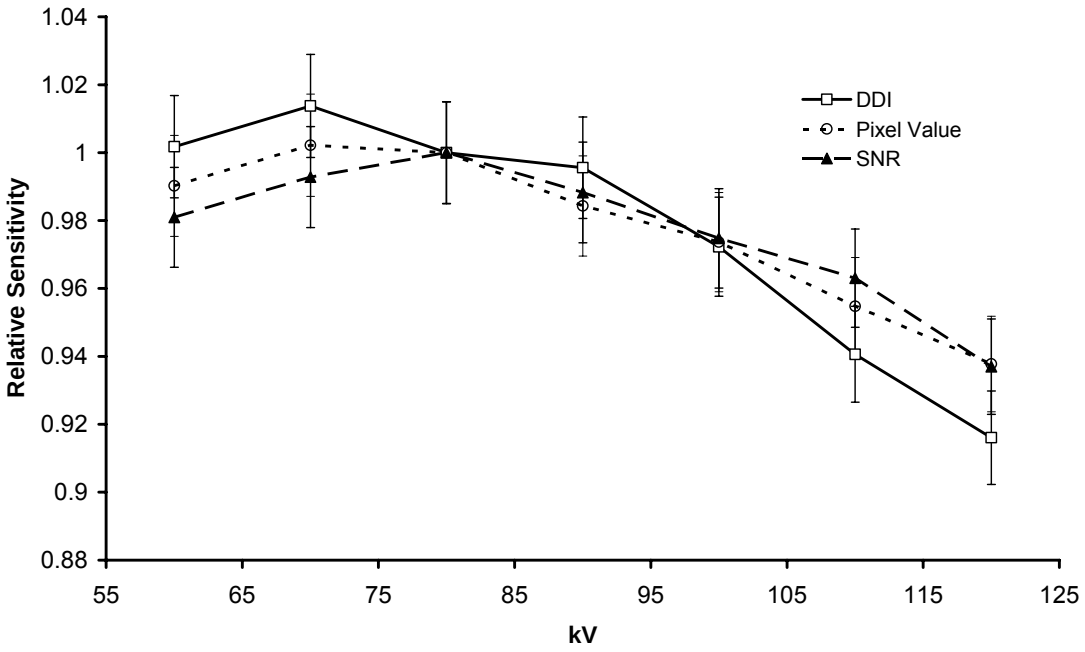

Figure 4:3 Comparison of the relative sensitivities of indicators that relate to image plate response for an Agfa CR system, normalised to the response at 80 kV. Error bars indicate an achievable tolerance of 3% in adjusting the AEC.

The DDI was chosen for the purpose of this study. Relative detector dose settings to give similar DDI values for various digital radiography systems and for maintaining a constant film density for a screen-film system are shown in Figure 4:4. Kodak and Fuji CR systems both use the phosphor $BaFBr_{85\%}I_{15\%}$:Eu employed in the calculation and trends are within a few percent of those predicted (Figure 4:2). The change with kV is less for the Agfa CR system where strontium is also incorporated in the phosphor [4]. The required image receptor doses to give a constant DDI rise more steeply below 80 kV than predicted by the calculations. This may result from additional attenuating material in the X-ray table-top, grid and cassette cover. Above 80kV the image receptor doses to give a constant DDI rise marginally less steeply than those predicted, but the practical measurements also include the energy response of the ionisation chamber in the AEC device.

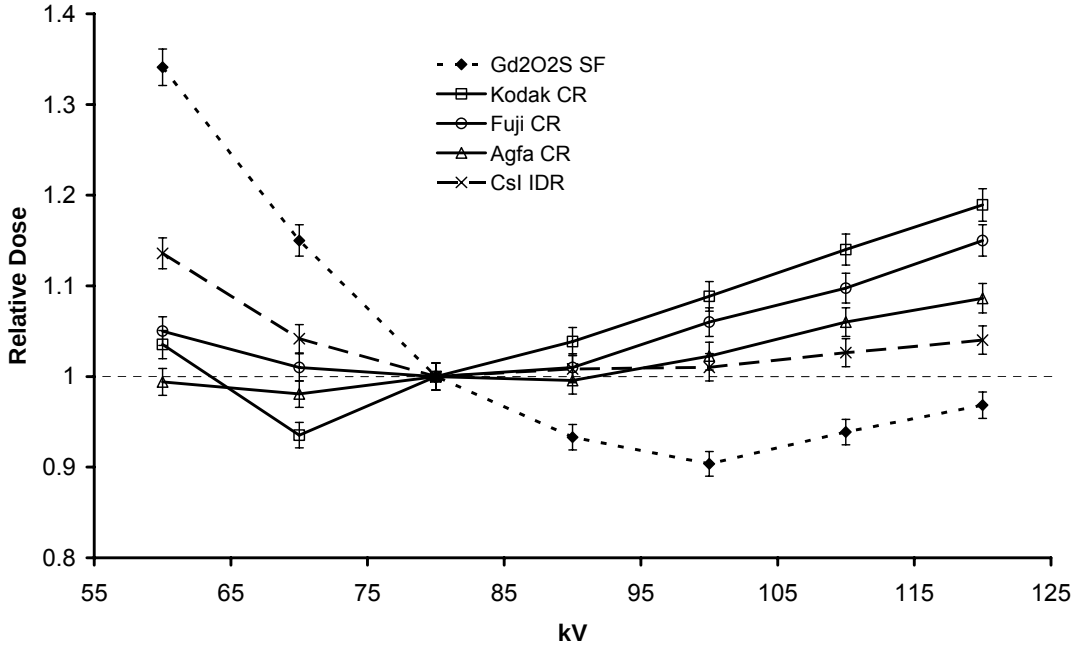

Figure 4:4 AEC settings for a rare-earth film-screen system, an IDR (CsI) system and three computed radiography systems derived from practical measurements to give a similar DDI value relative to the response at 80 kV. Error bars indicate an achievable tolerance of 3% in adjusting the AEC.

4.4.3 Absolute Dose level

The starting position chosen for setting up the DDI dose level for CR systems was that the image receptor dose should correspond to a 400 speed screen-film system at 80 kV. This is defined by ISO 92361 as $S = 10^{-3}$ Gy / k_s Gy, where k_s is the air kerma at a fixed distance behind the specified phantom to produce a net film optical density of 1.0 [5]. The standard measurement conditions specify four techniques at 50, 70, 90 and 120 kV using different amounts of aluminium or PMMA attenuating material. Measurements at ten hospitals using five different 400 speed index screen-film combinations gave image receptor doses between 2.3 μGy and 3.4 μGy with a mean of 2.8 μGy. A DAK of 2.7 μGy was chosen as a starting point (DAK_{ref}) for setting up CR systems in the West of Scotland.

4.4.4 Attenuating Phantom Material

Transmitted X-ray spectra similar to those for 200 mm water can be obtained using thin metal phantoms, and these are often used for tests by medical physicists and equipment engineers. Since the quality of the transmitted X-ray beam will affect the response of the CR and IDR image plates, calculations were performed to predict responses for several different attenuating phantoms. Relative AEC dose settings for CR and IDR systems that would be determined for a selection of phantoms are shown in Figure 4:5.

Phantoms made from water (200 mm), PMMA (200 mm), and aluminium (20 mm) all gave relative responses within ±0.5% between 80 kV and 125 kV, but when 2 mm of copper was used to attenuate the beam, the dose levels required to give the same image response at 100 kV and 125 kV were 4.5% and 9.5% higher respectively than at 80 kV. Spectra similar to those transmitted through 200 mm of water may be obtained by reducing the copper thickness to 0.5 mm, but use of this filter is impractical because of the high transmitted air kerma. Although the X-ray spectra transmitted through the different phantoms are similar, the air kerma levels are not. The mAs settings required to terminate the AEC with different thicknesses of phantom relative to those for 200 mm water are 1.4, 0.8, and 0.4 for 200 mm PMMA, 20 mm aluminium, and 2 mm copper respectively. The very high air kerma per mAs for a 0.5 mm thick copper phantom requires smaller exposure time durations that can be achieved in practice.

(a)

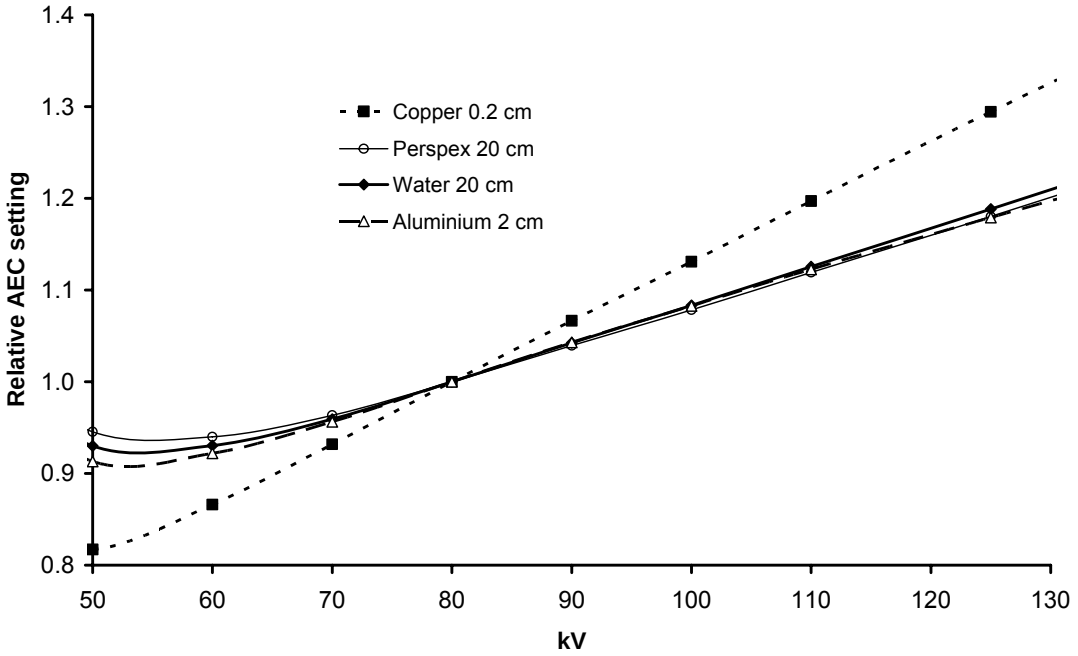

(b)

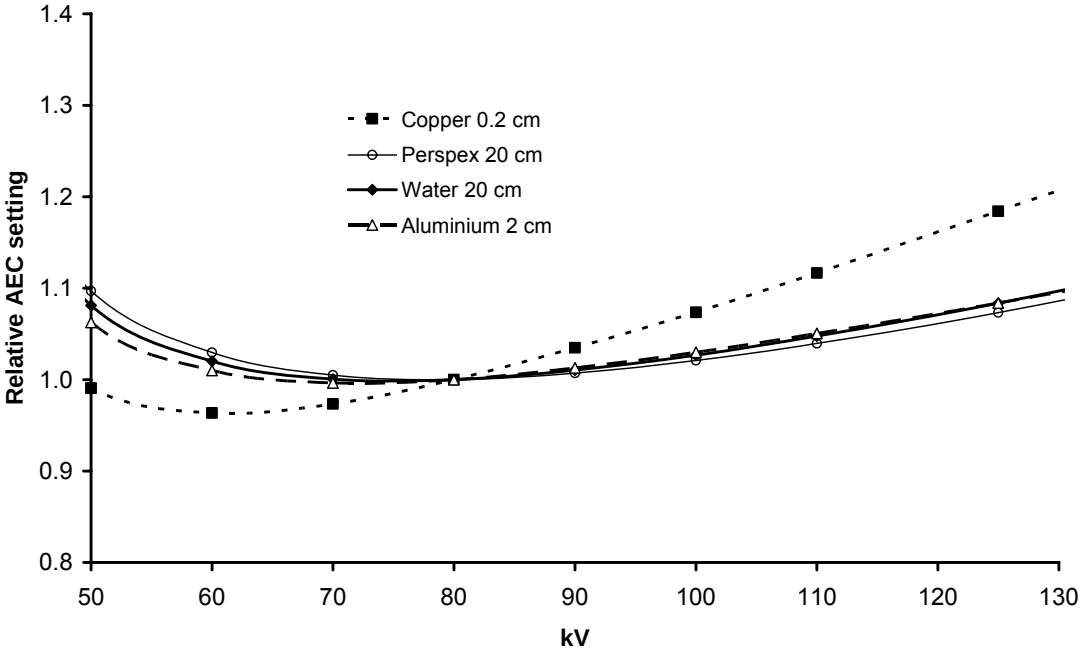

Figure 4:5 Calculated values for the relative AEC setting required for (a) a CR system and (b) an IDR system using four alternative phantom materials to simulate the X-ray beam transmitted through a patient.

4.4.5 Influence of Grid and Position of Attenuating Phantom

Measurements of the DAK corresponding to termination of the AEC on a CR system for a range of tube potentials with the water phantom at different positions and with and without a grid in place in front of the detector are shown in Figure 4:6. Experimental error in the measurement of DAK was largely due to variations in tube output (~3%) and AEC device reproducibility (~1.5%). Air kerma measurements with the water attenuator positioned at the tube and at the detector housing are similar to within experimental error, when the grid is in place. However, when the grid is removed the results are significantly different. With the water phantom placed at the tube the DAK is similar to that recorded with the grid in place up to 100 kV, but is about 10% lower at 120 kV. However when the water phantom is positioned near to the detector housing, the mean DAK recorded by the dosimeter drops to two thirds of its original value.

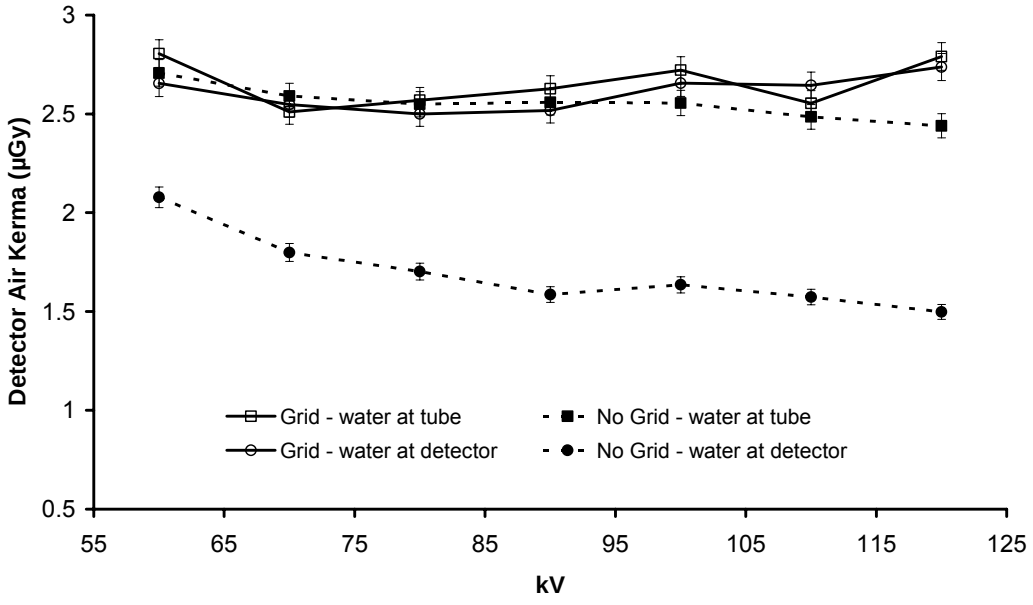

Figure 4:6 Plots of air kerma measured at the image detector for a CR system with the AEC set up to give a constant DAK across the range 60 – 120 kVp. Sets of results are shown for a 200 mm thick water phantom positioned at the image receptor and at the X-ray tube, with and without the grid in place in front of the dosimeter. Error bars indicate an experimental error of 3.3% in measuring DAK.

In Figure 4:7 the variation with tube potential of the incident air kerma measured at the detector housing for water and aluminium attenuators are compared for set ups with and without a grid. When the grid is in place, the incident air kerma values are higher by a factor of 1.56. There is no significant difference between results recorded using water or aluminium as an attenuator. The same X-ray equipment was used for the measurements in Figures 4;6 and 4:7 and the water at tube results differ only in position of the dosimeter in the Bucky tray and on the detector housing, behind and in front of the grid respectively.

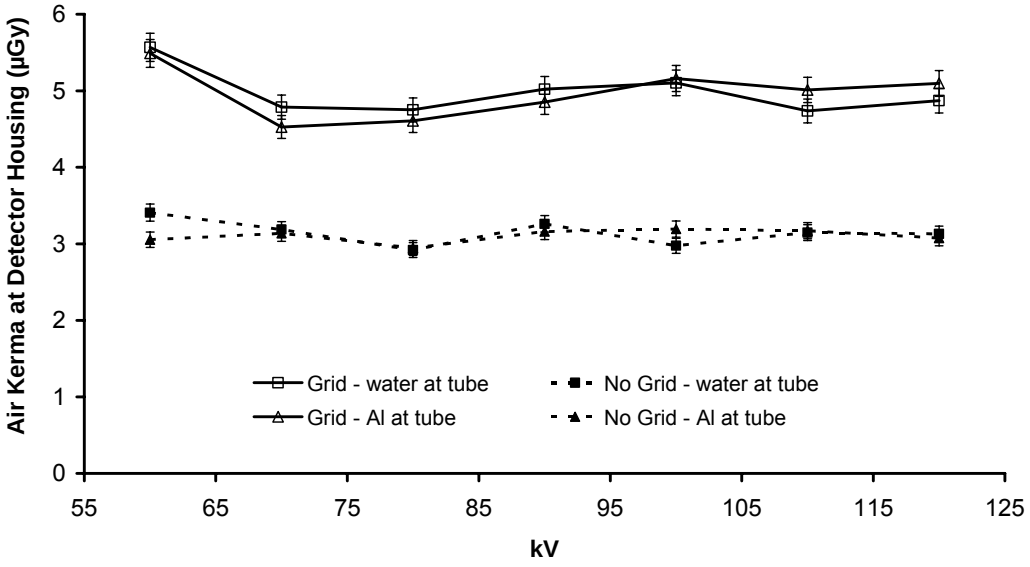

Figure 4:7 Plots of air kerma measured in front of the housing for the image detector and grid of a CR system with the AEC set up to give a constant DAK across the range 60 – 120 kVp. Sets of results are shown for a 200 mm thick water phantom and a 20 mm thick aluminium phantom, both positioned adjacent to the X-ray tube, with and without the grid in place. Error bars indicate an experimental error in of 3.3% in measuring DAK.

4.4.6 Dosimeter Type

Sets of measurement were repeated using an ionisation chamber. The disadvantage of the ionisation chamber is that it will also be sensitive to radiation scattered back from any

object on which it is placed. Results showed that the air kerma measurements for a CR system could be increased by 30% with a grid in place and 50% when no grid was used.

4.5 Discussion

4.5.1 Digital radiography requirements

Results from this study have demonstrated that the image receptor dose levels required for digital radiography systems need to increase with tube potential in order to give a similar detector response. The relative response of the DDI at different tube potentials follows a similar pattern to the SNR and relates to the level of image quality.

Maintaining a constant DDI is recommended as the method of choice for setting up AECs for digital radiography. Evaluation of the image receptor response prior to setting up a new imaging system using a simple spreadsheet calculation can provide valuable guidance on performance. Typical AEC calibration curves are stored in the memories of X-ray generators to suit the energy dependence of screen-film systems, but may not be available for digital radiography systems. Therefore it is important to adjust the response for use with CR or IDR systems at installation. The facility to adjust the shape (kV dependence) and position (AEC sensitivity) of the curve varies with X-ray generator manufacturer and/or model but can usually be configured within a tolerance of ±12% for the sensitivity and ±3% for the kV dependence.

A target reference DAK value (DAK_{ref}) should be chosen for setting up a digital radiography system that is suitable for the X-ray equipment being used and the image quality required for the range of examinations being performed. This will be influenced by local factors such as imaging requirements, beam filtration, table-top and grid attenuation.

The final decision on acceptability of noise at the dose level chosen should be made by the radiologists / radiographers in the department based on clinical requirements. In the West of Scotland the DAK_{ref} values employed are 2.7 ±0.2 μGy at 80 kV for CR imaging plates and 2 ±0.15 μGy for IDR systems. These DAK_{ref} levels relate to measurements made behind the grid. If the dosimeter can only be placed in front of the grid, a correction will need to be applied for grid attenuation (typically giving a 30% - 40% reduction). Additional copper filter options are available on many DR systems and the use of a 0.2 mm filter in an optimisation strategy would only give a difference of 1% in relative response at different kVs and so would not require AEC recalibration.

4.5.2 Measurement of image receptor dose

In order to set up an AEC system at different tube potentials, X-ray beams filtered to generate spectra similar to those transmitted through the body should be used (e.g. 200 mm water, 200 mm PMMA, 20 mm aluminium), Figure 4:5. X-ray spectra transmitted by 2 mm copper are sufficiently different to give a measurable discrepancy in AEC response and so use of a copper phantom is not advised. Output reproducibility problems were avoided when using the aluminium phantom by ensuring that the exposure time setting remained above 10 ms either by selection of a small mA and/or by selecting a small focal spot size.

The best type of radiation instrument to use for carrying out the measurements is a solid state dosimeter, as these are mounted on a lead backing plate and are less sensitive to differences in backscattered radiation. If an ionisation chamber is used, then a correction will need to be applied to account for the additional backscatter recorded, which may increase the measured dose by 30% with a grid or 50% without a grid.

The best arrangement for measurement of image receptor dose is to place the dosimeter on the receptor behind the grid. If this is not possible, then other alternatives can be used, but none is ideal. In all other cases the phantom must be positioned at the X-ray tube to reduce contributions from scatter. A 20 mm thick aluminium sheet will provide a more practical and safer phantom for use in this arrangement. The second option is to place the dosimeter on the cover in front of the grid and make a correction for grid attenuation. The disadvantage of this is that an accurate value for the attenuation of the grid may not be available. The other alternatives involve removal of the grid. If the dosimeter is placed on the image receptor, the measurement at 80 kVp is similar to that with the dosimeter behind the grid, but the cut-off air kerma falls with kV (figure 4:6), because of contributions from scatter to the AEC chamber air kerma. However, this provides a reasonable method of establishing DAK_{ref} and the DDI can then be used to set up the AEC at other tube potentials. When the dosimeter is placed on the outer cover of the detector housing, this gives a DAK that is 10% - 20% higher (Figure4:7) than that at the image receptor (Figure 4:6), because of attenuation by the cover and the difference in FDD, although a correction could be applied to allow for these.

Contributions from scattered radiation and different responses of radiation dosimeters can be the cause of confusion. Measurements where the dosimeter is placed behind the grid or where the phantom is positioned near to the X-ray tube, in order to minimise the amount of scatter detected, are consistent. However, when the water phantom is placed adjacent to the detector and the grid removed, the AEC cuts off the exposure at a lower detector air kerma level (Figure 4:6), because of the contribution from scattered radiation. The reason for this is the difference in angular response of the solid state dosimeter and the AEC ionisation chamber. The solid state device which incorporates filters in front of a small dosimeter element is more directional, the response reduces by as much as 50% at angles approaching 30 degrees, whereas the AEC ionisation

chamber is sensitive to radiation from all directions. Thus in a scatter field where radiation impinges from different directions the ionisation chamber records all the incident radiation with a similar weighting, whereas the response of the solid state dosimeter is lower for the scattered radiation incident at a higher angle.

4.5.3 Procedure for calibration of AEC Device

The following steps are recommended in calibrating an AEC device for digital radiography:

- Check the DDI calibration of the X-ray system using the method recommended by the manufacturer.
- Global DDI values should not be used to determine the absolute dose level for setting up AEC systems because of differences in equipment and set-up between different centres. It is recommended that DDI values are calibrated against DAK for each system. A discussion of the factors affecting the accuracy and reproducibility of DDIs is given in the appendix to this chapter (section 4.7).
- Adjust the AEC calibration to obtain the required target DAK_{ref} at 80 kVp. The air kerma for CR can be measured using a cassette with a cut out to take a solid state dosimeter.
- Measure DDI at 80 kV using this set up (DDI_{ref}).
- Measure DDI over the range of tube potentials to be used in clinical practice, 60-120 kV. For all measurements use the same field size, the same imaging plate and a similar time delay between exposure and readout for CR systems.
- Adjust the AEC calibration to achieve DDI values similar to DDI_{ref} at all tube potentials. Since the variation in response with kV is less for CsI IDR systems (Figures 4:2 and 4:4), adjustment of the AEC to give a constant air kerma level at all tube potentials may be considered acceptable.

The DAK required to achieve a constant DDI across the diagnostic kV range may be determined empirically through trial and error. When the relationship between DDI and exposure is known, the required air kerma may be calculated from the DDI observed (DDI_{kV}) and DAK recorded (DAK_{kV}) for each kV. Equations defining DDI for most CR systems may be rearranged to derive equations for the image receptor dose and these are given in Table 4:1.

Table 4:1 Calculation of DAK at particular kV from initial dose and DDI values recorded

Manufacturer	DDI definition	Required Image Receptor Dose
Agfa	$SAL / \sqrt{Dose} = constant$	$DAK_{kV} \times (SAL_{ref}^2 / SAL_{kV}^2)$
Fuji	$S \times Dose = constant$	$DAK_{kV} \times (S_{kV} / S_{ref})$
Kodak	$EI - 1000 \times \log_{10}(Dose) = constant$	$DAK_{kV} \times 10^{[(EI\ ref - EIkV)/1000]}$

NB: DAK_{kV} and DDI_{kV} are measured values at each kV before adjustment.

If the kV dependence of a digital detector is known, then direct measurements of DAK may be employed for AEC calibration, for example using multiplication factors derived from Figures 4:2 and 4:4 for tube potentials between 80 kV and 130 kV. This method is by far the quickest and simplest to use in the field.

Typical normalised target DAK values for selected CR systems are shown in Table 4:2. The values shown are a guide only and may vary with X-ray equipment, CR model and IP generation.

Table 4:2 Target DAK values for selected CR image plates normalised to 80kV.

kV	60	70	80	90	100	110	120
Agfa MD30	0.99	0.98	1.00	1.00	1.02	1.06	1.09
Fuji ST-VI	1.05	1.01	1.00	1.01	1.06	1.10	1.15
Kodak GP	1.04	0.94	1.00	1.04	1.09	1.14	1.19

The relatively smaller energy dependence of DR R image receptors compared to film-screen, coupled with modern X-ray generators producing more reproducible outputs,

should in theory allow a tighter tolerance in determining the correct AEC function with DR systems. The achievable tolerance in calibrating AECs using the DDI method was found to be approximately 14% and has three main components, the ability to configure the generator to deliver the target DAK (~13%), the measurement of DAK – exposure reproducibility (~1%), dosimeter calibration (~2%); and DDI accuracy and reproducibility (including readout delay and calibration tolerance etc. ~5%).

The acceptance limits for film optical density when evaluating AECs with conventional radiography have been set at ± 0.2 OD units. Wilkinson and Heggie demonstrated that a change of ± 0.2 OD on film corresponds to a change of ± 17 % in the air kerma to the film [6]. This correlates well with our estimated achievable tolerance in the DDI method. Based on the 17 % exposure variation the following values define equivalent limits of acceptability in terms of DDI for properly calibrated CR systems running at 400 speed equivalence: Fuji S ± 90; Kodak EI ± 70; and Agfa SAL ± 97. Similar values may be calculated for other digital X-ray systems.

4.6 Conclusions

The energy responses for digital radiography systems are different from those of screen-film combinations, and require the exposure to be increased at higher tube potentials. AEC systems may be set up using phantoms of water, PMMA or aluminium and the DDI or a measurement based on air kerma used to establish AEC cut-off levels. Use of a solid state dosimeter, which can be placed behind the anti-scatter grid and in front of the image receptor, is the preferred method. Particular care should be taken where the dosimeter cannot be placed behind the grid, as scatter contributions to the measurements can be

significant. In this case, the attenuating phantom must be placed at the X-ray tube in order to reduce scatter and the use of 20 mm of aluminium is recommended.

4.7 Appendix

4.7.1 Factors affecting the accuracy and reproducibility of DDIs

Manufacturers of digital X-ray systems promote DDIs as having a rather loose relation to DAK when used clinically. If factors such as the X-ray generator, inherent X-ray beam filtration, tube voltage, menu options, patient size, positioning set-up, collimation and elapsed time from exposure remain unchanged, the DDI is then a relative representation of DAK. These many variables all contribute to the wide range of DDIs for each examination type obtained clinically. As discussed in chapter 4, the calibration of DDI for each digital X-ray system are performed under specific, repeatable set-up conditions to minimise many of these variables. The relationship between DDI and DAK is thus more precise under controlled exposure conditions. The accuracy of the DDI value however, may also depend on the following factors:

4.7.2 Energy Dependence

The energy dependence of digital X-ray detectors understandably vary with detector technology but notably also varies for the same technology with manufacturer and generation of IP. CR exhibits a large energy dependence, relative to IDR or DDR but significantly less than traditional screen-film systems. The energy responses of selected DR systems are shown in Figure 4:4, as the relative reciprocal sensitivities. The response of a typical 400 speed index screen-film system is also included for comparison. Data were collected with a 20 cm water phantom placed on the table top, a focus to detector

distance of 115cm and with the IP or screen-film cassette placed in the Bucky tray, similar to a clinical situation. Experimental error was minimised by using the same model GE Proteus X-ray system for film and CR measurements. The difference in energy dependence between the three CR manufacturers may be attributed to subtle differences in composition and manufacturing of the IPs. Kodak and Fuji CR systems use phosphors composed of $BaF(Br_{85\%}I_{15\%}):Eu$ whereas Agfa use a phosphor material which includes Sr [4]. The thickness and density of the phosphor layer and its concentration of dopants differ between manufacturers. The energy responses shown in Figure 4:4 are dependent on local variables for example, inherent X-ray tube filtration and voltage response of the radiation detector forming part of the AEC device (usually an ionisation chamber). Other generations of IP from the same CR manufacturer may also exhibit an energy response different than those illustrated.

4.7.3 Calibration of DDI

Manufacturers each recommend specific beam quality and exposure conditions to calibrate their digital X-ray systems to produce the expected DDI value for a given incident exposure. In the past, measurements to check the calibration made using different dosimeter designs (ionisation chambers or lead backed solid state detectors etc.) with or without lead aprons to reduce backscatter, and with various field sizes, have resulted in some confusion. It is important that the DDI calibration of the digital system is checked using the method recommended by the manufacturer before any attempt at determining AEC function using the DDI is made.

4.7.4 Beam Quality Variations

Experimental work performed by Tucker and Rezentes demonstrate the dependence of pixel values (and hence DDI) on the amount of energy deposited on an IP[1]. At a given exposure, it is the spectral content that determines the amount of energy absorbed by the phosphor. The equations relating DDI with the exposure incident on the image receptor in table 4.1 are valid in only a general form as they are difficult to reproduce in field measurements. The constants defining these relationships are seen to vary from one installation to another as the ability to reproduce exact beam quality and exposure conditions vary [6,7]. This is a particular problem with Fuji CR systems as the procedure for calibration recommends an unfiltered 80 kVp beam. Under these circumstances the range of half value layers (HVLs) encountered in clinical practice is typically 2.5-4.0 mm Al and pixel values are most sensitive to variations in beam quality in this range of HVLs [1].

The exposure conditions suitable for testing AEC function should include attenuating material which mimics the attenuation and scatter properties of a real patient. Phantoms containing tap water, slabs of PMMA or blocks of solid water are commonly used. The constants in the equations relating DDI to exposure will need to be redefined depending on the type of attenuating material chosen [6,7]. This fact coupled with a DDI dependence on the inherent X-ray beam quality warrants caution if attempting to define target DDI values for AEC calibration across multiple X-ray installations.

4.7.5 IP DDI and readout time variations

DDI values are affected by the length of the time delay between exposure and readout. The slope of this decay is temperature dependent but also varies with IP generation and manufacturer. A consistent delay time should be used to increase the precision of DDI values. A variation of 2% in DDI values from IPs of the same type having received a

similar exposure may be expected. This error may be halved if using the same IP for DDI measurements.

4.7.6 Method of DDI calculation and field size dependence

As mentioned previously, DDI values are calculated from analysis of the image histograms taken over a specific region of interest and each manufacturer defines their DDI relating to the mean or median exposure determined from these histograms. The appropriate region of interest is calculated using sophisticated algorithms that help define the clinically relevant data. These algorithms discard unexposed regions outside the area of collimation and also areas which are directly exposed to the primary beam, outside the patient anatomy. The irradiated field size and relative fraction of the total image area which these 'discarded' regions make up affect the algorithm identifying the clinically relevant data and thus have a direct effect on the calculated DDI value.

Increasing field size also has the effect of increasing scatter towards the centre of the image causing it to be non-uniform. This non-uniformity is accentuated using increasing attenuation and higher tube potentials as used in testing AEC function, creating large differences between the mean and central exposures. When testing AEC systems with film, the optical density is usually sampled only at a reference point in the centre of the exposed area. Thus DDIs computed using the mean or median exposure to the image receptor introduce an additional energy dependence when compared to screen-film systems. For this reason a DDI based on exposure within a predefined area may be more indicative of AEC performance [8].

Kodak recommends selecting a region of interest over the central AEC chamber, whereby the window and level settings are adjusted to obtain target 'code values', as a

method to test AEC function with their CR systems [9]. AEC tests using Fuji CR systems may be performed on 'semi-automatic' mode. In this mode the S number is determined by analyzing the image histogram for a predetermined rectangular shaped subregion located at the centre of the IP. Similarly, AEC testing with Agfa CR may be calculated from a region of interest drawn in the centre of the image to produce a scan average level (SAL) value, from which the lgM may then be calculated.

4.8 References

[1] Tucker DM, Rezentes PS. The relationship between pixel value and beam quality in photostimulable phosphor imaging. Med Phys 1997 Jun;24(6):887-93.

[2] Aitchinger H, Dierker J, Joite-Barfus S, Sable M. Radiation Exposure and Image Quality in X-ray Diagnostic Radiology. Berlin: Springer; 2004.

[3] Martin CJ, Sutton DG. Practical Radiation Proitection in Healthcare. Oxford: Oxford University Press; 2002.

[4] Samei E, Seibert JA, Willis CE, Flynn MJ, Mah E, Junck KL. Performance evaluation of computed radiography systems. Med Phys 2001 Mar;28(3):361-71.

[5] International Organization for Standardization (ISO). Photography - Sensitometry of screen-film systems for medical radiography. Part 1: Determination of sensitometric curve shape, speed and average gradient. Geneva: ISO; 2004. Report No.: 9236-1.

[6] Wilkinson LE, Heggie JC. Determination of correct AEC function with computed radiography cassettes. Australas Phys Eng Sci Med 1997 Sep;20(3):186-91.

[7] Doyle P, Gentle D, Martin CJ. Optimising automatic exposure control in computed radiography and the impact on patient dose. Radiat Prot Dosimetry 2005;114(1-3):236-9.

[8] L.W.Goldman, M.V.Yester. Specifications, performance evaluations, and quality assurance of radiographic and fluoroscopic systems in the digital era. Wisconsin, US: Medical Physics Publishing; 2004. Report No.: 30.

[9] Kodak Medical Physics. Calibrating AEC Devices. 2001.
Ref Type: Pamphlet

5 Contrast-to-noise Ratio Model

5.1 Introduction

Digital radiography (DR) imaging systems have a large dynamic range and high detective quantum efficiency. These factors, coupled with the ability to process the image, remove some of the constraints on the exposure needed to produce an acceptable diagnostic image with screen-film techniques. The chest is one of the more difficult regions of the body to image with radiography because of the need to portray structures in tissues with both high and low attenuations. The limited dynamic range of conventional screen-film systems has lead to the development of techniques designed primarily to provide acceptable image contrast in areas with differing attenuation on the same film. The accepted exposure conditions for chest radiography with screen-film techniques may not necessarily be optimal for the more flexible digital systems.

The most important factor affecting imaging performance for the range of tissue attenuations in different parts of a chest radiograph is the spectral quality of the X-ray beam, determined primarily by the tube potential and the beam filtration. adiographic contrast relates to the choice of optimum quality for the X-ray beam and is crucial in determining whether the image signals created by key anatomical features relevant for diagnosis, are perceptible against the background of the surrounding tissue. Since spectral sensitivities of digital detectors are different from those of conventional rare-earth screen-film systems the spectral quality of the X-ray beam that will produce the best image with a digital detector is likely to be different for screen-film. The perceptibility of details within the image is degraded by noise, predominantly caused by statistical fluctuations of X-ray

photons and a measurement of the contrast-to-noise ratio (CNR) provides a useful indicator of gross imaging performance.

Image metrics such as modulation transfer function (MTF) and detective quantum efficiency (DQE) are important for characterising the intrinsic performance of digital detectors. However, in optimisation of clinical imaging performance the choices of tube potential, filter options and scatter reduction techniques to provide the best image contrast with the lowest dose are of prime importance. Although the CNR does not give information on the perceptibility of details of differing size, it does provide data on how well objects of different attenuation can be imaged and this relative performance should show similar trends for objects of all sizes.

Measurement of the CNR has been used in investigations into optimisation of exposure parameters for digital radiography of the chest [1-4]. In the present study, theoretical assessments of CNR using computer simulations have been compared with results of practical studies on a phantom to assess whether they can provide a useful adjunct in optimisation. The theoretical evaluation has been used to predict and compare imaging performance for a range of tube potentials with added copper filtration applied to techniques used in clinical practice. The potential role of computer simulation methodology in determining the optimum factors for clinical imaging with various digital X-ray systems is discussed in Chapter 6.

5.2 Method

A Siemens Aristos VX IDR vertical bucky system, designed for erect chest and skeletal examinations, was employed for the study. The X-ray tube (Opti 150/30/50HC, Siemens)

had filtration equivalent to 2.5 mm of aluminium, with the facility to include additional copper filters. The digital detector is a Trixell Pixium 4600, which has a caesium iodide (CsI) scintillator coupled to a photodiode thin film transistor array. The detector area is 43 x 43 cm^2 with a 3120 x 3120 pixel matrix and a pixel pitch of 143 μm. IDR images were obtained of a geometric chest phantom (07-646, Nuclear Associates, USA), which has been designed for monitoring the performance and assessing image quality of digital radiography systems, figure 5:1. It has a response for imaging systems which is similar to that of a normal PA chest radiograph in terms of attenuation and scattering properties [5,6], although the dynamic range of transmitted radiation is narrower than that found in clinical chest images [7]. The phantom provides a useful tool for comparing imaging performance in regions of differing attenuation and testing theoretical assessment of image quality, although the limitations in representing a clinical chest radiograph must be borne in mind. The phantom is constructed from sheets of copper and aluminium cut into shapes that resemble a chest radiograph. These are sandwiched between two sheets of acrylic to provide additional attenuation and scatter. The background attenuation in these parts of the phantom is represented by 50.8 mm of acrylic, 2.0 mm of aluminium with 0.5 mm of copper. Additional thicknesses of copper equal to 0.5 and 1.5 mm have been added to simulate attenuation in the heart, and subdiaphragm or abdomen regions respectively. This allows image quality characteristics to be studied for attenuations equivalent to different parts of the thorax and abdomen within one phantom. Copper disks of varying thickness and size are positioned in the lung, heart and abdomen regions of the phantom to evaluate contrast detail. The disk thicknesses ranged from 0.006 to 0.076 mm in the lung, from 0.013 to 0.127 mm in the heart, and from 0.051 to 0.406 mm in the abdomen region. Disk diameters ranged from 0.5 to 6 mm. A radiograph of the chest phantom is shown in figure 5:1.

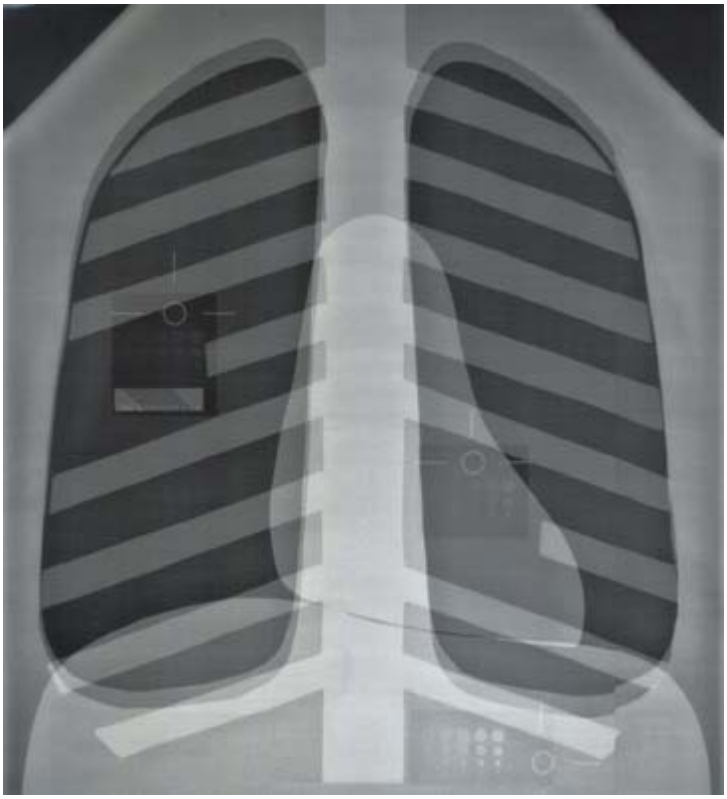

Figure 5:1 A Radiograph of Nuclear Associates Chest Phantom (model 07-646)

Radiographs of the phantom were acquired using three radiographic techniques employed in clinical practice in the West of Scotland. The first technique used a grid (80 cm^{-2}, ratio = 15) with a 1.8 m source to image distance (SID), the second involved using the same SID but without the grid, and the third technique used a 150 mm air gap and a SID of 3.6 m. Sets of 32 images were acquired for each of the three techniques. Each set contained images recorded with eight kilovoltages ranging from 60 to 133 kV with the beam filtered either by 2.5 mm of aluminium alone or by 2.5 mm of aluminium with additional 0.1 mm, 0.2 mm or 0.3 mm of copper. For each technique the exposure factors were chosen to give a similar dose behind the lung with two lateral ionisation chambers selected in the automatic exposure control (AEC). The AECs were set up to comply with the Siemens image quality assurance program (IQAP), for a sensitivity class of 560 (receptor dose of 1.8 μGy ± 20% using 2.1 mm Cu). All images were processed using

settings adopted in routine clinical practice for chest radiography. The images were compressed using JPEG lossless compression, stored in the DICOM 3.0 format and transferred to a research workstation via compact disk, as there was not an integrated picture archive and communication system in the hospital. Osiris freeware software was used for image analysis (Dr. Jean-Paul Vallee, University Hospital of Geneva, Switzerland).

Contrast detail observations were performed on a dedicated two mega pixel high luminance (> 400 cdm^{-2}) display monitor, calibrated to DICOM Standard PS 3-14 [8]. Three medical physicists viewed image sets acquired for each technique with the beam filtered by 2.5 mm of aluminium alone, and by 2.5 mm of aluminium with additional 0.2 mm, on three separate occasions, making a total of 432 image scores. Ambient lighting was kept to a minimum and the viewing distance was about 1 m. The contrast provided by disks in different parts of the image was calculated for the different X-ray beam qualities [9] employed. Contrast detail plots are normally used for images acquired using similar beam qualities. The variation of contrast with tube potential makes a simple plot of threshold contrast versus detail diameter difficult to interpret, and so plots of the number of details seen against detail diameter were made for each tube potential. The total number of details observed in the lung, heart and abdomen regions were also recorded for each image.

Values for the CNR were computed for all five of the 6 mm diameter disks for the lung, heart and abdomen regions of each image. Regions of interest (ROIs) containing approximately 800 pixels were drawn to compute the mean and standard deviation of pixel values. One ROI was positioned at each disk location (D) and five ROIs surrounding each disk (B). The contrast signal at each disk site was defined as the difference between the mean pixel value with the disk S_D and the mean of the mean pixel values in the five ROIs surrounding that disk site $\bar{S}_B$, ($S_D - \bar{S}_B$). Image noise was defined as the mean of the

standard deviations for the background ROIs, $\overline{\sigma}_B$. The CNR was computed from the ratio of the measured signal and the noise.

Before CNR measurements were performed two corrections were made on the image data. Firstly, the pixel values were linearised by applying the inverse signal transfer function (STF). The STF was obtained from a series of five open field exposures covering an exposure range of approximately 2 - 40 μGy for each kilovoltage setting. Secondly, a correction was made to reverse changes made to image pixel data as a result of image processing as applied in routine clinical practice, such as look up table selection, amplification adjustment and spatial frequency gain settings. The second correction was necessary to evaluate the overall performance of the IDR system using both raw image data and with the normal image processing applied to clinical chest radiographs. A simple phantom was designed to enable this correction to be made. The phantom was designed so that the histogram of pixel values would mimic that of a PA chest examination and allow the IDR system to process the phantom as if it were a standard adult chest. The phantom consisted of a grid of 24 copper filters of thicknesses ranging from 0.007 mm to 0.5 mm on a base comprising 50 mm thick PMMA and a 2 mm thickness of aluminium. Relative fluences were calculated from attenuation data for the X-ray spectra used for the imaging process. These data were used to derive the relationships between the pixel values in the clinical chest processed images and the raw pixel values for each X-ray spectrum employed. The relationship between the CNR in the chest processed image and that for the raw image data was then calculated.

The dose-area product was recorded for each exposure. For image acquisitions with no additional copper filtration a value for the effective dose for an equivalent chest PA radiograph was calculated from the dose-area product using effective dose conversion coefficient data (mSv / Gy cm^2) [10]. A logarithmic curve fit was applied ($r^2 = 0.99$) to

provide coefficients at kilovoltages (kVs) not supplied. PCXMC Monte Carlo software was used to calculate the effective dose in cases where additional copper filtration was used (Radiation and Nuclear Safety Authority, Finland). The effective dose was used in calculations of a figure of merit equal to the CNR^2 divided by the effective dose[3].

5.3 Theoretical Model

The theoretical model was developed in order to study the relationships between the CNR and beam quality in different parts of a chest image. If the model could predict the relationships between CNR and beam quality for the chest phantom, then it might provide useful information about how the CNR might vary with tissue thickness and allow imaging performance in different parts of a chest image to be predicted based on tissue attenuation data. It was hoped that use of a relatively simple model would enable variations due to factors such as image processing and automatic exposure control (AEC) setting to be identified so that appropriate adjustments could be made.

Photon fluences were calculated from data on X-ray photon spectra generated at different tube potentials for a constant potential unit with a tungsten rhenium anode having a 16^o target angle and filtered by 2.5 mm of aluminium [11]. Photon spectra equating to the photon fluence incident on a surface at 1.0 m from the focus were adjusted by means of the inverse square law to derive the number of photons incident on individual pixels at the image receptor. The fluences were adjusted for attenuation in filters and phantom materials using tabulated data on mass attenuation coefficients [12]. The fluence of X-ray photons of energy E transmitted through the phantom, and incident on the image receptor $\psi_r(E)$ was represented by:

$$\psi_r(E) = \psi_i(E)\sum_{t}^{T} e^{\frac{\mu_t(E)}{\rho_t}\cdot p_t d_t} \qquad \textbf{Equation 5:1}$$

where $\psi_i(E)$ is the photon fluence incident on the phantom, and $\mu_t(E)$, ρ_t and d_t are attenuation coefficient, density and thickness respectively for each layer of phantom material t through which the X-ray beam has passed. All calculations were performed for individual photon energies in 1 keV intervals covering the relevant energy spectrum.

The air kerma K_{air} incident on the image receptor and the AEC through the lung field of the chest radiograph for any X-ray spectrum was calculated for each tube voltage V from the equation:

$$K_{airV} = \sum_{0}^{E=kVp} \psi_{rV}(E) \cdot E \cdot \frac{\mu_{en}}{\rho} \qquad \textbf{Equation 5:2}$$

where μ_{en}/ρ is the mass energy absorption coefficient for air. In order to simulate the use of an AEC device behind the lung field for termination of each exposure, the values for the photon fluence were normalised to give similar values for the air kerma transmitted through the lung fields (K_{airV}) at each tube potential V. Relative mAs values at each kV were then adjusted to fit the form of the Siemens IQAP AEC correction curve. The fitted air kerma curve was then scaled to simulate a radiographic speed of 560 i.e. a detector dose of ~ 1.8 μGy at 81kV.

The energy absorbed in the CsI scintillator of the IDR system A(E), from photons of energy (E) can be calculated from the equation:

$$A(E) = \psi_r(E)(1 - e^{\frac{\mu_{en}(E)}{\rho_x}\rho_x d_x}) \qquad \textbf{Equation 5:3}$$

where $\psi_r(E)$ is the photon energy fluence incident upon the image receptor, and $\mu_{en}(E)/\rho_x$, ρ_x and d_x are the mass energy absorption coefficient, density and thickness respectively of

the X-ray image receptor phosphor. The relative efficiencies of detection for the different photon spectra transmitted through various parts of the phantom or the body were derived by summing equation 5:3 over all photons within the spectrum and dividing the result by the total photon fluence.

The difference in radiographic contrast C(E) resulting from photons of energy E for a feature with linear attenuation coefficient $\mu_2(E)$ in an object with attenuation $\mu_1(E)$ was derived from the equation:

$$C(E) = \frac{I_1(E) - I_2(E)}{I_1(E)} = \frac{\Delta I(E)}{I(E)} = 1 - e^{-[\mu_1(E) - \mu_2(E)]d} \approx \Delta\mu(E)d \quad \textbf{Equation 5:4}$$

where $I_2(E)$ and $I_1(E)$ are the intensities transmitted through the feature and the surrounding area, and d is the thickness of the feature. Equation 5:4 was summed over the relevant X-ray spectra in order to derive values for the image contrast. For a given beam quality, the contrast signal ΔI can be expressed in terms of the corresponding difference in the mean number of X-ray photons detected by each image pixel ($\Delta\overline{N}$). X-ray photons obey Poisson statistics, therefore the quantum noise, is proportional to the square root of the mean number of photons detected ($\sqrt{\overline{N}}$), and the CNR for an ideal image receptor with only quantum noise can be expressed as:

$$CNR = \frac{\Delta\overline{N}}{\sqrt{\overline{N}}} = \Delta\mu d\sqrt{\overline{N}} \quad \textbf{Equation 5:5}$$

where the number of photons (N) incident on an image receptor pixel of area (A) is given by:

$$N = \sum_{0}^{E=kVp} \psi_r(E) \cdot A \quad \textbf{Equation 5:6}$$

CNR values were calculated from the photon transmissions through different parts of the chest convolved with the response of the CsI detector to determine values for $\sqrt{\overline{N}}$ and these substituted together with the detail attenuation ($\Delta\mu$) and thickness (d) into equation (5). The calculations were then used to study the variation of CNR with tube potential and thickness of copper filtration.

The air kerma incident on the surface of the phantom or the body (subscript I) at a particular tube voltage V, K_{airVI} is given by:

$$K_{airVI} = \sum_{0}^{E=kVp} \psi_{iVI}(E) \cdot E \cdot \frac{\mu_{en}}{\rho} \qquad \textbf{Equation 5:7}$$

Equation 5:7 was used in deriving an entrance surface dose (ESD) equating to that for a chest radiograph by multiplying by the back scatter factor (BSF_V) for the corresponding tube potential and filtration for a chest radiograph [13]. A value for the effective dose (ED_V) was derived from the ESD using conversion coefficients ED_V/ESD (C_V) [10]. PCXMC Monte Carlo software was used to calculate ED_V and ESD in cases where additional copper filtration was used (Radiation and Nuclear Safety Authority, Finland).

$$ED_V = K_{airVI} \cdot BSF_V \cdot C_V \qquad \textbf{Equation 5:8}$$

System performance relating to both image quality and dose can be compared using a figure of merit (FOM), defined as the square of the CNR divided by a measure of dose. The FOM is independent of the number of photons or exposure level and so provides a useful quantity for comparing imaging performance for different X-ray beam qualities. For the purpose of this study, figures of merit FOM_{iV} were derived with a range of tube potentials for details in different parts of the chest phantom image (i) by dividing the CNR^2 by the effective dose as defined in equation (9).

$$FOM_{VI} = CNR_{VI}^2 / ED_V \qquad \textbf{Equation 5:9}$$

The calculations described so far only relate to the transmitted primary beam and do not contain any contribution from scattered radiation. An indication of the effect of scatter was obtained by superimposing a uniform background of noise on the image, increasing the variance by a factor $1/\sqrt{(1-S_{oV})}$ where S_{oV} is the scatter fraction for X-rays generated with a tube potential of V, taken for a 100 mm, 150 mm and 200 mm thickness of water [11], this being the closest approximation to the lung, heart and abdominal areas of the chest for which scatter fraction data were available.

Theoretical values for the CNRs including scatter (CNR_{Vs}) were derived from the formula:

$$CNR_{Vs} = CNR_V \sqrt{(1-S_{oV})} \qquad \textbf{Equation 5:10}$$

The impact of a 15/80 grid was represented by incorporating data for grid scatter factors (S_g) and the primary transmission (T_{pV}), to give CNR_{igV}:

$$CNR_{igV} = CNR \sqrt{[T_{pV} (1-S_{gV})]} \qquad \textbf{Equation 5:11}$$

These equations were used to evaluate the variation in CNR and FOM with tube potential for the different areas of the chest phantom for comparison with practical measurements made on images. The details in the phantom used in the calculations were made from copper with thicknesses of 0.076 mm, 0.127 mm and 0.406 mm in the lung, heart and abdomen regions respectively.

5.4 Results

Results of the scoring of the number of details seen in images for the lung and abdomen regions of the phantom taken using the grid technique are shown in Figure 5:2. The standard error in the number of details recorded from nine observations (three observers on three occasions) was 0.14. The plots show the number of details seen in images recorded at various tube potentials for disks with areas ranging from 0.2 to 28 mm^2. Optimizing the window and level settings for each individual region of the phantom resulted in the same number of details recorded as images displayed with the default window and level display settings of 4095 and 2047 respectively. For the lung, the number of details visible fell as tube potential was increased from 60 kV to 133 kV, whereas for the abdomen detail visibility tended to first increase with tube potential and then gradually decrease as tube potential was increased further. The pattern is similar for all detail sizes, although the number of details seen are different.

Plots of the total number of details of all sizes seen by the observers in each test object against tube potential (Figure 5:3) demonstrate trends in detail perception with beam quality. The plots relate to different techniques used, and show improvement in detail perceptibility with removal of scatter. In all cases the images recorded with a grid showed the largest number of details. Differences between use of a grid and an air gap to remove scatter were small for imaging details in the lung, but there was a more significant difference between the two techniques for the abdomen.

(a)

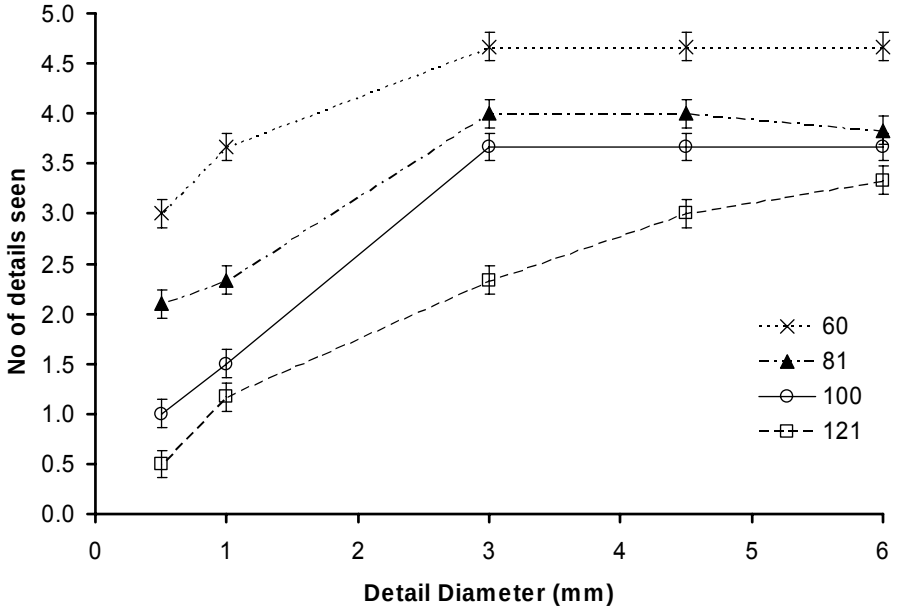

(b)

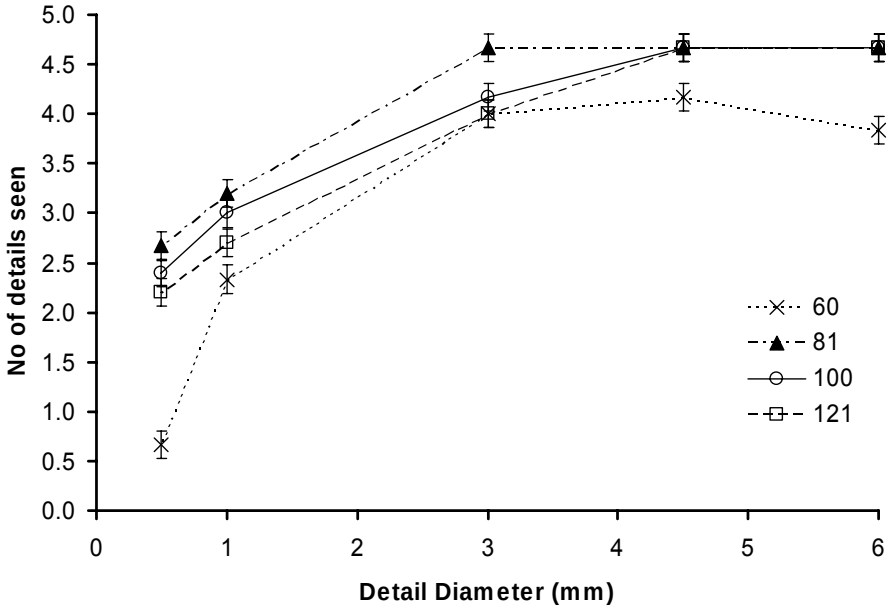

Figure 5:2 Detail visibility curves showing the number of details seen plotted against the detail diameter for a range of tube potentials using the grid technique for (a) the lung, and (b) abdomen regions. Error bars indicate a 0.14 standard error from nine observations (three observers on three occasions).

(a)

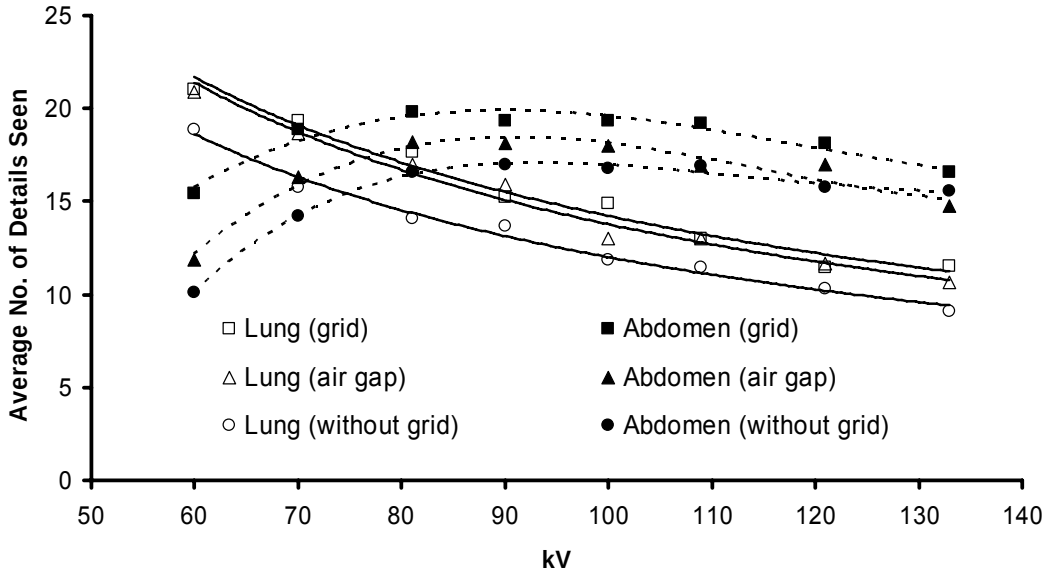

(b)

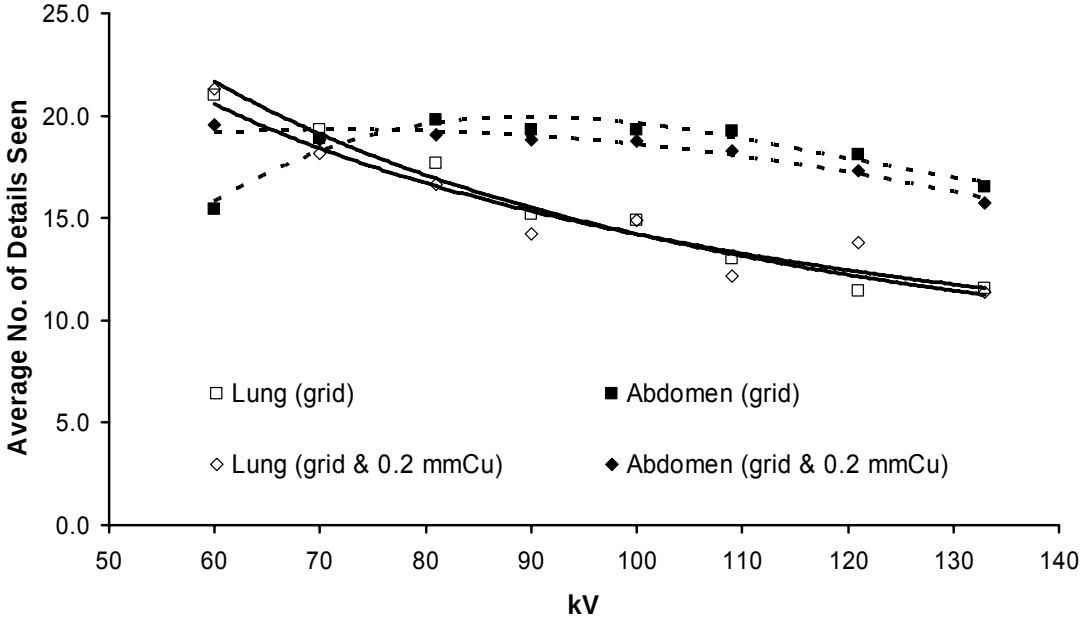

Figure 5:3 Average umbers of details of all sizes detected in contrast detail test objects in the lung (solid line) and abdomen (dotted line) regions of the phantom plotted against tube potential for images recorded using the grid, no grid and air gap techniques using (a) 2.5mm filtration and (b) 2.5mmAl filtration and 0.2mm Cu.

The STF for the Trixell Pixium 4600 digital detector is shown in Figure 5:4. There is a linear relationship between the pixel value and the incident exposure for a given beam quality. However, there is some dependence of the STF on tube potential, with the system being most sensitive around 80 kV. The variation is likely to be due partly to detector response and partly attenuation in layers between the phantom and image detector array. To account for this dependency linear fits were applied to data for each tube potential (r^2 = 1) and the image data were corrected using the resulting equations.

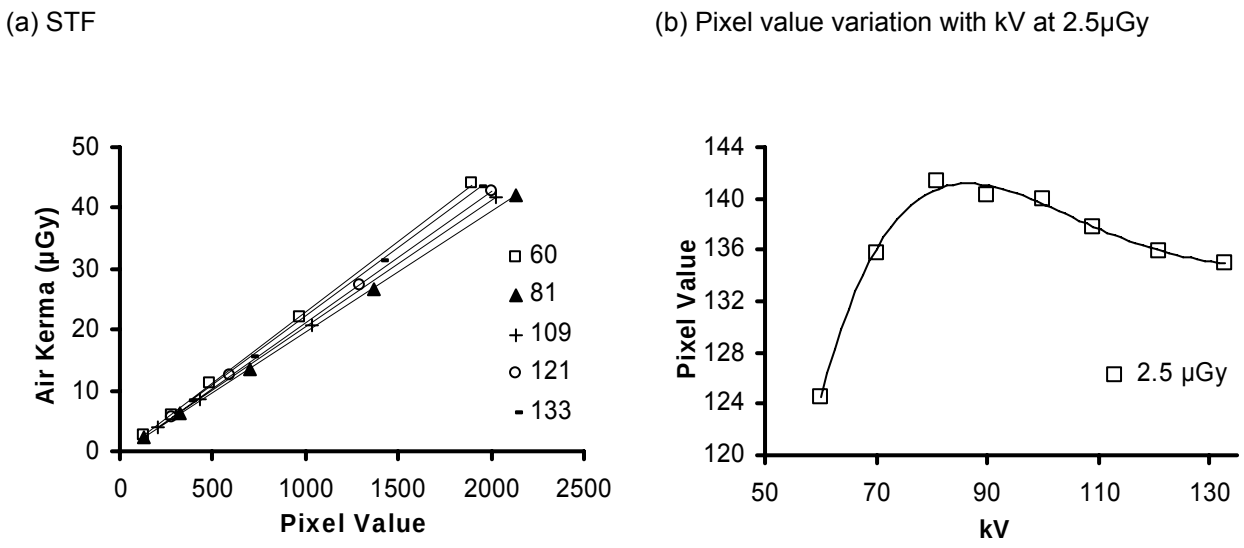

Figure 5:4 (a) Plots of air kerma incident on the image plate against pixel value for different tube potentials used in deriving the STF and (b) Pixel value against kV for an incident air kerma of 2.5µGy

A radiograph of the LUT phantom and resulting image pixel histogram are shown in figure 5:5 (a). A typical adult chest radiograph is shown in figure 5:5 (b) with associated pixel histogram.

(a) (b)

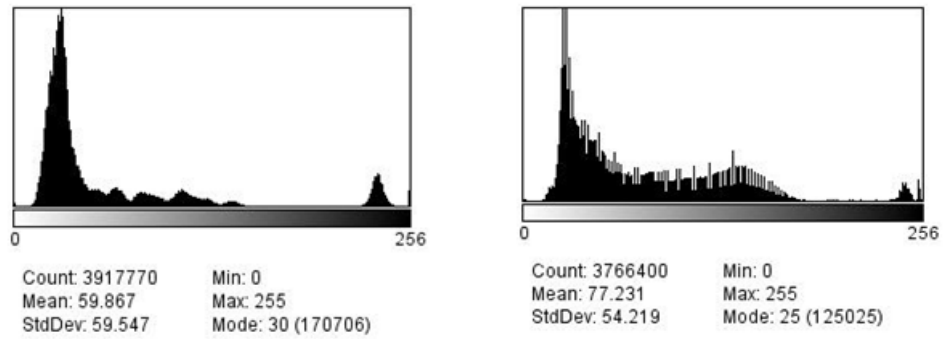

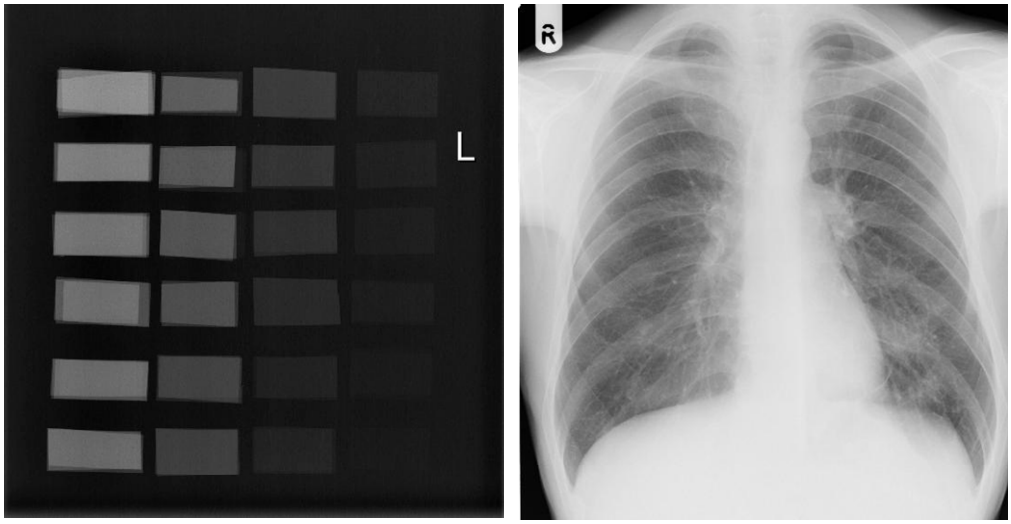

Figure 5:5 (a) A Radiograph of the LUT phantom with associated image histogram and **(b)** A typical adult chest radiograph with image histogram. The similar histogram shapes will 'trick' the IDR system into processing both images as thought they were PA chest examinations.

The relationship between pixel values for the chest processed image data and the raw image data is shown in Figure 5:6. Again, curve fits were applied for each tube potential ($r^2 = 0.99$) and the image data were corrected using the resulting equations.

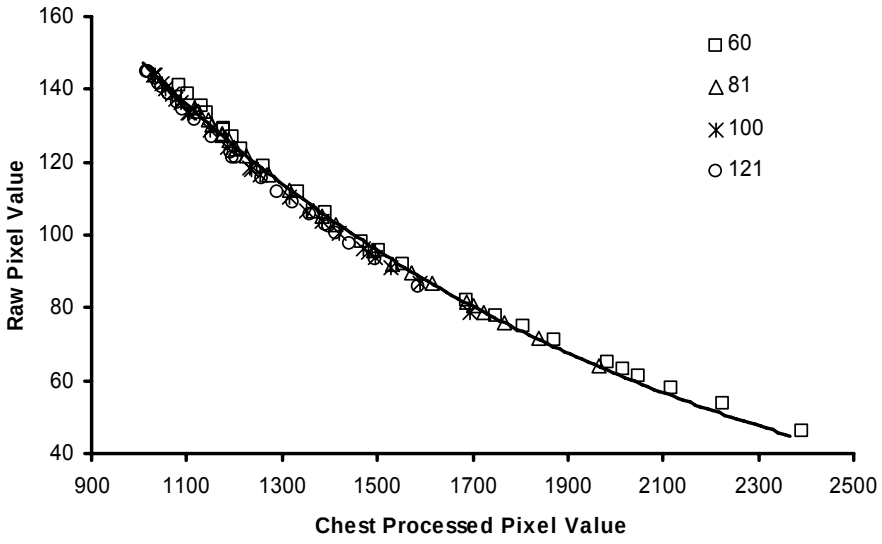

Figure 5:6 Plot of raw pixel values against image processed pixel values obtained using clinical settings routinely used for chest radiography.

Relationships between the CNR and tube potential in different parts of images of the chest phantom recorded using the grid and air gap techniques to reduce scatter are shown in Figure 5:7.

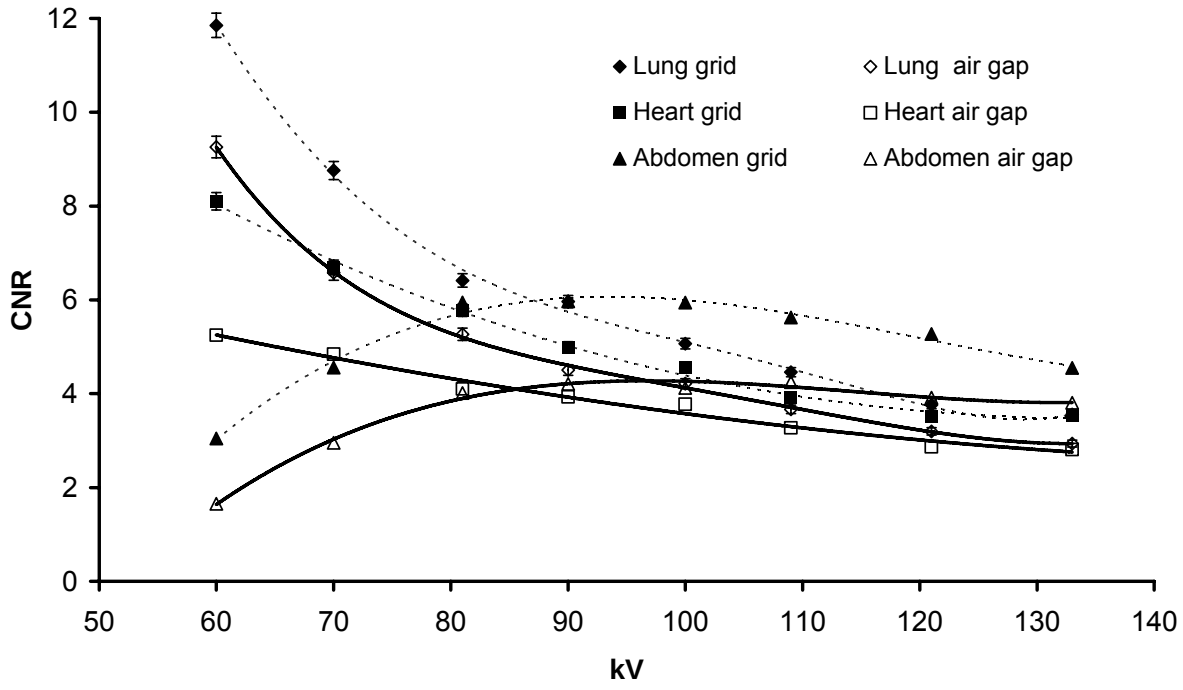

Figure 5:7 Plots of the measured values of CNR against tube potential, for the lung, heart and abdomen regions of the phantom, using a grid and an air gap technique to reduce scatter. Error bars indicate where the error in the value is greater than the size of the data symbol.

CNR fractional errors were calculated from the partial derivatives of the function defining the CNR. In most cases the error in the value was less than the size of the data symbol. The CNR was highest in the lung region at low tube potentials (60-80kV) and gradually fell as the tube potential was increased. The CNR for the heart followed a similar trend, but the values were lower and declined more slowly changing little at higher tube potentials. The CNR in the high attenuation abdomen region gradually increased as the tube potential was raised, reaching a maximum at 90-110 kV and then fell as the tube potential was increased further. Results for the two scatter reduction techniques followed a similar pattern with tube potential, but the average CNR values with the air gap were 20% lower in the lungs, 25% lower in the heart and 30% lower in the abdomen regions.

The variations with tube potential for each region of the phantom mimicked trends seen in the contrast detail observations (Figure 5:3), although the overall performance in the contrast detail analysis for the lung region was poorer relative to the abdomen than might have been expected from the CNR measurements.

The trends in CNRs with tube potential calculated using the theoretical simulation (equation 5) for the transmitted primary radiation are shown in Figure 5:8.

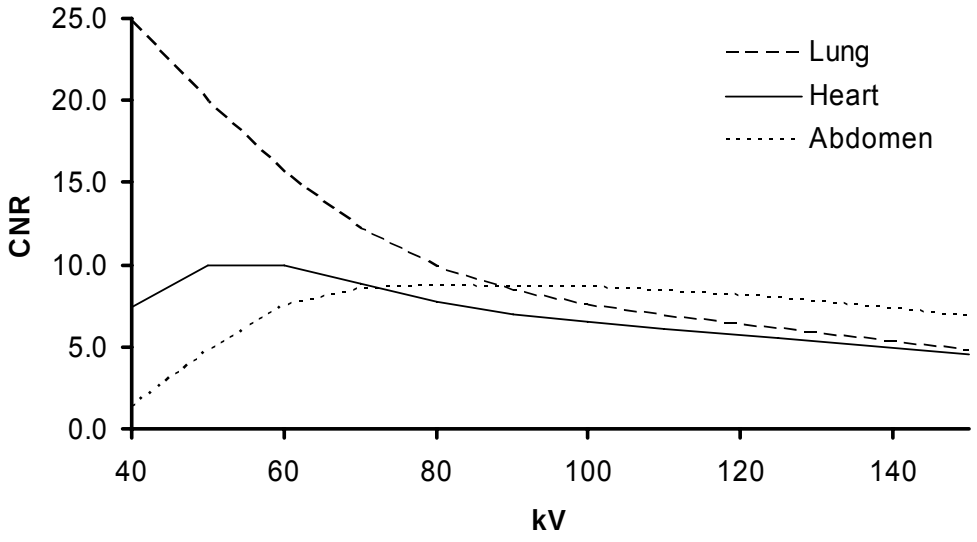

Figure 5:8 Plots of CNR against tube potential, calculated from the model simulation for the transmitted primary beam for different regions of the phantom.

Practical measurements of CNR for imaging of the chest phantom with scatter and with a grid are compared with theoretical simulations, using equations 5:10 and 5:11 respectively, in Figures 5:9. The trends seen in the practical measurements and simulations for the lung and heart regions were similar, but measured CNRs for the abdomen declined more rapidly below 80 kV than the theoretical predictions. Values for the FOM, which takes into account the effective dose to the patient as well as the image

quality (equation 5:9), were derived from the practical measurements and the theoretical simulations, and are plotted in Figure 5:10. The trends in practical measurements and simulations are again in reasonable agreement, although the result for the abdomen fell more rapidly at lower tube potentials. For imaging the lung, the FOM was highest at 60 kV - 70 kV, and for the heart 70 kV – 90 kV. The change in FOM for the abdomen followed a different pattern, peaking at 90 kV – 120 kV. The FOM for lung imaging was slightly higher when no grid was used than for imaging with a grid, because the effective dose was lower, but the FOMs for imaging the heart and abdomen were higher with a grid.

(a)

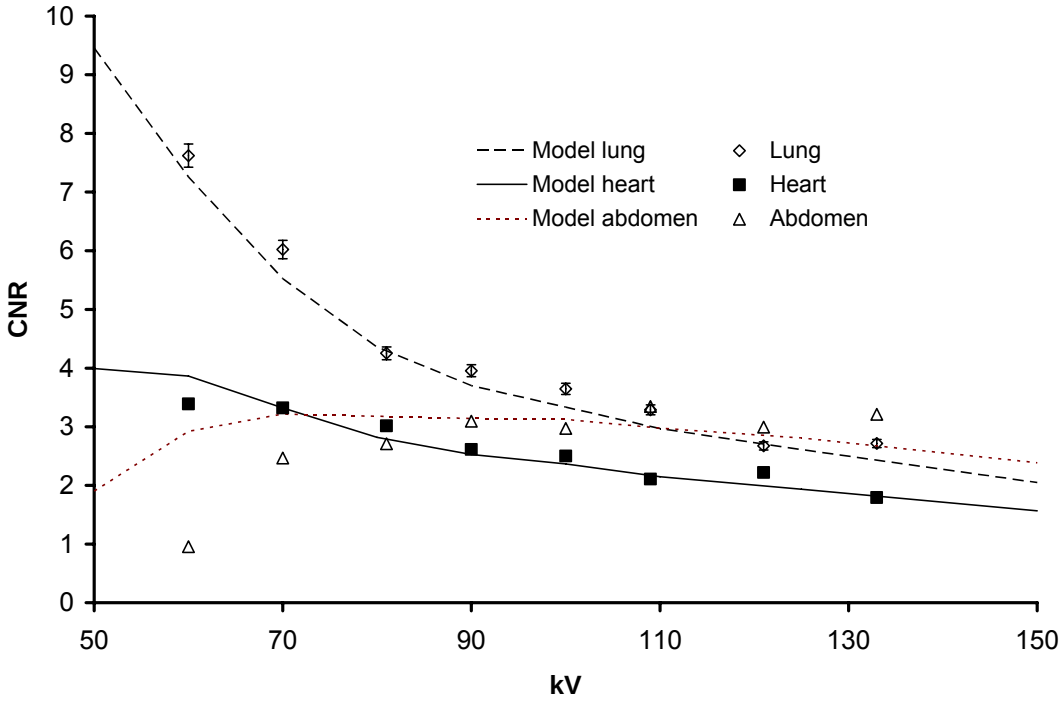

(b)

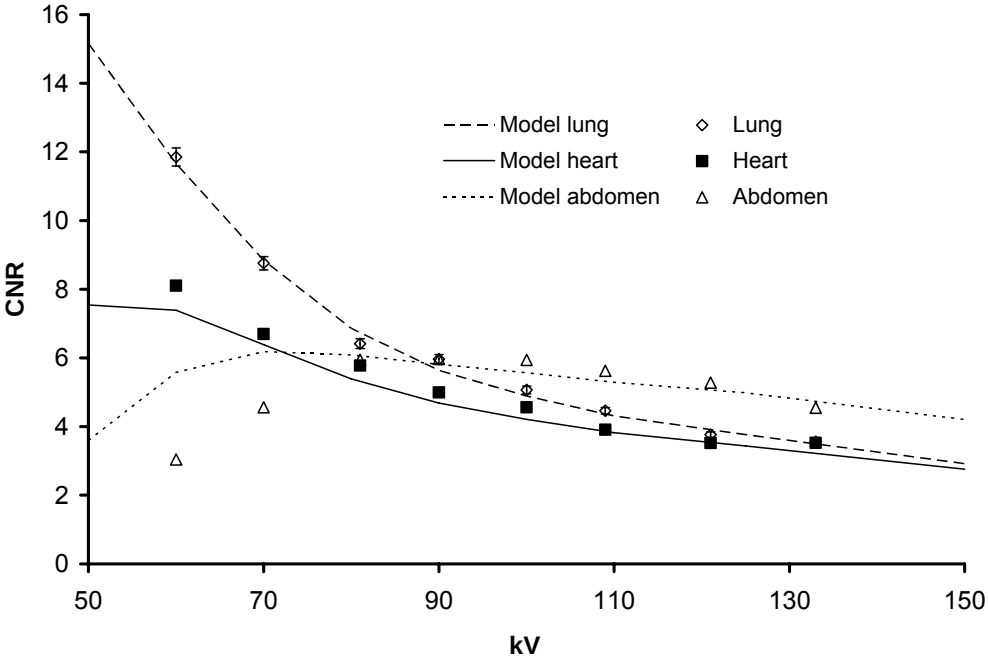

Figure 5:9 Plots of measured values of CNR against tube potential with curves derived from the model, for different regions of the phantom (a) for primary and scatter, and (b) with grid to remove scatter. Error bars indicate where the error in the value is greater than the size of the data symbol.

(a)

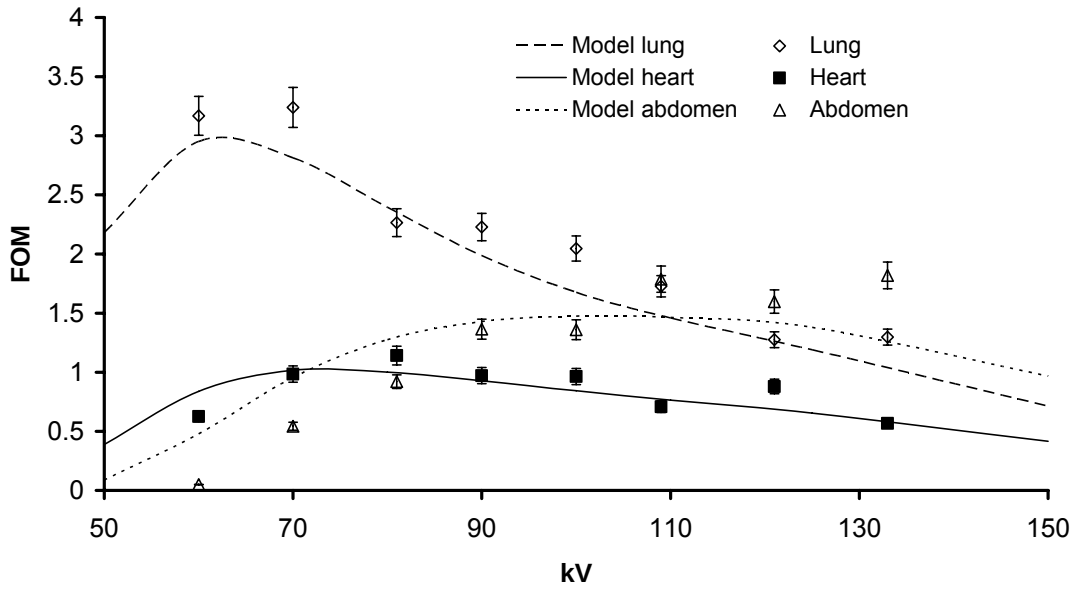

(b)

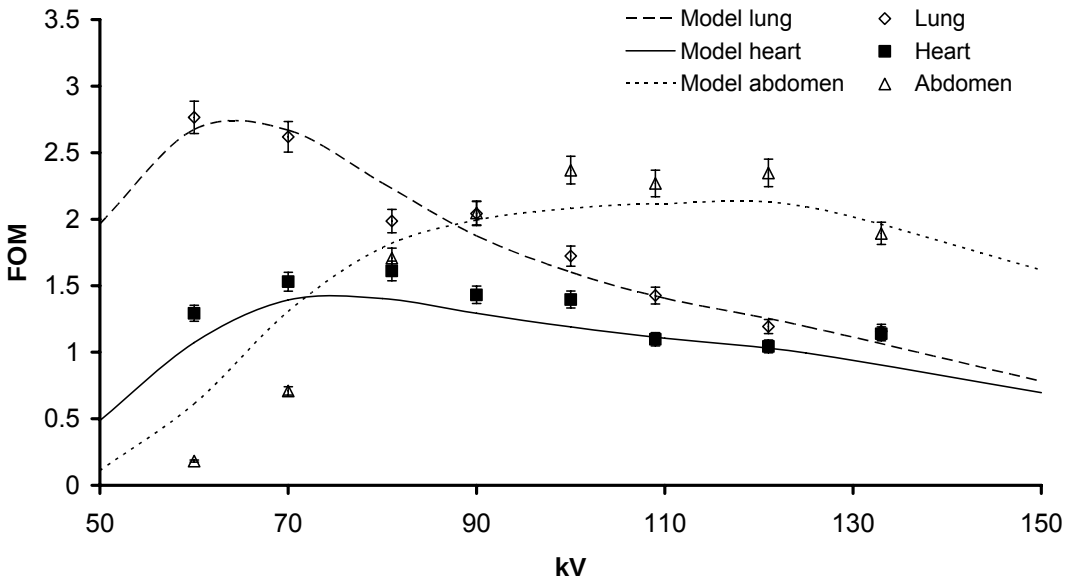

Figure 5:10 Plots of measured and calculated values of FOM against tube potential, for different regions of the phantom (a) for primary and scatter and (b) with grid to remove scatter. Error bars indicate where the error in the value is greater than the size of the data symbol.

The FOM from practical measurements recorded using the air gap and grid techniques to reduce scatter are compared in Figure 5:11.

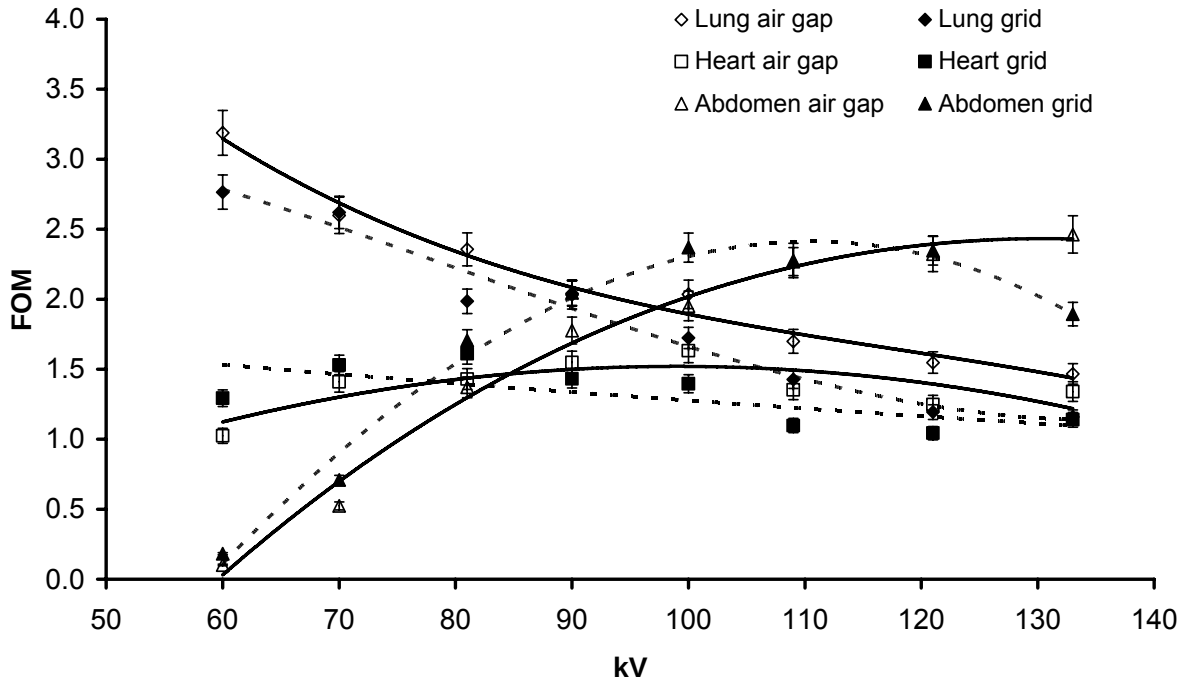

Figure 5:11 Plots of measured values of FOM against tube potential, for different regions of the phantom with grid and air gap techniques to remove scatter. Error bars indicate where the error in the value is greater than the size of the data symbol.

For the lung, the FOM for the air gap technique was higher, but for the abdomen, the FOM for the grid technique was higher. For the heart the FOM at 60-80 kV is higher when a grid is used, while at 80-130 kV the FOM with an air gap is higher. Theoretical simulation of the air gap technique was considered beyond the capability of the simple model and only experimental measurements were employed for this comparison.

Similar measurements were made incorporating a 0.2 mm thick copper filter in the X-ray beam and CNRs and FOMs derived from practical measurements and theoretical simulations are compared in Figure 5:12. Again there is reasonable agreement between the two, apart from the data for the abdomen at lower tube potentials. CNRs and FOMs from

practical measurements for X-ray beams with and without the additional copper are compared in Figure 5:13. The 0.2 mm thick copper filter reduced the average CNR by 3% for the lung, while that for the heart and abdomen increased by 1% and 2% respectively. However, the lower entrance surface dose required to maintain the same level of exposure at the image receptor behind the lung for the lower tube potentials meant that the FOMs were significantly higher for images recorded with the copper filter.

(a)

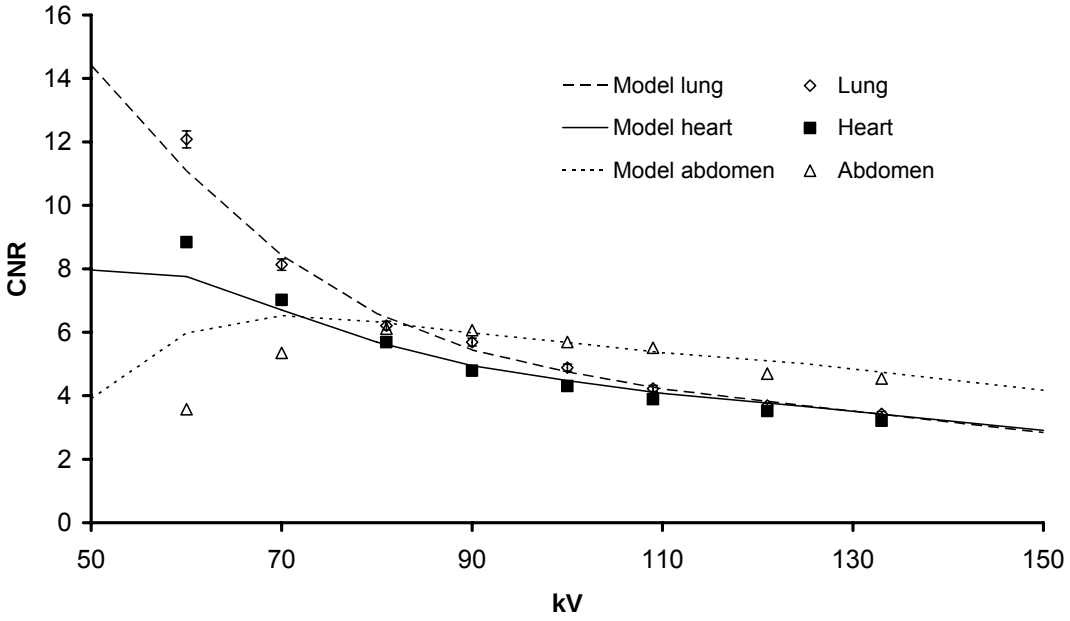

(b)

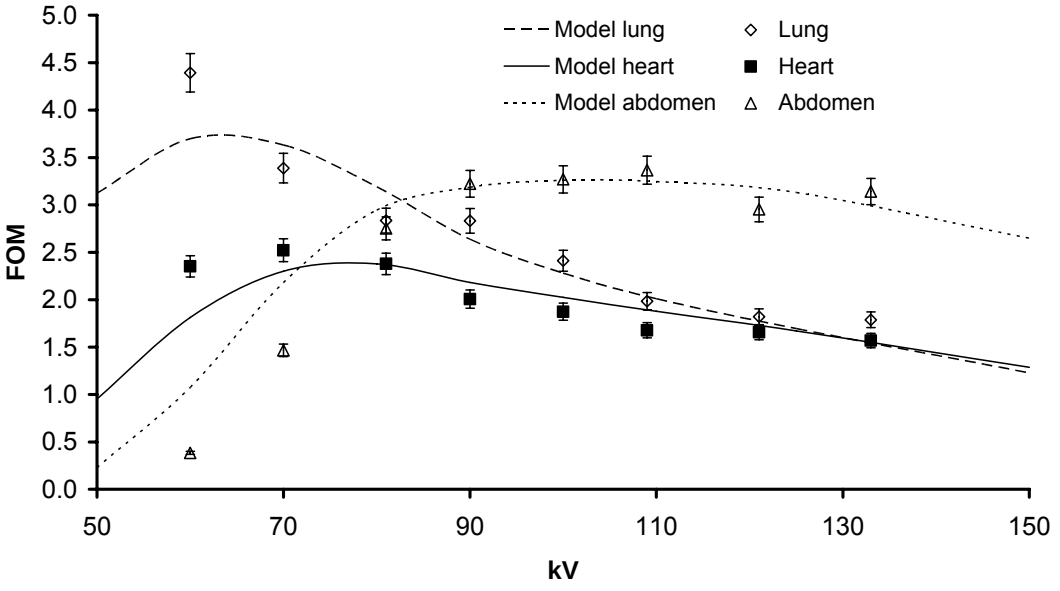

Figure 5:12 Plots of measured values and curves calculated from the model for (a) the CNR and (b) the FOM against tube potential for X-ray beams with an added 0.2 mm of copper filtration, using the grid technique. Error bars indicate where the error in the value is greater than the size of the data symbol.

(a)

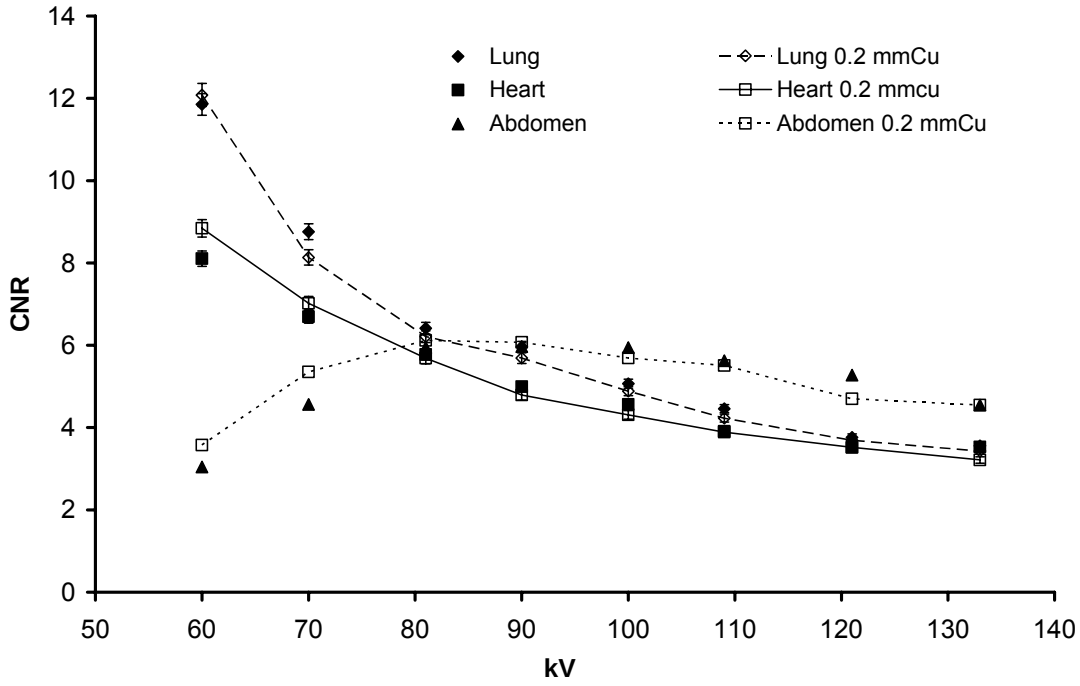

(b)

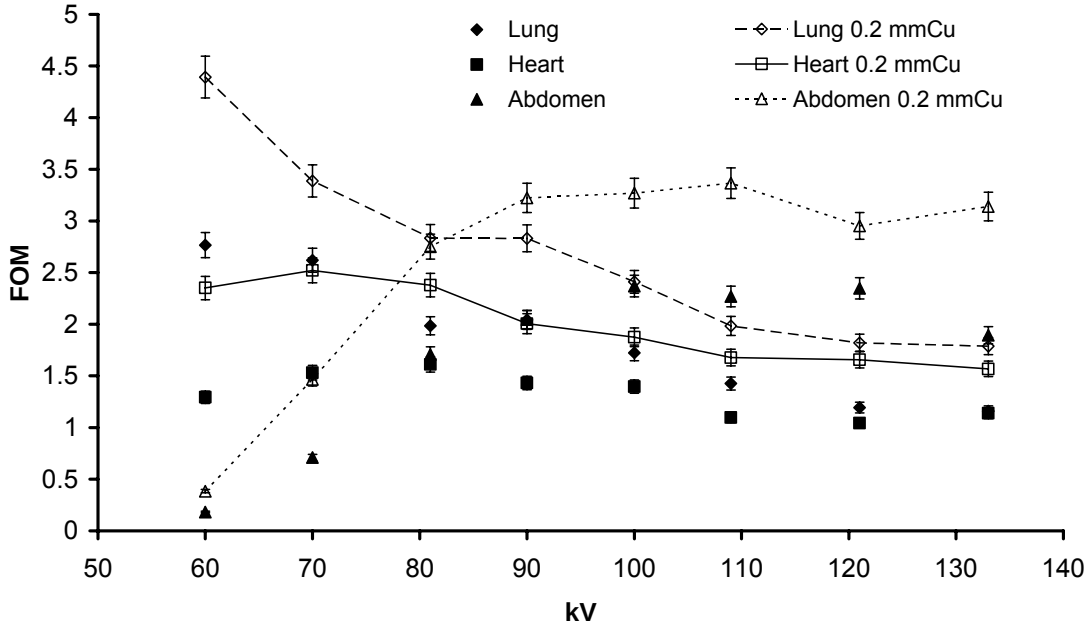

Figure 5:13 Plots of measured values for (a) the CNR and (b) the FOM against tube potential, comparing data with and without an additional 0.2 mm of copper filtration. Error bars indicate where the error in the value is greater than the size of the data symbol.

5.5 Discussion

Traditionally the limited dynamic range of conventional screen-film systems required the use of higher tube potential settings. The Council of European Communities (CEC) Guidelines [14] give an example of good technique for postero-anterior (PA) radiographs of the chest as use of a 400 speed class wide latitude screen-film combination with 125 kV X-rays, a 180 cm source-to-image distance (SID) and a grid. A relatively high tube potential and a wide latitude (lower contrast) film are recommended in order to obtain good penetration through the higher attenuation regions and maintain the range of exposure levels through both the lung and the mediastinum within the dynamic range of the film. However, other studies suggest that higher contrast film provides a better level of image quality [15]. Digital radiography systems have redefined the conventional relationship between image receptor exposure and contrast through the broader dynamic range and the capacity for processing after image acquisition, which allows the contrast and brightness of an image to be optimised independently. Thus parameters that are most appropriate for chest imaging need to be re-evaluated.

With hundreds of different X-ray examinations performed in a typical radiography department the scope for optimisation is vast. Optimisation techniques must be simple to implement and practical. Optimisation in diagnostic radiology is generally regarded as finding the lowest dose to the patient that does not jeopardise a correct diagnosis. However, describing the image quality needed for 'correct diagnosis' is not straightforward. Image quality parameters such as MTF and DQE enable the performance of the image receptor to be characterized, such measurements are essential for equipment evaluation, but are beyond the scope of most radiography / medical physics departments. Optimisation of technique in a radiology department usually comprises choices of tube potential, filtration and method of scatter removal and there is a need to find a metric

which can be applied to clinical imaging tasks to compare and evaluate different options. Contrast-to-noise ratio has been examined as such a metric in this study.

Scoring of the visibility for details in regions of the chest phantom with differing attenuation showed that more details could be seen in the lung images taken with lower tube potentials, while for those of the abdomen more details were visible when tube potentials of 90-110 kV were used (Figure 5:2 and 5:3). The significance of contrast detail relationships at different tube potentials is more difficult to translate into performance indicators directly, since the contrast depends on X-ray beam quality. However, they do allow some comparisons to be made. Summing of the number of details visible gives an indication of gross imaging performance. Figure 5:3 shows the improvement in imaging performance achieved through use of a grid. It also demonstrates that the air gap technique is effective in improving image quality for the lung, but less so for the abdomen from which there is a higher level of scatter.

Contrast is the most important factor influencing choice of tube potential for imaging tissues with different attenuations. The contrast-to-noise ratio determined for objects containing several hundred pixels has the potential to provide a useful parameter for comparing imaging performance for X-ray beams with different beam qualities. The relationship between the CNR measurements and tube potential (Figure 5:7), in general reflects the variation in the number of details detected (Figure 5:3), and shows a larger percentage difference between the results with the grid and air gap techniques for the abdomen than for the lung. The main difference between the CNR and the overall detail detection results is that when results for the lung are compared with those for the abdomen, the number of details detected is lower than would have been expected from the CNR results. This may be due to the poorer response of the human visual system to contrast changes in the darker (lung) region of the phantom, as predicted by the Barten model [16].

The results in this study show that the CNR and detail detection are higher in the lung and heart regions at lower tube potentials, while those in the abdomen are higher for tube potentials of 90-110 kV (Figures 5:3 and 5:9). Thus the optimum tube potential depends on whether relatively high CNR values are required in the lung, and what level of image quality is needed in the heart or abdomen regions to make a clinical diagnosis. In a real chest radiograph, the exposure level behind the lung is significantly greater than for the other regions and the limiting factor for the CNR is anatomical noise rather than quantum noise [17], so the heart and abdomen regions are more important for determining the optimum potential.

The FOM provides a comparison of imaging performance with different beam qualities that takes dose into account and for this study the effective dose, which is linked more closely to risk, was used (equation 5:9). The FOM for the lung was highest at 60–70 kV, while that for the heart was higher at 70-90 kV and that for the abdomen at 90-120 kV (Figure 5:10). With regard to techniques for scatter reduction, FOMs are highest for imaging of the lung at low tube potentials without a grid (Figure 5:10), but the FOM for imaging of more attenuating tissues is poor, unless a technique for scatter removal is employed. The FOM results for lung imaging are higher for the air gap technique, although the grid technique is better for imaging the abdomen (Figure 5:11). Values for the FOM are significantly higher for beams with copper filtration, because of the lower effective dose (Figure 5:13).

Thus the choice of the optimum technique and exposure paramters may vary with the criteria to be fulfilled for a given diagnostic task. The use of copper filtration has minimal effect on image quality and since it reduces the dose significantly it provides an advantage. The disadvantage is that a higher tube current will be required to compensate for attenuation in the filter and for this reason a 0.2 mm thick Cu filter may provide a compromise. With regard to the technique for scatter removal, since the dose for the air

gap technique is lower than that with a grid, this is the better one to use for imaging lung tissue. However, since the imaging performance appears less satisfactory for the heart and abdomen regions, it may be appropriate to base selection of the technique on the clinical requirements, with the air gap being used as routine, and a grid technique where detail in the mediastinum is crucial. The best compromise for tube potential to image the chest phantom would appear to be 90-110 kV, although for cases where only imaging of the lung was important, tube potentials of 70 kVp or even lower might provide the best contrast. However, it must be borne in mind that the attenuation and background noise properties of materials making up the phantom are different from those of tissue [7,17] and this will influence imaging performance for different beam qualities.

Studies of the use of digital systems for chest imaging have drawn different conclusions about the optimum tube potential. Practical measurements on computed radiography (CR) systems have shown that the signal to noise ratio (SNR) for lung and heart imaging was highest at 60 kV – 80 kV [1] and that the image quality, with regard to detecting lung abnormalities in phantoms and human volunteers, was superior in images recorded using 80-110 kV than with higher tube potentials [18,19]. A study of the SNR for a selenium based DDR system (Thoravision), concluded that when effective dose was taken into account, the optimum tube potential was between 90 and 110 kV [2]. However, a recent study of a CsI IDR detector systems concluded that 120 – 130 kV, with a 0.2 mm copper filter was the optimum imaging condition [3], although the FOM for the lung from this study was higher between 95 kV and 110 kV. A theoretical study of CNR and FOM for a CsI IDR system also concluded that 120 kV and 0.2 mm of copper was optimum, although the entrance surface dose was used in calculations of the FOM rather than effective dose [20]. The assessment carried out in this study on a phantom that mimics the range of attenuations in a chest radiograph gives broadly similar conclusions to the majority of other studies on optimisation of chest radiography. Results indicate that tube potentials of

90 kV – 110 kV should be optimum with an additional 0.2 mm of copper filtration providing an additional dose advantage. As far as the technique for scatter reduction is concerned, a study of screen-film radiography showed little difference in image quality between use of the grid and air gap technique [21], so the dose advantage of the air gap technique meant that this was preferred, in agreement with the present results.

This study has indicated that the CNR could provide a useful method for evaluating the potential image contrast obtainable from different X-ray beam spectra. Digital imaging systems provide the potential for increasing perceived image contrast locally by using different gradients depending on the area being examined *e.g.* lung or abdomen. Use of the CNR for assessing images is not limited by the range of contrast that can be displayed in a single image, but allows the potential contrast achievable to be separated from perception of the displayed image. The application of signal to noise ratios (SNRs), CNRs and FOMs for optimisation of techniques has been applied to experimental measurements of phantoms simulating chest imaging conditions [1-4]. If realistic values of the CNR can be calculated from data on X-ray spectra and object attenuations, calculations can be used to predict the CNR and its variation with beam quality. SNRs derived by Monte Carlo simulation for an anatomical phantom have been applied in assessing optimisation of tube potential and grid characteristics for imaging lung tissue with screen-film systems [22], although not for specific clinical equipment.

In the present study, a simpler theoretical approach using attenuation data has been applied to a particular imaging system. The calculated values have been matched to the performance of the particular imaging system through application of the STF and the AEC response at different tube potentials. Calculated results have been shown to be in reasonable agreement with experimental measurements (Figures 5:9, 5:10 and 5:12). Use of the chest phantom, for which the composition is known, has allowed such comparisons to be made under several different imaging conditions, and this is seen as a prerequisite to

use of this approach for optimisation studies on new systems in order to ensure that results provide a realistic representation of system performance. However, once these have been established, then potentially the method could be used to simulate the imaging of tissues within the body. This should provide a method linked more closely to practical clinical imaging performance, and could overcome some of the drawbacks in use of phantoms with very different elemental compositions from tissue. Such calculations could be useful in optimisation tasks when considering the choice of tube potential and filtration options for imaging patients of different sizes. One other factor that must be considered, when applying the technique to optimisation of clinical imaging, is that the quantum noise level may not be the limiting noise factor for the CNR. A study of detection of low contrast nodules in the lung indicated that for this task anatomic noise rather than quantum noise was the limiting factor [17]. Thus additional noise factors will need to be added for computation of CNR values for specific clinical imaging tasks.

5.6 Conclusion

A technique has been investigated that may be useful in optimisation of clinical radiographic imaging. The CNR has been measured in different parts of a phantom simulating the chest and results have been shown to follow a similar pattern to contrast detail detection techniques. Results suggest that tube potentials between 90 kV and 110 kV are optimal for imaging the range of attenuations in the phantom. Imaging of the more attenuating tissues of the heart and abdomen required a technique for removal of scattered radiation, although this was not necessarily required for lung imaging. The FOM, which takes account of effective dose for a chest radiograph, was higher for the lung when an air gap technique was used to remove scatter, but that for the heart and abdomen was higher for the grid technique. A simple theoretical simulation of the CNR and FOM has been

developed and adjusted to describe the performance of an IDR system by inputting data on the STF and AEC responses. Theoretical predictions show good agreement with results measured from images of the phantom and so provide a validation of the calculation methodology. It should be possible to apply the calculation technique to imaging of tissues in order to investigate optimisation of exposure parameters.

5.7 References

[1] Chotas HG, Floyd CE, Jr., Dobbins JT, III, Ravin CE. Digital chest radiography with photostimulable storage phosphors: signal-to-noise ratio as a function of kilovoltage with matched exposure risk. Radiology 1993 Feb;186(2):395-8.

[2] Launders JH, Cowen AR, Bury RF, Hawkridge P. Towards image quality, beam energy and effective dose optimisation in digital thoracic radiography. Eur Radiol 2001;11(5):870-5.

[3] Samei E, Dobbins JT, III, Lo JY, Tornai MP. A framework for optimising the radiographic technique in digital X-ray imaging. Radiat Prot Dosimetry 2005;114(1-3):220-9.

[4] Doyle P, Martin CJ, Gentle D. Dose-image quality optimisation in digital chest radiography. Radiat Prot Dosimetry 2005;114(1-3):269-72.

[5] Chotas HG, Floyd CE, Jr., Johnson GA, Ravin CE. Quality control phantom for digital chest radiography. Radiology 1997 Jan;202(1):111-6.

[6] Baydush AH, Ghem WC, Floyd CE, Jr. Anthropomorphic versus geometric chest phantoms: a comparison of scatter properties. Med Phys 2000 May;27(5):894-7.

[7] Mah E, Samei E, Peck DJ. Evaluation of a quality control phantom for digital chest radiography. J Appl Clin Med Phys 2001;2(2):90-101.

[8] National Electrical Manufacturers Association (NEMA). Digital Imaging and Communications in Medicine (DICOM) Part 14: Greyscale Display Standard Function. Virginia, US: NEMA; 2004. Report No.: PS 3.14.

[9] Reilly AJ, Sutton D. Spectrum processor. York: The Institute of Physics and Engineering in Medicine; 1997. Report No.: 78.

[10] Hart D, Jones DG, Wall BF. Wall Estimation of effective dose in diagnostic radiology from entrance surface dose and dose-area product measurements. Chilton: National Radiation Protection Board; 1994. Report No.: R262.

[11] Aitchinger H, Dierker J, Joite-Barfus S, Sable M. Radiation Exposure and Image Quality in X-ray Diagnostic Radiology. Berlin: Springer; 2004.

[12] International Commission on Radiation Units and Measurements (ICRU). Tissue Substitutes in Radiation Dosimetry and Measurement. Bethesda, MD: ICRU; 2008.

[13] Jones DG, Wall BF. Organ doses from medical X-ray examinations calculated using Monte Carlo techniques. Chilton: NRPB; 1985. Report No.: R186.

[14] European Commission. European guidelines on quality criteria for diagnostic radiographic images. 1996. Report No.: EUR 16260 EN.

[15] Tingberg A, Herrmann C, Lanhede B, Almen A, Sandborg M, McVey G, et al. Influence of the characteristic curve on the clinical image quality of lumbar spine and chest radiographs. Br J Radiol 2004 Mar;77(915):204-15.

[16] Barten PGJ. Physical model for the Contrast Sensitivity of the human eye. Proc.SPIE [1666], 57-72. 1992.

[17] Samei E, Flynn MJ, Eyler WR. Detection of subtle lung nodules: relative influence of quantum and anatomic noise on chest radiographs. Radiology 1999 Dec;213(3):727-34.

[18] Dobbins JT, III, Rice JJ, Beam CA, Ravin CE. Threshold perception performance with computed and screen-film radiography: implications for chest radiography. Radiology 1992 Apr;183(1):179-87.

[19] O.Nobuhiro. Optimal beam quality for chest computed radiography. Invest.Radiol. 31[3], 126-131. 1996.

[20] Dobbins JT, III, Samei E, Chotas HG, Warp RJ, Baydush AH, Floyd CE, Jr., et al. Chest radiography: optimization of X-ray spectrum for cesium iodide-amorphous silicon flat-panel detector. Radiology 2003 Jan;226(1):221-30.

[21] Lanhede B, Bath M, Kheddache S, Sund P, Bjorneld L, Widell M, et al. The influence of different technique factors on image quality of chest radiographs as evaluated by modified CEC image quality criteria. Br J Radiol 2002 Jan;75(889):38-49.

[22] Sandborg M, McVey G, Dance DR, Alm CG. Schemes for the optimization of chest radiography using a computer model of the patient and x-ray imaging system. Med Phys 2001 Oct;28(10):2007-19.

6 Application of CNR Model

6.1 Introduction

A model to simulate contrast-to-noise ratio (CNR) and figure of merit (FOM) from X-ray spectra data and calculations of absorbed energy was developed. Details of this model are described in the previous chapter with application to digital chest radiography. CNR values were simulated for a geometric chest phantom and adjusted to describe the performance of a particular indirect digital radiographic (IDR) system by inputting data on phosphor sensitivity, the signal transfer function (STF), the choice of scatter removal technique and the automatic exposure control (AEC) responses. The simulated values showed good agreement with results measured from images of a phantom and so provide validation of the calculation methodology. In the present study the model was used with a similar calculation methodology, to investigate optimising exposure factors using thicknesses of patient constituent materials such as muscle, soft tissue, fat and bone, measured from sections of adult computed tomography (CT) scans. CNR and absorbed energy calculations for a range of digital radiographic image receptors commonly used in Radiology departments were investigated and practical suggestions regarding tube potential, filtration options and relative dose levels are made.

The CNR performance of grids and air gaps as methods of scatter reduction for digital radiography were also investigated. Scatter is inevitably generated in a patient in any radiographic examination. As a result image contrast is reduced and scatter acts as an additional noise source. The popularity of grids in screen-film radiography is due to the effective contrast improvement resulting from the grids selective removal of more scatter

than primary radiation. In conventional radiography the cost of the contrast improvement is a corresponding increase in patient exposure which is necessary to compensate for the reduced X-ray fluence reaching the screen-film and thus maintain a diagnostically acceptable optical density range. Grid choice in conventional radiography was therefore a balance between the contrast improvement factor and the Bucky factor, which describes the necessary exposure increase.

With the wide dynamic range and variable gain of digital systems however, the image receptor exposure does not necessarily have to be increased to obtain an image of suitable diagnostic quality [1]. The perceptibility of image details in such a digital image is limited primarily by noise and the effect of scatter reduction methods should therefore be considered according to both the change in radiographic contrast and the noise level, promoting the CNR as a suitable quantity. Considering quantum noise, the largest noise component, CNR values were computed for a range of frequently used grid types and two practical choices of air gap (15 cm and 20 cm). A more comprehensive analysis of scatter reduction methods considering both quantum and system noise for a CsI IDR system was also performed. Data were compared with the ideal grid and practical conclusions on the choice of scatter reduction method for digital systems are made.

6.1.1 Background Theory

The most important factor affecting radiographic contrast and thus imaging performance for the range of tissue attenuations found in standard fluoroscopic and radiographic examinations is the spectral quality of the X-ray beam, determined primarily by the tube potential and the beam filtration. Imaging performance however, is also characterised by the energy response and sensitivity of the image receptor to the incident X-ray beam. The

responses of phosphors used in a range of digital image receptors are explored in this chapter in terms of CNR and photon energy absorbed. To define the context of this application and to highlight the importance of beam quality in imaging performance the basic attenuation and interaction processes and their relative contributions are first briefly reviewed.

6.1.1.1 Photoelectric absorption & Compton scatter

For an X-ray beam incident on an image receptor, there exists three alternatives for each photon: It can penetrate the material without interacting; it can interact with the material and be completely absorbed depositing all its energy; or finally, it can interact and be scattered from its original direction possibly depositing part of its energy [2]. In the formation of a radiological image emphasis must be made on the different mechanisms responsible for the transfer of energy to the image receptor and the production of scattered radiation. The most important of these mechanisms are photoelectric absorption and Compton scattering as they result in the transfer of energy to electrons which then impart that energy to the image receptor [3].

The probability of a particular photon interaction process occurring is usually expressed in terms of the atomic cross section, σ. In the energy region ≤ 100keV the photoelectric effect becomes most important and the following relation is approximately valid.

$$\sigma_{pe} \propto \frac{Z^4}{E^3} \qquad \textbf{Equation 6:1}$$

where σ_{pe} is the interaction cross section per atom for the photoelectric effect, Z is the atomic number and E is the energy of the incident X-rays. The probability of photoelectric

absorption increases rapidly with the atomic number so it produces good contrast between tissues with different elemental compositions.

The atomic cross section for Compton scattering, σ_{ce} may be described by the following expression [2].

$$\sigma_{ce} = \frac{\mu_{ce}}{\rho} . \frac{A}{N_A} \qquad \textbf{Equation 6:2}$$

where, μ_{ce} is the linear attenuation coefficient, A the relative atomic weight (grams/mole), and N_A Avogadro's number (atoms/mole). Unlike photoelectric interactions where the photon is totally absorbed, Compton scattering is an inelastic process in which the X-ray photon losses some of its energy and is deflected from its original path, creating a background of random events or noise that degrades the image. Rearranging equation 6:2, the mass attenuation coefficient for Compton scattering can be expressed in terms of N_A/A or the number of atoms per gram. The probability of Compton scattering is therefore mostly independent of Z or tissue composition and dependent on tissue density, and the overall contribution to radiographic contrast is also relatively independent of photon energy, figure 6:1.

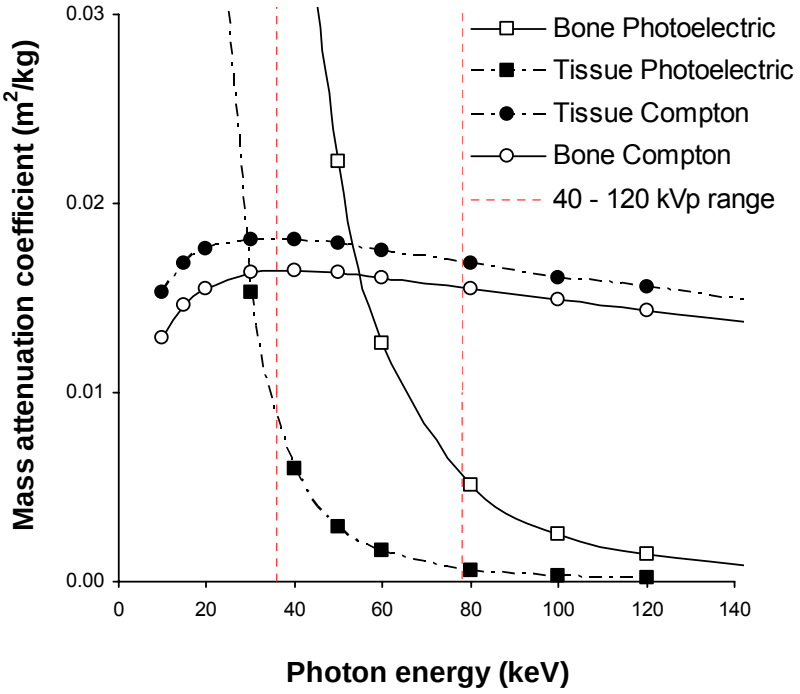

Figure 6:1 Attenuation coefficients for photoelectric absorption and Compton scattering in cortical bone and soft tissue, as a function of photon energy [4]. The mean photon energy range for diagnostic spectra typically used in medical imaging is highlighted in red.

6.2 Methodology

The responses of different image receptors with tube potential and filter options were investigated with the aid of a spreadsheet attenuation model (described in Chapters 5). Data sets consisting of X-ray spectra, mass attenuation coefficients and mass energy absorption coefficients in 1 keV intervals from 1 keV to 150 keV were used [2,4].

The energy absorbed in each image receptor *A(E)* was calculated for the appropriate range of energy intervals using equation 4.1. Data for the phosphors used in the calculations are listed in table 6.1 [5,6].

Table 6:1 Data used in computing energy responses of image receptor phosphors [5,6]

Phosphor	Thickness (μm)	Density (g/cm^3)
Caesium Iodide (CsI)	500	4.51
Selenium (Se)	500	4.25
Gadolinium Oxysulphide (Gd_2O_2S)	200	7.34
Barium Fluro-bromide-iodide ($BaFBr_{85\%}I_{15\%}$)	200	4.8
Barium Fluro-bromide (BaFBr)	200	4.9
Calcium Tungstate (CaWO4)	200	6.06

In order to assess the response of a phosphor to poly-energetic diagnostic X-ray beams (and compare X-rays of different radiation qualities), the absorption must be averaged over all the photons impinging on the image receptor and the sensitivity of each image receptor to diagnostic X-ray beams were calculated using equation 4:2.

Photon fluences were computed using equation 5.1 with data for X-ray spectra at different tube potentials, adjusting for attenuation through different filter materials and tissues and substituting tabulated mass attenuation coefficients [2,4]. Representative thicknesses of the various tissues within the different parts of the chest (lung region), abdomen and pelvis traversed by the X-ray beam were measured from sections of a 'reference' adult whole body CT scan while also inspecting coloured photographs of the transverse regions corresponding to the CT slices. The images were available as part of the Visual Human Project (National Library of Medicine, Bethesda, USA)[7]. The data are given in table 6:2.

Table 6:2 Tissue types and thicknesses used in CNR computations.

Material	Thickness (cm)			
	Lung	Heart	Abdomen	Pelvis
ADIPOSE	3	3	5	5
BONE	1	1.5	1	4
LUNG	4	1.5	0	0
MUSCLE	5	12	10	6
BREAST	1	0	0	0
TISSUE	0.5	0.5	12	12
AIR	14	8	1	1
WATER	0.5	2.5	1	1

Values for the entrance air kerma (EAK) were computed using equation 5:2. The EAK was used to show how dose varies with tube potential for different filtration options and for different representative patient thicknesses and detector types.

CNR values were computed using equation 5.5. The signal of interest is a large (*i.e.* not resolution limited) low contrast feature, so that the effect of the spatial resolution on the system can be neglected. Pixel dimensions of 150 μm were employed in the estimates of N and contrast values were computed for a feature of 2 mm thick muscle as a simulated lesion, within a background of composite materials chosen from table 6:2 for a particular examination. For chest radiography in which different tissues are portrayed in the same image, CNRs have been calculated based on similar levels of air kerma transmitted through the lung field in order to mimic exposures terminated by an automatic exposure control device. For the abdomen and pelvis examinations air kerma level adjustments were made to give a similar system dose as if the AECs were situated behind the abdomen and pelvis respectively.

Image receptor performance relating to both image quality and patient dose can be compared using an image quality figure or figure of merit (FOM). CNR is proportional to $\sqrt{N}$, whereas patient dose is proportional to the no. of photons N, so a FOM that is independent of N and relates solely to differences in radiation quality can be defined as the quotient of CNR^2, divided by a measure of dose (equation 5:9), either the system dose or the effective dose where appropriate, were applied in the calculations. PCXMC Monte Carlo software was used to calculate the effective dose for the range of tube potentials investigated for the chest, abdomen and pelvis examinations (Radiation and Nuclear Safety Authority, Finland).

The performance of grids and air gaps as methods of scatter reduction for digital radiography were investigated by computing values for a contrast-to-noise improvement

factor, CNR_{if}. The contrast to noise improvement factor is the ratio of the CNR obtained with a grid or airgap CNR_{sr} to that obtained without the grid or airgap, $CNR_{p\&s}$,

$$CNR_{if} = \frac{CNR_{sr}}{CNR_{p\&s}} \qquad \textbf{Equation 6:3}$$

Considering the case of an ideal detector and only quantum noise the improvement which the grid or air gap brings to the CNR is equal to the product of the primary radiation transmission T_p and the square root of the Bucky factor, B [8],

$$CNR_{if}^{q} = T_p \times \sqrt{B} \qquad \textbf{Equation 6:4}$$

In the case of real digital radiographic systems there are other noise sources to consider, although all are smaller in magnitude. In which case the total noise amplitude, N_{amp} can be described by the addition of noise equivalent quanta arising from quantum noise only, NEQ_q and noise equivalent quanta arising from system noise, NEQ_s giving the total noise equivalent quanta, NEQ_t [9],

$$N_{amp} = NEQ_q + NEQ_s = NEQ_t \qquad \textbf{Equation 6:5}$$

The total CNR improvement factor including system noise CNR_{if}^{T} can be expressed as [9]

$$CNR_{if}^{T} = CNR_{if}^{q} \times \sqrt{\frac{1 + NEQ_s / NEQ_{q0}}{1 + B \cdot NEQ_s / NEQ_{q0}}} \qquad \textbf{Equation 6:6}$$

where NEQ_{q0} is the total photon fluence of the primary and scattered radiation at the entrance of the grid or air gap after transmission through the patient.

Experimental data collected from the evaluation of CsI radiographic detectors (discussed in Chapter 3) were used to compute the ratio NEQ_s/NEQ_q. DQE is often fundamentally expressed as the ratio of the square of the signal to noise ratio $(SNR_{out})^2$ at

the output of an imaging system to that at the input $(SNR_{in})^2$, where the signal is defined as the signal difference as a fraction of the number of available photons, N [2,10]. CNR is the preferred notation in this thesis (equation 5.5), therefore reserving signal to be defined as simply the mean pixel value in a region of interest of a digital image. NEQ_t is the total noise equivalent quanta arising from quantum and system noise, this is equivalent to the number of X-ray quanta which actually interacts and transfers energy to the imaging system, $(CNR_{out})^2$,

$$DQE = \frac{(CNR_{out})^2}{(CNR_{in})^2} = \frac{NEQ_t}{(CNR_{in})^2} \qquad \textbf{Equation 6:7}$$

The value of NEQ_t was calculated for the CsI radiography systems using the average DQE results presented in figure 3.16 and the energy integrating value of $(CNR_{in})^2$ at 81kVp from table 3.1.

When considering only photon quantum noise DQE is equivalent to the quantum detection efficiency, η (= $1- e^{-\mu(E)d}$, where $\mu(E)$ is the linear attenuation coefficient and d is the thickness of the CsI phosphor) and only the number of photons attenuated are considered, not the transfer of energy to the detector. By substituting η for DQE and NEQ_{q0} for NEQ_t into equation 6:7 and using the photon counting value of $(CNR_{in})^2$ at 81kVp from table 3.1, the value of NEQ_{q0} was calculated. NEQ_s was determined as the last unknown in equation 6:5 and the ratio NEQ_s/NEQ_{q0} was thus obtained.

Air gaps are usually specified by the air gap distance alone. The distance chosen must be great enough to provide an improvement in image quality while remaining within the constraints of acceptable focal spot blurring and geometrical magnification. The physical parameters primary transmission T_p, and selectivity Σ, were calculated for a 15 cm and a 20 cm air gap at a focus to image distance of 180 cm, using a geometrical computation method validated by Sorenson and Floch [11]. According to this model the

scattered radiation behaves as if it originated from a point source located at some distance, *x* from the exit side of object being imaged, towards the focal spot. Sorenson and Floch found that for a wide range of experimental parameters (kVp, SID, object thickness, field size) the distance *x* lies consistently in the range 15 – 20 cm. Using this model an effective scatter point source distance of $x = 17.5$ cm was chosen for this study.

6.3 Results and Discussion

6.3.1 Beam Quality

6.3.1.1 Filtration

X-ray beams used for medical imaging contain photons with a wide range of energies. Figure 6:2 shows typical patient incident X-ray spectra that may be expected to produce a 400 speed equivalent pelvic radiograph with a digital X-ray system at a receptor dose of 3 μGy. Additional filtration with thicknesses of 0.1mm Cu, 0.2mm Cu and 0.2mm Cu and 2mm Al are included for comparison.

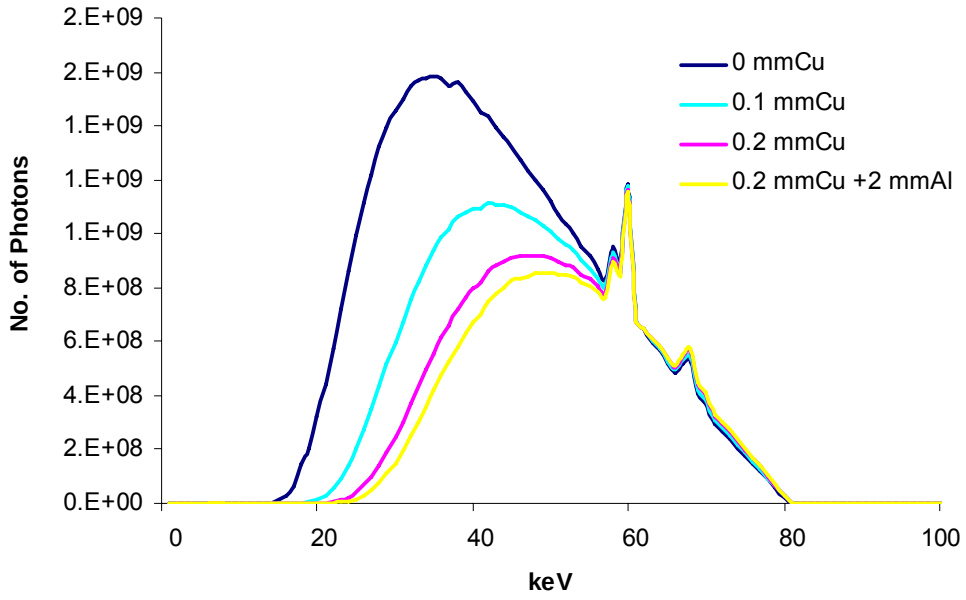

Figure 6:2 Typical patient entrance X-ray spectra for a 400 speed equivalent pelvic radiograph. Additional filtrations of 0.1mm Cu, 0.2mm Cu and 0.2 mm Cu and 2mm Al, commonly used in medical practice are shown. X-ray spectra data includes inherent filtration of 2.5mm Al.

The copper filters are seen to absorb a high proportion of low energy photons (20-50keV). The greater the proportion of photons absorbed however reduces the intensity of the transmitted X-ray beam, particularly at lower energies thus decreasing the skin dose to the patient significantly. X-ray spectra transmitted through a typical patient pelvis (table 6:2), which ultimately impinges on the image receptor to form the image, are shown in figure 6:3 (a). Similar intensities of transmitted X-rays are required for beams with various filters to achieve a similar system dose level or detector air kerma (DAK). However a small but noticeable increase exists in the relative number of photons incident on the detector as the beam filtration is increased. The difference is greater for spectra transmitted through less penetrating areas, for example the lung, figure 6:3 (b).

(a) pelvis examination

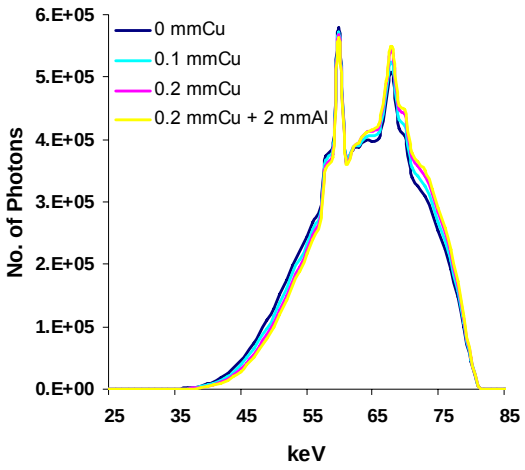

(b) chest examination

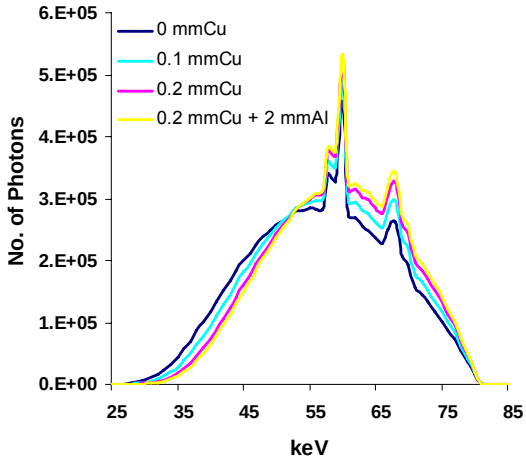

Figure 6:3 Typical X-ray spectra incident on the image receptor to produce a (a) a 400 speed equivalent pelvic radiograph and (b) a 400 speed equivalent chest radiograph. Additional filtrations of 0.1mm Cu, 0.2mm Cu and 0.2mm Cu and 2mm Al, commonly used in medical practice are shown. X-ray spectra data used include inherent filtration of 2.5mm Al.

The relative increase in the mean energy for more heavily filtered X-ray beams and the increase in the number of photons available to interact with the image receptor ultimately affect the quality of the recorded image signal. The small mean energy increase will result in a slight drop in image receptor sensitivity but this is outweighed by the increase in signal *i.e.* the number of photons contributing to the image, particularly when a photon counting quantum limited detector is modelled. The signal improvement can be expressed as an increase in CNR as beam filtration is increased. The rate of decline of CNR with tube potential for more heavily filtered beams is expected to increase, as phosphor sensitivity decreases with increasing mean energy and the relative noise increases with the square root of the number of photons. This behaviour is conveyed in figure 6:4 where the figure of merit (for a constant DAK of 3 μGy with a CsI IDR system) is plotted against tube potential for a 2 mm thick muscle feature in a background of 200 mm water, to approximate a patient abdomen. The increase in FOM with 0.1 mm, 0.2 mm and 0.3 mm

copper filters was 3.3% (maximum at 83 kVp), 6% (maximum at 81 kVp) and 7.7% (maximum at 79 kVp), respectively. The corresponding relative increase in FOM with each additional 0.1 mm filter was thus 3.3%, 2.7% and 1.7% (and expected to fall to 0.3% as the trend continues with 0.4 mm copper added). This is one of the reasons digital radiography systems used in general radiography do not offer more than 0.3 mm copper as available filter options. The choice of filter thickness is also made considering the extra tube loading required to reach the system dose level. The tube output would need to be increased by almost 50% at 80 kVp to provide the necessary DAK to compensate for a filter of 0.2 mm copper. This has an impact on tube lifetime and cost benefit analysis of using additional copper filtration is considered further in Chapter 7.

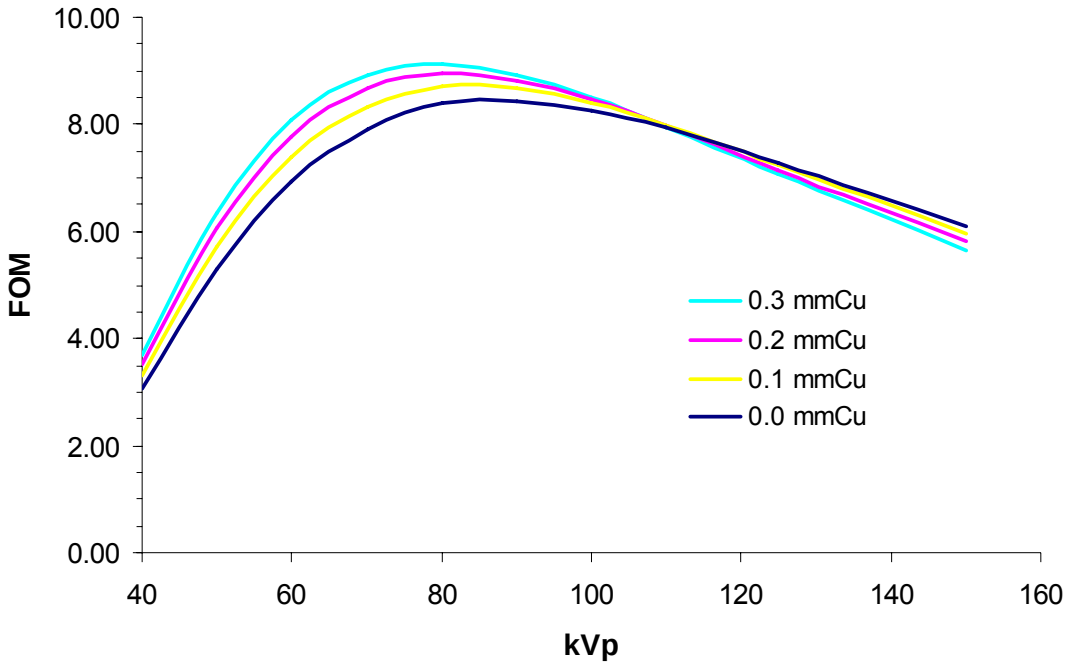

Figure 6:4 Plots of FOM against kVp for various copper filters with a CsI digital radiography system, calculated using a 2 mm thick muscle feature in a background of 200 mm water to approximate a patient abdomen at a 3μGy DAK.

Plotting FOM values against kVp with various phantom thicknesses *eg.* 5 to 40 cm water, and recording the tube potential corresponding to the maximum FOM for each phantom thickness, enables the complete regulation curves to be determined for digital radiography or flat panel fluoroscopy systems (similar to isowatt curves used in modern image intensifiers). Kilovoltage-miliamperesecond-regulation curves were calculated for a CsI IDR system at a 3 μGy dose level, where the FOM for a 2 mm muscle feature was always at a maximum, figure 6:5. The diagonal cross-wise running curves correspond to the kVp and mAs values necessary for a constant system dose using varying phantom thicknesses simulating patient attenuation with 0.0 mm (no dash), 0.1 mm (short dash) and 0.2 mm (long dash) copper and 5 cm, 10 cm, 15 cm, 20cm, 25 cm, 30 cm and 40 cm water. The diagonal cross-wise running curves indicate practically how the exposure factors one must select to drive a digital X-ray system to achieve a constant image receptor dose when presented with various representative patient thicknesses (5 to 40 cm water) and with both standard spectra (2.5 mmAl) and spectra filtered with additional copper, which could be included in an optimisation programme.

The X-ray spectra incident on a 2mm thick muscle detail included with each phantom thickness were filtered with 2.5 mm aluminium and additional thicknesses of 0 mm, 0.1 mm, 0.2 mm, 0.3 mm and 0.9 mm copper filters to show what effect additional filters have on the FOM and thus image quality. For example, the maximum FOM data read from figure 6:4 corresponds in figure 6:5 to the points (87, 9.64); (83, 12.56); (81, 15.62); and (79, 19.36) for CsI 0.0 mm, 0.1 mm, 0.2 mm and 0.3 mm copper respectively, with a phantom attenuation of 20 cm water and 0.0 mm copper. The corresponding mAs values were computed from the CNR model discussed in the methodology and in chapter 5, for a specific X-ray tube for which spectra data were available [2]. Figure 6:5 demonstrates that maximum FOM and thus image quality is achievable by selecting exposure factors which allow the mean photon energies of incident X-ray spectra (kVp's) to match the energy

response of the detector and not simply by just choosing an mAs value, for particular patient thicknesses. Better image quality was achieved at lower tube potentials as the amount of filtration was increased. The relative drop in optimum kV with the addition of the copper filters had the effect of counteracting the drop in sensitivity caused by the beam hardening, as the range of photon energies in the incident spectra were optimised to match the energy response of the CsI detector. Conversely, as the phantom thicknesses were increased the optimum kVp increased also as higher photon energies were required to maintain transmitted X-ray intensities and keep the system dose level constant. A reduction in the tube potential of 10 kVp for example, was necessary to achieve the maximum FOM for X-ray beams filtered with 0.2 mm copper incident on a 20 – 30 cm thick water phantom. However an increase in tube potential, is necessary to maximise the FOM when patient attenuator thickness is increased, the rate of increase depending on the radiation quality of the incident X-rays. A 10 kVp increase was necessary for imaging a 30 cm water phantom relative to one 20 cm thick but for the same phantoms the required increase falls to 8 kVp, 6 kVp and 5 kVp for beams filtered with 0.1 mm, 0.2 mm and 0.3 mm copper, respectively.

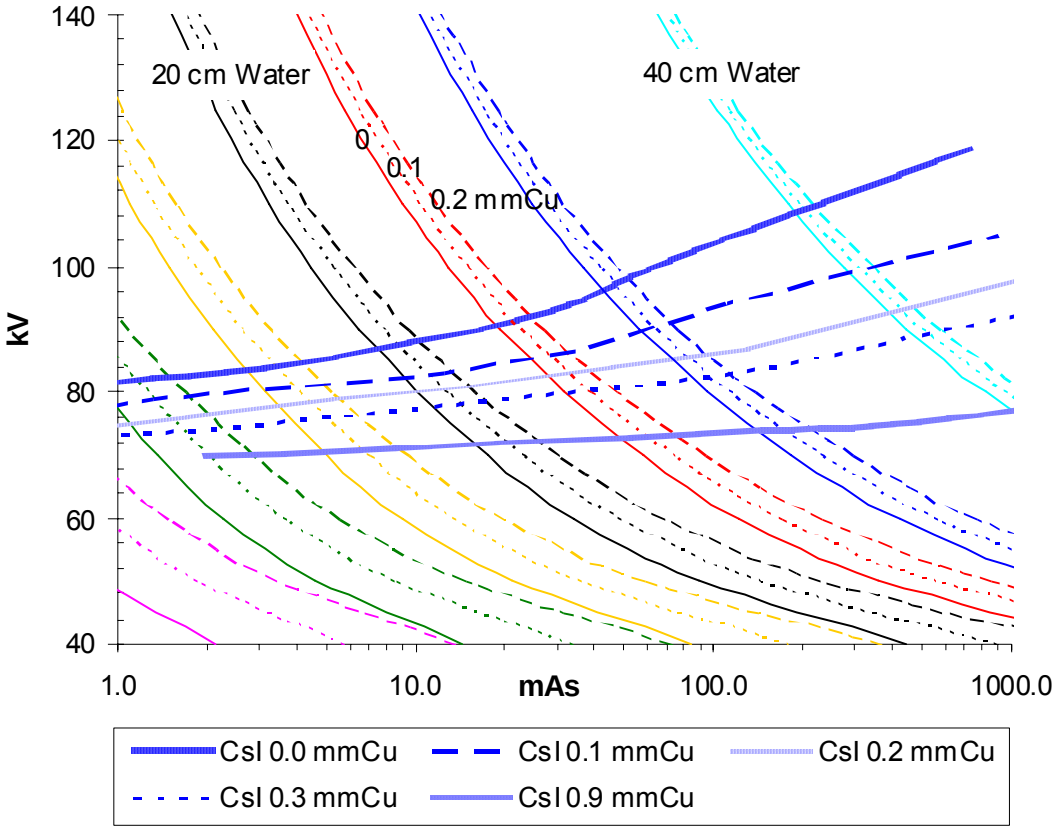

Figure 6:5 Calculated kV-mAs-regulation curves for a CsI radiography system with a selection of copper filtration options, with which the FOM and thus image quality is always at a maximum. Cross wise diagonal curves represent exposure factors to achieve a constant system dose of 3 µGy for various patient attenuators.

An indication of how entrance air kerma for a PA chest examination is expected to vary with tube potential and filter options is shown in figure 6:6, using data from table 6:2. At 75 kVp a reduction of 50% in EAK with a corresponding ~40% reduction in effective dose can be achieved by using 0.2 mm copper. The relative effective dose falls at a slower rate as lower energy photons make a larger contribution to the dose absorbed at the skin surface than that absorbed for deeper organs within the body. In general the effective dose variation with tube potential will depend on the projection examined at the relative position of radio-sensitivity organs in the body.

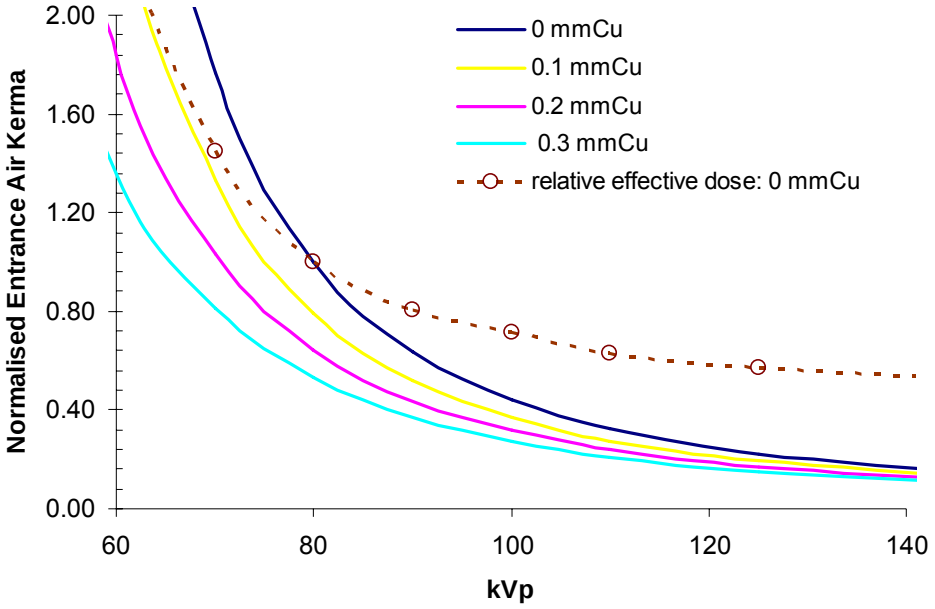

Figure 6:6 Normalised entrance air kerma computations using different copper filter options for a PA chest examination terminated using an AEC device behind the lung. X-ray spectra data used include inherent filtration of 2.5mm Al.

6.3.1.2 Tube Potential

The potential difference applied between the anode and cathode of an X-ray tube will limit the maximum photon energy available and determine the overall shape of the X-ray spectra used for imaging. The optimum potential depends on the thickness of the body part being imaged, the level of radiographic contrast required for diagnosis and the energy response of the image receptor. Consideration must also be given to the effect of tube potential on patient dose. It was mentioned in the previous section that a copper filter of 0.2 mm used in an AP chest examination can achieve a reduction in effective dose by as much as 40%. However similar reductions are possible by increasing the tube potential alone, for example a reduction of 50% in effective dose is possible simply by increasing the tube potential from 70 to 90 kVp, figure 6:6. This also has the advantage of increasing the X-

ray intensity transmitted through the mediastinum but with a trade-off of reduced contrast in the lung field. In this case the optimum kVp will depend on the patient size and requirements necessary for diagnosis but the level of image quality attainable will also be a factor of the energy response and absolute sensitivity of the image receptor used. Figure 6:7 shows how the EAK declines with tube potential for imaging conditions adjusted to give a similar imaging response at each tube potential.

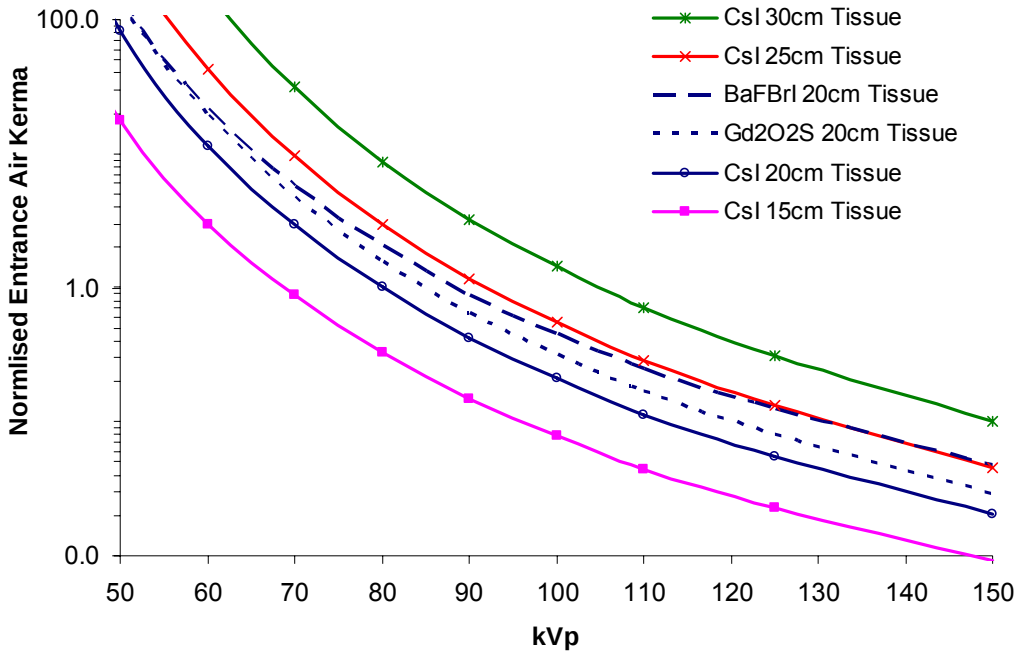

Figure 6:7 Normalised Entrance air kerma as a function of the tube potential with different phosphors, required to give a similar response for imaging a 20 cm thick piece of tissue. Results are also shown for EAK required to obtain images for a CsI detector with different thicknesses of tissue, intended to approximate an abdominal section of the body with patients of various size.

Results are plotted for CR and IDR phosphors for imaging a 20 cm thick piece of tissue, intended to approximate a patient abdomen to show how differences in the energy response and absolute sensitivity translate into patient dose. Results are also shown for 15 cm, 25 cm and 30 cm thick sections for a CsI phosphor to demonstrate the changes in dose

required for imaging different patient sizes. For example, in order to obtain the same image quality in radiographs of an abdomen corresponding to a medium to large patient (30 cm tissue) relative to that required of a small to medium patient (20 cm tissue) one would need to increase the EAK by a factor of ten at 70 kV. However, increasing the tube potential by ten to 80 kVp requires only a more moderate increase of a factor of two in EAK for the same image receptor signal. The optimum solution therefore would be a compromise between increasing tube potential to achieve acceptable patient dose levels while maintaining image contrast to enable clinical diagnosis to be made.

Figure 6:7 also demonstrates the increase in EAK needed to maintain a constant image signal with tube potential for gadolinium oxysulphide (Gd_2O_2S) and barium flurohalide (BaFBrI) image receptors. The comparatively shallower slopes and the relatively greater exposures required to maintain image quality is a direct consequence of their energy response and absolute sensitivity, respectively. Phosphor sensitivity and energy dependence are discussed in more detail in the following section.

6.3.2 Phosphor Sensitivity

6.3.2.1 Absorbed Energy

An important feature of the photoelectric effect is the increase in the probability of an interaction when an incident photon has energy just above the energy required to free a bound electron from its particular atomic shell. This is expressed as a sharp increase in the linear mass attenuation coefficients, referred to as absorption edges, figure 6:8. Absorption edges associated with K shell electrons have important applications as contrast agents in radiology. Consideration of mass attenuation coefficient values must be made when predicting image quality by simulation calculation such as computing CNR values, particularly when the subject for optimisation is a simulated feature or lesion. Figure 6:8

demonstrates how iodine, aluminium and copper have significantly different coefficients and therefore care must be taken if these materials are used to mimic tissue for such simulations. Metal or Iodine features are however useful in practical test objects where empirical data may be collected to help validate simulation models such as the method described in Chapter 5.

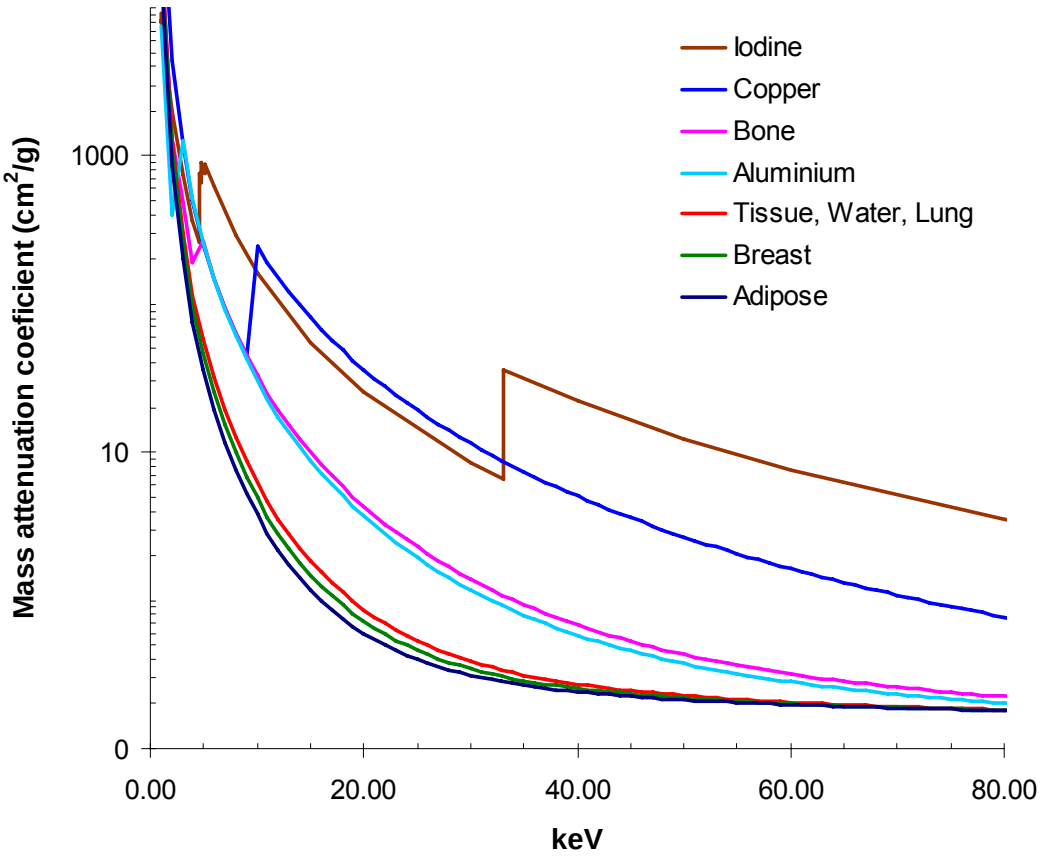

Figure 6:8 Mass attenuation coefficients of various materials, as a function of photon energy.

The K absorption energies for constituent materials play an important role in characterising the response of image receptors with photon energy. The position of the K-edges for digital radiography phosphors are shown in figure 6:9 corresponding to: 35.98 keV (Cs) and 33.2 keV (I) for CsI; 33.2 keV (I) and 37.4 keV (Ba) for BaFBrI and BaFBr; 50.2

keV (Gd) for Gd_2O_2S; 69.5 keV (W) for $CaWO_4$; and 12.5 keV for Se. Absorption edges associated with other outer shell electrons are too low to be of any practical significance.

The variations in sensitivity of digital radiography phosphors with absorbed photon energy are shown in figure 6:10.

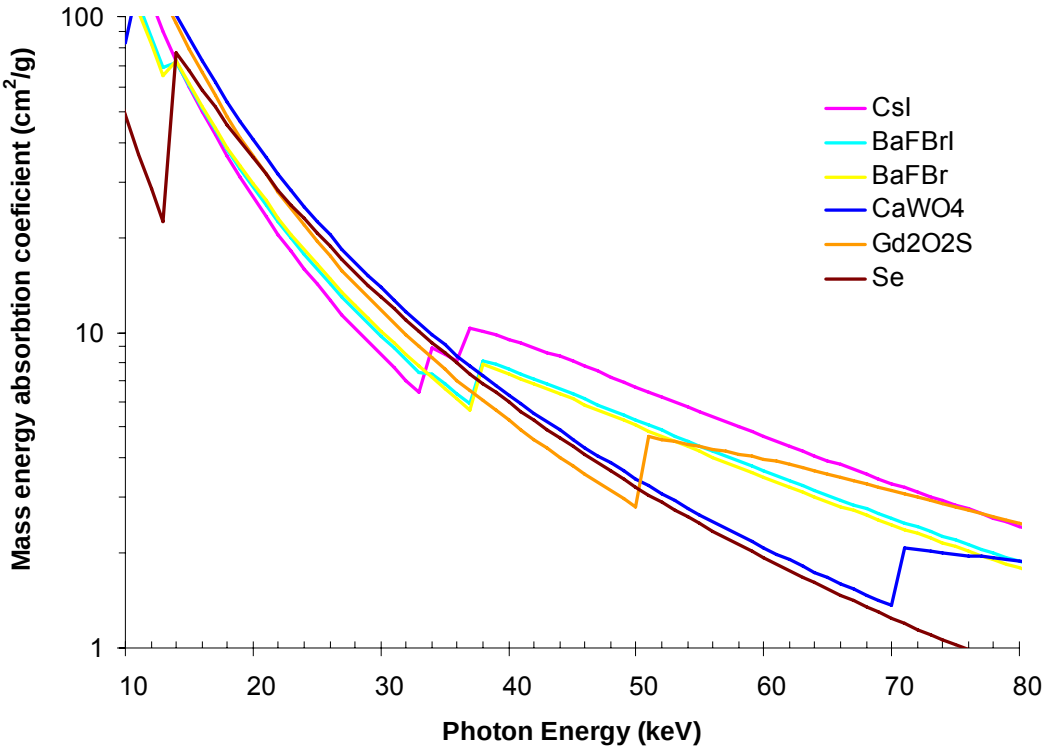

Figure 6:9 Mass energy absorption coefficients for phosphors used in digital radiography, computed using data listed in table 6:1.

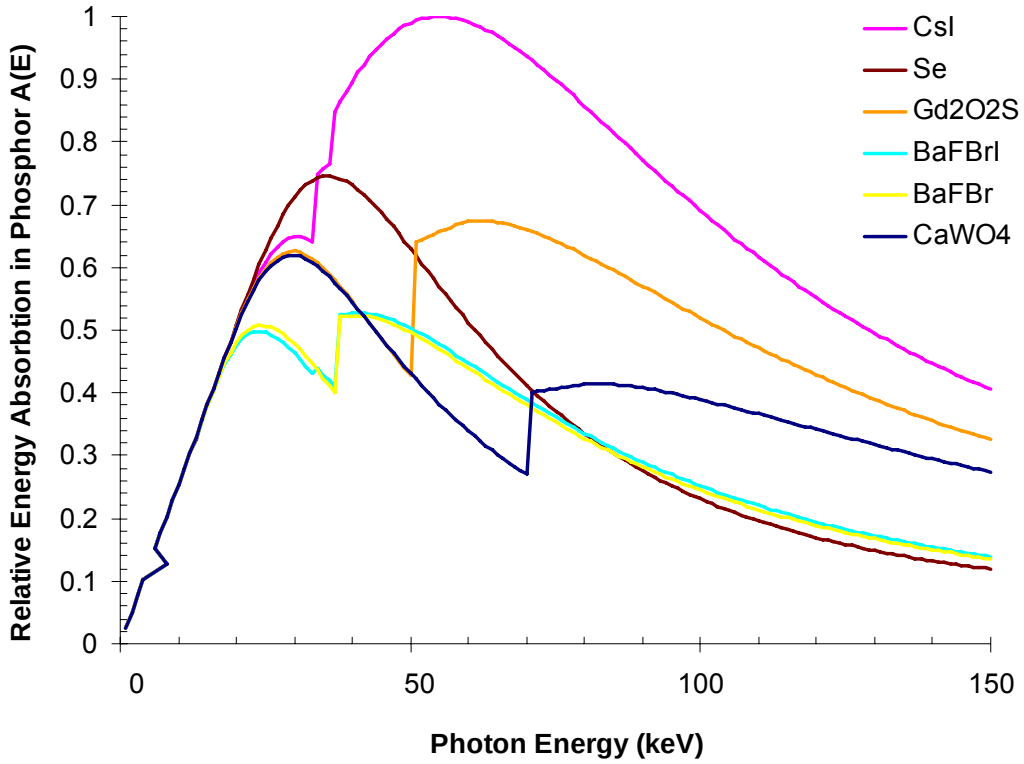

Figure 6:10 Relative energy absorbed in digital radiography phosphors as a function of incident photon energy, computed using data listed in table 6:1.

Relative sensitivities of the same phosphors to X-ray beams corresponding to different tube potentials have been calculated and are portrayed in figure 6:11. The X-ray spectra were corrected for transmission through 2.5 mm aluminium and 200 mm tissue to approximate standard patient attenuation.

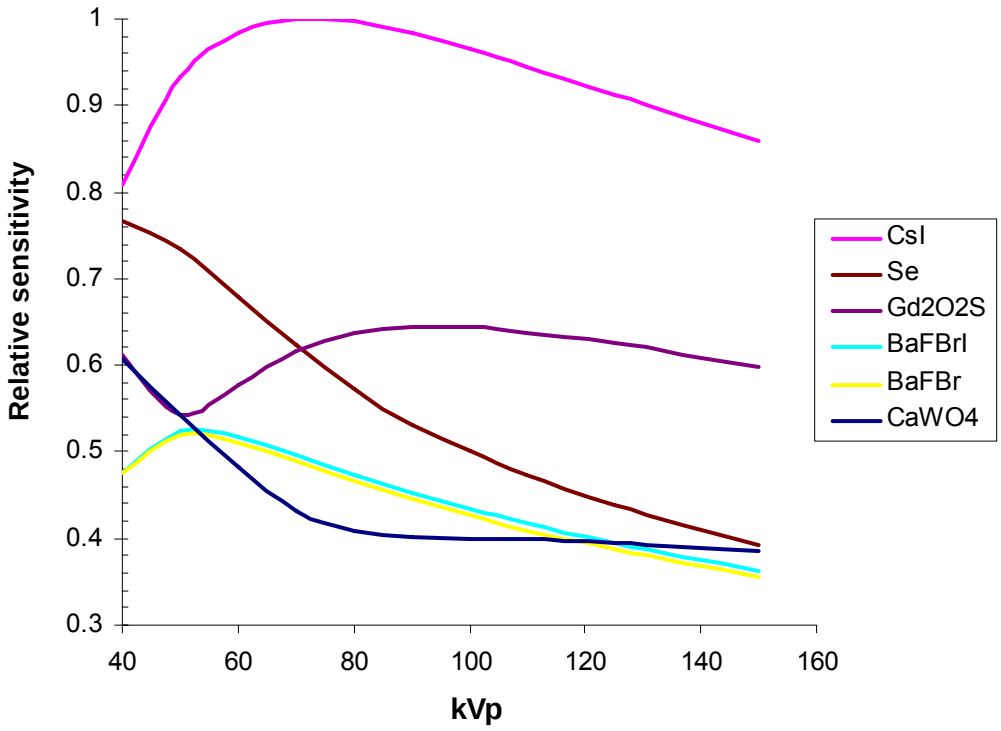

Figure 6:11 Relative phosphor sensitivity as a function of tube potential, for phosphors commonly used in digital radiography, computed using phosphor data listed in table 6:1 and X-ray spectra transmitted through 2.5 mm Al and 200 mm tissue.

Caesium iodide image receptors are significantly more sensitive than the other systems available due to a combination of the relatively large mass attenuation coefficient and the ability to utilise the light guiding character of the CsI needle structure and incorporate a thick phosphor layer. The percentage relative sensitivities of the image receptors averaged over the tube potential range 60 to 125 kVp are: CsI - 97%; Gd_2O_2S - 63%; Se - 55%, BaFBrI - 45%; BaFBr - 46%; and CaWO4 - 42%.

Gadolinium oxysulphide screen-film systems have been successfully used in clinical practice for a relatively long time. Doyle and Martin reported a mean image receptor dose of 2.8 μGy at ten hospitals using 400 speed index screen-film combinations [12]. The sensitivity of indirect digital radiography (IDR) systems is similar to that for the screen-film equivalent. Using the relative sensitivity values computed from figure 6:11, a

mean image receptor dose of 2.8 μGy for Gd_2O_2S suggests approximate dose levels of: 1.8 μGy for CsI; 3.2 μGy for Se; 3.9 μGy for BaFBrI; 3.8 μGy for BaFBrI; and 4.2 μGy for CaWO4.

CsI IDR systems provided by three manufacturers (Philips, Siemens & Cannon) have been successfully set up in hospitals in the West of Scotland and Northern Ireland with image receptor doses of 1.8±0.2 μGy. However larger variations exist for barium flurohalides, the phosphor most widely used in computed radiography (CR). Comparison of the imaging performance of the CR phosphor with Gd_2O_2S, used in screen-film systems suggests an increase in radiation exposure of 30% to 40% to compensate for the lower sensitivity, figure 6:11. However, this is offset by sophisticated image processing techniques, noise reduction algorithms and the better contrast and dynamic range of digital systems, which in the majority of cases allows satisfactory imaging with a CR system employing a similar dose level to that of screen-film systems at 80 kVp, typically 2.5-3 μGy. This approach had been adopted in the West of Scotland and Northern Ireland with satisfactory results for all but one manufacturer, where dose levels up to 4 μGy at 80kVp are required. The higher dose level is needed to compensate for the relatively simpler noise reduction algorithms employed and imaging plate technology that has undergone relatively few generation improvements compared to other CR vendors on the market.

Apart from providing a comparison of the absolute sensitivity levels, figure 6:11 also illustrates a marked difference in the sensitivity trend of the selected image receptors with tube potential. The sensitivity of Gd_2O_2S increases with tube potential by 12% between 60 kVp and 100 kVp, whereas that of the CR phosphors decline by 19% over this range. This change in energy response has important implications for calibrating automatic exposure controls (AECs) for use with digital image receptors. Calibrating AECs for use with digital X-ray image receptors is discussed in detail in Chapter 4.

6.3.2.2 Contrast-to-noise Ratio

There is a great need for a metric which can be calculated theoretically and empirically and can describe gross imaging performance without approaching the constraints implied by the resolution limitations of an imaging system. For large low contrast details, described in Fourier space as having a low spatial frequency, the modulation transfer function of digital imaging systems approaches 100% and assessments of image quality based on such details should therefore be comparable among different digital systems. CNR is the metric of choice in this study and is used to allow both a comparison of digital radiography systems utilising different phosphors and an examination of how each are affected by radiation quality. Values of the CNR have been calculated for a chest examination with data listed in table 6:2 for the lung, heart and abdomen regions. Different thicknesses of tissue feature were used in different parts of the image in order to view the relationships on the same scale. Results are shown for a range of digital radiography phosphors and give an indication of how the visualisation of tissue structure varies in different parts of the chest image and how this changes with tube potential, figures 6:12, 6:13 and 6:14. The chest examination was simulated under the conditions in which the air kerma behind the lung field remained constant, in order to mimic the termination of exposures with an AEC device.

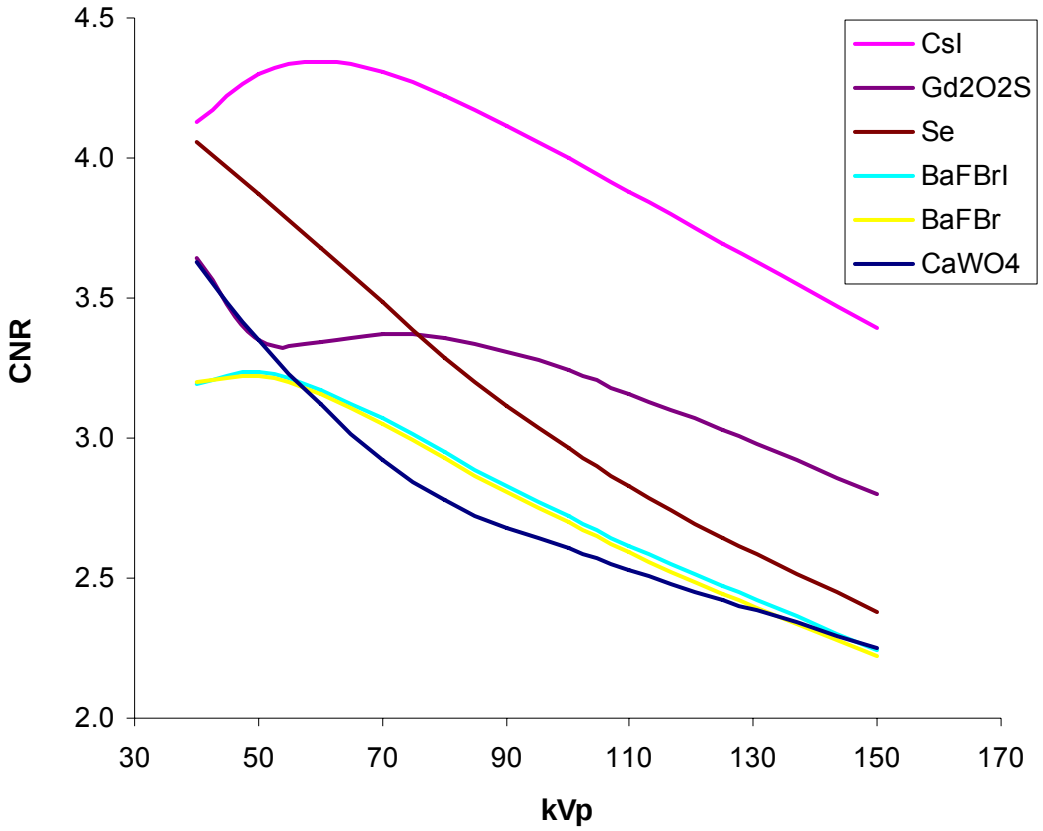

Figure 6:12 Variation in contrast-to-noise ratio with tube potential for a 1 mm muscle feature in the lung region of a chest image, for an exposure terminated by an AEC device behind the lungs. Results are shown for a range of digital radiography systems. Data listed in tables 6:1 and 6:2 were used in the calculations.

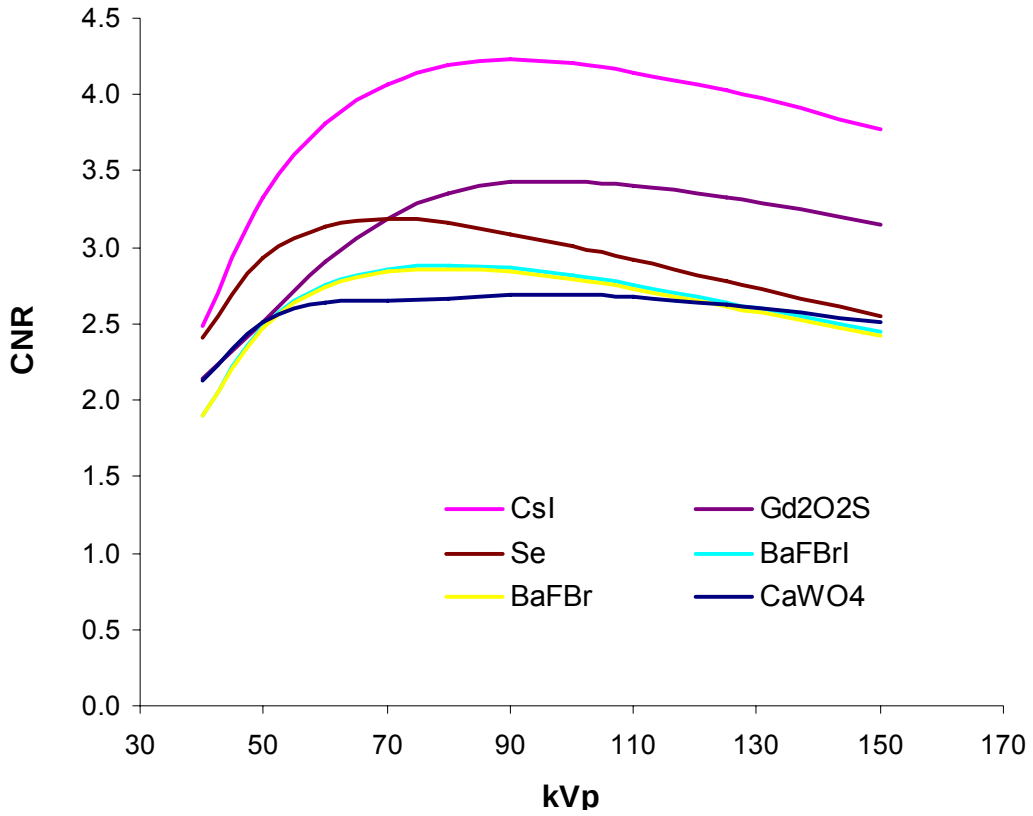

Figure 6:13 Variation in contrast-to-noise ratio with tube potential for a 3 mm muscle feature in the heart region of a chest image, for an exposure terminated by an AEC device behind the lungs. Results are shown for a range of digital radiography systems. Data listed in tables 6:1 and 6:2 were used in the calculations.

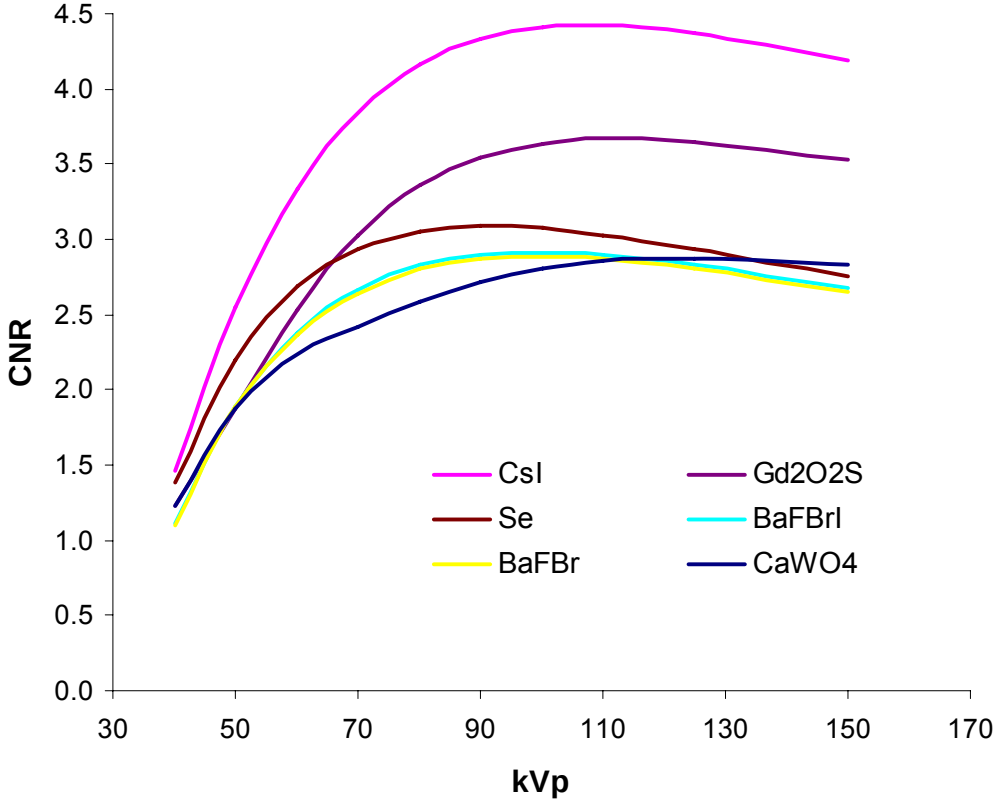

Figure 6:14 Variation in contrast-to-noise ratio with tube potential 5 mm muscle feature in the abdominal region of a chest image, for an exposure terminated by an AEC device behind the lungs. Results are shown for a range of digital radiography systems. Data listed in tables 6:1 and 6:2 were used in the calculations.

There are differences in imaging performance with different phosphors, resulting from the variation in energy response and sensitivity depicted in figure 6:10 and figure 6:11. The CsI phosphor results follow a similar trend to those presented for a chest phantom in Chapter 5. The CNR for the lung declines with tube potential for all of the phosphors studied except gadolinium oxysulphide, in which case it stays approximately constant between 50 and 90 kVp. In practice the noise is not only due to quantum mottle but also has structural and anatomical components (Chapter 3). For lung tissue, for which the number of photons in the image is higher, the anatomic noise may dominate[13]. In the heart and abdominal areas of the chest greater contrast-to noise ratios are achieved at higher tube potentials, 80 – 110kVp for the heart, figure 6:13, and > 90 kVp for the abdominal area, figure 6:14. Although for the selenium and CR phosphors there is a slight reduction in CNR values with increasing kVp in these areas. In practice both high and low kVp techniques are used for chest radiography. With CR 80-90 kV is generally used and this seems a good compromise in maintaining image quality over the entire image. Higher kV techniques are favoured with IDR systems and in the West of Scotland and Northern Ireland 100 -110 kV preferred. Tube potentials are often increased further still however as this is sometimes required to achieve the necessary transmission in the abdominal regions in populations of larger patients.

CNR values were also computed for abdomen and pelvis examinations where in each case simulations were made with the AEC device positioned behind the abdomen and pelvis respectively, as used in clinical practice. The energy response and relative sensitivity of the different phosphors behaved similarly, although the CNR values fell with increasing tube potential at a greater rate. Figure 6:15 shows the results for the pelvis examination. The results are comparable to figure 6:13. The relatively larger gradients seen in the CNR values for the pelvis are the result of beam hardening in examinations with greater tissue attenuation, in which case better sensitivity and thus image quality is

achieved toward lower tube potentials and X-ray spectra with lower mean energies, figure 6:10. Provided of course that the X-ray transmission is high enough to ensure the level of quantum noise and patient dose are acceptable.

A useful application of computing CNR values for different regions of the body is that the reciprocal will determine AEC device settings needed to maintain a constant CNR for a particular examination. Figure 6.16 shows the reciprocal of the CNR result plotted in figure 6.12 and normalised to 80 kVp. The dose required to adjust the AEC at a particular kVp is simply the square root of the CNR increase relative to 80 kV.

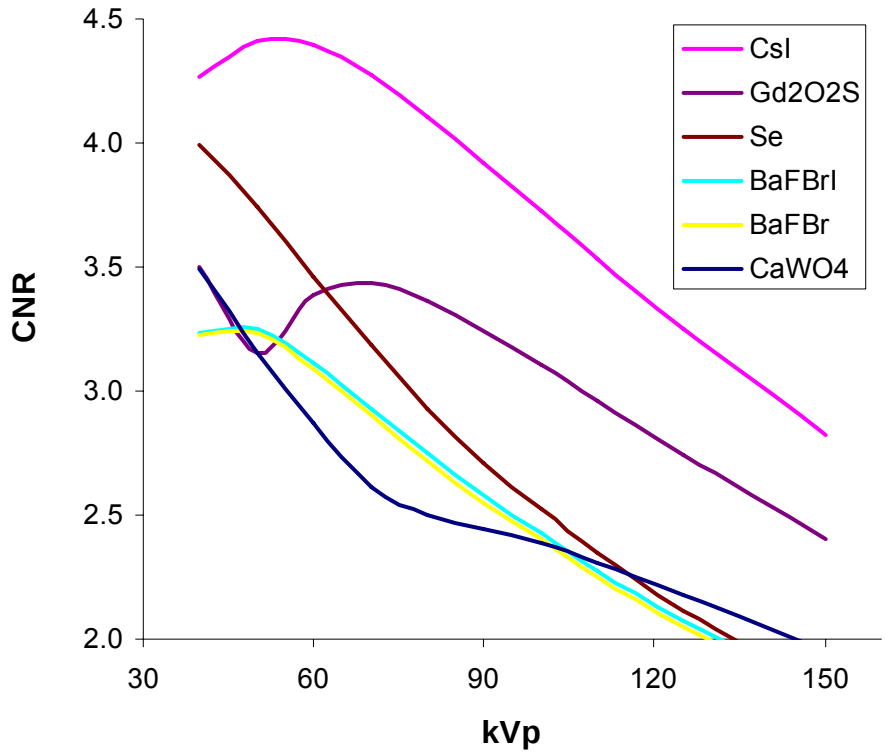

Figure 6:15 Variation in contrast-to-noise ratio with tube potential for a 5 mm muscle feature in the pelvic region, for an exposure terminated by an AEC device behind the pelvis. Results are shown for a range of digital radiography systems. Data listed in tables 6:1 and 6:2 were used in the calculations.

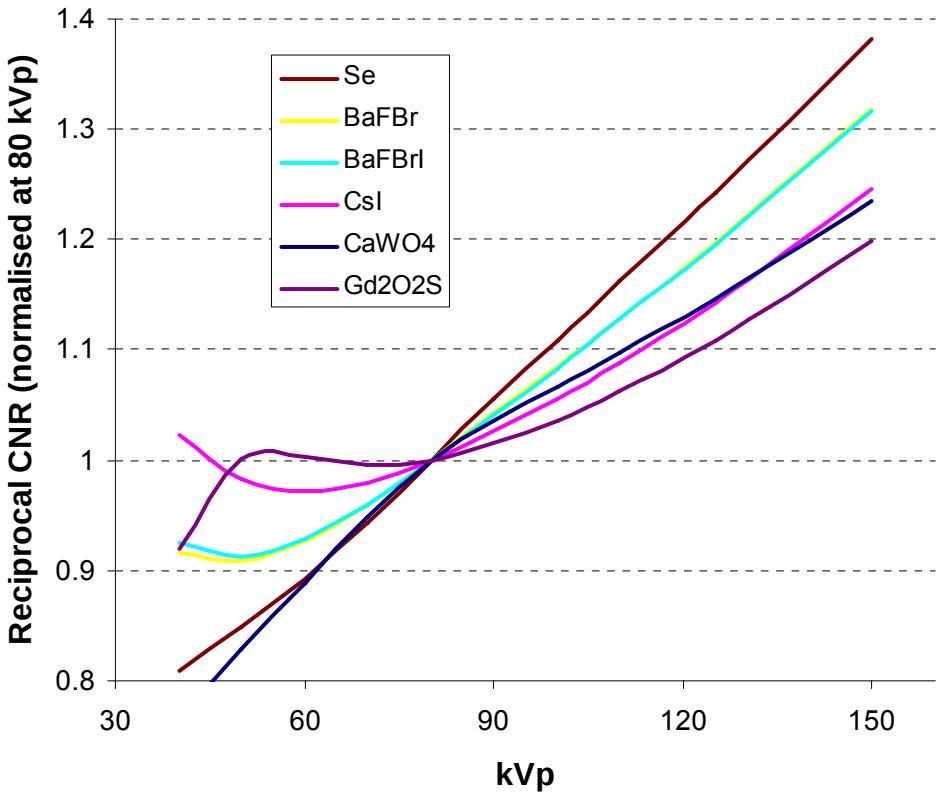

Figure 6:16 Variation in reciprocal CNR with kVp for a 1 mm muscle feature in the chest, for an exposure terminated by an AEC device behind the lung. Results are shown for a range of digital radiography systems. Data are the reciprocal of that shown in figure 6:12.

Similar to results computed for various copper filters in Section 6.3.1.1, calculating FOM values with various phantom thicknesses, enables regulation curves to be determined for different digital radiography systems. KV-mAs-regulation curves were calculated for digital radiography image receptors at a 3 μGy system dose level, where the FOM for a 2 mm muscle feature was always at a maximum, figure 6:17. The diagonal cross-wise running curves correspond to phantom thicknesses of 0.0 mm, 0.1 mm and 0.2 mm copper with 5 cm, 10 cm, 15 cm, 20cm, 25 cm, 30 cm and 40 cm water. The X-ray spectra incident on each phantom thickness was filtered with 2.5 mm aluminium. The optimised exposure factors for the various phosphors are clearly very different. Most surprising are the high tube potentials to achieve the maximum figures of merit with gadolinium oxysulphide phosphors. Although the relatively high position of the k-edge in figure 6:10

and the variation in relative sensitivity in figure 6:12 explains the trend. This behaviour may sometimes be masked in conventional radiography where intensifying screens and optical density values must also be considered. However the increasing sensitivity and reduction in relative dose with increasing kVp is evident in figure 4.4, where a constant optical density is maintained.

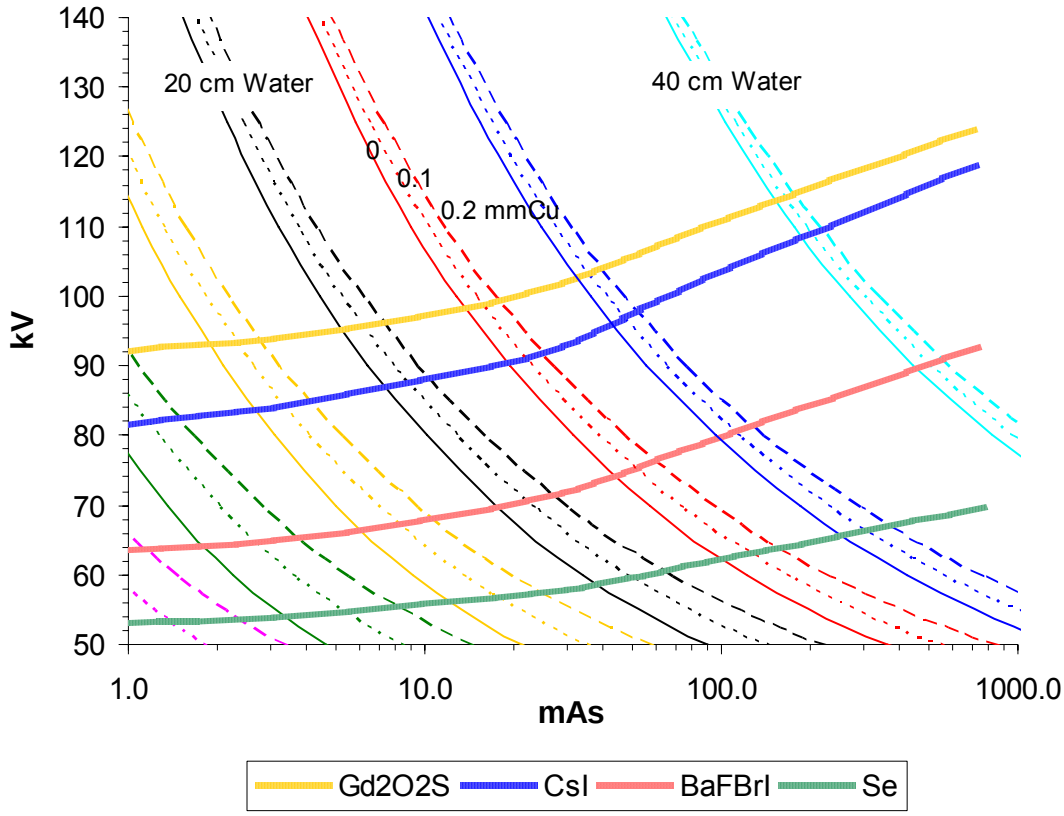

Figure 6:17 Calculated kV-mAs-regulation curves for digital radiography phosphors, with which the FOM is always at a maximum. Cross wise diagonal curves represent exposure factors to achieve a constant system dose of 3 μGy for various patient attenuators.

6.3.3 Scatter Reduction

The results reported up to this point in the chapter relate to the transmitted primary beam and do not take into account scattered radiation reaching the image receptor. They nevertheless allowed us to demonstrate basic relationships between radiation quality, image quality and dose that can be applied in optimisation of digital radiography systems.

The simulations also allowed us to examine the relative differences in energy response of phosphors. In this section results are presented which consider scatter and the principal methods aimed at removing it, use of a grid and air gap.

Figure 6:16 demonstrates the effect of scatter and use of a 15/80 grid (grid ratio 15:1 / strip density 80 lines/cm) on CNR values for simulated chest, abdomen and pelvis examinations with a CR system. CNR values were computed using data listed in table 6:1 and table 6:2 and equations 5:10 and 5:11. Clinical scatter fraction data were available for the lung, abdomen and pelvis examinations at 120 kV, 60 kV and 80kV respectively[2] and these were adjusted for other tube potentials using the scatter factor trends from 15 cm, 20 cm and 25 cm water at a 35 cm x 40 cm field size to approximate each region.

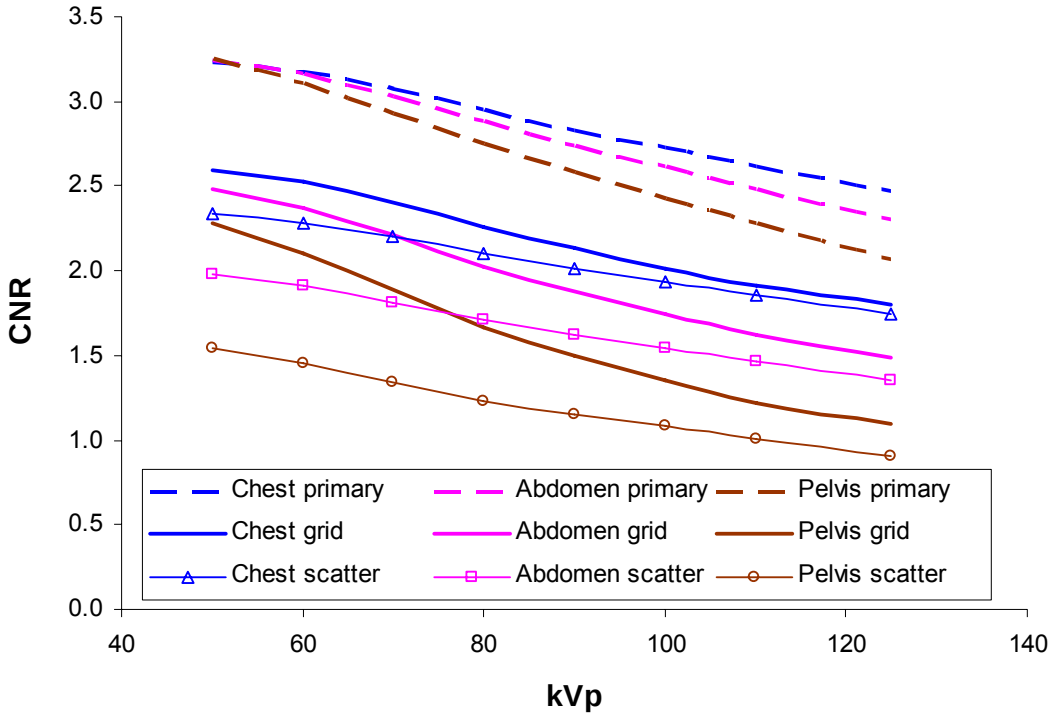

Figure 6:18 Variation of contrast-to-noise ratio with tube potential for a BaFBrI CR phosphor. X-ray spectra were corrected for transmission through the chest, abdomen, and pelvis, table 6:2. Results are presented for primary transmission only, primary and scatter with no grid and primary and scatter with a 15/80 grid.

The improvement in image quality with a 15/80 grid is conveyed as an increase in CNR relative to the data presented which includes scatter with the primary, figure 6:18. CNR values with a grid gradually reduce with increasing tube potential as the levels of scatter increase. As briefly mentioned in the introduction to this chapter, the wide dynamic range and variable gain of digital systems mean that the image receptor exposure does not necessarily have to be increased to obtain an image of suitable diagnostic quality. In conventional radiography increasing exposure levels were required to maintain appropriate optical densities but digital systems are noise limited and not contrast limited. FOM values were calculated for different body parts at a constant system dose of 3μGy with a CR system. Results show the improvement in image quality afforded by use of a 15/80 grid even with the increase in effective dose to the patient required to maintain a constant system dose.

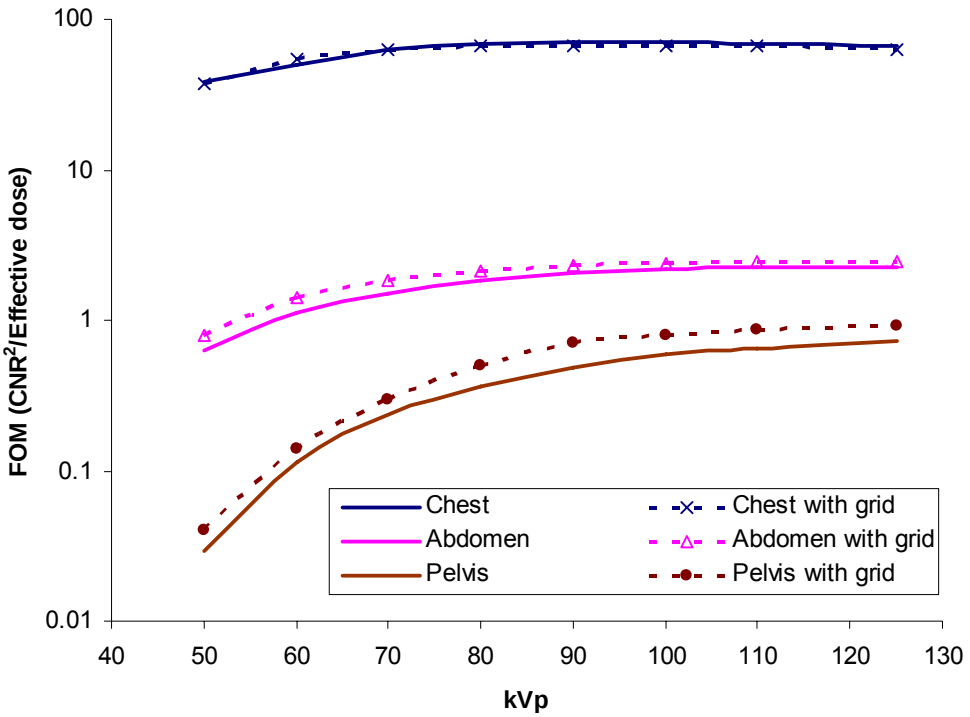

Figure 6:19 FOM as a function of kVp for imaging different body parts. A constant system dose of 3μGy was maintained and the mAs values used to compute the effective dose for the grid data were increased by the grid Bucky factor.

The magnitude of improvement in image quality with a 15/80 grid was greater for areas of the body where there is a greater scatter to primary ratio, figure 6:19. For chest examinations where image quality in the lung is considered paramount, using a 15/80 grid seems to have no measurable advantage. However it must be bourn in mind that scatter fractions can vary strongly from point to point within an image. In a typical chest radiograph scatter fractions of 0.5 in the lung field, 0.8 in the heart region and 0.9 in the abdominal area have been reported [14]. The decision on whether or not to use a grid therefore depends on the imaging requirements across the entire chest image. Figure 6:19 also indicates the improvements in image quality possible when imaging the abdomen and pelvis with a grid.

The improvement in image quality when applying scatter reduction methods with digital radiography systems can be quantified by computing the relative increase in CNR when implementing these methods. This parameter is the contrast-to-noise ratio improvement factor, CNR_{if} (defined by equation 6:3). CNR_{if} values were calculated for a range of grids common in general radiography and paediatrics using published grid data [2] in equation 6:4, Table 6:3. For comparison, results are also shown for a 15 cm and 20 cm air gap, figure 6:20. The physical properties to describe the behaviour of the air gaps were calculated using the inverse square law for values of primary transmission, and the effective scatter point model [9] for values of selectivity.

Table 6:3 Grid data[2] used to compute CNR_{if}

	Grid			Air Gap	
	8/40	17/70	15/80	20 cm	15 cm
Selectivity (Σ)	6.6	13.6	7.8	4.4	3.42
Primary Transmission (Tp)	0.64	0.64	0.74	0.81	0.81

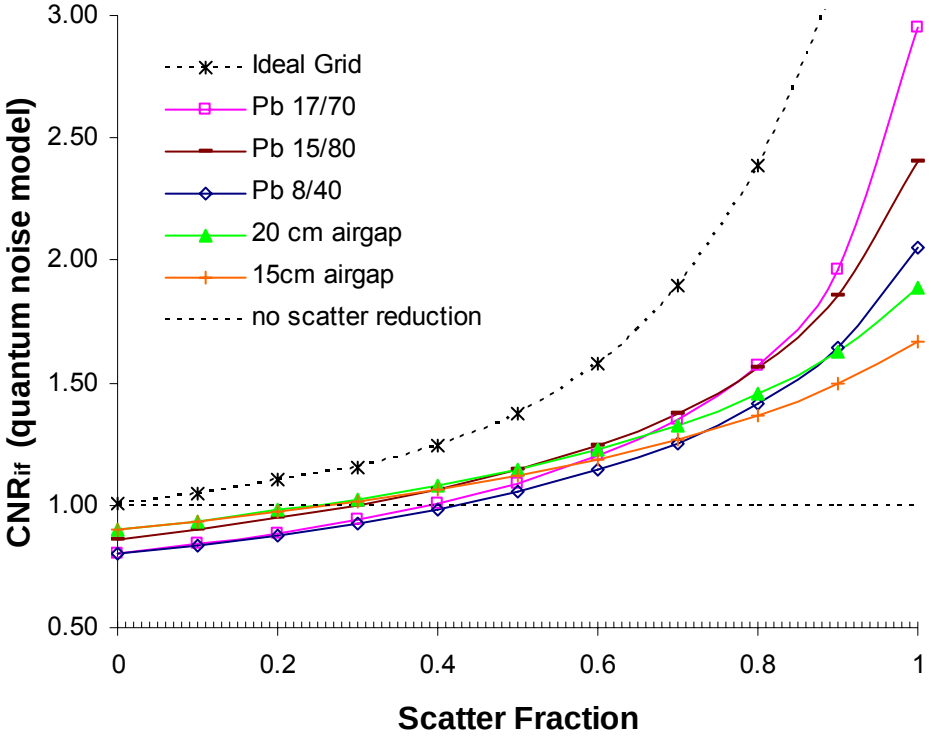

Figure 6:20 Contrast-to-noise ratio improvement factor as a function of scatter fraction for a range of popular scatter reduction methods in general and paediatric radiography. CNR values were computed assuming only quantum noise sources (quantum noise model).

It is evident from figure 6:20 that using a grid or air gap actually reduces image quality where very low scatter fractions are involved (< 0.3). The greater selectivity of grids compared to air gaps provides improved image quality when using grids in situations where the scatter fractions are relatively large (> 0.6). The performance of the air gaps however are better for lower scatter fractions (0.3 - 0.6). Similar results were found in the chest phantom study and are presented in Chapter 5, where the FOM values for lung imaging are higher for the air gap technique and the grid technique was better for imaging the abdomen, figure 5:11.

The case of an ideal detector with quantum noise only is sufficient to model the relative performance of different grid types or air gaps of different thicknesses. To examine the improvement in CNR for a particular digital system to make specific practical recommendations however, requires a more comprehensive noise model as the system noise for the detector in question and not just the number of quanta detected needs consideration [9]. The total CNR_{if} values considering both quantum and system noise for a CsI digital radiography system were calculated using equation 6:6. A value of 0.3 was computed for the ratio NEQ_s/NEQ_{q0}. Results for a selection of grid types and practical air gap distances are shown in figure 6:21 for a CsI radiography system.

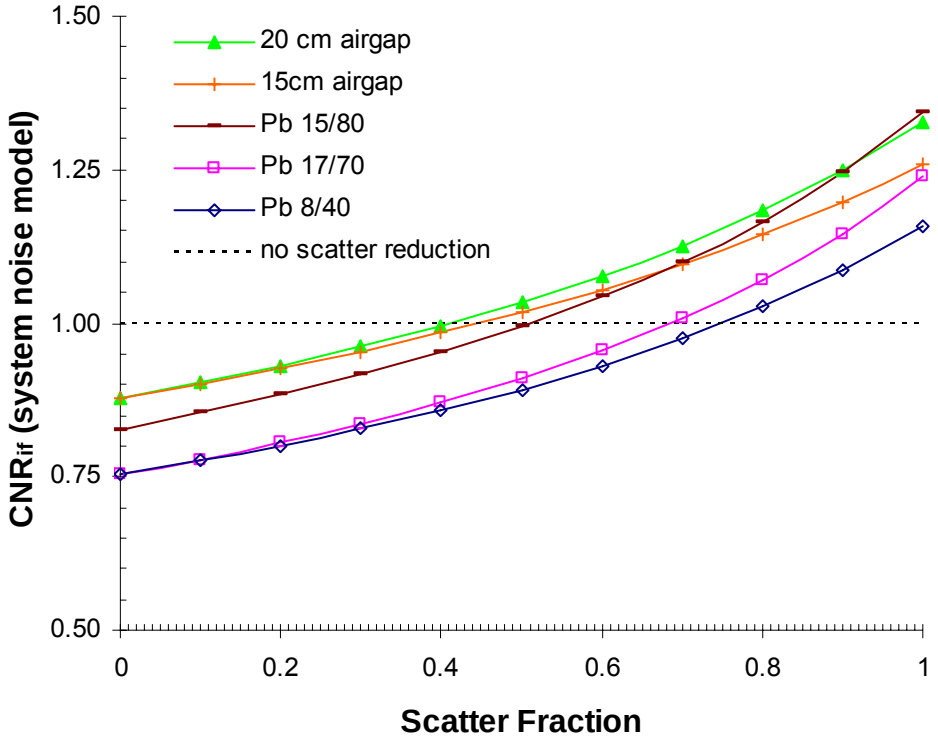

Figure 6:21 Contrast-to-noise ratio improvement factor as a function of scatter fraction for a range of popular scatter reduction methods in general and paediatric radiography. CNR values were computed using both system and quantum noise sources (system noise model) for a CsI detector.

Comparing the curves with figure 6:20 there is a reduction in CNR_{if} when both system and quantum noise are considered. The reduction is more pronounced for scatter reduction

methods with a higher Bucky factor *i.e.* the grids. When incorporating a more complete noise model the performance of a 15 cm and 20 cm air gaps are superior to those of a selection of grid types frequently used in radiography. Similar results were found in a theoretical assessment [9] of a digital system in a study by Neitzel although the data were not corrected for the drop in primary transmission through the extra air gap distance and as a result the air gap data presented were higher than those practically achievable (converging to one for a scatter factor of zero).

6.3.4 Conclusions and Recommendations

Predicting image quality by simulation calculation such as performed in this study can deepen our understanding of image acquisition and image quality parameters and ultimately improve radiologists' performance for detection of lesions in medical images. It can also save on time and resources in the implementation and optimisation of digital radiography systems in the clinical environment. The features of interest optimised in this study consisted of thicknesses of several mm of muscle, as discussion with radiologists indicated such features are most comparable to a lesion, itself being an important and clinically relevant feature in general radiographic examinations of the chest, abdomen and pelvis. However, the spreadsheet model and method outlined are easily adapted to suit other specific clinical examinations, such as use of a blood vessel filled with iodine contrast medium to optimise angiographic procedures or barium for examinations of the digestive tract.

The application and findings of the CNR model discussed in this chapter may be summarised into the following points to form a useful strategy to aid in optimising digital detectors for clinical use:

1. Obtain physical data on image receptor

Six phosphors commonly used in digital X-ray imaging systems were examined in this study, table 6:1. Data on the phosphor thickness and deposition density have a large effect on calculations of absorbed energy and relative sensitivity, equations 4:1, 4:2 and knowledge of the specific data for the particular system examined is a prerequisite in being able to model its behaviour.

When using physical data on image receptors to compare the relative dose efficiency or to assess the expected clinically operational dose levels, consideration also must be given to the 'fill factor' and the phosphor 'packing factor'. The fill factor is the fractional area of a digital radiographic detector which actually contains the sensitive element (photocathode or capacitor), the rest of the detector area contains the readout electronics. Similarly the phosphor layers used in computed radiography (CR) imaging plates are not 100% phosphor but contain a plasticiser to bind the phosphor grains together. The efficiency of CR phosphors are reduced by a phosphor 'packing factor', reflecting the reduction in the mass loading of the phosphor layer. For the detectors examined in this study both factors approach 0.6 [5, 15] and therefore do not affect the relative energy absorption values shown in figure 6:10. However as technology progresses these values are likely to change and verification with the relevant manufacturer that the correct phosphor data is being used is therefore recommended

2. Calculate the phosphor energy absorption, A(E)

The k-absorption edges of phosphors used in radiology vary significantly, figure 6:9 and knowledge of the phosphor type and thickness enables the computation of the

amount of energy absorbed, figure 6:10 and thus allows an assessment of the relative sensitivity and energy response of an image receptor to clinically relevant X-ray spectra, figure 6:11. The sensitivity and energy dependence of phosphors are critical in determining what the optimum exposure factors are likely to be.

3. Compute CNR for clinically relevant feature

For the purpose of this study simulating general radiographic examinations of the chest, abdomen and pelvis, the clinically relevant features were 1 mm, 3 mm and 5 mm thick muscle. Calculating CNR values for clinically relevant features enables an examination of gross imaging performance of changes in radiation quality and energy response without approaching the constraints implied by the resolution limitations of an imaging system. The variation in CNR with tube potential for the lung region of a chest radiograph for example, is shown in figure 6:12. The energy response and optimum tube potential differs significantly for each of the image receptors studied, particularly when the CNR is also used to examine other regions of the same image *i.e.* the heart, figure 6:13 and abdominal areas, figure 6:14 of the chest. The CsI phosphor results show similar trends to those determined empirically with a chest phantom, presented in Chapter 5. The CNR plots allow us to draw useful conclusions regarding the expected clinical operation of the various phosphors. For example 80-90 kVp seems appropriate for CR whereas higher tube potentials of 100-110 kVp are indicated for the CsI IDR system. Better image quality is achievable for pelvic radiographs at lower tube potentials (figure 6:15) however, for gadolinium oxysulphide phosphors 70-80 kVp gives the best image quality.

4. Evaluate extra filtration options

One of the most useful advantages of digital radiography systems is the ability to adjust image contrast, either at image acquisition or display. This frees the imaging system from the constraints affecting the relatively narrower latitude and contrast limited screen/film systems. The reduction in radiographic contrast expected with the addition of metal filters may thus be compensated for in a digital system and the image quality criterion is the level of noise alone. An investigation into whether 0.2 mm copper affects detail detectability for high and low contrast details using receiver operator characteristic (ROC) methodology with a CsI IDR system is described in Chapter 7, no significant difference was found for the phantom studied.

Many digital radiography systems are now commercially available with a number of metal filter options, usually consisting of copper and/or aluminium and particular thicknesses may be automatically pre-programmed for use with specific examinations. Large dose savings can be achieved with additional filtration, for a 75kV chest examination for example, a reduction of 50% in EAK and ~40% in effective dose is possible by using 0.2 mm copper, figure 6:6. Where available, additional filtration options should therefore be evaluated and considered for clinical use, especially for fluoroscopy and paediatrics where deterministic effects and radiation doses are particularly significant.

5. Calibrate AEC to A(E) or constant DDI

The energy responses of digital radiography systems are different than those of screen/film combinations, and require the exposure to be increased at higher tube potentials. At installation, when a digital radiography system is accepted into clinical use, the appropriate kV compensation curve must be selected and adjusted if required.

Various methods of determining the kV compensation curve and absolute dose level required to calibrate AEC devices for DR and CR systems are discussed in detail in Chapter 4. It is also possible to determine AEC calibration curves for a specific clinical task to maximise the CNR values at each kVp, figure 6:16. Care must be exercised if adopting this approach however as the system may only be optimised to provide maximum image quality for the specific feature used to compute the CNR *e.g* 2 mm muscle, which may not be indicative of radiographic image quality for alternative examinations.

6. Review scatter removal requirements and technique

Scatter is inevitably generated in a patient in any radiographic examination. As a result radiographic contrast is reduced and scatter acts as an additional noise source. As mentioned in Section 6.1, the choice of scatter removal technique in conventional radiography was a balance between the contrast improvement afforded, C_{if} and the necessary exposure increase or Bucky factor, B. C_{if} is proportional to B and the constant of proportionality for a given exposure condition is the grid / air gap primary transmission T_p. In digital imaging where both the radiographic contrast and the noise level need to be considered, any improvement in image quality by a grid or air gap is more appropriately evaluated using measures of how both contrast and noise change, for example the contrast-to-noise ratio improvement factor, CNR_{if}. For a given exposure condition, CNR_{if} is proportional to $\sqrt{B}$ (equation 6:3) and therefore has - relative to C_{if} and contrast limited screen/film systems - less dependence on the Bucky factor and more emphasis on the primary transmission T_p. Since air gaps do not absorb primary quanta they have inherently better signal transfer with higher T_p values than grids, although they have comparatively lower selectivity. This gives air gaps the

advantage with mid-to-low scatter fractions (0.6 – 0.3) with grids remaining the better choice of scatter removal technique for larger scatter fractions > 0.6, figure 6:20.

Depending on the exposure conditions (geometry, kVp, filtration) the requirements of the technique used to remove scatter will need to be reviewed for digital radiography. Whether or not scatter removal is even necessary also needs consideration as depending on the scatter fractions involved, image quality may in fact be degraded and worse than using no scatter reduction method, figures 6:20 and 6:21.

More in depth analysis of the improvements in image quality achievable with grids and air gaps may be performed taking into account the effect of both quantum and system noise (equations 6:6, 6:7) although the analysis requires the availability of detailed NPS and DQE data for the detector under study (Chapter 3). Comparing the results of this model, figure 6:20 with those of the simple quantum model figure 6:16, however allows the same general conclusions. Both models suggest improved performance for air gaps over grids for medium to low scatter factors and both models suggest the best choice of grid for digital systems is the 15/80 grid, achieving comparable or better performance than air gaps for high scatter factors. Calculations using grid technical performance data and equation 6:4 should therefore prove useful in evaluating new or existing scatter removal methods for digital systems and indicate if improvements can be made or further investigation is needed.

7. Use A(E), CNR and FOM data to review exposure factors

In the UK and in many other European countries when digital radiography systems are first installed in a clinical environment the existing exposure factors (usually from the previous conventional radiography techniques using screen/film) are adopted. The rational is that this will allow radiographers and day to day users of the system more

latitude in coming to terms with the new technology and steep learning curve. This approach helps to provide a relatively smooth transition and supplies the radiologists with images that are similar to those they are used to reporting, images from a high kVp chest technique with a grid for example look significantly different to those acquired at lower tube potentials. The manufacturers' software or applications specialist then usually pays a return visit to the clinical site some months later to give selected 'key' users of the system more advanced training and to address any image quality issues, if required. The disadvantage in this approach is that if image quality is considered acceptable, then no changes are made and the exposure factors as used conventionally remain in use. The situation is unlikely to change unless a survey of patient doses highlights a particular examination as requiring further investigation. It does not however gauge if the digital system is operating most effectively with maximum image quality and full use of its features.

Simulations of CNR, FOM and A(E) of the type presented in this study provide a useful starting point and an indicator as to what to expect from digital radiography systems, even before they are installed clinically and allow general conclusions to be drawn on what tube potentials and relative dose levels are likely to be optimum. Two different Canon IDR systems for example are installed in one hospital in the West of Scotland, one is a 43 cm x 43 cm CXDI 40C which is a CsI:Tl detector ~600 μm thick the other detector is a 43 cm x 43 cm CXDI 40G which has the same 160 μm pixel pitch but the image receptor is Gd_2O_2S:Tb ~ 200 μm thick. The relatively higher sensitivity of the CsI system in this case allows for lower exposure factors to be used however examinations are performed at similar tube potentials. General Electric also have a number of IDR systems in the West of Scotland whereby some use Gd_2O_2S:Tb phosphors and some use CsI.

kV-mA regulation curves have proved very useful for setting up and adjusting the automatic brightness control on image intensifiers (which also use CsI phosphors albeit with sodium rather than thallium doping). Knowledge of the phosphor efficiency decrease with age allows the gradients of these curves to be adjusted at service visits to provide optimal image quality for a range of patient thicknesses, field sizes and filtrations. Similar curves may be produced with X-ray spectra data and spreadsheet software using the method discussed in this study. Figure 6:17 gave an example of regulation curves for common CR and DR phosphors where FOM is always at a maximum. As mentioned in the discussion, the optimum tube potential for Gd_2O_2S phosphors were unexpectedly high as the need for acceptable contrast, among other factors, kept the tube potentials down when the phosphor was used in conventional radiography. Optimum tube potentials of 80-110 kVp for CsI detectors were probably expected. Selenium detectors were initially marketed by Eastman Kodak as part of their DirectView DR range but the company have recently moved to CsI phosphors and Se detectors for general radiography are relatively uncommon in the UK. The optimum tube potential for the CR phosphor was lower than expected where 70 kVp was optimum for a 2 mm muscle feature in a water phantom of standard 20 cm thickness.

8. Survey patient doses, set DDI ranges and identify specific system attributes

Clinical efficiency and effectiveness in radiology is maximised when the best image quality achievable and appropriate available features are utilised for the existing digital radiography equipment. Practical optimisation in a radiology department however, is generally a balance between time and cost resources available (helped by the amount of interest and support in the local department) and the magnitude of the previous patient dose survey results for standard examinations or levels of satisfaction

with current image quality. When new digital equipment is installed it is useful to work with the manufacturers' application specialist (possibly attending application specialis training sessions, particularly useful for interventional and cardiology suites) to familiarise oneself with specific system attributes and image processing options available *e.g.* grid suppression, post-processing options. AEC calibration and review of available filter options and scatter reduction methods should be performed as soon as possible. A survey of patient doses using a representative sample of patient size and examination type should be performed after the equipment is installation process has completed. It is useful to review results of similar equipment at other centres. Technical data for digital systems is often easier to obtain at the tender response stage of procuring digital radiography equipment. Following the outcome of the patient dose survey steps 4, 5, 6 or 7 may need review. Setting DDI ranges is recommend by some manufacturers however unless this is performed automatically or is frequently updated it may be more useful and reproducible to record representative dose-area-product values (see Appendix Chapter 4).

6.4 References

[1] Chan HP, Lam KL, Wu YZ. Studies of performance of antiscatter grids in digital radiography: effect on signal-to-noise ratio. Med Phys 1990 Jul;17(4):655-64.

[2] Aitchinger H, Dierker J, Joite-Barfus S, Sable M. Radiation Exposure and Image Quality in X-ray Diagnostic Radiology. Berlin: Springer; 2004.

[3] Medical Science Series: Physics for Diagnostic Radiology. second ed. Bristol, UK: Institute of Physics Publishing; 1999.

[4] International Commission on Radiation Units and Measurements (ICRU). Tissue Substitutes in Radiation Dosimetry and Measurement. Bethesda, MD: ICRU; 2008.

[5] L.W.Goldman, M.V.Yester. Specifications, performance evaluations, and quality assurance of radiographic and fluoroscopic systems in the digital era. Wisconsin, US: Medical Physics Publishing; 2004. Report No.: 30.

[6] Rowlands JA. The physics of computed radiography. Phys Med Biol 2002 Dec 7;47(23):R123-R166.

[7] The Visual Human Project.
http://www.nlm.nih.gov/research/visible/visible_human.html . 2-12-2008.
Ref Type: Internet Communication

[8] Chan HP, Lam KL, Wu YZ. Studies of performance of antiscatter grids in digital radiography: effect on signal-to-noise ratio. Med Phys 1990 Jul;17(4):655-64.

[9] Neitzel U. Grids or air gaps for scatter reduction in digital radiography: a model calculation. Med Phys 1992 Mar;19(2):475-81.

[10] International Electrotechnical Commission. Medical electrical equipment: characteristics of digital X-ray imaging devices - part 1: determination of the detective quantum efficiency. Geneva, Switzerland: IEC; 2003. Report No.: 62220-1.

[11] Sorenson JA, Floch J. Scatter rejection by air gaps: an empirical model. Med Phys 1985 May;12(3):308-16.

[12] Doyle P, Martin CJ. Calibrating automatic exposure control devices for digital radiography. Phys Med Biol 2006 Nov 7;51(21):5475-85.

[13] Samei E, Flynn MJ, Eyler WR. Detection of subtle lung nodules: relative influence of quantum and anatomic noise on chest radiographs. Radiology 1999 Dec;213(3):727-34.

[14] Niklason LT, Sorenson JA, Nelson JA. Scattered radiation in chest radiography. Med Phys 1981 Sep;8(5):677-81.

[15] Ogawa E., Arakawa S., Ishida M., Kato H. Quantitative analysis of imaging performance for computed radiography systems. Proc.SPIE 4682, 421-431. 1996. Ref Type: Journal (Full)

7 ROC Study

7.1 Introduction

7.1.1 Study Objective

In Chapter 5 both experimental measurements and theoretical computations of contrast-to-noise ratio using a chest phantom, suggest the addition of 0.2 mm of copper filtration will have a negligible effect on image quality. The analysis however was only indicative, as the limited number of details and range of detail sizes available in the chest phantom allowed. The aim of this study is to use ROC methodology on image data obtained with the same X-ray detector, to include the observer in the imaging chain and examine the effect of additional copper filtration on image quality to include both detector and observer performance, to include a wider range of detail sizes and contrasts.

7.1.2 Background theory of ROC Methodology

Although some diagnoses are more complex, a basic classification tool in medicine is the binary test which yields two discrete results (e.g. positive and negative), to infer an unknown, such as whether a disease is present or absent. In radiological imaging a diagnostic test looks for a particular 'signal', however defined, and attempts to ignore or reject other events, which are called 'noise'. The discrimination is not made perfectly because noise events may mimic signal events. Observations of noise alone events and noise plus signal events produce values of a decision variable that may be assumed to vary

from one occasion to another, with overlapping distributions of the values associated with the two classes of events. Modern detection theory treats the problem as one of distinguishing between two statistical hypotheses[1]. A diagnostic test can therefore be thought of as a means to separate a population into two subsets one where the disease is present, and one where it is absent. The accuracy of these tests is commonly assessed using measures of sensitivity *SN* and specificity *SP*, where

$$SN = \frac{TP}{TP + FN} \text{ and,} \qquad \textbf{Equation 7:1}$$

$$SP = \frac{TN}{FP + TN}, \qquad \textbf{Equation 7:2}$$

TP, *TN*, *FP*, and *FN* are the counts of true positives, true negatives, false positives, and false negatives, respectively.

From equation 7:1, the sensitivity depends only on *TP* and *FN i.e.* measurements of diseased subjects, similarly specificity as defined in equation (2) depends only on healthy subjects (*TN* and *FP*), and so neither one depends on the prevalence of disease in the test population. For this reason sensitivity and specificity are more popular measures of diagnostic test accuracy than measures such as percentage of correct diagnoses etc.[2]

With two alternative events and two corresponding diagnostic alternatives, the data are those of a two-by-two decision matrix[3], table 7:1. The event is considered to be positive or negative, and the diagnosis made is correspondingly positive or negative. Therefore there are two correct outcomes *TP* and *TN* and there are two ways in which the actual event and the diagnosis can disagree *i.e.* two kinds of errors, *FP* and *FN*. Data from a diagnostic test consist of observed frequencies from those four possible outcomes.

Table 7:1 Decision matrix for two events and two diagnostic alternatives.

	Event	
Diagnosis	Positive	Negative
Positive	*TP*	*FP*
Negative	*FN*	*TN*
Total	*TP* + *FN*	*FP* + *TN*

It should be noted that in light of a positive event, the diagnosis is either positive or negative and the proportions of positive and negative diagnosis, $TP/(TP+FN)$ and $FN/(TP+FN)$ sum to 1. Likewise for a negative event the *FP* and *TN* fractions are complements. Therefore in a test of a diagnostic system all the relevant information with regard to accuracy can be obtained by recording the fractions *TP* or *FN* and either *FP* or *TN*. The most popular choices[1] are to record the top row in table 1, *i.e* the true positive fraction *TP* (= *SN*, equation 7:1) and the false positive fraction *FP* (=1-*SP*, equation 7:2). These form the basis of accuracy measures of diagnostic tests and are fundamental to producing receiver operating characteristic (ROC) curves where (1- specificity) and the sensitivity form the X and Y axes respectively.

When the results of a test are binary such as the presence or absence of disease, then the test has only one pair of sensitivity and specificity values. However in many diagnostic situations making a decision in binary mode is difficult, impractical or clinically unrealistic. The diagnostic confidence levels or decision criteria to interpret radiological images may vary considerably among observers. Radiologists can differ in their estimates of prior probabilities and of costs and benefits and so adopt different criteria[1]. As the decision criterion becomes more lax for example, the sensitivity increases while the

specificity decreases, and vice versa. As a result a single pair of sensitivity and specificity values is insufficient to describe the full range of diagnostic performance of a test[2].

ROC methodology was derived to deal with multiple pairs of sensitivity and specificity values. Better decision performance is indicated by ROC curves that lie higher in the unit square (toward the top left), figure 7:4. The curve itself represents all the compromises between sensitivity and specificity that can be achieved by a diagnostic system as the decision criterion or confidence threshold is varied, therefore defining a measure of accuracy that is independent of both the prevalence of disease and of the decision criterion to adopt a positive diagnosis[4]. Each discrete point on the graph (or operating point) is generated by using different confidence thresholds for a positive test result.

In medical imaging the operating points are usually generated using one of two main experimental approaches[5]. In the first approach the observer is required to view sequential images and give a binary response as either yes / no (positive or negative) for each image. The images are then reread on several occasions with the reader motivated to give a stricter or a more lenient confidence threshold. The observer's responses for each occasion are then compared with the truth, thus forming *TP* and *FP* pairs, each of which is plotted as a point in the unit square. This approach follows the concept of ROC methodology but it is experimentally inefficient requiring each observer to read the images N times to generate N points on the ROC curve.

In the second approach to generating operating points the observer is required to comment using different levels of confidence to report his/her impression of the state of truth, for example on whether a suspected lesion is present or not. The categories are usually given quantitative labels such as: (1) definitely present; (2) probably present; (3) possibly absent; (4) probably absent; and (5) definitely absent. It is not necessary for

different observers to interpret the ratings categories the same way[4]. To help reduce bias in the results (and avoid data degeneracy) it is however useful to select the ratings to generate *TP* and *FP* pairs that help stratify the operating points uniformly along the ROC curve *i.e* choosing the categories with roughly the same frequency if the disease prevalence was ~ 50%[6].

The idea behind the ratings method is shown schematically in figure 7:1. The vertical lines represent the four confidence thresholds that define the boundaries between the five ratings categories described above. To compute the operational points to plot the ROC curve we use the ratings responses to establish an equivalent response as if the test were a binary test (similar to the first approach). For example, a rating of (5) definitely absent, represents a 'yes' or positive response in a 'yes/no' experiment whereby the observer adopts a very strict confidence threshold; and we can interpret cases with any other rating as those equivalent to a no or negative response in that experiment. We can then analyze the rating data to calculate a TP and FP pair, *i.e* one operational point on the ROC curve. A second point on the curve may be computed by summing the responses from categories (4) and (5) for example and calling them positive (equivalent to a 'yes' response in 'yes/no' experiment). Third and fourth points are calculated similarly, and thus we have 4 operational points derived from five category ratings. Practically, observers find it difficult to partition subjective judgments into more than five or six categories and so the majority of ROC studies found in the literature which use the rating method contain ROC curves plotted from only 4 or 5 operational data points[1,3,4,7,8].

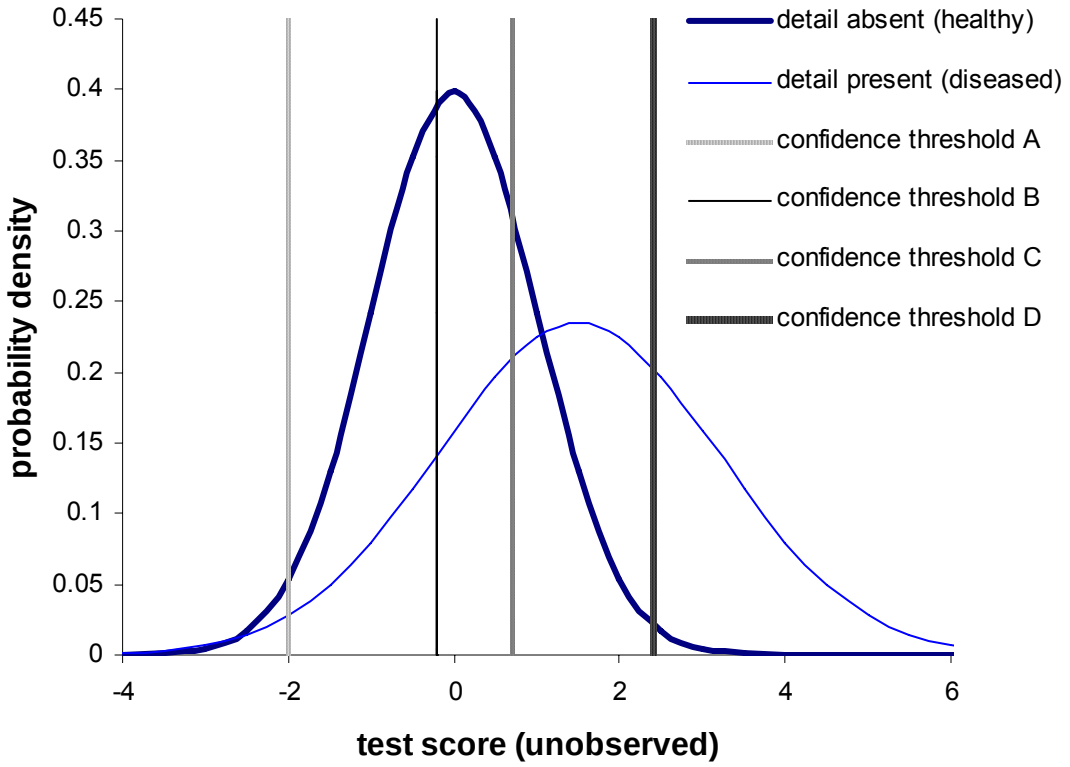

Figure 7:1 Probability density of a diagnostic test with two populations, healthy and diseased, assumed to follow a binormal distribution.

Once the operating points are known an ROC curve can be fitted to the ordinal data either empirically or parametrically. The empirical method involves simply joining the operating points, including points (0, 0) and (1, 1). The area under the ROC curve, *Az* may be determined from the empirical ROC curve using the trapezoidal rule however this has been shown to produce a large downward bias in the estimate of *Az* and is rarely used for medical imaging tasks[3,9,10]. The alternative is to apply a parametric model whereby we assume the test data or some transformation of the test data, follow a certain distribution. The most common approach is to assume a binormal distribution (two Gaussian distributions: one representing test results of the 'healthy' and the other representing test results of the 'diseased'), figure 7:1. This assumption has been shown to be remarkably robust for the variety of data distributions typically found in ROC studies[10-12]. Using

parametric methods to estimate the true ROC curve can reduce the estimated error and increase the statistical power of a study[11]. The resulting curve is called the fitted or smooth ROC curve. There are commercial and shareware computer programs that calculate the fitted ROC curve on the basis of a binormal distribution; these programs make use of maximum likelihood statistical estimates[13]. A number of studies provide a comparison of computer programs popular among ROC methodologists[11,14].

When a binormal distribution is assumed, the shape of the ROC curve is entirely determined by two parameters: a, the standardized difference of the means μ of the distributions of test results; and b, the ratio of the standard deviations σ of the distributions of the healthy, H and diseased, D, where

$$a = \frac{\mu_D - \mu_H}{\sigma_H} \quad \text{and} \quad b = \frac{\sigma_H}{\sigma_D} \qquad \textbf{Equation 7:3}$$

The curve actually takes the form of a straight line if drawn on normal deviate axes, where a is the 'Y' intercept and b is the slope[4]. In 'ROC' space the curve may be parameterized as[11]:

$$Sensitivity = b.(1 - Specificity) + \varphi.a \qquad \textbf{Equation 7:4}$$

and the area under the curve Az is calculated by:

$$A(z) = \varphi\left(\frac{a}{\sqrt{1+b^2}}\right) \qquad \textbf{Equation 7:5}$$

where φ is the standard normal cumulative distribution function. The task of curve fitting therefore becomes one of computing numerical values for a and b, the curve may then be plotted and/or Az determined.

7.2 Materials and Methods

7.2.1 Study Phantom

TRG, a statistical contrast-detail phantom designed for use in general radiography was chosen for this study (model 07-750, Nuclear Associates, USA). The phantom consists of twelve columns of ten disks each. Columns 1 to 6 are made from polyvinylchloride (PVC) disks, intended to be a high contrast bone substitute and columns 7 to 12 are made from polymethyl-methacrylate (PMMA) which act as low contrast details intended to represent muscle. Half of the disks in each column contain a hole. The size of the hole varies from 0.5 to 1.0 mm in the PVC disks in column 1 to 6 and from 0.9 to 2.0 mm in the PMMA disks in columns 7 to 12. The depth of the holes is equal to their diameter with each hole positioned eccentrically on each disk. The presence of holes was randomized independently for each radiograph. The probability of a hole being present at any location was 0.5. Ten different arrangements of the disks on the TRG phantom were created. A radiograph of the phantom is shown in figure 7:2. The total size of the phantom is 16 x 14 cm.

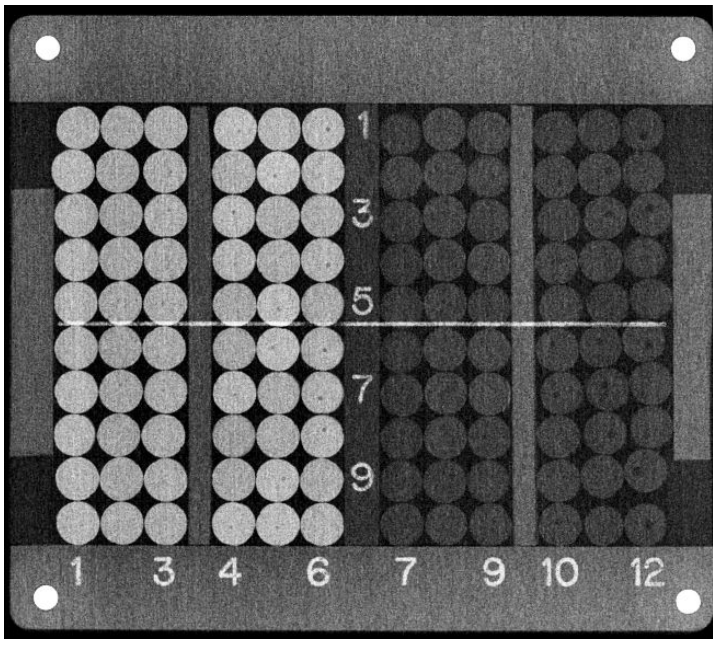

Figure 7:2 Radiograph of TRG statistical phantom (Nuclear Associates, USA).

7.2.2 Image acquisition and display

A Siemens Aristos indirect digital radiography (IDR) system, designed for erect chest and skeletal examinations, was employed for this study. The X-ray tube (Opti 150/30/50HC, Siemens) had filtration equivalent to 2.5 mm of aluminium, with the facility to include additional copper filters. The digital detector is a Trixell Pixium 4600, which has a caesium iodide (CsI) scintillator coupled to a photodiode thin film transistor array. The detector area is 43 × 43 cm^2 with a 3120 × 3120 pixel matrix and a pixel pitch of 143 μm. To increase scatter radiation, IDR images were acquired of the TRG phantom sandwiched between two sheets of 2.5 cm thick PMMA and two sheets of 1 mm thick Aluminium, with one sheet of each material on either side. The phantom provides a useful tool for comparing imaging performance for both high contrast (bone substitute) and low contrast (muscle substitute) details. The extra PMMA and Aluminium gave scatter conditions similar to those in the geometric chest phantom as discussed in Chapter 5.

Radiographs of the phantom were obtained using a radiographic technique employed in clinical practice for chest radiography: a source-to-image distance (SID) of 1.8 m, using an anti-scatter grid. Ten sets of images were acquired. Five sets contained images recorded at 8 kVs ranging from 60 to 133 kV with the beam filtered by 2.5 mm of aluminium alone and the remaining five sets with the beam filtered by 2.5 mm of aluminium with additional 0.2 mm of copper. The choice of 0.2 mm represents a good compromise between tube loading and the reduction of patient dose. For each technique the exposure factors were chosen to give a similar dose behind to the image receptor with the central ionization chamber selected in the automatic exposure control (AEC). The AECs were set up to comply with the Siemens image quality assurance program (IQAP), for a sensitivity class of 560 (receptor dose of 1.8 μGy ± 20% using 2.1 mm Cu). The positions of the details in the test object were varied randomly after each exposure using an array of details chosen from a selection of 10 known arrangements, table 7:3. All images

were processed using a linear look-up table and no un-sharp masking or spatial frequency enhancements were used. The images were compressed using JPEG lossless compression, stored in the DICOM 3.0 format and transferred to a research workstation via compact disk. Osiris freeware software was used for image analysis (Dr Jean-Paul Vallee, University Hospital of Geneva, Switzerland).

There were a total of 80 radiographs to analyse. Contrast detail observations were performed on a dedicated two mega pixel high luminance (>400 cdm^{-2}) display monitor, calibrated to DICOM Standard PS 3-14 [15]. Three experienced observers (two physicists and one technologist) viewed five image sets acquired with and without additional copper filtration. Ambient lighting was kept to a minimum and the viewing distance was about 1 m. Observers were permitted to adjust the brightness and contrast controls (using image viewing software) to perceived optimum levels. The phantom images were displayed for reading at a zoom factor of 2, without applying software pixel interpolation.

7.2.3 Data Analysis

ROC curves were generated using the rating data method, as described in section *Background theory on ROC methodology*. The probability of the existence of a critical detail *i.e.* a hole in a specific position, was expressed using a rating scale of 5 categories: (1) definitely present; (2) probably present; (3) possibly absent; (4) probably absent; and (5) definitely absent. Each category was expressed as a percentage 100, 75, 50, 25 and 0% and entered into a spreadsheet program by selecting the relevant rating from a dropdown list for each cell, table 7:2 (light grey boxes).

Table 7:2 An example of the spreadsheet program used to input and analyse observer data.

Image:	F		Array:	4											
75	100	25	100	0	100	1	100	25	25	25	0	100
75	50	100	50	100	25	2	50	75	100	100	100	0
25	0	100	100	0	0	3	50	50	25	0	100	100
50	25	0	75	25	100	4	75	25	75	25	25	25
75	100	100	0	100	0	5	75	75	75	0	0	0
75	50	25	0	100	100	6	25	50	50	100	100	100
50	100	75	100	50	100	7	75	50	50	100	100	0
50	75	25	0	0	100	8	75	75	100	50	100	25
75	50	0	25	100	0	9	75	75	0	25	0	100
75	0	0	100	100	0	10	25	0	50	100	0	100
1	2	3	4	5	6		7	8	9	10	11	12
75	100	100	100	100	100	+	50	25	100	100	100	100
50	25	100	100	100	100		75	25	75	25	100	100
75	100	100	75	100	100		75	50	75	100	100	100
50	100	75	100	100	100		75	75	100	100	100	100
50	0	0	100	100	100		25	0	50	100	100	100
25	50	25	50	0	25	-	100	75	25	25	0	0
25	0	0	0	0	0		50	50	25	0	25	25
75	50	25	0	25	0		75	75	50	0	0	0
75	75	25	0	50	0		25	50	50	50	0	0
75	50	0	25	0	0		75	75	0	25	0	25

% Rating	100	75+	50+	25+	0+		100	75+	50+	25+	0+
(+) counts	20	4	3	1	2	+	16	6	3	4	1
(-) counts	0	4	5	8	13	-	1	5	6	8	10
Manual	0.67	0.80	0.90	0.93	1.00	TPF	0.53	0.73	0.83	0.97	1.00
ROC	0.00	0.13	0.30	0.57	1.00	FPF	0.03	0.13	0.40	0.67	1.00

The data input by the observer were then compared with the true positions of the details. Visual basic macros were written for this purpose. An example of one of the 10 arrays used in the study is given in table 7:3. The real position of a detail is marked with a '1' and the absence of a detail a '0'. The macro selects the data entered in the light grey boxes, table 7:2 and compares it to determine if the true detail is present or not by selecting the correct array formation, in this case array 4. The program then outputs the data into two subsets of responses where the true detail is present (+) and responses where the true detail is absent (-). This table of data are shown in table 7:2, under the light grey boxes, where (+) and (-) responses are separated by a line. As an example look at the first four responses in column 6 table 7:3 (encircled red), the true positions are 1001 and the observer's responses were 100, 25, 0, 100, corresponding position, table 7:2 (encircled red). The two 100 responses were a 'hit' or (+) response and the 25 was a miss or (–)

response. All five details in column 6 were correctly chosen by the observer (red brackets), represented by five 100's and the 25 was a miss (-) (red triangle).

Table 7:3 An example of one of ten arrays of details used to randomise the positions of details in the TRG phantom.

Array	4

bone substitute							muscle substitute					
1	2	3	4	5	6		7	8	9	10	11	12
0	1	0	1	0	1	1	0	1	0	0	0	1
1	0	1	0	1	0	2	1	0	1	1	1	0
0	0	1	1	0	0	3	0	0	0	0	1	1
1	1	0	1	0	1	4	1	1	1	1	0	0
1	1	1	0	1	0	5	0	0	1	0	0	0
0	0	0	0	1	1	6	0	1	0	1	1	1
1	1	1	1	0	1	7	1	0	0	1	1	0
1	0	0	0	0	1	8	0	0	1	0	1	0
0	0	1	0	1	0	9	1	1	0	0	0	1
0	1	0	1	1	0	10	1	1	1	1	0	1

The total numbers of corrected responses or counts were then summed for each of the five categories. These are shown in table 7:2 as (+) counts and (-) counts for the bone substitute (left) and muscle substitute (right). For example, the number of positive counts in the 25% category for bone was only 1, the observers' response, the true response and the mark recorded are highlighted in blue boxes. There are many commercial and freeware programs to parameterise this data to produce ROC curves. In this study the ROCKIT program (Kurt Rossmann Laboratories, University of Chicago) was used to perform the parametric curve fitting and error analysis[13]. Diagnostic accuracy was measured using the area under the binormal ROC curves, *Az*. A total of 3,600 observations were analysed (1800 high contrast and 1800 low contrast): 2 contrasts x 10 rows x 6 sizes = 120 interpretations per radiograph x 2 radiographic techniques (without and without copper filtration) x 5 detail arrangements x 3 observers. The total 3,600 interpretations equals 300 interpretations per hole size (there are 10 test objects per hole size per radiograph).

As with any semi-automated approach using computer software it is prudent to check the quality of raw data which is input. Particularly with rating ROC methodology as regardless of how many observations are made curve fitting algorithms are still applied to only 5 operational data points. The true positive fractions and false positive fractions of the (+) and (-) count data listed in table 7:2 were used to manually calculate the operational data points for each of the categories (shown in yellow). These are cumulative fractions of 30 (5 categories x 6 different objects) for example, the 100% category had 20 (+) counts the true positive fractions (TPF) was therefore 20/30 = 0.67, similarly the 75% category had 4 positive counts and the corresponding TPFis 0.67 + 4/30 = 0.8.

The images were read over a two month period and presented anonymously to the observers. The tube potential, radiographic technique and most importantly choice of the 10 arrangements of the arrays of details in the phantom, were randomised in order to remove any reading order or memory bias effects[16,17].

7.2.4 Investigation of image quality with detail diameter

ROC curves give a clear indication of the true or false detection of details. The curves generated in this study provide an indication of the probability of detecting pathology substitute details of a given size and contrast under defined irradiation conditions. The greater the detail size or the better the imaging technique the higher the ROC curve is situated. The probability of a true answer or diagnostic accuracy P_{det} is calculated by means of *SN* and *SP* values[18] where

$$P_{\text{det}} = \frac{TP + TN}{TP + TN + FP + FN} = \frac{SN + SP}{2} \qquad \textbf{Equation 7:6}$$

TP, *TN*, *FP*, and *FN* are the fractions of true positives, true negatives, false positives, and false negatives, respectively. To examine image quality variations with detail size (*i.e.* hole diameter) for the cases with and without copper filtration the probability of detecting each particular detail were calculated using equation (6) and the results segregated by hole size.

7.2.5 Hypothesis testing and statistical significance

In comparing two imaging systems or two techniques for the same imaging system with ROC analysis, thought must be given to how a possible difference between two ROC curves must be quantified. This in turn dictates the null hypothesis that one must use to evaluate the statistical significance of the difference between the ROCs. In general this will depend on how the imaging techniques or systems are employed in clinical practice. In this study we are interested in evaluating the effect of additional copper filtration on image quality and we adopt a strict definition of equivalent system performance such that the two techniques are considered different unless we can show that the ratings data sets arose from the same binormal ROC curve. Therefore we define the null hypothesis as stating: there is no difference between the data sets which created the ROC curves for the 0.0 mmCu and the 0.2 mmCu cases *i.e.* copper filtration has no measurable effect on image quality, and the research hypothesis states: there is a measurable difference in image quality when adding 0.2 mmCu filtration.

The null hypothesis was addressed using a bivariate Chi-square test of the simultaneous differences between the *a* parameters and between the *b* parameters of the two ROC curves.

7.3 Results

An example of the raw data (operational points) determined empirically from two different observers are shown in figure 7.3 (a) and (b). The data represent one reading from each observer at each of eight different tube potentials ranging from 60 to 133 kVp.

(a)

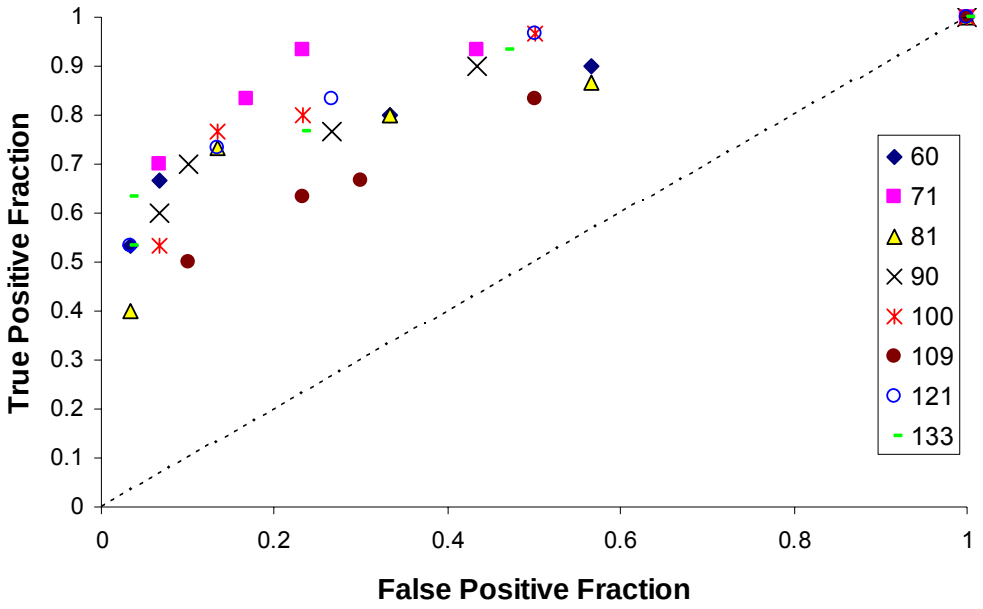

(b)

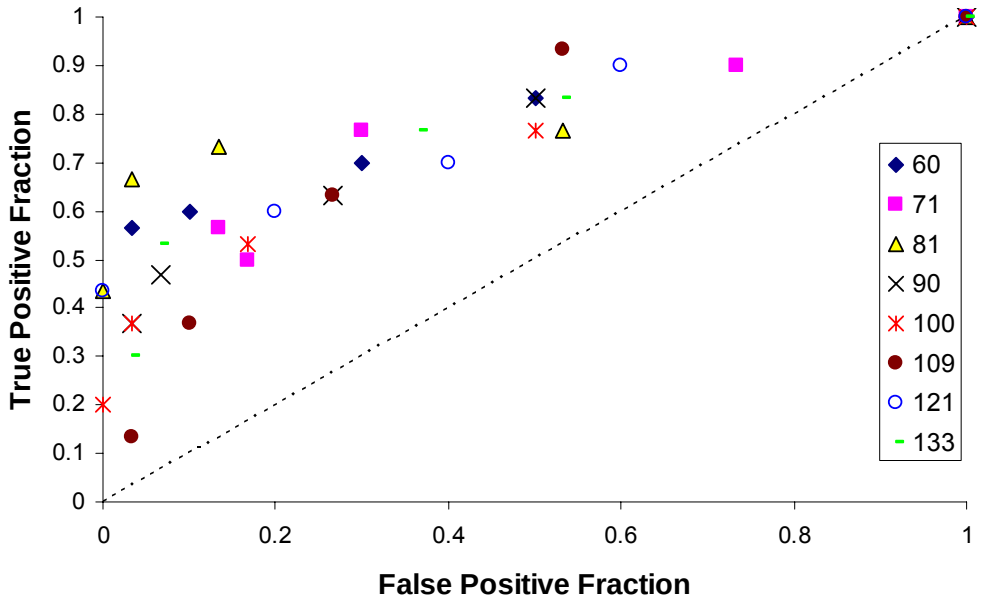

Figure 7:3 An example of manually calculated operational data points for two different observers (a) and (b) for only one reading at each of eight tube potential ranging from 60 – 133 kVp.

The ROCKIT program[13] was used to produce a set of parameters *a*, *b, Az* and standard error of *Az*, SE(*Az)* for both high contrast and low contrast details for each radiograph read by the observers. The observer averaged values of *a* and *b*; *Az* and SE(*Az*) are listed in table 7:4(a) for high contrast and table 7:4(b) for low contrast details, respectively. The mean values of *a* and *b* were used to plot ROC curves using a specialised program called PlotROC (Kurt Rossmann Laboratories, University of Chicago)[13].

Table 7:4 Parametric values computed using ROCKIT for (a) high contrast and (b) low contrast details, data are mean of three observers.

(a)

High Contrast (bone substitute)

	0.0 mmCu				**0.2 mmCu**			
kVp	*a*	*b*	*Az*	*SE(Az)*	*a*	*b*	*Az*	*SE(Az)*
60	1.19	0.35	0.86	0.06	1.27	0.74	0.85	0.06
71	1.07	0.75	0.78	0.07	0.79	0.58	0.74	0.07
81	0.76	0.60	0.74	0.07	0.86	0.69	0.73	0.07
90	1.10	0.71	0.81	0.07	0.95	0.57	0.79	0.06
100	0.84	0.58	0.75	0.09	0.80	0.72	0.73	0.07
109	0.59	0.75	0.66	0.08	0.51	0.59	0.66	0.07
121	0.84	0.83	0.74	0.07	0.63	0.71	0.68	0.08
133	0.34	0.79	0.60	0.09	0.46	0.72	0.64	0.08
mean:	0.84	0.67	0.74	0.07	0.78	0.67	0.73	0.07

(b)

Low Contrast (mucsle substitute)

	0.0 mmCu				**0.2 mmCu**			
kVp	*a*	*b*	*Az*	*SE(Az)*	*a*	*b*	*Az*	*SE(Az)*
60	1.50	0.80	0.85	0.05	1.24	0.58	0.86	0.05
71	1.32	0.76	0.84	0.05	1.82	0.85	0.89	0.05
81	1.16	0.42	0.83	0.06	1.83	1.22	0.84	0.06
90	1.28	0.86	0.82	0.06	1.73	1.26	0.84	0.06
100	1.04	0.69	0.80	0.06	1.36	0.92	0.80	0.06
109	1.04	0.61	0.78	0.06	1.42	1.27	0.81	0.06
121	0.91	0.60	0.78	0.06	1.02	0.56	0.80	0.06
133	1.07	0.70	0.79	0.06	1.15	0.95	0.75	0.06
mean:	1.16	0.68	0.81	0.06	1.45	0.95	0.82	0.06

ROC curves were examined for bone substitute material without copper filtration, to analyse the effect of varying tube potential on image quality. The results are illustrated in figure 7:4. The diagonal line corresponds to chance *i.e.* a probability of 0.5.

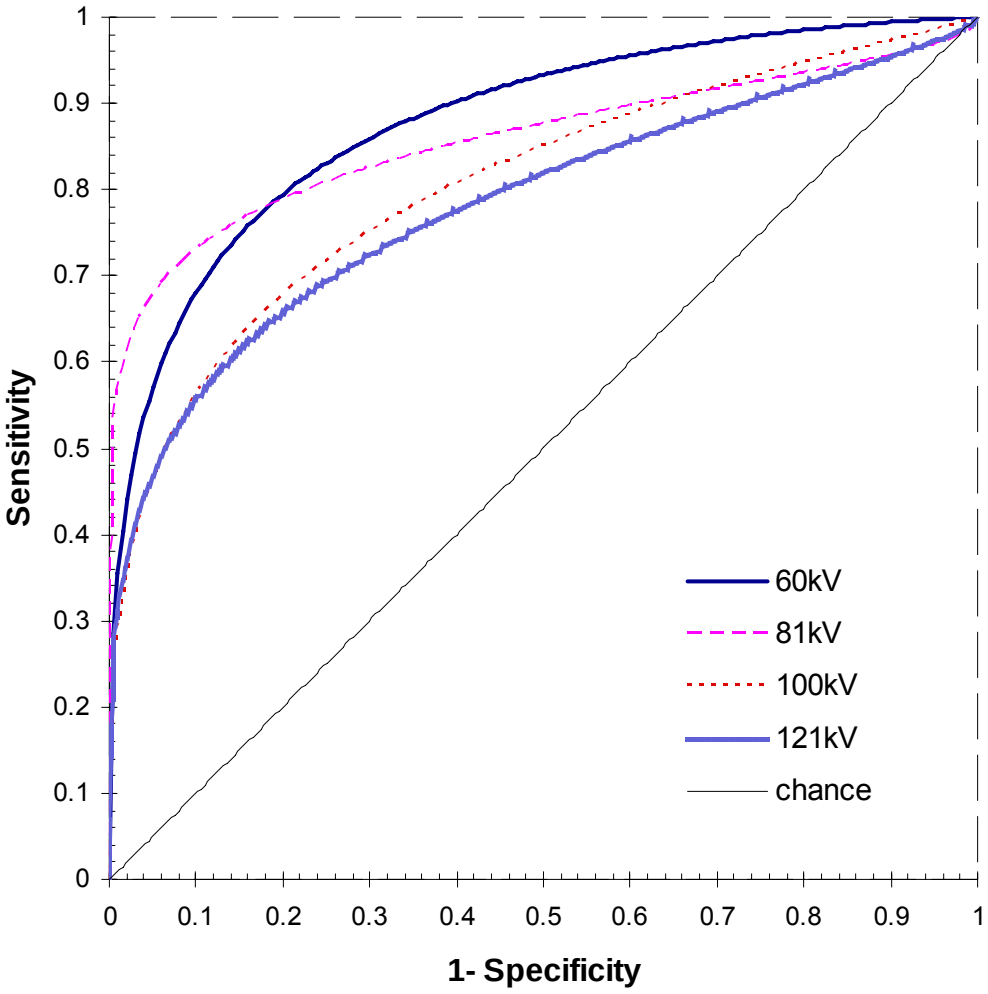

Figure 7:4 Pooled ROC plots for bone substitute material for a range of tube potentials.

ROC curves were determined for images acquired at eight different kVs ranging from 60 to 133kVp, for cases with and without copper filtration. The curves showed a similar trend to those shown in figure 7:4 for bone, for the muscle substitute material and the ranking of higher diagnostic accuracy for lower tube potentials were not affected by the addition of 0.2 mm Cu. The clearest way of presenting this data is to plot the areas under each of the ROC curves generated against tube potential; the results are shown in figure 7:5(a) for bone substitute and 7:5(b) for muscle substitute, respectively. The data are pooled for three observers.

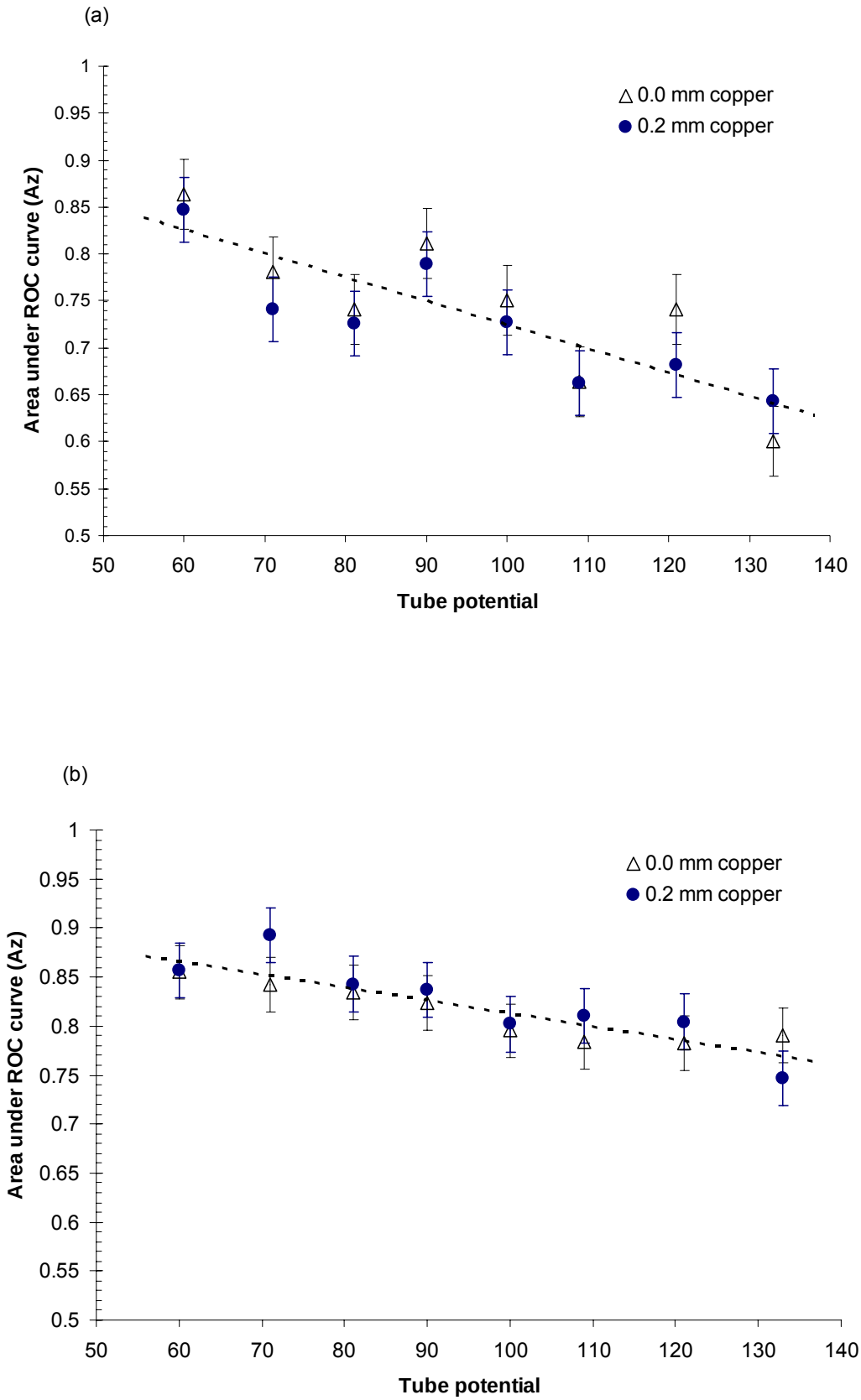

Figure 7:5 The area under the ROC curve plotted as a function of tube potential for (a) bone substitute and (b) muscle substitute materials. The error bars indicate the standard error in the measurement of *Az*.

Values of *a* and *b* averaged for all kVps and over 3 observers were used to plot ROC curves to compare muscle and bone substitute materials with and without copper filtration, figure 7:6. There is less than 1% difference in the mean values of *Az* for examinations taken with and without copper filtration, this difference is within the standard error estimate and is not statistically significant.

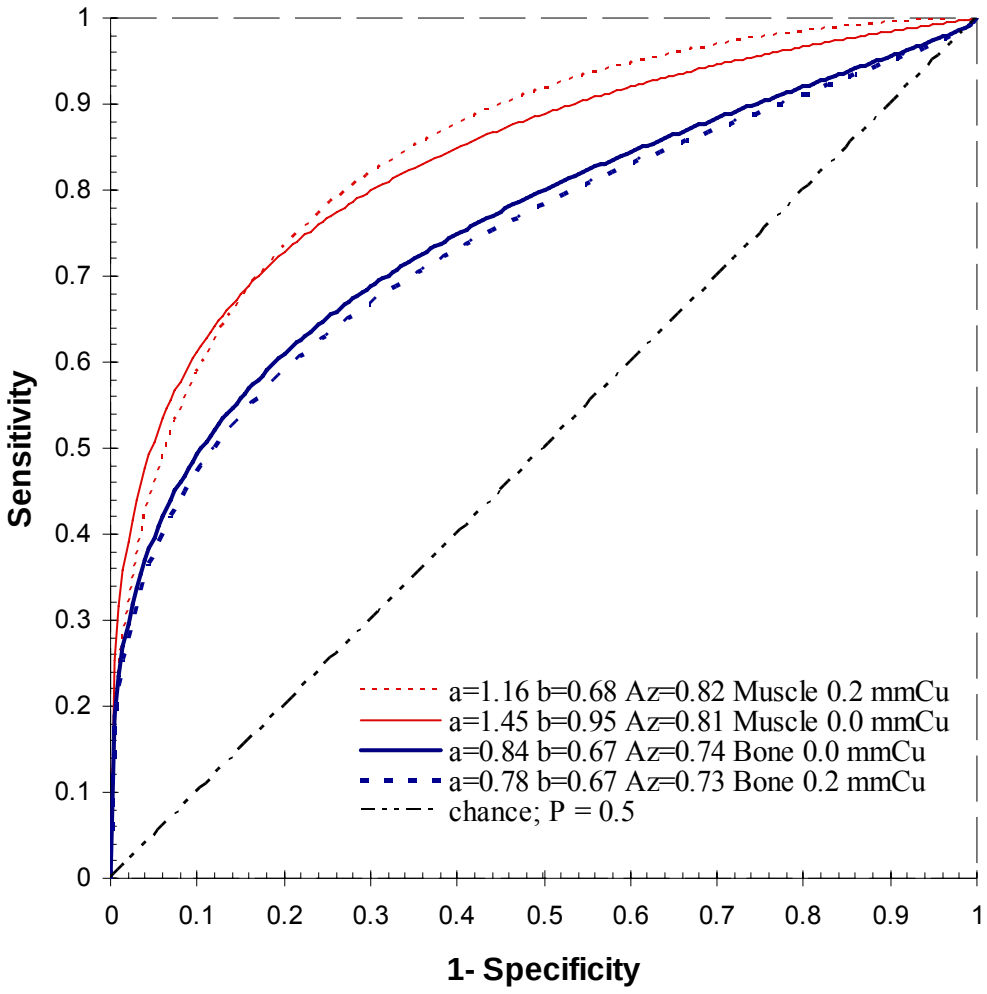

Figure 7:6 ROC plots for muscle and bone substitute materials with 0.0 mmCu and 0.2 mmCu added filtration. Data are pooled over the diagnostic kV range for three observers.

The results of the Chi-square tests are shown in table 7:5. Since P-values are greater than 0.05 for all tube potentials studied there is no strong evidence that the areas

under the ROC curves differ and we have obtained a statistically non-significant result *i.e.* we failed to disprove the null hypothesis. Since we do not have evidence the null hypothesis is false we have to accept that the addition of copper filtration makes no measurable difference to observed image quality.

Table 7:5 Mean Chi-square test results for three observers at eight tube potentials. The null hypothesis is accepted, where P> 0.05.

kV	60	71	81	90	100	109	121	133	
Bone subsitiute									mean
χ^2	1.58	1.88	2.81	0.16	0.64	3.15	0.34	1.59	*1.52*
P value	0.5	0.5	0.3	0.9	0.7	0.3	0.9	0.5	*0.55*
Muscle substitute									
χ^2	1.88	0.97	2.26	0.92	0.77	0.51	2.08	1.46	*1.35*
P value	0.4	0.6	0.3	0.6	0.7	0.8	0.4	0.5	*0.55*

The ROC curves in figures 7:5 and 7:6 show the true and false positive fractions in detecting TRG details of ten different sizes. There is an overlap of detail diameters on the bone and muscle substitute materials at 0.9 mm and 1.0 mm. There were 300 individual interpretations of each detail size made by the observers. The probability of detecting a particular hole size in a given disk was calculated using equation 7:6. The results are plotted as a function of hole or detail diameter in figure 7:7.

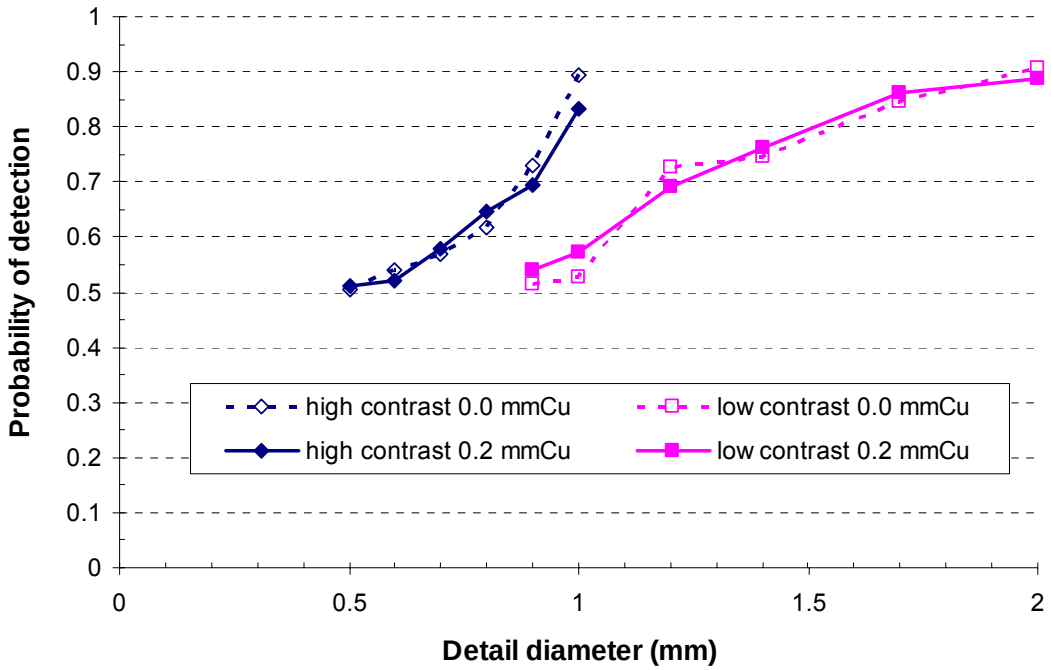

Figure 7:7 Probability of detecting a hole in a given disk of the TRG phantom, as a function of hole detail diameter.

7.4 Discussion and Conclusion

All ROC parameters in this study were computed for each observer individually, and then averaged to compute the data presented herein, table 7:4. A common error in ROC methodology involving more than one observer is to pool all the data across the observers to produce one large data set, which is then fit by a program for example ROCKIT, to produce the pooled ROC curve. This however is likely to produce biased results and underestimates of *Az* as the approach assumes all observers operate at essentially the same operating points[17]. For multi-observer studies it is recommended that *a* and *b* parameters are calculated for each observer individually and then averaged to produce a pooled study ROC curve[17].

It should be noted that the majority of ROC programs (including ROCKIT) consider only variations due to case sampling and do not include within reader and between reader variations[19]. The standard deviation of the estimates of *Az* derived from each observers interpretations in this study was 0.04, giving a coefficient of variation of 5% in the values of *Az*. The observers employed in this study are experienced (> eight years) and within reader and between readers variations are likely to be small, they are also unlikely to introduce bias in the study as the images were presented randomly and anonymously.

An important consideration in designing an ROC study is in determining the appropriate sample size to demonstrate the required statistical power. The sample size needs to be sufficiently large such that if an important difference in performance exists it is unlikely to go undetected in a test of significance. Knowing in advance the approximate standard errors associated with an estimate of *Az*, it is possible to calculate how many cases need to be studied so that a comparison of two imaging techniques will have a specified degree of statistical power or sensitivity. This power depends on how small the probabilities α and β of committing a type I or type II error are. (Type I errors are errors in rejecting the null hypothesis, when it is actually true *i.e* a sensitivity type error and Type II errors are errors in accepting the null hypothesis when it is actually false *i.e.* a specificity type error). Typically one seeks a power (100- β) of 90% or 95% so that if an actual difference exists we are 90% or 95% certain that the difference will be reflected in samples that will be declared 'statistically significant'. Traditionally, one uses a type I error probability or α of 0.05 (5%) as the criterion for a significant difference[9,19].

To estimate the sample size needed for this study a trial run was first performed. A small number of test images were acquired with and without copper filtration and the areas under the resulting ROC curves were calculated. The initial results showed typical values

of *Az* ranging from 0.78 to 0.83. From tabulated data published in the literature[9] the sample size of the number of 'healthy' and 'diseased' subjects required to provide a probability of 95% of detecting various differences between the values of *Az* under the ROC curves was estimated. Using a one sided test of significance with a p value = 0.05, there were 889 'healthy' subjects required and 889 diseased subjects required. The statistical power in the present study was achieved with 900 interpretations of details where the hole detail was present (diseased) and 900 interpretations where the detail was absent (healthy).

Similar to the contrast-to-noise ratio results for the lung presented in Chapters 5 and 6, in the present study greater diagnostic accuracy is afforded by lower tube potentials, figure 7:4 and figure 7:5. Indeed the image receptor dose level, the X-ray transmission and scatter conditions are similar for the TRG phantom set-up and that of the chest phantom. Figures 7:5 (a) and (b) show the change in *Az* with tube potential for the high contrast bone substitute and low contrast lung substitute materials, respectively. There is a greater spread in the results for the bone substitute material and the diagnostic accuracy indicated by Az, falls with increasing kV at a steeper rate than that of the muscle substitute data. The greater spread of data in figure 7:5(a) may be attributed to the relative increase in noise particularly quantum mottle, associated with the reduced X-ray flux passing through the high contrast details. With such a low signal level the reduction in radiographic or inherent contrast with increases in tube potential has a marked effect and the energy response of the detector becomes significant. This behaviour is also demonstrated in figure 6:4 where increasing mean photon energy of relatively more filtered beams fall with tube potential at a steeper rate.

More important to the objectives of this study, figure 7:5 also illustrates that the addition of 0.2 mm copper filtration does not give a statistically significant difference in diagnostic accuracy when compared with a similar technique without copper filtration.

These findings are also demonstrated in figure 7:7 where a different analytical technique, based on the probability of detecting particular details was used. The addition of 0.2 mm copper at the mid-diagnostic energy range 70 - 80 kV has an entrance surface dose saving of typically 50% with a corresponding reduction in effective dose of approximately 40%, depending on the projection (see Chapter 6). Since image quality has been shown to be unaffected by this amount of additional copper filtration. The only disadvantage in using the extra filtration is that the tube output will need to be increased to compensate for the reduction in photon fluence. The tube output would need to be increased by almost 50% at ~ 80 kV in order to compensate for a filter of 0.2 mmCu, figure 6:5. This may have an impact on the tube lifetime and also on exposure times.

7.5 References

[1] Swets JA. Measuring the accuracy of diagnostic systems. Science 1988 Jun 3;240(4857):1285-93.

[2] Obuchowski NA. Receiver operating characteristic curves and their use in radiology. Radiology 2003 Oct;229(1):3-8.

[3] Park SH, Goo JM, Jo CH. Receiver operating characteristic (ROC) curve: practical review for radiologists. Korean J Radiol 2004 Jan;5(1):11-8.

[4] Metz CE. ROC methodology in radiologic imaging. Invest Radiol 1986 Sep;21(9):720-33.

[5] Green DM, Swets JA. Signal detection theory and psychophysics. Huntington, New York: Krieger; 1974.

[6] Walsh SJ. Limitations to the robustness of binormal ROC curves: effects of model misspecification and location of decision thresholds on bias, precision, size and power. Stat Med 1997 Mar 30;16(6):669-79.

[7] Goodenough DJ, Rossmann K, Lusted LB. Radiographic applications of receiver operating characteristic (ROC) curves. Radiology 1974 Jan;110(1):89-95.

[8] Metz CE. Receiver operating characteristic analysis: a tool for the quantitative evaluation of observer performance and imaging systems. J Am Coll Radiol 2006 Jun;3(6):413-22.

[9] Hanley JA, McNeil BJ. The meaning and use of the area under a receiver operating characteristic (ROC) curve. Radiology 1982 Apr;143(1):29-36.

[10] Hajian-Tilaki KO, Hanley JA, Joseph L, Collet JP. A comparison of parametric and nonparametric approaches to ROC analysis of quantitative diagnostic tests. Med Decis Making 1997 Jan;17(1):94-102.

[11] Lasko TA, Bhagwat JG, Zou KH, Ohno-Machado L. The use of receiver operating characteristic curves in biomedical informatics. J Biomed Inform 2005 Oct;38(5):404-15.

[12] Hanley JA. The robustness of the "binormal" assumptions used in fitting ROC curves. Med Decis Making 1988 Jul;8(3):197-203.

[13] University of Chicago. Reciever Operating Characteristic program software downloads. http://www-radiology.uchicago.edu/krl/KRL_ROC/software_index6.htm. Date accessed: 2008 Sep 30.

[14] Zweig MH, Campbell G. Receiver-operating characteristic (ROC) plots: a fundamental evaluation tool in clinical medicine. Clin Chem 1993 Apr;39(4):561-77.

[15] National Electrical Manufacturers Association (NEMA). Digital Imaging and Communications in Medicine (DICOM): Part 14. Greyscale Display Standard Function PS 3.14. Tarrytown, NY: NEMA; 2000.

[16] Metz CE. ROC analysis in medical imaging: a tutorial review of the literature. Radiol Phys Technol 2008;(1):2-12.

[17] Metz CE. Some practical issues of experimental design and data analysis in radiological ROC studies. Invest Radiol 1989 Mar;24(3):234-45.

[18] Gurvich VA. Statistical approach for image quality evaluation in daily medical practice. Med Phys 2000 Jan;27(1):94-100.

[19] McNeil BJ, Hanley JA. Statistical approaches to the analysis of receiver operating characteristic (ROC) curves. Med Decis Making 1984;4(2):137-50.

[20] National Council on Radiation Protection and Measurements (NCRP). Limitation of Exposure to Ionizing Radiation. Maryland, USA; 1993. Report No.: 116.

[21] J D Robb and G A M Webb. Value of Unit Collective Dose for Use in the 1990s. Holburn, London: National Radiation Protection Board (NRPB); 1993. Report No.: 2, Volume 4.

8 Summary and Conclusions

8.1 Summary and Final Conclusions

Digital radiography (DR) systems have been in widespread use in the UK for over a decade. As with all clinical equipment, appropriate methods are required to evaluate and optimise the performance of these systems, to ensure and maintain quality and effectiveness in the radiology department. Current testing methods routinely used to examine DR performance suffer known short comings, mainly due to the subjective nature of the test results, an apparent gap between physical test object based results and clinical performance and difficulty in maintaining a constant decision threshold among observers with time. Objective image quality based measurements of noise power spectra (NPS) and modulation transfer function (MTF) are the 'gold standard' for assessing image quality[1]. The advent of DR systems and access to digital image data has opened up new opportunities in applying such measurements to routine quality control. Advantages these metrics afford are due to their objective nature, the comprehensive noise analysis they permit and in the fact that they have been reported to be more sensitive to changes in detector performance[2].

The standardisation of testing methodology with the IEC 62220-1 report[3] published in 2003 was the first step as this allows manufacturers and medical physicists to directly compare results. Chapter 3 provides useful recommendations in the application of the IEC standard, with some minor adjustments, to a clinical environment. The total uncertainty in the measurement of DQE was 6%. This is within the tolerance the standard allows and is

encouraging considering some practical modifications to the measurement technique were necessary, for example, a shorter source to image distance and use of the X-ray tubes internal collimators to define the field size. Measurement uncertainties of 3.5% for the MTF and 3.4% for the NPS were found. However an unexpectedly large variation of 11% ±0.6% was found in the measurement of detective quantum efficiency (DQE) at zero spatial frequency for the 14 detectors studied, although the mean value of 0.68 at 4μGy was similar to that reported in the literature[4]. The measurements of DQE will be repeated at future QC visits and in time it is hoped will allow an analysis of detector faults and how they may manifest as changes in DQE, NPS or MTF.

In Chapter 4 it was conveyed how the energy responses of digital radiography systems differ from those of screen/film combinations. It was demonstrated how this affects automatic exposure control (AEC) calibration for DR systems and increasing exposures at higher tube potentials were required. The uses of various parameters to calibrate AECs were explored and two equivalent methods are recommended based on a measurement of the detector dose indicator or detector air kerma. Practical advice on dosemeter selection and recommendations on choice and positioning of patient equivalent phantoms are also given.

There is a strong need for a metric which can be calculated theoretically and empirically and can describe gross imaging performance without approaching the constraints implied by the resolution limitations of an imaging system. For large low contrast details, described in Fourier space as having a low spatial frequency, the modulation transfer function of digital imaging systems approach 100% and assessments of image quality based on such details should therefore be comparable among different digital systems. Contrast-to-noise ratio (CNR) was used in this thesis to allow both a comparison of digital radiography systems utilising different phosphors and an

examination of how each are affected by radiation quality. Chapter 5 detailed the development of a model to simulate CNR to optimise beam quality for chest radiography with an indirect digital radiography system (IDR). CNR values were simulated for a chest phantom and adjusted to describe the performance of the IDR system by inputting data on phosphor sensitivity, the signal transfer function (STF), the scatter removal method and the automatic exposure control (AEC) responses. The simulated values showed good agreement with empirical data measured from images of the phantom and so provide validation of the calculation methodology. The study allowed useful conclusions to be drawn on what beam qualities are optimum for chest radiography. The CNR results showed that CNR and detail detection are higher in the lung and heart regions at lower tube potentials, while those in the abdomen are higher for tube potentials of 90-110kVp. However when the effective dose was taken into account and a figure of merit (FOM) was used, optimum results were found for the lung at 60-70 kVp, while that for the heart was higher at 70-90kVp and that for the abdomen at 90-120kVp. With regard to technique for scatter removal, the FOM results for lung imaging were higher for the air gap technique and the grid technique was better for imaging the abdomen.

As the theoretical CNR results were validated with measurements from images of the chest phantom, it was possible to apply the calculation technique to imaging of tissues to investigate optimisation of exposure parameters. Application of the CNR model was discussed in Chapter 6. The model was used to investigate the behaviour of a range of imaging phosphors in terms of energy response and variation in CNR with tube potential and various filtration options. Results indicated large dose savings could be achieved using additional metal filters, for example a saving of 40% in effective dose is possible using 0.2 mm copper for a PA chest examination. Regulation curves of the type commonly used in image intensifiers were developed for a CsI IDR system. Exposure factors which provide maximum image quality for imaging a simulated lesion of 2 mm

muscle were presented for different X-ray beam filtrations and patient attenuator thicknesses. The regulation curves demonstrated that image quality is maximised by reducing the tube potential when extra copper filter thicknesses are used.

The relative phosphor sensitivity and energy response with tube potential were calculated for phosphors commonly used in digital radiography. Caesium iodide image receptors are significantly more sensitive than the other systems available due to a combination of the relatively large mass attenuation coefficient and the ability to utilise the light guiding character of the CsI needle structure and incorporate a thick phosphor layer. The percentage relative sensitivities of the image receptors averaged over the tube potential range 60 to 125 kVp were: CsI - 97%; Gd_2O_2S - 63%; Se - 55%, BaFBrI - 45%; and CaWO4 - 42%. Using these relative sensitivity values a crude assessment of the dose levels the phosphors are likely to operate clinically at are 1.8 μGy for CsI; 2.8 μGy for Gd_2O_2S; 3.2 μGy for Se; 3.8 μGy for BaFBrI; and 4.2 μGy for CaWO4. CsI IDR systems provided by three manufacturers (Philips, Siemens & Cannon) have been successfully set up in hospitals in the West of Scotland and Northern Ireland with image receptor doses of 1.8±0.2 μGy. However larger variations exist for barium flurohalides, the phosphor most widely used in CR. Comparison of the imaging performance of the CR phosphor with Gd_2O_2S, used in screen-film systems suggests an increase in radiation exposure of 30% to 40% to compensate for the lower sensitivity. However, this is offset by sophisticated image processing techniques, noise reduction algorithms and the better contrast and dynamic range of digital systems, which in the majority of cases allows satisfactory imaging with a CR system employing a similar dose level to that of screen/film systems at 80 kVp, typically 2.5-3 μGy. This approach had been adopted in the West of Scotland and Northern Ireland with satisfactory results for all but one manufacturer, where the expected dose levels up to 4 μGy at 80kVp are required. The higher dose level is needed to compensate for the relatively simpler noise reduction algorithms employed and imaging

plate technology that has undergone few technological improvements compared to other CR vendors on the market.

The CNR results presented in Chapter 6 simulated general radiographic examinations of the chest, abdomen and pelvis, for clinically relevant features of muscle. This enabled gross imaging performance of changes in radiation quality and energy response without approaching the constraints implied by the resolution limitations of the detectors studied. The energy response and optimum tube potential differed significantly for each of the phosphors studied, particularly when the CNR is also used to examine other regions of the same image *i.e.* the lung, heart and abdominal areas of the chest. The CsI phosphor results show similar trends to those determined empirically for theses areas with a chest phantom, presented in Chapter 5. Plots of CNR values allowed us to draw useful conclusions regarding the expected clinical operation of the various phosphors. For example 80-90 kVp was appropriate for maintaining image quality over the entire chest radiograph in CR whereas higher tube potentials of 100-110 kVp were indicated for the CsI IDR system. Better image quality is achievable for pelvic radiographs at lower tube potentials for the majority of detectors however, for gadolinium oxysulphide 70-80 kVp gives the best image quality. Chapter 6 also presented regulation curves for Gd_2O_2S, CsI, BaFBrI and Se to demonstrate the exposure factors required to maintain maximum image quality when imaging a 2 mm thick piece of muscle at a constant system dose level for a range of patient attenuator thicknesses. The optimum tube potentials for imaging a 2 mm thick muscle feature in thicknesses of water ranging from 5-40 cm thick were: 90-110kVp for CsI; 80-100kVp for Gd_2O_2S; 65-85kVp for BaFBrI; and 55-70kVp for Se.

Results presented in Chapter 6 also demonstrated how the efficiency of scatter reduction methods varies with scatter factor. It was shown with computations of FOM that for a constant detector dose, better image quality is achieved with the use of a 15/80 grid for the abdomen and pelvis examinations, however not necessarily for the chest if image

quality in the lung is considered paramount. It must be bourn in mind however that scatter fractions can vary strongly from point to point within an image and in a typical chest radiograph scatter fractions of 0.5 in the lung field, 0.8 in the heart region and 0.9 in the abdominal area have been reported [5]. The decision on whether or not to use a grid therefore depends on the imaging requirements across the entire chest image. The improvements in image quality when applying scatter reduction methods was determined by assessing the improvement in CNR they afford, termed the CNR improvement factor, CNR_{if}. The performance of various scatter reduction methods: 17/70; 15/80; 8/40 Pb grids and 15 cm and 20 cm air gaps were evaluated in terms of CNR_{if} using two different models. The first assumed quantum noise only and a photon counting detector. The second model incorporated quantum noise and system noise for a specific CsI detector and assumed the detector was energy integrating. Data presented in Chapter 3 was used for the real value of system noise. The quantum noise model results indicated that using a grid or air gap can actually reduce image quality where very low scatter fractions are involved (< 0.3). The greater selectivity of grids compared to air gaps provides improved image quality when using grids in situations where the scatter fractions are relatively large (> 0.6). The performance of the air gaps however are better for lower scatter fractions (0.3 - 0.6). Similar results were found in the chest phantom study presented in Chapter 5, where the FOM values for lung imaging are higher for the air gap technique and the grid technique was better for imaging the abdomen. Comparing the results of this model, with those of the system noise model allowed the same general conclusions. Both models suggest improved performance for air gaps over grids for medium to low scatter factors and both models suggest the best choice of grid for digital systems is the 15/80 grid, achieving comparable or better performance than air gaps for high scatter factors. The simpler noise model should therefore be sufficient to evaluate new or existing scatter removal methods for digital systems and indicate if improvements can be made or further investigation is needed.

Chapter 6 finally outlines a recipe or strategy that may be used to optimise DR equipment. This is summarised in the following steps:

1. Obtain physical data on image receptor
2. Calculate the phosphor energy absorption, A(E)
3. Compute CNR for clinically relevant feature
4. Evaluate extra filtration options
5. Calibrate AEC to A(E) or constant DDI
6. Review scatter removal requirements and technique
7. Use A(E), CNR and FOM data to review exposure factors
8. Survey patient doses, set DDI ranges and identify specific system attributes

Both experimental measurements and theoretical computations of CNR using a chest phantom presented in Chapter 5, suggested the addition of 0.2 mm of copper filtration will have a negligible effect on image quality. The analysis was only indicative however, as the number of details and range of detail sizes available in the chest phantom were limited. A more comprehensive study examining the effect of copper filtration on image quality was performed using receiver operator characteristic (ROC) methodology to include both observer and detector performance. The study was detailed in Chapter 7. A total of 3,600 observations from 80 radiographs and 3 observers were analysed to provide a confidence interval of 95% in detecting various differences between the values of *Az*, the area under the ROC curves - accepted as an indicator of diagnostic accuracy. No statistical difference was found in image quality when 0.2 mm copper was used and the benefit of the dose saving promote it as a valuable optimisation tool.

There is a disadvantage in using the extra filtration in that the tube output will need to be increased to compensate for the reduction in photon fluence. It was demonstrated that the tube output would need to be increased by almost 50% at ~ 80 kV in order to compensate for a filter of 0.2 mm copper.

8.2 Suggestions for Further Work

- MTF and NPS are universally accepted as 'gold standard' image quality metrics. They allow objective specification of digital detector performance. However very little is known on how common detector faults manifest as changes in MTF or NPS. Such data will need to be collected over time from equipment known to be in good adjustment. It is only then we can consider setting tolerances for the remedy or suspension of digital detectors from clinical service based on these parameters.

- Results presented in Chapter 5 showed a positive correlation between empirical measurements of CNR and the number of details observed in a phantom. More work is needed to investigate how CNR measurements compare with the visibility of details for a larger range of contrasts and details sizes, possibly saving much time on routine QC.

- The CNR model developed for this thesis was applied to a variety of image receptors used in general radiography. The model is easily adaptable to other specialist areas of radiography such as paediatrics and mammography. The regulation curves presented in Chapter 6 may also be explored for application to fluoroscopy, particularly for new flat panel systems.

- Results presented in Chapter 6 indicate that the air gap scatter reduction method is at least equal, and for medium to low scatter factors superior to grids for a CsI system. The efficiency of scatter reduction techniques and relative merits of using an air gap need to be explored further.

- Image processing options specific to different digital radiography manufacturers need to be investigated and possibly standardised. The current ad-hoc way of adjusting image processing reactively when image quality is questionable is not

sufficient to realise the full benefit and level of image quality achievable from the technology.

- Thousands of digital systems are now in use in the UK a survey specifically focused on digital imaging, indicating exposure factors and techniques, similar to the national reference dose reports would prove very beneficial.

8.3 References

[1] International Commission on Radiation Units and Measurements (ICRU). Medical Imaging - the assessment of image quality. Bethesda, MD: ICRU; 1996. Report No.: 54.

[2] Marshall NW. Retrospective analysis of a detector fault for a full field digital mammography system. Phys Med Biol 2006 Nov 7;51(21):5655-73.

[3] International Electrotechnical Commission. Medical electrical equipment: characteristics of digital X-ray imaging devices - part 1: determination of the detective quantum efficiency. Geneva, Switzerland: IEC; 2003. Report No.: 62220-1.

[4] Centre for Evidence Based Purchasing. Digital Imaging Systems for General Radiography. A comparative technical report. London, UK: CEP; 2005. Report No.: 05078.

[5] Niklason LT, Sorenson JA, Nelson JA. Scattered radiation in chest radiography. Med Phys 1981 Sep;8(5):677-81.

[6] J D Robb and G A M Webb. Value of Unit Collective Dose for Use in the 1990s. Holburn, London: National Radiation Protection Board (NRPB); 1993. Report No.: 2, Volume 4.

9 Bibliography

1999, *The Ionising Radiations Regulations*, The Stationary Office Limited, London, SI 1999 / 3232 Health and Safety.

The Visual Human Project. http://www.nlm.nih.gov/research/visible/visible_human.html . 2-12-2008. Ref Type: Internet Communication

Aitchinger, H., Dierker, J., Joite-Barfus, S., & Sable, M. 2004, *Radiation Exposure and Image Quality in X-ray Diagnostic Radiology* Springer, Berlin.

Barten, P. G. J. Physical model for the Contrast Sensitivity of the human eye. Proc.SPIE [1666], 57-72.1992.

Baydush, A. H., Ghem, W. C., & Floyd, C. E., Jr. 2000, "Anthropomorphic versus geometric chest phantoms: a comparison of scatter properties", *Med.Phys.*, vol. 27, no. 5, pp. 894-897.

Boone, J. M., Seibert, J. A., Sabol, J. M., & Tecotzky, M. 1999, "A Monte Carlo study of x-ray fluorescence in x-ray detectors", *Med.Phys.*, vol. 26, no. 6, pp. 905-916.

Buhr, E., Gunther-Kohfahl, S., & Neitzel, U. 2003, "Accuracy of a simple method for deriving the presampled modulation transfer function of a digital radiographic system from an edge image", *Med.Phys.*, vol. 30, no. 9, pp. 2323-2331.

Burgess, A. E. 1999, "The Rose model, revisited", *J.Opt.Soc.Am.A Opt.Image Sci.Vis.*, vol. 16, no. 3, pp. 633-646.

Carton, A. K., Vandenbroucke, D., Struye, L., Maidment, A. D., Kao, Y. H., Albert, M., Bosmans, H., & Marchal, G. 2005, "Validation of MTF measurement for digital mammography quality control", *Med.Phys.*, vol. 32, no. 6, pp. 1684-1695.

Centre for Evidence Based Purchasing 2005, *Digital Imaging Systems for General Radiography. A comparative technical report.*, CEP, London, UK, 05078.

Chan, H. P., Lam, K. L., & Wu, Y. Z. 1990, "Studies of performance of antiscatter grids in digital radiography: effect on signal-to-noise ratio", *Med.Phys.*, vol. 17, no. 4, pp. 655-664.

Chotas, H. G., Floyd, C. E., Jr., Dobbins, J. T., III, & Ravin, C. E. 1993, "Digital chest radiography with photostimulable storage phosphors: signal-to-noise ratio as a function of kilovoltage with matched exposure risk", *Radiology*, vol. 186, no. 2, pp. 395-398.

Chotas, H. G., Floyd, C. E., Jr., Johnson, G. A., & Ravin, C. E. 1997, "Quality control phantom for digital chest radiography", *Radiology*, vol. 202, no. 1, pp. 111-116.

Cunningham, I. A. & Reid, B. K. 1992, "Signal and noise in modulation transfer function determinations using the slit, wire, and edge techniques", *Med.Phys.*, vol. 19, no. 4, pp. 1037-1044.

Cunningham, I. A. & Shaw, R. 1999, "Signal-to-noise optimization of medical imaging systems", *J.Opt.Soc.Am.A* no. 16, pp. 621-632.

Cunningham, I. A. 2000, "Applied Linear Systems Theory," in *Handbook of Medical Imaging: Volume 1. Physics and Psychophysics*, Beutel J., Kundel H.L., & Van Metter R.L., eds., SPIE, Bellingham, USA, pp. 79-159.

Dendy, P. P. & Heaton, B. 1999, *Medical Science Series: Physics for Diagnostic Radiology*, second edn, Institute of Physics Publishing, Bristol, UK.

Dobbins, J. T., III, Rice, J. J., Beam, C. A., & Ravin, C. E. 1992, "Threshold perception performance with computed and screen-film radiography: implications for chest radiography", *Radiology*, vol. 183, no. 1, pp. 179-187.

Dobbins, J. T., III 2000, "Image Quality Metrics for Digital Systems," in *Handbook of Medical Imaging: Volume 1. Physics and Psychophysics*, Beutel J., Kundel H.L., & Van Metter R.L., eds., SPIE, Bellingham, USA, pp. 161-219.

Dobbins, J. T., III, Samei, E., Chotas, H. G., Warp, R. J., Baydush, A. H., Floyd, C. E., Jr., & Ravin, C. E. 2003, "Chest radiography: optimization of X-ray spectrum for cesium iodide-amorphous silicon flat-panel detector", *Radiology*, vol. 226, no. 1, pp. 221-230.

Doyle P, Honey I, Mackenzie, A., Marshall, N. W., & Smail M. 2009, *Measurement of the Performance Characteristics of Diagnostic X-ray Systems: Digital Imaging Systems*, Institute of Physics and Engineering in Medicine, Fairmount House, York, 32 part vii.

Doyle, P., Martin, C. J., & Gentle, D. 2005, "Dose-image quality optimisation in digital chest radiography", *Radiat.Prot.Dosimetry.*, vol. 114, no. 1-3, pp. 269-272.

Doyle, P., Gentle, D., & Martin, C. J. 2005, "Optimising automatic exposure control in computed radiography and the impact on patient dose", *Radiat.Prot.Dosimetry.*, vol. 114, no. 1-3, pp. 236-239.

Doyle, P. & Martin, C. J. 2006, "Calibrating automatic exposure control devices for digital radiography", *Phys.Med.Biol.*, vol. 51, no. 21, pp. 5475-5485.

European Commission 1996, *European guidelines on quality criteria for diagnostic radiographic images* EUR 16260 EN.

Evans, D. S., Workman, A., & Payne, M. 2002, "A comparison of the imaging properties of CCD-based devices used for small field digital mammography", *Phys.Med.Biol.*, vol. 47, no. 1, pp. 117-135.

Fetterly, K. A. & Hangiandreou, N. J. 2001, "Effects of x-ray spectra on the DQE of a computed radiography system", *Med.Phys.*, vol. 28, no. 2, pp. 241-249.

Goodenough, D. J., Rossmann, K., & Lusted, L. B. 1974, "Radiographic applications of receiver operating characteristic (ROC) curves", *Radiology*, vol. 110, no. 1, pp. 89-95.

Green, D. M. & Swets, J. A. 1974, *Signal detection theory and psychophysics* Krieger, Huntington, New York.

Gurvich, V. A. 2000, "Statistical approach for image quality evaluation in daily medical practice", *Med.Phys.*, vol. 27, no. 1, pp. 94-100.

Hajian-Tilaki, K. O., Hanley, J. A., Joseph, L., & Collet, J. P. 1997, "A comparison of parametric and nonparametric approaches to ROC analysis of quantitative diagnostic tests", *Med.Decis.Making*, vol. 17, no. 1, pp. 94-102.

Hanley, J. A. & McNeil, B. J. 1982, "The meaning and use of the area under a receiver operating characteristic (ROC) curve", *Radiology*, vol. 143, no. 1, pp. 29-36.

Hanley, J. A. 1988, "The robustness of the "binormal" assumptions used in fitting ROC curves", *Med.Decis.Making*, vol. 8, no. 3, pp. 197-203.

Hart, D., Jones, D. G., & Wall, B. F. 1994, *Wall Estimation of effective dose in diagnostic radiology from entrance surface dose and dose-area product measurements*, National Radiation Protection Board, Chilton, R262.

Illers, H., Buhr, E., & Hoeschen, C. 2005, "Measurement of the detective quantum efficiency (DQE) of digital X-ray detectors according to the novel standard IEC 62220-1", *Radiat.Prot.Dosimetry.*, vol. 114, no. 1-3, pp. 39-44.

Institute of physics and Engineering in Medicine (IPEM) 2005, *Recommended standards for routine performance testing of diagnostic X-ray imaging systems.*, IPEM, Fairmount House, York, 91, 2nd Edition.

International Commission on Radiation Units and Measurements (ICRU) 1996, *Medical Imaging - the assessment of image quality.*, ICRU, Bethesda, MD, 54.

International Commission on Radiation Units and Measurements (ICRU) 2008, *Tissue Substitutes in Radiation Dosimetry and Measurement*, ICRU, Bethesda, MD.

International Electrotechnical Commission 2003, *Medical electrical equipment: characteristics of digital X-ray imaging devices - part 1: determination of the detective quantum efficiency.*, IEC, Geneva, Switzerland, 62220-1.

International Organization for Standardization (ISO) 2004, *Photography - Sensitometry of screen-film systems for medical radiography. Part 1: Determination of sensitometric curve shape, speed and average gradient*, ISO, Geneva, 9236-1.

J D Robb and G A M Webb 1993, *Value of Unit Collective Dose for Use in the 1990s*, National Radiation Protection Board (NRPB), Holburn, London, 2, Volume 4.

Jones, D. G. & Wall, B. F. 1985, *Organ doses from medical X-ray examinations calculated using Monte Carlo techniques*, NRPB, Chilton, R186.

Kodak Medical Physics. Calibrating AEC Devices. 2001. Ref Type: Pamphlet

Kruger, R. A., Anderson, R. E., Koehler, P. R., Nelson, J. A., Sorenson, J. A., & Morgan, T. 1981, "A method for the non-invasive evaluation of cardiovascular dynamics using a digital radiographic device", *Radiology*, vol. 139, no. 2, pp. 301-305.

L.W.Goldman & M.V.Yester 2004, *Specifications, performance evaluations, and quality assurance of radiographic and fluoroscopic systems in the digital era*, Medical Physics Publishing, Wisconsin, US, 30.

Lanhede, B., Bath, M., Kheddache, S., Sund, P., Bjorneld, L., Widell, M., Almen, A., Besjakov, J., Mattsson, S., Tingberg, A., Herrmann, C., Panzer, W., Zankl, M., & Mansson, L. G. 2002, "The influence of different technique factors on image quality of chest radiographs as evaluated by modified CEC image quality criteria", *Br.J.Radiol.*, vol. 75, no. 889, pp. 38-49.

Lasko, T. A., Bhagwat, J. G., Zou, K. H., & Ohno-Machado, L. 2005, "The use of receiver operating characteristic curves in biomedical informatics", *J.Biomed.Inform.*, vol. 38, no. 5, pp. 404-415.

Launders, J. H., Kengyelics, S. M., & Cowen, A. R. 1998, "A comprehensive physical image quality evaluation of a selenium based digital x-ray imaging system for thorax radiography", *Med.Phys.*, vol. 25, no. 6, pp. 986-997.

Launders, J. H., Cowen, A. R., Bury, R. F., & Hawkridge, P. 2001, "Towards image quality, beam energy and effective dose optimisation in digital thoracic radiography", *Eur.Radiol.*, vol. 11, no. 5, pp. 870-875.

Mackenzie, A. & Honey, I. D. 2007, "Characterization of noise sources for two generations of computed radiography systems using powder and crystalline photostimulable phosphors", *Med.Phys.*, vol. 34, no. 8, pp. 3345-3357.

Mah, E., Samei, E., & Peck, D. J. 2001, "Evaluation of a quality control phantom for digital chest radiography", *J.Appl.Clin.Med.Phys.*, vol. 2, no. 2, pp. 90-101.

Marshall, N. W. 2006, "Retrospective analysis of a detector fault for a full field digital mammography system", *Phys.Med.Biol.*, vol. 51, no. 21, pp. 5655-5673.

Marshall, N. W. 2007, "Early experience in the use of quantitative image quality measurements for the quality assurance of full field digital mammography x-ray systems", *Phys.Med.Biol.*, vol. 52, no. 18, pp. 5545-5568.

Martin, C. J. & Sutton, D. G. 2002, *Practical Radiation Proitection in Healthcare* Oxford University Press, Oxford.

McNeil, B. J. & Hanley, J. A. 1984, "Statistical approaches to the analysis of receiver operating characteristic (ROC) curves", *Med.Decis.Making*, vol. 4, no. 2, pp. 137-150.

Metz, C. E. 1986, "ROC methodology in radiologic imaging", *Invest Radiol.*, vol. 21, no. 9, pp. 720-733.

Metz, C. E. 1989, "Some practical issues of experimental design and data analysis in radiological ROC studies", *Invest Radiol.*, vol. 24, no. 3, pp. 234-245.

Metz, C. E., Wagner, R. F., Doi, K., Brown, D. G., Nishikawa, R. M., & Myers, K. J. 1995, "Toward consensus on quantitative assessment of medical imaging systems", *Med.Phys.*, vol. 22, no. 7, pp. 1057-1061.

Metz, C. E. 2006, "Receiver operating characteristic analysis: a tool for the quantitative evaluation of observer performance and imaging systems", *J.Am.Coll.Radiol.*, vol. 3, no. 6, pp. 413-422.

Metz, C. E. 2008, "ROC analysis in medical imaging: a tutorial review of the literature", *Radiol.Phys.Technol.* no. 1, pp. 2-12.

National Council on Radiation Protection and Measurements (NCRP) 1993, *Limitation of Exposure to Ionizing Radiation* Maryland, USA, 116.

National Electrical Manufacturers Association (NEMA) 2004, *Digital Imaging and Communications in Medicine (DICOM) Part 14: Greyscale Display Standard Function*, NEMA, Virginia, US, PS 3.14.

Neitzel, U. 1992, "Grids or air gaps for scatter reduction in digital radiography: a model calculation", *Med.Phys.*, vol. 19, no. 2, pp. 475-481.

Neitzel, U. 2005, "Status and prospects of digital detector technology for CR and DR", *Radiat.Prot.Dosimetry.*, vol. 114, no. 1-3, pp. 32-38.

Niklason, L. T., Sorenson, J. A., & Nelson, J. A. 1981, "Scattered radiation in chest radiography", *Med.Phys.*, vol. 8, no. 5, pp. 677-681.

O.Nobuhiro, H. N. S. M. K. T. K. N. a. A. Y. Optimal beam quality for chest computed radiography. Invest.Radiol. 31[3], 126-131. 1996.

Obuchowski, N. A. 2003, "Receiver operating characteristic curves and their use in radiology", *Radiology*, vol. 229, no. 1, pp. 3-8.

Ogawa E., Arakawa S., Ishida M., & Kato H. Quantitative analysis of imaging performance for computed radiography systems. Proc.SPIE 4682, 421-431. 1996.

Park, S. H., Goo, J. M., & Jo, C. H. 2004, "Receiver operating characteristic (ROC) curve: practical review for radiologists", *Korean J.Radiol.*, vol. 5, no. 1, pp. 11-18.

Ranger, N. T., Samei, E., Dobbins, J. T., III, & Ravin, C. E. 2005, "Measurement of the detective quantum efficiency in digital detectors consistent with the IEC 62220-1 standard: practical considerations regarding the choice of filter material", *Med.Phys.*, vol. 32, no. 7, pp. 2305-2311.

Reilly, A. J. & Sutton, D. 1997, *Spectrum processor*, The Institute of Physics and Engineering in Medicine, York, 78.

Rose, A. 1948, "The sensitivity performance of the human eye on an absolute scale", *J.Opt.Soc.Am.*, vol. 38, pp. 196-208.

Rowlands, J. A. & Yorkston, J. 2000, "Flat Panel Detectors for Digital Radiography," in *Handbook of Medical Imaging: Volume 1. Physics and Psychophysics*, Beutel J., Kundel H.L., & Van Metter R.L., eds., SPIE, Bellingham, USA, pp. 223-328.

Rowlands, J. A. 2002, "The physics of computed radiography", *Phys.Med.Biol.*, vol. 47, no. 23, p. R123-R166.

Samei, E., Flynn, M. J., & Reimann, D. A. 1998, "A method for measuring the presampled MTF of digital radiographic systems using an edge test device", *Med.Phys.*, vol. 25, no. 1, pp. 102-113.

Samei, E., Flynn, M. J., & Eyler, W. R. 1999, "Detection of subtle lung nodules: relative influence of quantum and anatomic noise on chest radiographs", *Radiology*, vol. 213, no. 3, pp. 727-734.

Samei, E., Seibert, J. A., Willis, C. E., Flynn, M. J., Mah, E., & Junck, K. L. 2001, "Performance evaluation of computed radiography systems", *Med.Phys.*, vol. 28, no. 3, pp. 361-371.

Samei, E. & Flynn, M. J. 2002, "An experimental comparison of detector performance for computed radiography systems", *Med.Phys.* , vol. 29, no. 4, pp. 447-459.

Samei, E. & Flynn, M. J. 2003, "An experimental comparison of detector performance for direct and indirect digital radiography systems", *Med.Phys.*, vol. 30, no. 4, pp. 608-622.

Samei, E., Dobbins, J. T., III, Lo, J. Y., & Tornai, M. P. 2005, "A framework for optimising the radiographic technique in digital X-ray imaging", *Radiat.Prot.Dosimetry.*, vol. 114, no. 1-3, pp. 220-229.

Samei, E., Buhr, E., Granfors, P., Vandenbroucke, D., & Wang, X. 2005, "Comparison of edge analysis techniques for the determination of the MTF of digital radiographic systems", *Phys.Med.Biol.*, vol. 50, no. 15, pp. 3613-3625.

Sandborg, M., McVey, G., Dance, D. R., & Alm, C. G. 2001, "Schemes for the optimization of chest radiography using a computer model of the patient and x-ray imaging system", *Med.Phys.*, vol. 28, no. 10, pp. 2007-2019.

Siewerdsen, J. H., Antonuk, L. E., El-Mohri, Y., Yorkston, J., Huang, W., Boudry, J. M., & Cunningham, I. A. 1997, "Empirical and theoretical investigation of the noise performance of indirect detection, active matrix flat-panel imagers (AMFPIs) for diagnostic radiology", *Med.Phys.*, vol. 24, no. 1, pp. 71-89.

Sorenson, J. A. & Floch, J. 1985, "Scatter rejection by air gaps: an empirical model", *Med.Phys.*, vol. 12, no. 3, pp. 308-316.

Swets, J. A. 1988, "Measuring the accuracy of diagnostic systems", *Science*, vol. 240, no. 4857, pp. 1285-1293.

Tingberg, A., Herrmann, C., Lanhede, B., Almen, A., Sandborg, M., McVey, G., Mattsson, S., Panzer, W., Besjakov, J., Mansson, L. G., Kheddache, S., Alm, C. G., Dance, D. R., Tylen, U., & Zankl, M. 2004, "Influence of the characteristic curve on the clinical image quality of lumbar spine and chest radiographs", *Br.J.Radiol.*, vol. 77, no. 915, pp. 204-215.

Tucker, D. M. & Rezentes, P. S. 1997, "The relationship between pixel value and beam quality in photostimulable phosphor imaging", *Med.Phys.*, vol. 24, no. 6, pp. 887-893.

University of Chicago 2008, "Reciever Operating Characteristic program software downloads. http://www-radiology.uchicago.edu/krl/KRL_ROC/software_index6.htm", *Date accessed*.

Walsh, S. J. 1997, "Limitations to the robustness of binormal ROC curves: effects of model misspecification and location of decision thresholds on bias, precision, size and power", *Stat.Med.*, vol. 16, no. 6, pp. 669-679.

Wilkinson, L. E. & Heggie, J. C. 1997, "Determination of correct AEC function with computed radiography cassettes", *Australas.Phys.Eng Sci.Med.*, vol. 20, no. 3, pp. 186-191.

Workman, A. & Cowen, A. R. 1993, "Signal, noise and SNR transfer properties of computed radiography", *Phys.Med.Biol.*, vol. 38, pp. 1789-1808.

Yaffe, M. J. & Rowlands, J. A. 1997, "X-ray detectors for digital radiography", *Phys.Med.Biol.*, vol. 42, no. 1, pp. 1-39.

Zhao, W., Ji, W. G., Debrie, A., & Rowlands, J. A. 2003, "Imaging performance of amorphous selenium based flat-panel detectors for digital mammography: characterization of a small area prototype detector", *Med.Phys.*, vol. 30, no. 2, pp. 254-263.

Zweig, M. H. & Campbell, G. 1993, "Receiver-operating characteristic (ROC) plots: a fundamental evaluation tool in clinical medicine", *Clin.Chem.*, vol. 39, no. 4, pp. 561-57